Novel silicon sensors for neutron detection

Consuelo Guardiola Salmerón

Department of Physics

Universitad Autónoma de Barcelona

A thesis submitted for the degree of

PhilosophiæDoctor (PhD) in Physics

2012

El Dr. Manuel Lozano Fantoba, profesor de investigación del Consejo Superior de Investigaciones Científicas (CSIC), la Dra. Celeste Fleta Corral, investigadora del Instituto de Microelectrónica de Barcelona (IMB-CNM, CSIC), y el Dr. Enrique Fernández Sánchez, catedrático de la Universitat Autònoma de Barcelona (UAB),

CERTIFICAN:

Que la memoria titulada **"Novel silicon sensors for neutron detection"** presentada por Consuelo Guardiola Salmerón para optar al grado de Doctora en Física por la Universitat Autònoma de Barcelona ha sido realizada bajo su dirección en el Instituto de Microelectrónica de Barcelona del Consejo Superior de Investigaciones Científicas.

Barcelona,
Noviembre 2012

Directores de Tesis: Dr. Manuel Lozano Fantoba y Dra. Celeste Fleta Corral.
Tutor de Tesis: Prof. Enrique Fernández Sánchez.

Abstract

The accurate detection and dosimetry of neutrons in mixed and pulsed radiation fields is a demanding instrumental issue with great interest both for the industrial and medical communities. Recent studies of the neutron contamination around medical linear accelerators have increased the concern about the secondary cancer risk for radiotherapy patients undergoing treatment in photon modalities at energies greater than 8 MeV. In this thesis, an innovative alternative to standard detectors with an active method to measure neutrons around a medical linac has been developed in response to that need. Novel ultra–thin silicon detectors with 3D electrodes adapted for neutron detection have been fabricated and optimized for such purpose. The active volume of these sensors is only 10 μm thick, allowing a high gamma rejection, which is necessary to discriminate the neutron signal in the radiotherapy peripheral radiation field with a high gamma background. These neutron detectors are not only a promising solution to estimate patient risk since they may provide medical staff a fast feedback for optimal treatment planning, but expand the functional applications of current neutron detectors for other environments with mixed gamma-neutron radiation fields such as nuclear and aerospace environments or microdosimetry. Moreover, the intrinsic features of the silicon devices like robustness, small size, consumption and weight, make them ideal for portable systems.

The research presented in this work describes first the Monte Carlo simulations to optimize the design of the prototypes, secondly the fabrication processes of the detectors, and third the electrical characterization and calibration with radioactive sources of these sensors. Finally, it is shown the good performance of the novel ultra–thin 3D silicon detectors for neutron detection inside a radiotherapy room.

Contents

List of Figures **vi**

List of Tables **xii**

Scope of the thesis **xiv**

1 Introduction **1**

1.1 Motivation 1

1.2 Neutron environments 5

1.2.1 Radiotherapy linear accelerators 6

1.2.2 Nuclear security 10

1.3 Framework: research projects 11

1.3.1 Generalitat de Catalunya Project: RAMPO 11

1.3.2 Spanish National Project: NEUTOR III 11

1.3.3 European Project: REWARD 12

2 Neutrons **14**

2.1 General characteristics of neutrons 14

2.2 Neutron interactions 16

2.2.1 Elastic scattering 23

2.2.2 Inelastic scattering 24

2.2.3 Neutron capture 25

2.2.4 Fission reaction 28

2.3 Neutron detection methods 28

2.3.1 Slow neutron detection 30

2.3.2 Fast neutron detection 33

2.4 State-of-the-art in active neutron detectors . . . 33
2.4.1 Gaseous detectors . . . 34
2.4.1.1 ^3He-filled gas proportional counters . . . 35
2.4.1.2 Boron Trifluoride (BF_3) proportional tubes . . . 37
2.4.1.3 Boron-lined Proportional Counters . . . 40
2.4.2 Scintillators . . . 40
2.4.3 Semiconductor detectors . . . 43
2.4.3.1 Planar silicon neutron detectors . . . 48
2.4.3.2 Microstructured neutron detectors . . . 58

3 Monte Carlo simulations 66
3.1 Monte Carlo method . . . 66
3.1.1 Method and applications . . . 67
3.1.2 Variance reduction . . . 69
3.1.3 Monte Carlo codes for Nuclear and Particle Physics . . . 70
3.2 MCNPX simulation code . . . 72
3.2.1 Geometry, materials, source . . . 73
3.2.2 Particle transport: neutron, gamma, and electron transport . . . 76
3.2.3 Input file . . . 77
3.2.4 Variance reduction in MCNPX . . . 79
3.2.5 Out File: tallies and analysis . . . 79
3.3 GEANT4 simulation toolkit . . . 81
3.3.1 Mandatory user classes . . . 90
3.3.2 User action classes . . . 93
3.3.3 Optional user action, initialization, and analysis classes . . . 94
3.3.4 Execution and out-files . . . 95
3.4 Simulation results for planar designs . . . 96
3.4.1 Simulated thermal neutron detection efficiency . . . 99
3.4.2 Simulated reaction product spectra . . . 104
3.5 Prototypes of 3D silicon neutron detectors . . . 107
3.5.1 Simulations of Microstructured Designs . . . 108

4 Silicon sensors for neutron detection **115**

4.1 Planar silicon detectors . . . 117

4.1.1 P-i-N planar silicon detectors . . . 117

4.1.2 Schottky barrier silicon diodes . . . 118

4.1.2.1 Fabrication process of Schottky diodes . . . 119

4.1.2.2 Characterization of Schottky diodes . . . 122

4.2 Ultra-thin 3D silicon detectors . . . 124

4.2.1 3D architecture for silicon detectors . . . 125

4.2.2 Ultra-thin 3D layouts . . . 129

4.2.3 Fabrication process of ultra-thin 3D detectors . . . 133

4.2.4 Characterization of ultra-thin 3D detectors . . . 140

5 Experimental validation of the silicon neutron detectors **143**

5.1 Preliminary tests . . . 144

5.1.1 Proof–of–concept with planar PIN diodes . . . 144

5.1.2 Neutron detection with Schottky diodes . . . 147

5.2 Experiments with ultra–thin 3D detectors . . . 157

5.2.1 Gamma–ray rejection factor . . . 158

5.2.2 Neutron-gamma ray discrimination . . . 160

5.2.3 Neutron detection efficiency in a nuclear reactor beam . . . 162

5.3 Application at LINAC workplaces . . . 167

5.3.1 Simulated neutron fields in radiotherapy treatment rooms . . . 167

5.3.2 Measurements and results . . . 170

5.3.2.1 Detector sensitivity to gamma-rays . . . 170

5.3.2.2 Closed field at 6 MV and 15 MV . . . 172

5.3.2.3 Detector sensitivity to fast neutrons . . . 174

5.3.2.4 Detector response: Linearity . . . 174

5.3.2.5 Detector response versus irradiation rate: no-saturation effect . . . 176

5.3.2.6 Detector sensitivity in RT rooms . . . 177

5.3.2.7 Energy spectra . . . 177

5.4 Discussion & Summary . . . 181

6 Conclusions and Future Work **183**

6.1 Conclusions 183

6.2 Ongoing and future work 186

Appendixes **188**

A Coating methods of neutron converters **188**

A.1 Carboranes 189

A.1.1 Spin-coating method 190

A.1.2 Filling of 3D structures 192

A.2 Microcrystalline ^{10}B solids 193

A.2.1 ^{10}B Coatings 193

A.2.2 Backfilled ^{10}B 204

A.3 Boron Carbide 209

B Readout electronics **213**

B.1 First Readout Electroincs 215

B.2 New Readout Electronics 218

C Characterization techniques **220**

C.1 Electrical characterization 220

C.2 Calibration with radioactive sources 223

D Other applications **226**

D.1 Medicine nuclear: particle therapy 226

D.2 Nuclear security 230

References **232**

Scientific contributions **238**

List of Figures

1.1 Block diagram of common neutron detectors 3
1.2 Geometry of a medical linear electron accelerator 7
1.3 Neutron weighting factor 9
1.4 Sketch of monitoring tags in REWARD 12
1.5 REWARD operation 13

2.1 Feynman diagram for the neutron beta decay. 15
2.2 Neutron interactions. 17
2.3 Total neutron cross–sections of ^{3}He, ^{6}Li, ^{10}B. 20
2.4 Total neutron cross–sections of ^{113}Cd, ^{155}Gd. 21
2.5 Elastic scattering diagram for the laboratory frame. 24
2.6 Total neutron cross sections of ^{1}H, ^{14}N, and ^{23}Na. 26
2.7 Working principle of a ^{3}He counter 35
2.8 Regions of a gaseous ionization detector 36
2.9 Pulse height spectrum in a ^{3}He-filled gas proportional counter 38
2.10 Image of a typical BF3 tube 38
2.11 Pulse-height spectrum for a BF_3 proportional counter 39
2.12 Sketch of a boron-lined counter 41
2.13 Pulse Amplitude Spectrum from a boron-lined proportional counter . . 41
2.14 Schematic diagram of a scintillation detector 42
2.15 Working principle of a scintillator detector for neutrons 43
2.16 Schematic of a PIN diode 45
2.17 Working principle of a planar semiconductor detector for neutrons . . . 47
2.18 Schematic of the standard 2D and 3D design for silicon neutron detectors 48
2.19 Sketch of planar detector irradiated by neutrons. 49

2.20 Thermal neutron absorption probability in solid converters 51
2.21 Thermal neutron mean free path as a function of the ^{10}B density 53
2.22 Range of the reaction products of ^{10}B 54
2.23 Calculated planar detection efficiency for thermal neutrons 57
2.24 Schematic of a 3D design 59
2.25 Schematic diagram of a perforated semiconductor detector 60
2.26 Schematic of possible incident beams. 62
2.27 Cross-section details of two perforated silicon neutron detectors. 63
2.28 Silicon neutron detector with etching pillar structure. 64
2.29 Image of etched hexagonal holes filled with B_4C. 65

3.1 Varian LINAC modeled in MCNPX 74
3.2 Initial run file in MCNPX 78
3.3 Examples of GEANT4 simulations with GATE and GAMOS architectures 82
3.4 ATLAS detector simulated with GEANT4 83
3.5 GEANT4 class categories 87
3.6 Boolean operations on CSG 91
3.7 Planar silicon detector simulated with MCNPX. 98
3.8 Planar silicon detector simulated with GEANT4. 99
3.9 Simulated thermal neutron detection efficiency with MCNPX in a planar detector covered with ^{10}B for several densities. 101
3.10 Simulated thermal neutron detection efficiency for planar silicon detectors covered with ^{10}B with MCNPX and GEANT4 codes. 102
3.11 Simulated thermal neutron detection efficiency for planar silicon detectors covered with o-carboranes using MCNPX and GEANT4 codes. . . . 103
3.12 Simulated spectra of energy deposited in a planar silicon detector covered with ^{10}B of d=1 g/cm^3 106
3.13 Simulated spectra of energy deposited in a planar silicon detector covered with ^{10}B of d=2.5 g/cm^3 106
3.14 Schematic of a 3D design of trenches 107
3.15 Sketch of the 3D-pattern with microchannels filled with ^{10}B 110
3.16 Dependence of the simulated efficiency versus trench width for several ^{10}B densities 111

3.17 Dependence of the efficiency versus trench width for several silicon wall widths . . . 112
3.18 Dependence of the efficiency versus trench width for several channel depths 113
3.19 Dependence of the efficiency versus channel width for several silicon wall widths . . . 114
3.20 Dependence of the efficiency versus silicon wall width for several channel widths . . . 114

4.1 Sketch of a p–i–n PAD detector . . . 117
4.2 Schottky diode structure fabricated at IMB–CNM . . . 119
4.3 Photo of a wafer of Schottky detectors fabricated at the IMB–CNM clean room facilities. . . . 121
4.4 Image of a Schottky diode fabricated at IMB–CNM . . . 122
4.5 I–V curves for Schottky diodes . . . 123
4.6 C–V curve for Schottky diodes . . . 124
4.7 Cross sections of 3D and planar geometrics . . . 126
4.8 Schematic cross section of a 3D semiconductor detector . . . 127
4.9 Front side 3D pattern . . . 127
4.10 Capacitance of the 3D and planar detectors versus silicon thickness . . . 129
4.11 Cross-section of the ultra–thin 3D design. . . . 130
4.12 Schematic of the ultra–thin 3D detector front-side . . . 130
4.13 Microscope images of the first ultra-thin 3D detectors . . . 132
4.14 Improvement of the ultra-thin 3D designs . . . 132
4.15 Steps of a DRIE etching of a trench. . . . 134
4.16 Aspect ratio for hole as a function of the etching time . . . 134
4.17 Fabrication process of the U3DTHIN: Holes N . . . 135
4.18 Fabrication process of the U3DTHIN: Holes P . . . 136
4.19 Fabrication process of the U3DTHIN: Metallization . . . 136
4.20 Fabrication process of the U3DTHIN: Passivation . . . 137
4.21 Pattern masks used for the U3DTHIN fabrication process . . . 137
4.22 Photograph of manufactured wafer with ultra-thin 3D detectors . . . 138
4.23 Optical microscope images of an ultra-thin 3D detector . . . 138
4.24 SEM images of the cross-section of the U3DTHIN detector . . . 139

4.25 SEM image of the columnar electrodes of the U3DTHIN detector 140
4.26 I–V curves of ultra-thin 3D detectors 141
4.27 C–V curves of ultra-thin 3D detectors 141
4.28 Photographs of two U3DTHIN detectors on PCB 142

5.1 Neutron spectrum from a $^{241}AmBe$ source 144
5.2 Silicon PIN pad covered by moderation/conversion layers 145
5.3 Diagram of the first experimental setup 146
5.4 Experimental test configuration 146
5.5 Oscilloscope signal for the preliminary experiment with $^{241}AmBe$ 147
5.6 Deposit of O-carboranes 148
5.7 Fluence of moderated neutrons within polyethylene 150
5.8 Experimental test configuration with Schottky diodes 151
5.9 Pulse height distribution of the Schottky detector 152
5.10 Oscilloscope signal of neutron detection with a Schottky diode 152
5.11 Count rate of the Schottky detector 153
5.12 Simulated pulse height distributions of the Schottky 157
5.13 Spectrum of ^{137}Cs in silicon detectors 159
5.14 Simulated spectra of energy deposited in planar silicon detectors irradiated with ^{137}Cs gamma source 159
5.15 Pulse height distribution measured using a $^{241}AmBe$ γ-n source. 161
5.16 Experimental setup in the ITN's nuclear reactor 163
5.17 Linear response of the ultra-thin 3D detector tested with the ITN's nuclear reactor 165
5.18 Measured pulse height distribution of the ultra-thin 3D detector with o–carborane 166
5.19 Simulated fluence spectral distribution inside a radiotherapy room . . . 168
5.20 Simulated detection efficiency inside radiotherapy room. 169
5.21 Comparison of the simulated detection efficiencies for two possible incident neutron beams 169
5.22 Experimental set–up in the Santiago de Compostela's Hospital 171
5.23 Total counts accumulated versus irradiation fluence for a bare ultra-thin 3D detector 173

5.24 Linear response of the ultra-thin 3D detector covered with ^{10}B. 175
5.25 Response of the ultra-thin 3D detector versus irradiation rate. 176
5.26 Measured total counts as a function of the ^{10}B layer thickness. 178
5.27 Measured pulse height distribution with $^{10}B_4C$ 0,5, 1, and 1.5 μm thick 179
5.28 Spectra of an ultra-thin 3D detector with ^{10}B coatings 180

A.1 Chemical structures of carboranes 189
A.2 Manual Spinner used to deposit O-carboranes 191
A.3 Profile of an o–carborane/matrix deposition with spinner 192
A.4 Micro-pipettes used to fill 3D structures 193
A.5 SEM images of the columnar holes filled with o–carborane 193
A.6 Sketch of the type of stresses 196
A.7 Image of ^{10}B hot–pressed chunks 198
A.8 Electron-Beam Gun Machine for Physical Vapor Deposition 199
A.9 Photos of the ^{10}B coating over silicon substrate 201
A.10 Measured Profile of an evaporated coating by EBPVD 202
A.11 SEM images of the cross section of electron-beam deposited 10B coatings on silicon substrate 203
A.12 EDX analysis of 1μm thick ^{10}B layer 204
A.13 Perforated prototypes backfilled with ^{10}B 205
A.14 ^{10}B nanoparticles grown inside trenches 206
A.15 Backfilled ^{10}B of 3 μm thick 208
A.16 RF Sputtering machine for PVD 210
A.17 Microscope photo of 1.5 μm of $^{10}B_4C$ coating over an ultra–thin 3D detector 211
A.18 $^{10}B_4C$ coatings over ultra–thin 3D detectors 211

B.1 Electronic circuit that represents a detector 214
B.2 Built–in portable readout electronics 216
B.3 Readout electronic basic sketch in a nuclear detector 216
B.4 Electronic diagram of the readout electronics with preamplifier, amplifier and pulse shaping. 217
B.5 Electronic diagram of the new readout electronics 218
B.6 Picture of the new portable readout electronics system 219

C.1 Set-up used for the electrical characterization 221
C.2 Capacitance-voltage curve for p-on-n PAD detectors 222
C.3 I–V curve of a typical planar diode 223
C.4 Set–up of calibration 224
C.5 Spectrum from an alpha calibration source 224

D.1 Chronological diagram of the implementation of hadron therapy 227
D.2 Depth dose curves for photons, neutrons, and protons 228
D.3 Ultra-thin 3D detector slimmed 230
D.4 Illustration of stacked ultra-thin 3D detectors 231

List of Tables

1.1 Radiation weighting factors. 8

2.1 Neutron characteristics. 15
2.2 Neutron classification as a function of its kinetic energy. 16
2.3 Neutron interaction types. 18
2.4 Capture reactions of neutron converters. 27
2.5 Mean-free-paths of thermal neutrons into solid converters. 50
2.6 Range of reaction products from neutron capture in different materials. 52
2.7 Ranges of the $^{10}B(n,\alpha)^{7}Li$ reaction products in ^{10}B. 54

3.1 Materials used in this study in the MCNPX code. 75
3.2 Particle libraries in MCNPX. 77
3.3 Tallies in MCNPX. 80
3.4 Converter composition 97

4.1 Average Current @10V and @100V for wafer #4. 123
4.2 Layout features of the ultra-thin 3D detectors. 131
4.3 Characteristics of the U3DTHIN design-A. 142
4.4 Characteristics of the U3DTHIN design-B. 142

5.1 Moderator and converter characteristics 145
5.2 Moderation effect of the neutrons emitted from an $^{241}AmBe$ source within polyethylene cylinder. 149
5.3 Gamma and Neutron emission per 10^6 alphas of $^{241}AmBe$ source. . . . 155
5.4 ^{137}Cs source characteristics 158
5.5 Converter composition 161

5.6 Neutron flux and gamma field powered in the ITN nuclear reactor. . . . 164
5.7 Boron-based compounds on ultra-thin 3D detectors 172
5.8 Spectra with closed field at 6 and 15 MV with 800 total MU. 174
5.9 Counts for Sample A3 with and without Cadmium shielding 174

A.1 Main adhesive matrixes and solvents used with carboranes 189
A.2 O-carboranes used as converter coatings 190
A.3 Spin-Coating Parameters 192
A.4 ^{10}B Characteristics 194
A.5 Coefficients of thermal expansion of several materials at 300 K. 197
A.6 Samples with consecutive evaporation of Ti and ^{10}B. 200
A.7 Experimental conditions used in the EBPVD for ^{10}B coatings 200
A.8 ^{10}B Thicknesses measured by profiler 202
A.9 Temperature cycle testing parameters 204
A.10 B_4C Characteristics 209

Scope of the thesis

The present work is dedicated to develop an active measurement sensor for the detection of the neutrons that are generated by linear accelerators in radiotherapy treatment rooms. For this purpose, this thesis deals with novel silicon particle detectors optimized with Monte Carlo simulations, their design, fabrication and characterization, as well as their validation in medical facilities.

The work performed along this thesis intends, first, to establish and consolidate a research line in neutron detection focused on silicon sensors. Second, to set up a Monte Carlo simulation-platform for the study of the interaction of the radiation with the matter with the aim of optimizing particle detectors. Third, to advance in CMOS microfabrication techniques to overcome challenges in the neutron detection field. Finally, to characterize the neutron detectors developed in this work with linear accelerators used in medical facilities.

This manuscript is organized in 6 chapters and 4 appendixes as follows:

- Chapter 1 presents an overview of the thesis and includes a brief summary about the framework in which the present study has been carried out.
- Chapter 2 is devoted to review the state-of-the-art in neutron detection.
- Chapter 3 describes the Monte Carlo method and its implementation in this study with the GEANT4 and MCNPX simulation codes.
- Chapter 4 deals with the neutron detectors developed in this thesis: their design optimized with Monte Carlo simulations, the main CMOS microfabrication steps, characterization, and calibration.

- Chapter 5 presents the experiments carried out with the neutron detectors presented in Chapter 4 with some standard radiation sources and inside a radiotherapy treatment room.
- Finally, Chapter 6 summarizes the conclusions of this work as well as the ongoing work and the future prospects.

Four appendixes have been added to the manuscript as complementary information: Appendix A details the deposit methods developed to coat/fill the sensors to adapt them for neutron detection. Appendix B displays the custom-made readout electronics system used to carry out the experimental tests. Appendix C describes briefly the main techniques used to characterize electrically the detectors and to calibrate them with standard radioactive sources. Finally, Appendix D deals with other medical application in which the presented detectors may be potentially used.

1

Introduction

1.1 Motivation

One of the goals of the Radiation Detectors Group at the Instituto de Microelectrónica de Barcelona (IMB-CNM, CSIC) during the last four years has been to expand its research activities from the High Energy Physics (HEP) detection field to Medical Physics applications. In this area, the accurate detection and dosimetry of neutrons is a key concern for the medical community. Staff and patients are at risk of possible additional doses from the photoneutron production in radiotherapy linear accelerators (LINACs) working at photon energies greater than 8 MeV. In this work, we have tried to develop an alternative to standard neutron detectors to be used in these workplaces.

Radiotherapy treatments (RT) with electron LINACs are used worldwide to treat cancerous tissue. When the primary electron beam collides with the target (Au or W) to produce photons, neutrons can be generated by the photoneutron reaction within the heavy materials at the LINAC head (target, primary collimators, flattening filter,

multileaf collimator, jaws, and other minor components). This generally occurs in treatments with the LINAC photon beam above 8–10 MeV, especially in Intensity Modulated RT (IMRT)[1]. With these high megavoltage RT treatments becoming more prominent to improve the conformality of the therapeutic dose, neutron exposure of the patient is increasingly becoming more significant. The out–of–field produced radiation can deliver an undesirable and damaging peripheral secondary dose around the treated organ which may induce secondary cancers [1].

An active characterization of RT environments is complex due to the pulsed nature of the mixed γ–neutron field and the high γ–ray background, so new neutron sensors aiming at portable neutron measurement systems with high γ–rejection have been incrementally demanded.

There are three main types of active–detectors based on the ionization produced by charged particles in matter [2]: gaseous detectors, semiconductors, and scintillators (Figure 1.1). All these detectors are based on the fact that charged particles or photons ionize the sensitive volume of the detector, inducing a small charge pulse. Instead, neutrons are not charged particles so they are not able to cause direct ionization processes by Coulomb interaction. However neutrons may produce charged particles in some materials by means of two basic methods: (i) by absorption in a material with high neutron capture which emits charged particles or photons, and (ii) by scattering with light nuclei that can unleash recoiled ions, the cross-section of each process depending on the material. The charged particle products of the neutron reaction can be subsequently detected by an ionization-based detector. For slow neutrons, an isotope which captures neutrons to produce charged particles is normally used. Fast neutrons are usually detected via the protons produced by elastic scattering with the hydrogen nuclei of neutron moderator materials (water, polyethylene or paraffin). Besides, neutrons appear usually in mixed fields with gamma radiation which makes the neutron identification difficult and involves other complications inherent in the n–γ discrimination.

For decades ^3He tube–based detectors have been the preferred solution to obtain high n–γ discrimination. These detectors work in the pulse–readout mode where

[1]IMRT is an advanced RT technique used to minimize the irradiation of the normal tissue. This usually is achieved by moving the multileaf collimators during the treatment, delivering a *modulated* and non-uniform radiation field.

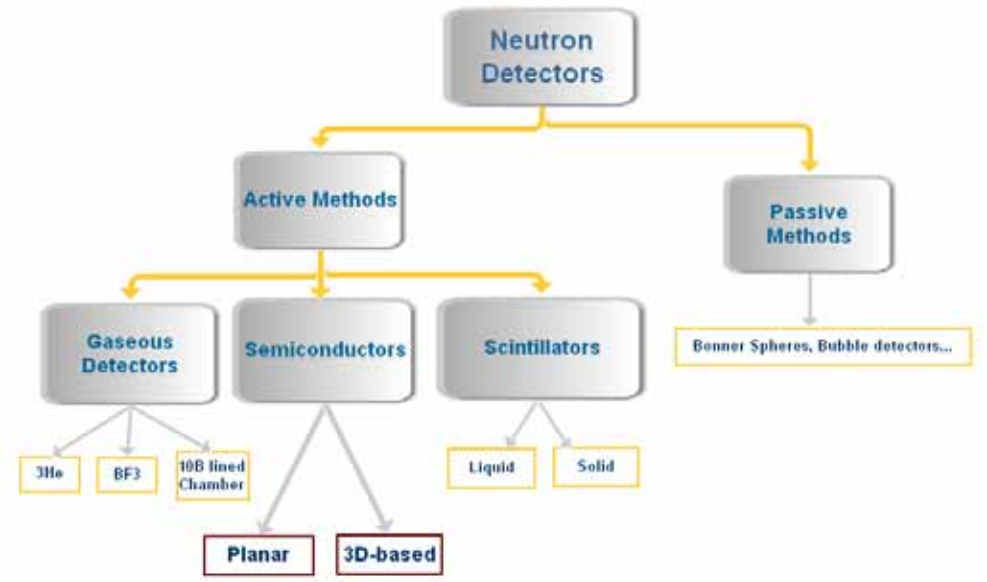

Figure 1.1: Block diagram of common neutron detectors - The diagram shows some of the most common neutron detectors. The types that are the focus of this work are underlined.

neutron and γ–ray signals are distinguished by their amplitude. ^6Li is normally used in neutron-sensitive inorganic scintillators through LiI doped with Eu. The highly enriched ^{6}LiI(Eu) crystals (96% ^{6}Li) exhibit high thermal neutron detection efficiency. However both ^3He and ^6Li–based scintillator detectors share some undesirable characteristics: not only they are bulky and require costly operating conditions (high pressures ≈10 bar and voltages ≈10 kV for ^{3}He detectors; connection to bulky photomultiplier working at hundred of volts, need for hermetic assembly due to the hygroscopic nature of LiI(Eu) crystals for ^6Li–based scintillators), exhibit slow-rise time, but also face difficulties in material supply: ^3He and ^6Li are expensive, ^3He reserves are foreseen to be consumed in the coming decades and ^6Li requires special authorizations for exportation [3]. These features do not allow for the versatility that some environments require and jeopardize the full applicability of these detectors.

In contrast, semiconductor–based detectors (SD) offer many useful features, such as compactness and robustness, low weight, bias voltage, and battery consumption, a high count rate capability, and active readout. These advantageous characteristics make them ideal for portable systems which require integrated signal acquisition and

low power. Their compactness, which is originated from the high density of the semiconductor material, allows a short range of the nuclear reaction products, but also increases the probability of interaction of the γ–rays. The ideal semiconductor candidate for neutron detection is silicon which provides a relatively low Z for moderate γ–ray interaction probability (silicon has atomic number 14, which is lower than the Z of other semiconductors used as particle detectors like Ge (Z=32), CdTe (Z=48/52), or CdZnTe (Z=48/30/52)), and above all a high technological know–how thanks to the mature microelectronics industry based on silicon [4].

Since the 1950s SDs have been used in nuclear physics for charged particle detection or gamma spectroscopy, with special importance on high energy physics in the last decades. However, the adaptation of a SD to detect neutrons entails certain complexities inherent in the particular neutron physics and therefore it is an issue still to be improved. Since neutrons do not interact with matter by direct ionization, they cannot be easily detected by means of a semiconductor as the latter relies on the creation of free carriers inside its depleted region. In order to turn a SD into a neutron detector, it is necessary to use an appropriate element (*converter*) able to capture neutrons by ejecting charged particles that can ionize the semiconductor and therefore can be detected. Thus, a semiconductor neutron detector consists of a SD covered or backfilled by a converter, or where the converter is part of the detector bulk [5]. In general, the semiconductor neutron detectors can be organized in two big groups depending on their structure or how the converter is inserted into the detector: planar and microstructured SD, both based on the principle of the PN junction to form a particle detector.

The simplest layout of a SD is the planar configuration, the neutron converter is deposited on the detector surface. This configuration has a low efficiency due to geometrical constrictions (as it is explained in Section 2.4.3.1). In contrast, microstructured SDs are presented as possible technological solutions where the SD is perforated with microstructures etched inside its bulk. These 3D structures would considerably multiply the efficiency value since they overcome the planar–geometric restriction by increasing the contact surface between the neutron converter and the SD sensitive volume with perforated patterns. In fact, more than twenty years ago, R.A. Muminov and L.D. Tsvang demonstrated that neutron detection efficiency would increase to 40%, and higher, if rectangular channels filled with converter material

were distributed along the semiconductor detector surface [6]. Although there have been a plethora of studies about this field, very few research groups have been able to manufacture a microstructured detector adapted for neutron detection due to its technological complexity. For years it has been suggested that the efficiency could reach 50%, highlighting that this issue remains incompletely resolved and novel designs may bring improvements.

In order to guide the creation of new prototypes it is necessary to develop simulations that optimize the parameters of the designs. Monte Carlo simulations have been used to such purpose. Two software packages, MCNPX and GEANT4, have been employed to assure the reliability of the detector prototype phase. Some of these designs that are feasible technologically have been developed in the IMB–CNM's clean room facilities. These detectors have shown to be a promising approach to neutron detection, and led us to propose new technology paths to build semiconductor–based neutron detectors. Moreover, the simulations allow to verify the experimental results to avoid systematic errors in the measurements.

Apart from RT environments, there are other applications where the neutrons are mixed with a large γ–ray background such as space exploration, biological imaging, or nuclear security. Hence, the neutron detectors presented in this work may be used not only for medical environments but also for requests of other physical applications as is explained in the following sections.

1.2 Neutron environments

There are several areas in which the neutron detection is also demanded [7], for instance in:

- Dosimetry: to assess the contribution of neutrons in environments where they can be present such as nuclear reactors and nuclear medicine.
- Medicine: neutrons are applied for treatment of cancer in boron capture neutron therapy (BCNT) and for activating of nuclei for radioisotope production in nuclear medicine.
- Radiation safety: neutron radiation can be a hazard when is associated with fissile material, space travel, accelerators, and nuclear reactors.

- Special Nuclear Material (SNM) detection: SNMs, such as ^{233}U and ^{239}Pu, decay by spontaneous fission, yielding neutrons. Neutrons detectors can be used to monito SNMs.

- Cosmic ray detection: secondary neutrons are one component of particle showers produced in the Earth's atmosphere by cosmic rays. Dedicated ground–level neutron detectors, namely neutron monitors, are employed to monitor variations in the cosmic ray flux.

- Imaging: neutrons may be used to imaging of biological tissue and materials.

- Materials characterization: elastic and inelastic neutron scattering enables experimentalists to characterize the structure of materials from scales ranging from Angstroms to about one micron.

The present work has been mainly focused on developing neutron sensors for covering some of those medical applications and more recently for being used in the radiation safety area, for the reasons given as below.

1.2.1 Radiotherapy linear accelerators

As said above, at treatments in which the photon beam energy of the LINAC (Figure 1.2) is above 8–10 MeV[1], neutrons may be emitted by photo-neutron evaporation reactions with materials that form the LINAC head. This is a serious concern when a high number of monitor units (MU[2]) is employed in the treatment like in modern intensity modulated RT (IMRT). With these high megavoltage RT treatments becoming more prominent to improve the conformality of the therapeutic dose, neutron exposure of the patient is increasingly more significant. The out-of-field produced radiation can deliver an undesirable and damaging peripheral dose (due to scattered and leakage

[1]For LINACs the MV unit stands for Mega-Volt, i.e. it is the unit of the electric potential used by the linear accelerator to produce the photon beam. The photon beam is made up of a spectrum of energies such that the maximum energy is approximately equal to the beam electric potential (in MeV units, i.e. Mega-electron Volts), but the mean gamma-ray energy is only around a third part of this maximum energy.

[2]A MU is a machine output of a LINAC which is calibrated to deliver an absorbed dose under particular conditions, e.g. 100 MU gives 1 Gy photon dose measured at the depth of 5 cm in tissue-equivalent phantom at 95 cm SSD for a 10×10 cm^2 field.

photons and photoneutrons) in the treated organ which may induce secondary cancers. Evaluating that secondary dose produced by neutron contamination requires knowledge

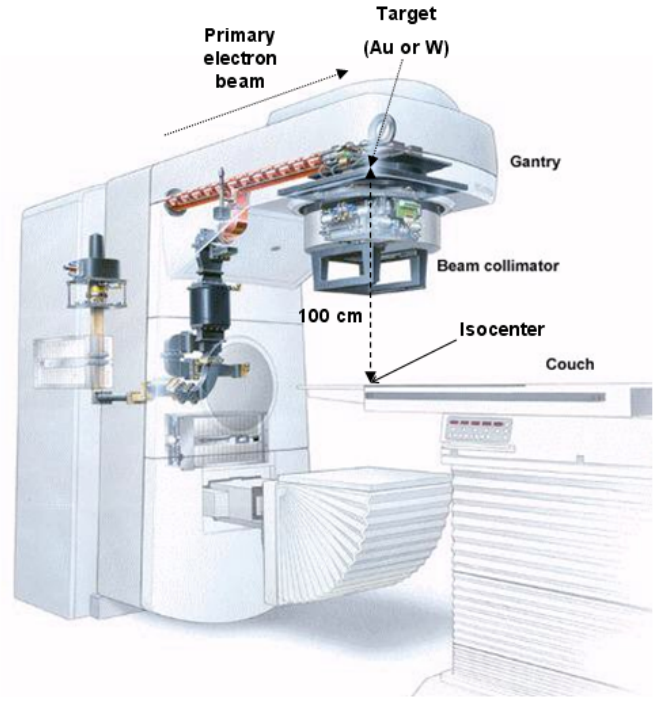

Figure 1.2: Geometry of a medical linear electron accelerator - Sketch of a typical medical accelerator used in cancer radiotherapy where the main components are indicated.

of the neutron fluence inside the treatment room. In order to estimate the biological effects it is necessary to convolute the dose by the radiation weighting factor (W_R) which describes the probability of stochastic radiation effects and depends on the kind of particle and its energy. Table 1.1 shows the radiation weighting factors for the main radiation particles used in nuclear medicine. Figure 1.3 displays the neutron W_R that varies from 2.5 to 20 for slow and fast neutrons respectively. The neutron W_R factor is considerably higher than the photons, electrons, and protons weighting factors.

Inside the patient's body, when neutrons go through tissue (composed mainly of light elements such as O (65% of mass), C (18%), H (10%), N (3%), Ca (1.4%), P (1.1%) and K (0.25%)), they interact by scattering/absorption with these nuclei. This produces moderation, recoils, or capture processes which may ionize cells, damaging the tissue. Although the International Commission on Radiological Protection (ICRP) includes the patient radiation protection as a criterion for treatment optimization [9],

Table 1.1: Radiation weighting factors.

Particles	W_R
Electrons (all energies)	1
Photons (all energies)	1
Protons	2
Charged pions	2
Alpha particles	20
Fission fragments and heavy ions	20
Neutrons	
$E_n < 1$ MeV	$2.5 + 18.2\exp(-[\ln E_n]^2/6)$
1 MeV $< E_n <$50 MeV	$5.0 + 17.0\exp(-[\ln 2E_n]^2/6)$
$E_n >$50 MeV	$2.5 + 3.25\exp(-[\ln 0.04E_n]^2/6)$

neutron presence continues being extremely high and hence it is essential to assess the neutron radiation field in the treatment rooms to prevent secondary tumor risks.

Due to the pulsed nature of the mixed γ–neutron field and the high γ–ray background, the use of neutron passive detectors has been widespread recommended to avoid instrumental problems from active devices such as signal pile–up [10]. Previous works with passive methods have been based mainly on activation of foils in Bonner spheres [11], TLD dosimeters [12], and superheated bubble emulsions [13], among others. These methods are time consuming since the detectors need to be read in an external laboratory after the exposition, so they are not widely used in clinical facilities. There are two main challenges to overcome for active detectors: (i) the photon fluence may be extremely high inside the treatment room, which does not allow the use of standard detectors that discriminate the neutron signal and the gamma background; (ii) mixed γ–neutron fields are pulsed, in the order of hundreds of hertz, so the high γ–field may well trigger signal pile-up. For these reasons, there has not been an extended use of on–line or active monitoring of the neutron field in RT rooms yet. Albeit in 2010 F. Gómez et al. [14] presented a reliable method based on the interaction of neutrons with the borophosphorsilicate glass (BPSG) in SRAM-memory cells which causes upset in their logical states that is insensitive to the photon fluence and allows to measure the slow neutron radiation field. Hereafter new active methods aiming at portable neutron measurement systems with high γ-rejection have been demanded.

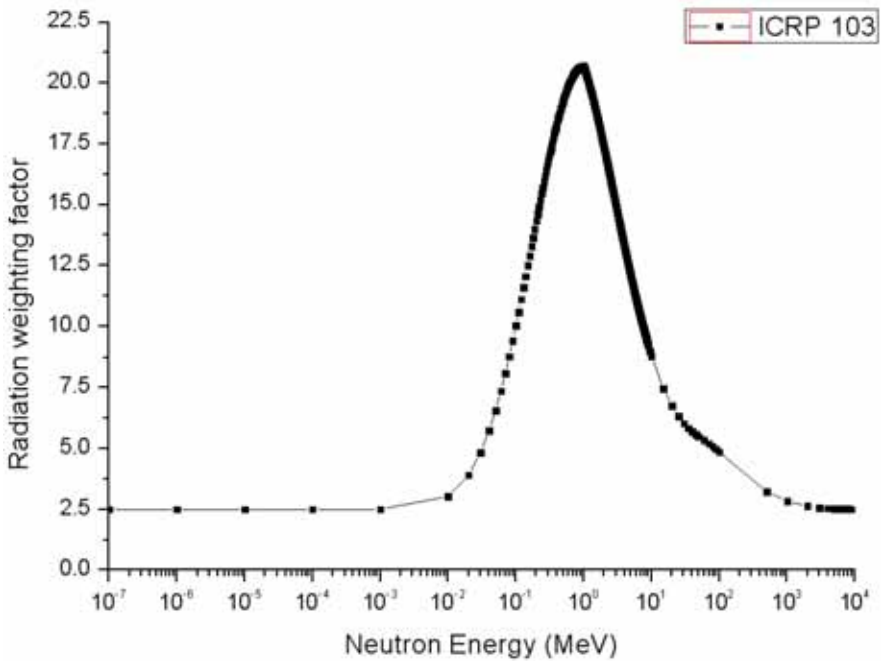

Figure 1.3: Neutron weighting factor - Neutron weighting factor versus neutron energy adopted in the 2007 Recommendations (ICRP Publications 103 [8]).

The neutron fluence depends on the geometry of the treatment rooms and the constitutive materials of the LINAC head, i.e. of the LINAC model [15]. The neutron fluence generated inside the LINAC head is roughly isotropic and it is known as *primary neutron spectrum*. However, neutrons may go through the shielding in all directions undergoing and losing energy either by inelastic scattering (dominates at low energies) or by (n,2n) reactions (at high energies), as well as by elastic scattering. All this favors a wide neutron spectrum in the room which is quite different from the primary one. Moreover, most of the LINACs are placed into rooms shielded with concrete whose hydrogen nuclei slow down the neutrons that may be captured inside the room walls and, therefore, emit γ-rays. As a consequence of all the possible interactions and scatterings, inside a LINAC room the neutron spectrum presents three main components [16]:

- A considerable component at low energy in the thermal range, with a peak around 0.025 eV, which is constant around all the room.
- A minor scattered component of epithermal neutrons at intermediate energies.

- A main peak around 1 MeV from the primary neutron spectrum.

The neutron field is accompanied by the main γ–field of the RT treatment.

1.2.2 Nuclear security

Neutron detection is essential to intercept radiological threats for security purposes since the materials used to manufacture nuclear weapons are mainly emitters of fission neutrons. In the last decade an increasing risk has arisen at world level coming from the unknown location of special nuclear materials (SNM), i.e. nuclear materials of weapons-grade, that were mainly fabricated in the former Soviet Union and that have not been strictly controlled since its disintegration. This type of materials may be sought by terrorist groups to build improvised nuclear weapons or 'dirty bombs' (conventional explosives mixed with a radioactive source that can be used as radiological dispersal devices). For instance, in the period 1993–2009, the IAEA Illicit Trafficking Database (ITDB) [17] confirmed a total of 1.773 incidents involving nuclear materials. Of these confirmed incidents, 351 involved unauthorized possession and related criminal activities, fifteen of them involving highly enriched uranium or plutonium, 500 incidents involved reported theft or loss (in 45% of the cases the lost or stolen materials were never recovered), and 870 incidents involved other unauthorized activities and events.

Another type of radioactive threat, more common, is the loss or abandonment of equipment containing radioactive materials such as medical radiotherapy sources, industrial radiology, or densitometry systems. The lack of control of these tools can have disastrous effects over the population's health [18].

Because of the high risk to citizens' health if these radiation sources are deliberately or accidentally manipulated (death is possible in hours if the exposure is high), most Western European countries have deployed a set of detection systems and maintain communication networks in order to try to avoid their introduction and spread. However, these systems are mostly set–up at borders (roads, ports, airports, and rail controls) and do not cover a large surveillance area but only zonal 'pinch point' sites. Moreover they are highly sensitive, expensive, of large dimensions and not at all portable. It is therefore imperative to explore alternative and complementary detection strategies to the systems already in place [19].

1.3 Framework: research projects

The present work has been carried out within the framework of three research projects: a project founded by the Generalitat de Catalunya (VALTEC09-2-0094), *RAMPO: Radiómetre múltiple portable*; a Spanish National Project (CIT-300000-2009-011), *NEUTOR III: Desarrollo de un monitor de neutrones de alta sensibilidad basado en diodo de silicio de capa fina con capa de conversor neutrónico*; and a FP7 European Project (FP7-SEC-2011-1), *REWARD: Real-time Wide-Area Radiation Surveillance System*. These projects are very briefly presented below.

1.3.1 Generalitat de Catalunya Project: RAMPO

RAMPO had a duration of two years, from October 2009 to October 2011, and had as goal to transfer to the technological market the radiation detectors that the IMB–CNM had developed for more than ten years. The market of radiation detectors is in constant progress because of the increasing incorporation to the society of new technologies that use radiation applications, e.g. in hospitals for the X–rays control, magnetic resonances, and particle accelerators for radiotherapy, in airports or security controls, and in nuclear power stations. Current needs require devices that are portable, low–priced, and capable of measuring several types of radiation at the same time. The RAMPO project emerged as a response to this concern. The first version of the neutron sensor as well as its portable electronics developed for this purpose are presented in Section 4.1.2 and Appendix B.1 respectively.

1.3.2 Spanish National Project: NEUTOR III

The NEUTOR III project was a continuation of the NEUTOR II National project which developed a passive neutron detection system based on SRAM technologies [14, 20]. NEUTOR III started in May 2009, with three years duration, and its purpose was to develop an active neutron sensor based on thin diodes to characterize in real–time the neutron field in a radiotherapy treatment room. The sensors developed were based on very ultra thin diodes covered with layers of boron–based compounds (with a high density of boron–10), able to combine a good sensitivity to neutrons and also a high γ–ray rejection.

The majority of the work developed in this thesis was conducted within the framework of this project. The designs, simulations, and manufacture processes for the neutron sensors created for this purpose are detailed in Section 4.2. The experimental validation of these sensors is shown and discussed in sections 5.2 and 5.3.

In addition, this project involved the development of the electronics (Appendix B.2) required for the acquisition and data transmission measurements to validate the results in radiotherapy accelerators and compare them with the previous NEUTOR II system.

1.3.3 European Project: REWARD

The Real Time Wide Area Radiation Surveillance System (REWARD) project started in December 2011 and has as aim the development of detection capabilities to detect radioactive sources and nuclear materials. This project proposes a novel mobile system for wide–area radiation surveillance in real–time. The system is based on the integration of new miniaturized solid–state radiation sensors: a CdZnTe detector for gamma radiation and a high efficiency neutron detector based on perforated silicon neutron detectors. The sensing unit will include a wireless communication interface to send the data remotely to a monitoring base station and a GPS system to calculate the position of the tag (Figure 1.4).

Figure 1.4: Sketch of monitoring tags in REWARD - The monitoring tags of the REWARD system will be installed in law enforcement vehicles or fixed stations and will send their location and measurement data to a central monitoring station if an abnormal situation is detected [21].

The system will also incorporate middleware and high–level software to provide

web–service interfaces for the exchange of information, providing top–level functionality, such as management of users, mobile tags, environmental data and alarms, database storage and management and a web–based graphical user interface. Finally, an expert system will continuously analyze the information from the radiation sensor and correlate it with historical data from the tag location in order to generate an alarm when an abnormal situation is detected.

The system may be useful for many different scenarios such as nuclear terrorism, lost radioactive sources, radioactive contamination or nuclear accidents. Possible deployment locations include not only emergency units and in general in any type of mobile or static equipment, but also inside public/private buildings or infrastructures (Figure 1.5). The sensing units will be portable thanks to their low size and low energy consumption.

IMB-CNM's radiation detector group are the project coordinators of this large research project and are also in charge of the development of the high efficiency neutron detectors. These novel prototypes are described in Section 3.5.

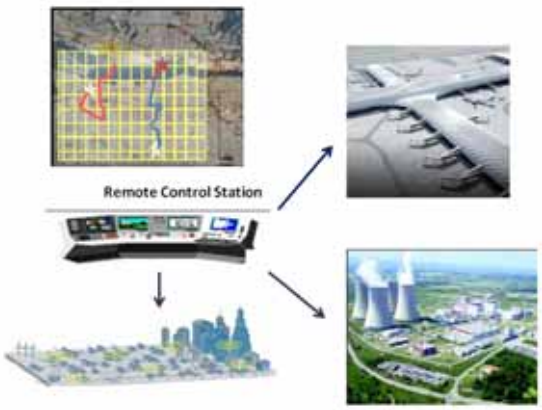

Figure 1.5: REWARD operation - The areas where the system has been deployed will be controlled in real time from a central remote control station. An expert system will continuously analyze the sensor information received from the monitoring tags to detect risk situations not predictable through the analysis of data from isolated stations [21].

2

Neutrons

2.1 General characteristics of neutrons

The neutron (n) is a subatomic neutral hadronic particle from the the baryon subfamily according to the Standard Model that consists of two down quarks (d), with an electric charge of -1/3, and 1 up quark (u), with charge +2/3 [1]. Neutrons and protons constitute the nuclei that make up the matter by means of the strong nuclear force. In a nucleus, the number of protons is the atomic number and defines the type of element that the atom forms, whereas the number of neutrons determines the isotope of such element. The main neutron features are summarized in Table 2.1. Bound neutrons in stable nuclei are usually stable, but if the neutrons are free or are bound in unstable nuclei, they are unstable and undergo beta decay into a proton, electron, and one electron-

[1] At a lower scale ($\prec 10^{-15}$ m), according to the gauge theory called Quantum Chromodynamics (QCD), the neutron is formed by vibrations of a field of quarks and gluons in constant interaction with each other.

Table 2.1: Neutron characteristics.

Mass m_n	$1.675{\cdot}10^{-27}$ kg = 1.0086 uma
Mean Lifetime τ_n (neutron free)	886.7 ± 1.9 s
Electric Charge	0 C
Spin	1/2
Isospin	1/2
Parity	+1
Electric Dipole Moment	$< 2.9{\cdot}10^{-26}$ e·cm
Magentic Moment μ_n	-1.913 μ_N

associated antineutrino, with a mean lifetime of almost 15 minutes, according to the reaction 2.1. This decay can also take place if the neutron has been artificially produced in nuclear reactions in particle accelerators or in nuclear fission and fusion reactors.

$$n \longrightarrow p + e^- + \overline{\nu}_e \tag{2.1}$$

Figure 2.1 displays the Feynman diagram for the neutron beta decay of Equation 2.1, which is governed by the weak interaction. The Feynman diagram shows how the baryon number is conserved: one of the down quarks of the neutron has to change its flavor decaying into an up quark, emitting a W^- boson via weak interaction. Then, the W^- boson decays immediately into an electron and an electron antineutrino to preserve the lepton number.

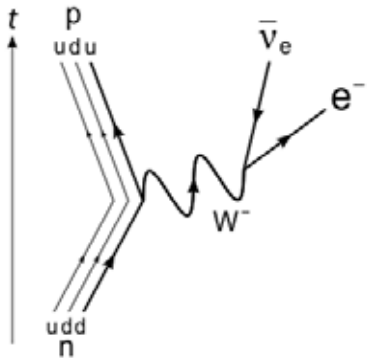

Figure 2.1: Feynman diagram for the neutron beta decay. - The Feynman diagram of the decay of a neutron into a proton, an electron, and an electron antineutrino. The process takes place via an intermediate W^- boson.

Table 2.2: Neutron classification as a function of its kinetic energy.

Neutron Type	Energy Range
Relativistic	≥1 MeV
Fast	0.1 MeV–1 MeV
Intermediate	1 keV–0.1 MeV
Epithermal	1 eV–1 keV
Thermal	≈0.025 eV
Cold	$5{\cdot}10^{-5}$–0.025 eV
Very cold	$2{\cdot}10^{-7}$–$5{\cdot}10^{-5}$ eV
Ultracold	$\leq 2{\cdot}10^{-7}$ eV

The neutron was discovered in 1932 by Chadwick [22] and thenceforth it has occupied an important position in the study of the Atomic and Nuclear Physics. Neutrons are frequently classified by their kinetic energy as is shown in Table 2.2 [23]. Although, to a first approximation, it is generally considered that the neutrons are slow when they have kinetic energy less than 0.5 eV (cadmium cut–off energy[1]), and fast when they have energies higher than this value [2]. Neutrons with energies below 1 eV reach thermal equilibrium with the surrounding atoms and present a Maxwellian energy distribution whose most probable energy is given by:

$$E_0 = k_B \cdot T \tag{2.2}$$

being k_B the Boltzmann constant[2] and T the medium temperature. Therefore, the most probable energy for thermal neutrons at a room temperature of 20°C is $E_0 \approx$ 0.0253 eV, which is equivalent to a velocity of ≈2200 m/s.

2.2 Neutron interactions

Neutrons do not have an electric charge and therefore they do not interact by Coulomb force with the orbital electrons of the medium, i.e. they do not produce primary

[1] It is the energy value taken as the boundary between the low energy neutrons that are absorbed by a cadmium sheet, i.e. $E_{neutron} \leq 0.5$ eV, and the higher energy neutrons that are not so absorbed.

[2] $k_B = 1.3806488 \times 10^{-23}$ J/K.

ionization directly, but they interact with matter via nuclear forces[1]. As a consequence, they can travel considerable distances within matter without interacting, i.e. they are highly penetrating. Nevertheless, neutrons can interact with atomic nuclei by the strong nuclear force mainly through the *scattering* and *capture* (or absorption) mechanisms (Figure 2.2):

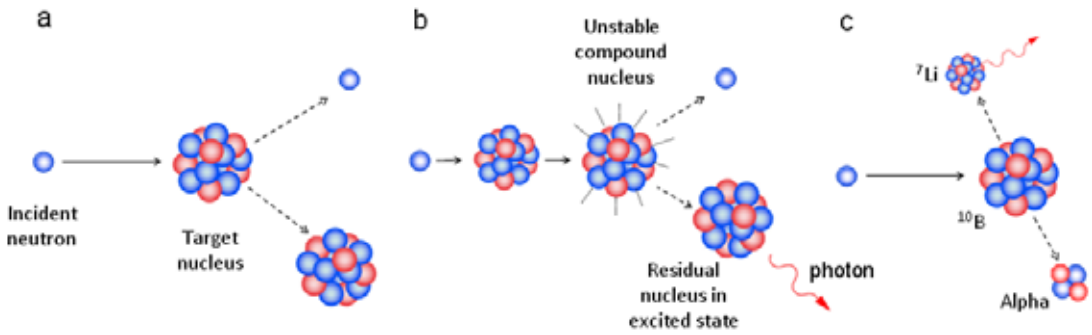

Figure 2.2: Neutron interactions. - Schematic of the three main interactions that a neutron can undergo when it interacts with the matter: (a) elastic scattering, (b) inelastic scattering, and (c) neutron capture (example with a ^{10}B-isotope).

- The **neutron scattering** interaction involves changing the energy and direction of the incident neutron, but the target nucleus remains with the same number of protons and neutrons. The scattering can be subdivided into elastic and inelastic. It is elastic scattering if the total kinetic energy of the incident neutron and target nucleus is conserved in the center-of-mass frame, i.e. if the energy that the incident neutron loses when it interacts with the target is transmitted in the form of kinetic energy to the recoil nucleus, which remains stable, and the direction of neutron propagation is modified. There is inelastic scattering if the incident neutron is absorbed by the target nucleus and then re-emitted, and therefore the nucleus absorbs internally some of the neutron energy, remaining in an excited state that later decays by gamma emission or some other form of radiation.

- A **neutron capture** triggers the emission of radiation within the target nucleus or its fission into heavy ions and/or fundamental particles, i.e. the target nucleus

[1]The nuclear force has very short range: in the order of fermis (1 fermi=10^{-15} m). When neutrons are very close to the target nucleus, they can interact by means of the attractive nuclear potential, causing nuclear reactions.

absorbs the incident neutron and emits other particles instead. There is a particular capture process for relativistic neutrons: *spallation*, in which the target nucleus is fragmented into an intranuclear cascade of several nucleons (protons and neutrons), α particles, nuclei, and de-excitation γ-rays, i.a.

Thus, depending on what process takes place, neutrons may change significantly their directions of incidence as well as their energies, give charged secondary particles or gammas, or disappear completely. Table 2.3 illustrates the classification of these possible neutron interactions. Generally, fast neutrons lose energy by elastic scattering back and forth, slowing down gradually until their energies are equal to the thermal energy of the surrounding matter. Then, thermal neutrons can undergo many elastic scatterings until to be absorbed by some target nucleus. In most of the cases, such absorption takes place either by radiative capture (n,γ), for most of the stable elements, or by (n,p) and (n,α) nuclear reactions, for some low Z nuclei.

Table 2.3: Neutron interaction types.

Process	**Reaction**	**Nomenclature**
Elastic Scattering	${}^{A}_{Z}\mathrm{X} + n \rightarrow {}^{A}_{Z}\mathrm{X} + n$	(n,n)
Inelastic Scattering	${}^{A}_{Z}\mathrm{X} + n \rightarrow {}^{A}_{Z}\mathrm{X} + n + \gamma$	(n,$n'\gamma$)
Radioactive Capture	${}^{A}_{Z}\mathrm{X} + n \rightarrow {}^{A+1}_{Z}\mathrm{X} + \gamma$	(n,γ)
Capture (n,α)	${}^{A}_{Z}\mathrm{X} + n \rightarrow {}^{A-3}_{Z-1}\mathrm{X} + \alpha$	(n,α)
Capture (n,p)	${}^{A}_{Z}\mathrm{X} + n \rightarrow {}^{A}_{Z-1}\mathrm{Y} + p$	(n,p)
Capture (n,2n)	${}^{A}_{Z}\mathrm{X} + n \rightarrow {}^{A-1}_{Z}\mathrm{X} + 2n$	(n,2n)
Fission	${}^{A}_{Z}\mathrm{X} + n \rightarrow Y + Z + \gamma$	(n,f)

The probability of interaction between an incident particle and a single target–nucleus is given by the microscopic cross–section per nucleus (σ) for each type of interaction. For instance, the particle absorption microscopic cross–section is defined as the probability of a particle being absorbed (given by the ratio of the number of captured particles to the number of incident particles over the target) divided by the atom density of the target material[1]. The cross–section depends on the target

[1]Thereby, if the neutron flux is known in a set-up, the reaction rate can be approximately estimated.

type, o nuclear element[1], the type of incident particle as well as its kinetic energy, type of nuclear reaction, and to a lesser extent on the relative angle between the target nucleus and the incident neutron, and the target nuclide temperature. Typical interaction cross–sections are between 10^{-27} cm^2 and 10^{-21} cm^2, so the cross–section unit commonly used is the barn (b), being 1 b = 10^{-24} cm^2. Since each type of interaction has its own cross–section and is independent of the probabilities of the others, the total cross–section is the sum of all the individual cross–sections:

$$\sigma_{total} = \sigma_{Ine.scatter} + \sigma_{Elas.scatter} + \sigma_{rad.capture} + \sigma_{non-rad.capture} + ... \tag{2.3}$$

A neutron has an apparent radius in the order of femtometer, i.e. $\approx 10^{-13}$ cm, and thus the cross section expected for the collision with other proton or neutron is $\approx 4 \cdot 10^{-26}$ cm^2 (0.04 barn). For nuclei, based on simplified nuclear models, the nuclear radius (R) of a stable nucleus is proportional to the cube root of the its atomic number A [24]:

$$R = r_0 \cdot A^{1/3} \tag{2.4}$$

with r_0 = 1.25 fm = $1.25 \cdot 10^{-13}$ cm. Then, the cross section for the interaction of a neutron with a nucleus is expected to be:

$$\sigma \propto \pi \cdot (R + \lambda(E))^2 \tag{2.5}$$

considering $\lambda(E)$ as the effective radius of the neutron which is given by the Broglie wavelength in the Ramsauer Model [25]:

$$\lambda(E) = \frac{h/2\pi}{\sqrt{2mE}} \tag{2.6}$$

With these assumptions and only as a qualitatively approximation, a estimate can be done as follows:

- For neutrons below 1 MeV, λ is >> R and thus σ can be considered as $\sigma \propto 1/E$. Figure 2.3 illustrates the energy dependence of the neutron capture cross–section at low energies for the ^3He, ^6Li, ^{10}B isotopes: the cross–sections become very large at thermal energies and decrease inversely proportional at $E_{neutron}$.

[1]Note that since neutrons interact with the nuclear potential of the nucleus, the cross-section depends on the type of isotope of the element.

- For higher energy neutrons, above 1 MeV, λ is neglected and σ is determined only by the nucleus size, $\sigma \propto \pi \cdot R^2$, i.e. σ is approximately constant but it has dependence on $A^{2/3}$. Figure 2.4 illustrates the energy dependence of the neutron capture cross section at high energies for the ^{113}Cd and ^{155}Gd isotopes: it is roughly constant from 10^{-2} to 20 MeV.

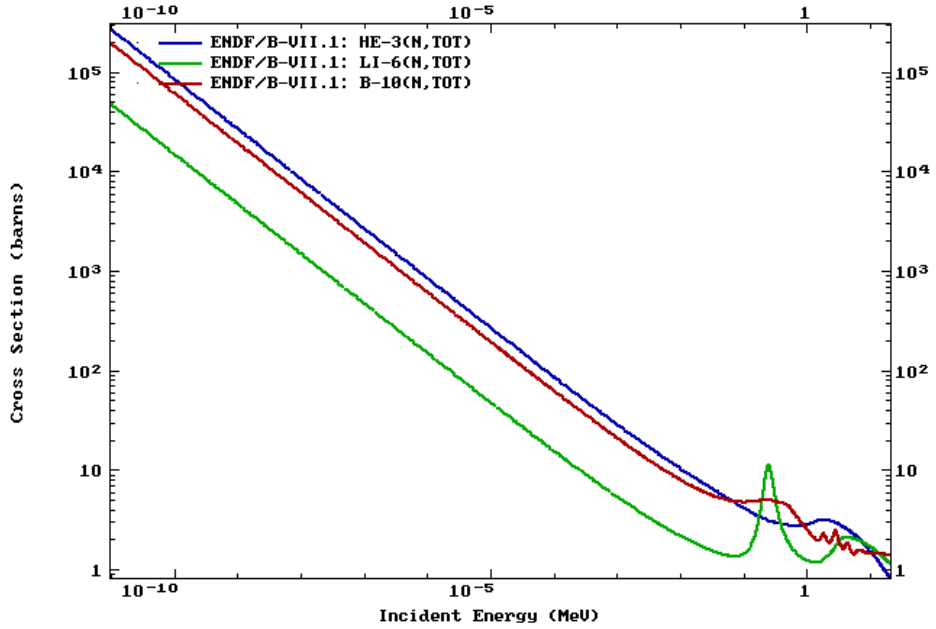

Figure 2.3: Total neutron cross–sections of ^3He, ^6Li, ^{10}B. - The cross–sections become very large at thermal energies and decrease inversely proportional at $E_{neutron}$. Data obtained from the ENDF database [26].

Note that this is only a very simple model to grasp the phenomenology of the neutron cross–section. It does not consider the neutron resonances (pronounced peaks at a particular energies) nor threshold energies of some nuclear reactions that modify the preceding behavior strongly as is shown in Figure 2.4 from 1 eV to 0.01 MeV for the ^{113}Cd and ^{155}Gd isotopes.

If σ is multiplied by the atom density N_i[1] of each element that forms the matter in which neutrons are travelling, the result is the sum of the macroscopic cross–sections

[1] $N_i = \rho \cdot N_A \cdot n_i / \mathrm{M}$, being ρ the density of the compound, N_A the Avogadro's number ($N_A = 6.022 \cdot 10^{23}$ mol^{-1}), n_i the number of atoms of element 'i' in one molecule, and M the molecular weight of the compound.

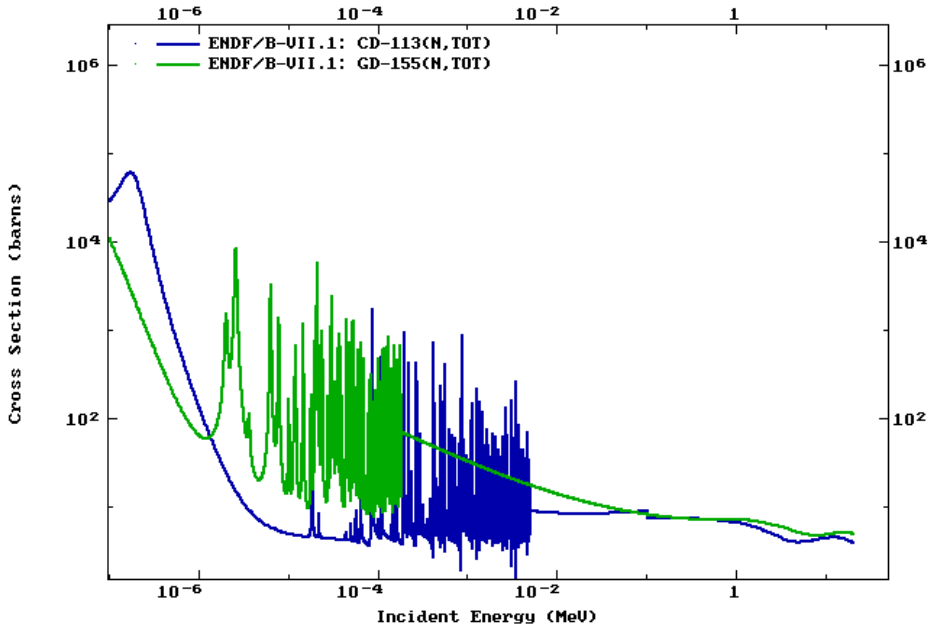

Figure 2.4: Total neutron cross–sections of ^{113}Cd, ^{155}Gd. - The cross–sections become roughly constant at energies higher than 0.01 MeV and show resonance peaks from 1 eV to 0.01 MeV. Data obtained from the ENDF database [26].

(Σ) of the individual elements (with dimensions of inverse length):

$$\Sigma_t = \sum_i (N_i \cdot \sigma_i) = \Sigma_1 + \Sigma_2 + \Sigma_3 \cdots \tag{2.7}$$

whose physical interpretation is the probability per unit path length for the process represented by the σ_i. For each physical process there is an associated macroscopic cross–section: $\Sigma_{Ine.scatter}$, $\Sigma_{Elas.scatter}$, $\Sigma_{rad.capture}$, $\Sigma_{non-rad.capture}$, and so on. Thereby the probability per unit path length that any type of interaction occurs is given by:

$$\Sigma_{total} = \Sigma_{Ine.scatter} + \Sigma_{Elas.scatter} + \Sigma_{rad.capture} + \Sigma_{non-rad.capture} + ... \tag{2.8}$$

Depending on if the incident particle beam is collimated or not, it is important to distinguish between two general and oversimplified experimental cases:

- First, if the neutron beam is narrowly collimated, the number of incident neutrons (I_0) is attenuated exponentially with the matter thickness that they go through

(r):

$$\frac{I}{I_0} = e^{-\Sigma \cdot r} = e^{-r/\lambda} \tag{2.9}$$

being

$$\lambda = 1/\Sigma \tag{2.10}$$

the neutron mean–free–path, which represents the average length travelled between two interactions by the particle. Hence, and as a general rule, when a neutron travels with a speed v, the neutron average time between interactions is λ/v. Note that the whole process is much more complex since, after each collision, the energy decreases and therefore the mean–free–path is affected accordingly.

- Secondly, for most of the experimental cases the neutron beam is either not collimated or the shielding around the setup may cause widening and scattering of the beam. As a result, equation 2.9 is not valid and computational support is required to predict the number of absorbed neutrons as well their distribution in energy after the interaction process. This is one of the reasons for what some Monte Carlo simulation packages (Chapter 3) are used for the studies presented in this thesis.

Additionally, depending on the distribution in energy of the initial neutron beam, the complexity of the overall interactions changes. As a first approximation, it is possible to consider two types of incident beams: a monoenergetic beam and a beam with certain distribution in energy. Thus for an initial neutron flux ϕ (neutrons per unit time and area), the reaction rate density (reactions per unit time and volume) for a certain process–i is given for each case as follows:

- If the neutron beam is monoenergetic, the reaction rate density is $\phi \cdot \Sigma_i$.
- If the beam has certain distribution in energy, the preceding reaction rate density can be generalized as $\int_0^\infty \phi(E)\Sigma(E)dE$.

Note again that with each collision the neutron energy decreases and therefore its cross–section changes, which alters the instantaneous reaction rate.

The main neutron interaction processes are presented briefly in the next subsections.

2.2.1 Elastic scattering

As said before, the neutron elastic scattering (n,n) interaction process occurs when a part of the incident neutron energy is transfered to a target nucleus, which may cause ionization in the surrounding material. The elastic scattering is particularly important because it can occur for any neutron energy, without threshold. In addition, the elastic scattering is responsible for the moderation or thermalisation[1] of fast neutrons.

From kinematic analysis and for non–relativistic neutron energies, the relationship between the initial neutron energy (E_n) that can be transferred to a nucleus of mass number A in a single collision (E_r) is given by equation 2.11:

$$E_r = E_n \cdot \frac{4 \cdot A}{(1+A)^2} \cdot cos^2\theta \tag{2.11}$$

in terms of the outgoing angle of the recoiling nucleus for the lab–frame (see Figure 2.5). The energy transfer to the recoil nucleus increases if the mass number of the target decreases and therefore it is maximum for hydrogen and high for light atoms. Inversely, the energy transferred to the recoil nucleus decreases with the atomic mass number of the target and the scattering angle. The average kinetic energy transferred to the recoil nucleus is given by:

$$\langle E_r \rangle = E_n \cdot \frac{2 \cdot A}{(1+A)^2} \tag{2.12}$$

This expression shows that to slow down the velocity of neutrons, with the fewest number of collisions, a light target nuclei (with small A) should be used. Thereby, the greatest average energy transfer in elastic scattering occurs in neutron–proton collisions: $\langle E_r \rangle = E_n/2$, being thus the average energy transferred to the recoil proton 50% the energy of the incident neutron[2]. This recoil proton in turn ionizes the medium. This happens mainly with hydrogen nuclei (A=1)[3] and, therefore, the most

[1] Thermalisation is the process in which particles reach thermal equilibrium by interaction with the surrounding. In the thermalisation of neutrons, they usually lose energy by collision with a moderator material.

[2] For instance a neutron of 2 MeV will have 1 MeV average energy after one elastic collision with a proton, 0.5 MeV after the second collision, and so on. To reach the thermal energy, 0.025 eV, such neutron should undergo 27 elastic collisions.

[3] Since the hydrogen nucleus has no excited states, only elastic scattering and neutron capture are viable. Energy transfer is maximized because the mass of the neutron is comparable to that of the hydrogen nucleus (proton). This is the most common type of interaction in biological mediums.

common hydrogenated materials used to moderate neutrons are water, paraffin, and polyethylene. After n–elastic collisions, the neutron energy changes from E_i to E_f according to the next equation:

$$E_f = E_i \cdot \left[\frac{A^2+1}{(A+1)^2}\right]^n \tag{2.13}$$

and therefore, to reach E_f from E_i, it is necessary:

$$n = \frac{log(E_f/E_i)}{log\left[\frac{A^2+1}{(A+1)^2}\right]} \tag{2.14}$$

elastic collisions in average.

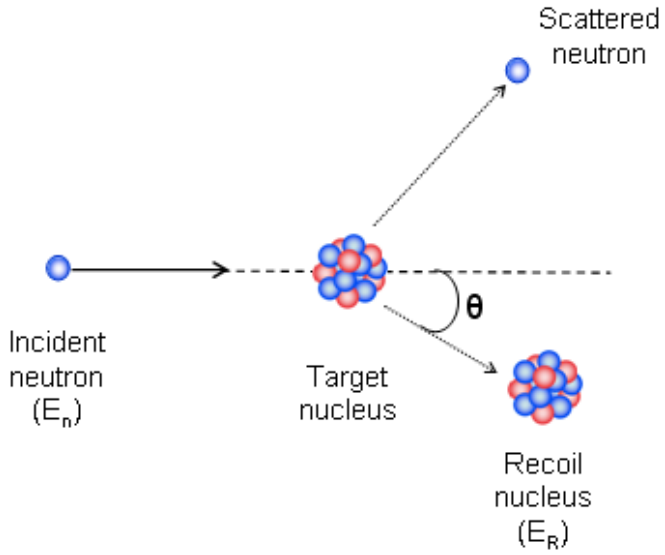

Figure 2.5: Elastic scattering diagram for the laboratory frame. - Sketch of the elastic scattering of a neutron that collides with a target nucleus.

2.2.2 Inelastic scattering

In the inelastic scattering (n,$n'\gamma$) an incident neutron is captured by the target nucleus provided that the neutron energy is high enough to take such nucleus to an excited state. The new compound–nucleus (incident neutron plus target nucleus) is unstable and decays immediately, in less than 10^{-14} s. When the compound–nucleus decays, it ejects another neutron with a kinetic energy lower than that of the initial neutron and

a residual nucleus that changes from an excited state to its ground state emitting one or more γ–rays.

The energy (E_f) of the neutron emitted by inelastic scattering is obtained from the application of the conservation laws of energy and momentum, resulting:

$$E_f = \frac{1}{(1+M)^2}\left[\omega\sqrt{E_i} \pm \sqrt{E_i(\omega^2+M^2-1) - M(M+1)E_r}\right]^2 \tag{2.15}$$

where ω is:

$$\omega = \frac{1}{2}\left[(M+1)\sqrt{\frac{E_f}{E_i}} - (A-1)\sqrt{\frac{E_i}{E_f}} + \frac{ME_r}{\sqrt{E_iE_f}}\right] \tag{2.16}$$

being E_i the incident neutron energy, M the quotient between the target nucleus mass and the neutron mass, and E_r the energy of the excited level of the residual nucleus. From equation 2.15, it is observed that

$$E_i(\omega^2+M^2-1) - M(M+1)E_r \tag{2.17}$$

must be $\geq$0. As a consequence, the incident neutron energy must be above a certain threshold, and at least it should be equal than the energy of the excited state of the residual nucleus (which, on the other hand, decreases when the mass number of the target nucleus increases). Hence in order to cause inelastic scattering neutron energies from 0.5 to 5 MeV are necessary for light nuclei, whereas for heavy nuclei, neutron energies in the keV range are enough.

2.2.3 Neutron capture

There are two categories of neutron capture: radiative capture, (n,γ), and non–radiative capture, e.g. (n,p), (n,d), (n,α), (n,t), (n, 2n).

In the radiative capture process the neutron is captured by the target nucleus, giving a compound nucleus in an excited state which decays emitting γ–rays[1]. It can occur for a wide range of neutron energies and it is always an exothermic reaction (positive Q–values).

[1]In general, the formed nucleus decays β^- since this compound nucleus has a N/Z ratio greater than the initial target nucleus.

One of the most common radiative capture takes place with hydrogen:

$$ {}^{1}_{1}\mathrm{H} + n \rightarrow ({}^{2}_{1}\mathrm{H})^{*} \rightarrow {}^{2}_{1}\mathrm{H} + \gamma \tag{2.18} $$

with Q=2.22 MeV. Figure 2.6 shows the dependence of the hydrogen cross–section as a function of the neutron energy. As a general rule it is considered that the neutron capture cross section follows the function $\sigma(E) = \sigma(E_{thermal}) \cdot \frac{v_{thermal}}{v}$, although there are nuclei which display pronounced resonances at intermediate energies. Thus, the neutron capture cross–section increases when the neutron velocity decreases, as is shown in Figures 2.3 and 2.6.

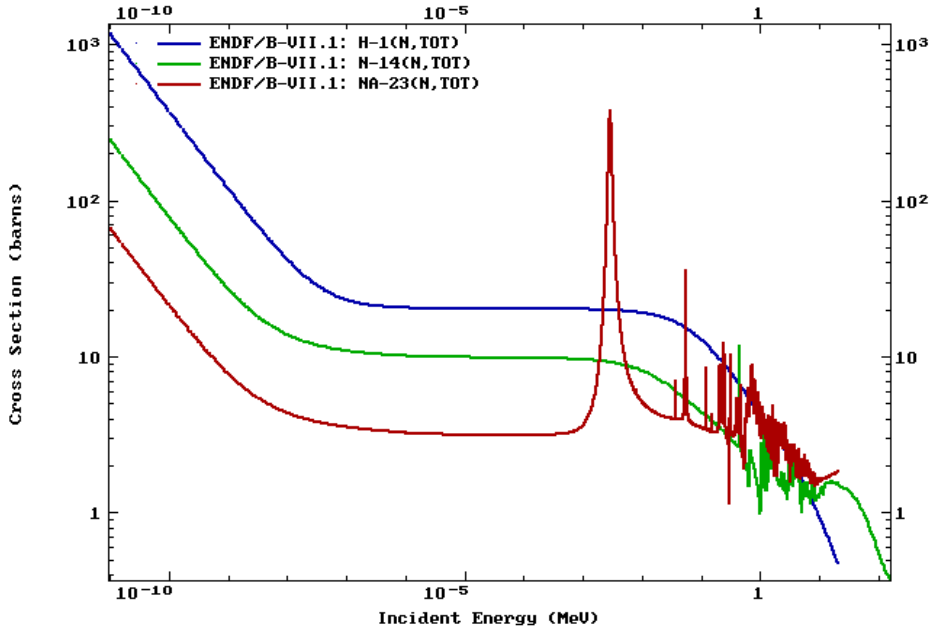

Figure 2.6: Total neutron cross sections of ^{1}H, ^{14}N, and ^{23}Na. - Data obtained from ENDF database [26].

In contrast, non–radiative capture reactions eject more than one neutron or charged particles like protons, alpha, deuterons, tritons, etc, i.e. are (n,p), (n,d), (n,α), (n,t), (n, 2n) reactions. Note that these reactions take place by quantum tunnelling since the energy of the incident particle is usually below the coulomb barrier of the compound nucleus. Most of these reactions are endoenergetic so only neutrons with energy above a threshold can cause them. Nevertheless, there are some nuclei that can undergo an exoenergetic reaction such as the ^{3}He, ^{6}Li, and ^{10}B isotopes, whose high neutron

cross–sections make them interesting for their use in neutron detection, as is explained in the next section. Some of the most significant reactions of neutron capture are listed in Table 2.4.

Table 2.4: Capture reactions of neutron converters.

Capture reaction	$\sigma_{n_{thermal}}$ **(barn)**
$n + {}^{3}\mathrm{He} \rightarrow {}^{3}\mathrm{H}(0.191MeV) + p(0.574MeV)$	5330
$n + {}^{10}\mathrm{B} \rightarrow \alpha(1.78MeV) + {}^{7}\mathrm{Li}(1.01MeV)$ 6,3% $n + {}^{10}\mathrm{B} \rightarrow \alpha(1.47MeV) + {}^{7}\mathrm{Li}(0.84MeV) + \gamma(0.48MeV)$ 93,7%	3840
$n + {}^{6}\mathrm{Li} \rightarrow {}^{3}\mathrm{H}(2.73MeV) + \alpha(2.05MeV)$	940
$n + {}^{113}Cd \longrightarrow {}^{114}Cd + \gamma(0.56MeV) + e^{-}$	20743
$n + {}^{155}Gd \longrightarrow {}^{156}Gd + \gamma(0.09, 0.20, 0.30MeV) + e^{-}$	60791
$n + {}^{157}Gd \longrightarrow {}^{158}Gd + \gamma(0.08, 0.18, 0.28MeV) + e^{-}$	255011

In this category there are two neutron capture reactions that are especially significant in radiobiology due to the damage that they can cause to live cells [23] (their cross-sections are displayed in Figure 2.6):

- Thermal neutron capture by ${}^{14}N$ via the ${}^{14}N(\mathrm{n,p}){}^{14}C$ reaction, where the expelled proton has 580 keV, enough energy to ionize the matter that crosses. Nitrogen is ∼3% in percent by mass of the human tissue.

- Thermal neutron capture by ${}^{1}H$: ${}^{1}H(\mathrm{n},\gamma){}^{2}H$, ejecting γ-rays with 2.225 MeV which may cause photoelectric, Compton or even pair creation effect, where the ejected electrons ionize the cell tissue. Most of the γ–rays produced by that reaction are absorbed in the body, so this process with thermal neutrons is the main contributor to dose in humans. Hydrogen is ∼10% in percent by mass of the human tissue.

Fast neutrons may lose their energy gradually by elastic scattering with hydrogen as explained above (neutrons with 0.5 to 5 MeV can lose 90% of their energy in collisions of this type)[1]. When they are thermalized, they can be captured by one

[1]For example, a 1 MeV neutron suffer about 20 collisions, crossing about 5 cm of tissue, before it is thermalized.

of the above processes or dispersed outside the body. On the other hand, the reactions that take place with relativistic neutrons can cause spallation reactions (n, Xn) or (n, np). A spallation reaction leads to an intranuclear cascade of direct reactions of several individual groups of nucleons ejected from the compound nucleus. The residual nucleus is in an excited state that decays by evaporating nucleons, being most of them neutrons.

2.2.4 Fission reaction

When a neutron interacts with a heavy nucleus (Z$\geq$92), the compound nucleus may split into two daughter nuclei of lighter mass. This process always releases one or more fast neutrons that, in turn, can trigger other fissions in a self-sustained nuclear chain reaction. Controlled chain reactions are usually used in nuclear reactors for research and power generation. The fission reactions are likely for uranium (^{233}U and ^{235}U), plutonium (^{239}Pu), thorium (^{232}Th), and higher mass actinides.

2.3 Neutron detection methods

Electrically neutral particles, such as neutrons, do not interact via electromagnetic forces and therefore they are not able to ionize the matter so their detection has to take place through the secondary charged particles generated by nuclear interaction. There are different methods to be applied as a function of the energetic range of study since, as it has been shown before, the neutron cross–section is strongly dependent on the neutron energy. One has to distinguish between detection of slow and fast neutrons: (a) if neutrons have high energy, they can suffer elastic scattering in a material that contains appreciable amounts of hydrogen such that the recoil protons may be detected; (b) if neutrons have low energy, they can undergo exoenergetic nuclear processes, i.e. slow neutrons can be detected through the charged particles as a result of a nuclear reaction with a converter with large neutron capture cross–section. Thus, for instance, neutrons may be detected by means of reactions such as (n,p), (n,α), (n,γ), (n,fission). In most cases when neutrons interact with the nuclei of a target they suffer elastic scattering, slowing down their energies gradually to the capture. Thereby most neutron sensors use some type of converter to produce secondary particles that ionize the sensitive detector bulk [2].

After dealing with neutron detection methods, it is important to specify the converter characteristics that are preferable for a good performance. It is assumed that a converter can be an isotope or a chemical compound which is formed by isotopes that capture neutrons. A good converter should satisfy the following conditions:

- It should have a high neutron cross–section in the energetic range of interest. Besides, a high cross–section would allow to build efficient detectors with small dimensions.
- The converter should be made up of elements with high isotopic abundance of those isotopes which capture neutrons.
- It should be as inexpensive as possible to incorporate it into large detection devices.
- A converter which emits charged particles, e.g. (n,p) or (n,α), is more advisable than one that creates non-ionizing radiation, e.g. (n,γ) or (n,2n), since charged particles are usually easier to detect in typical radiation detectors.
- The reaction products from the converter should have enough energy to cross the converter and to reach the sensitive detector bulk. Even so, it is likely that some events are not detected due to the energy loss that the reaction products suffer when they cross the converter. This may give rise to a low-energy continuum in the spectrum that deteriorates the expected energy distribution.
- The converter should have a high reaction Q–value (i.e. high energy given to the reaction products) that, on the one hand, allows to discriminate against the low–amplitude events caused by γ–rays (as has already been mentioned in Section 1.2, in many applications there are intense fields of γ-rays mixed with the neutron field), and on the other hand, is advantageous for the noise–to–signal ratio.

Other considerations to take into account are:

- The range of the reaction products coming from the converter conditions the size of the detector because the detection volume has to be at least as large as the range of these particles.

- This range depends on the states of aggregation of the detection medium and the converter. For instance, if the detection medium is solid, the range of the reaction products is of a few tenths of micrometers, whereas if the detection medium is gaseous the range may be of several centimeters.

- The short range in a semiconductor detector of the reaction products coming from some converters could allow to design neutron detectors for imaging with high spatial resolution (provided the range of such particles is shorter than the pixel size of the imaging detector).

- Most of the reaction products do not deposit the full energy within detector sensitive volume, since they lose part of such energy along their trajectories inside the converter. Therefore, in the pulse height distribution collected by the detector appears a low energy tail instead of a single full-energy peak. This counting plateau may make the discrimination against low amplitude events difficult (like events induced by γ–rays).

Some of the possible neutron converter isotopes, with relative high natural abundance are [27]: ^{157}Gd, ^{155}Gd, ^{252}Cf, ^{113}Cd, ^{239}Pu, ^{10}B, ^{6}Li, ^{197}Au, ^{3}He, ^{135}Xe, ^{235}U, ^{238}U, ^{232}Th, ^{39}K, ^{14}N, ^{56}Fe, ^{23}Na, ^{1}H, ^{29}Si, ^{30}Si, ^{28}Si, ^{14}C, ^{16}O, sorted by their thermal neutron capture cross–sections. These isotopes could make up a chemical compound that works as a converter. On the other hand, some selected materials, for instance indium, gold, rhodium, iron, aluminum, niobium, silicon, etc, have extremely large capture cross–sections within a very narrow band of energy. Hence, the characterization of the neutron energy spectrum could be possible if we designed a suitable assembly of multiple absorbers.

Nevertheless, note that not all the converters may be combined with all the radiation detector types (gaseous, scintillator, or solid-based detectors) as it is detailed in Section 2.4.

2.3.1 Slow neutron detection

Slow neutrons undergo mainly elastic scattering reducing their speed gradually until they approach equilibrium at the thermal temperature of the medium. In this thermalization process, neutrons undergo diffusion, i.e. they disperse and expand into the

medium. Then, they can be captured through one of the (n,p), (n,α) or (n,γ) absorption reactions whose charged products can ionize the surrounding atoms. For slow neutrons the reactions of interest are mainly (n,p) and (n,α) because they favor the detection efficiency with the high kinetic energy of the reaction products. The main isotopes used for this purpose, their nuclear reactions, and thermal cross–sections are listed in Table 2.4. The neutron capture reactions of the isotopes that eject charged particles, which fulfill the converter requirements listed above, are briefly discussed as follows.

The ^3He(n,p)^3H reaction.

^3He is an isotope widely used for neutron detection in gas detectors (see subsection 2.4.1). When a neutron interacts with a ^3He nucleus, such nucleus may capture the incident neutron, ejecting a proton and a tritium nucleus in opposite directions, according to the next reaction:

$$n +^3 He \rightarrow^3 H + p \tag{2.19}$$

with a Q-value of 0.764 MeV. Because the energy of the incoming slow neutron is low, the energy imparted to the reaction products is just the whole Q-value. Moreover, since the incident neutron kinetic momentum is very small, these reaction products must have a net momentum practically equal to zero. As a consequence, both reaction products are ejected in opposite directions and the overall energy of the reaction is distributed between them by the conservation of energy and momentum principles as follows (in the center–of–mass frame):

$$E_H + E_p = Q = 0.764 MeV \tag{2.20}$$

$$m_H \cdot v_H = m_p \cdot v_p \tag{2.21}$$

whose simultaneous solution gives: $E_H = 0.191$ MeV and $E_p = 0.573$ MeV.

The cross section for this reaction is displayed in Figure 2.3, where is observed that the cross section falls off with a 1/v or 1/E energy dependence. Specifically, for this reaction the thermal neutron cross section ($\sigma_{n_{th}}$) is 5330 barns.

The natural abundance of ^3He is extremely low: 0.000137%. Besides, commercial ^3He is made in nuclear reactors so is relatively expensive and its reserves are foreseen

to be consumed in the coming decades [3].

The $^{10}B(n,\alpha)^7Li$ reaction.
When a ^{10}B nucleus captures a thermal neutron, it produces two charged particles through one of the following reactions:

$$n +^{10}\mathrm{B} \rightarrow \alpha(1.78MeV) +^{7}\mathrm{Li}(1.01MeV) \tag{2.22}$$

$$n +^{10}\mathrm{B} \rightarrow \alpha(1.47MeV) +^{7}\mathrm{Li}(0.84MeV) + \gamma(0.48MeV) \tag{2.23}$$

being the first reaction the ground state and the second one the excited state. The branching fraction of these reactions is 6% and 94% and their Q–values are 2.792 and 2.310 MeV respectively. The ^{10}B isotope has a $\sigma_{n_{th}}$ of 3840 barns for the thermal neutron capture reaction and, as the above cases, its cross-section follows the 1/v trend (Figure 2.3). The natural abundance of ^{10}B is 20%.

The $^{6}Li(n,\alpha)^3H$ reaction.
If a ^{6}Li nucleus captures a neutron, it emits a 2.05 MeV alpha and a 2.73 MeV tritium nucleus. This nuclear reaction is:

$$n +^{6} Li \rightarrow^{3}_{1} H + \alpha \tag{2.24}$$

with a Q–value=4.78 MeV. Again by kinematic principles, these reaction products are oppositely directed when the energy of the incident neutron is low enough. Its cross-section is also inversely proportional to incident neutron velocity (Figure 2.3), being $\sigma_{n_{th}}$=940 barns. The natural abundance of ^{6}Li is 7%.

The ^{10}B and ^{6}Li isotopes are suitable for solid detectors (see subsections 2.4.2 and 2.4.3) or gas detectors (subsections 2.4.1.2 and 2.4.1.3), whereas the ^{3}He isotope, due to its gaseous nature, is only used in gas detectors (subsection 2.4.1). In this work, for silicon detectors, the ^{10}B isotope has been used as neutron converter instead of ^{6}Li since ^{10}B is cheaper, has a higher neutron cross-section, and a higher natural isotopic abundance than the ^{6}Li isotope.

2.3.2 Fast neutron detection

The main fast neutron detection methods are based either on using neutron moderation or elastic scattering [28]. In the first case, the neutrons are slowed down via elastic and inelastic scattering with a suitable moderator up to low energies and then some slow neutron detection method is applied. In the second case, it is possible to detect the recoil nuclei coming from elastic scattering thanks to that the elastic cross–section for fast neutrons is large in several materials. For instance, the hydrogen–rich materials such as polyethylene, paraffin, water, etc, can deliver recoil protons through the (n,p) elastic reaction with fast neutrons. This reaction is not isotropic because the direction of flight of the recoil proton is a function of the direction of the the incoming neutron. Moreover, observing recoil nuclei with the time-of-flight (ToF) method enables neutron energy measurements by assessing their velocities.

2.4 State-of-the-art in active neutron detectors

Depending on the time needed for a response, radiation detectors can be classified in two types: active and passive detectors. In an active detector the response to the radiation is given immediately. This category comprises gaseous and semiconductor detectors, based on ionization, and scintillator detectors, based on excitation. The passive detectors need to be read at a later stage in order to ascertain the level of exposure recorded. Examples include film badges, thermoluminescent dosimeters (TLDs), and radiographic films. Each of them is more appropriate depending on the application field.

In this work we will focus on active detection. The main properties of active radiation detectors that have to be considered when selecting a detector for a particular application are the following:

1. Dead time: minimum time at which detector recovers enough to start another signal. It may be set by limiting processes in the sensor or by the associated electronics.

2. Time resolution: minimum time interval that must elapse after detection of an ionizing particle before a second particle can be detected.

3. Linearity: a detector is lineal if there is a linear relationship between the energy of the detected radiation and the response of the detector.

4. Energy resolution: the accuracy with which the system can measure the energy of a radiation and its ability to distinguish radiations of slightly different energies.

5. Sensitivity: ability to produce a valid detector signal. The weaker the radiation source, the more sensitive the detector needs to be.

6. Intrinsic detection efficiency: ratio between the number of events recorded by the detector and the number of particles hitting the detector.

7. Geometric detection efficiency: solid angle that the detector presents to the source.

8. Absolute detection efficiency: product of geometric and intrinsic efficiencies. For a given geometry it is the ratio between the number of events recorded by the detector and the total particles emitted by the radiation source.

9. Gamma discrimination (for neutron detectors): ability to distinguish between gamma and neutron radiation events. This is needed because neutron radiation is typically accompanied by a gamma emission.

In the particular case of the neutron detectors, in order to evaluate the response and to compare performances, there are three main coefficients: (a) gamma rejection factor, (b) neutron/gamma-ray discrimination, and (c) neutron absolute detection efficiency. These parameters are specifically evaluated in Chapter 5 for the detectors presented in Chapter 4.

As said above, there are three main types of active neutron detectors: based on ionization of gases and semiconductors, and scintillators. Each of them is briefly reviewed in the following subsections.

2.4.1 Gaseous detectors

Gaseous detectors are devices filled with a gas which is ionized when a charged particle or photon goes through it. Hence, the amount of ionization in a gas volume is a measure of the amount of radiation present. There are three main types of neutron gaseous

detectors: ^3He-filled gas proportional counters, boron trifluoride (BF_3) proportional tubes, and boron-lined proportional counters. They are briefly outlined below in subsections 2.4.1.1, 2.4.1.2, and 2.4.1.3 respectively. These devices measure only the neutron number (count rate) and not the energy of the neutrons. They offer high thermal neutron detection efficiency with good gamma discrimination. As they are based on reactions with slow neutrons, in order to detect high energy neutrons these detectors are usually surrounded with a moderator such as high density polyethylene. These detectors are one of the most common devices used to detect the presence of high-energy subatomic particles as well as neutrons in real time. They can cover large areas and thus have high geometric detection efficiencies. However, they are bulky and need to operate at high voltages (hundreds to thousands of volts), and at high pressures (≈10 bar). Additionally their use is limited to low counting rates due to their large dead time (200–400 μs).

2.4.1.1 ^3He-filled gas proportional counters

The proportional counters filled with ^3He are the 'gold standard' thermal neutron detectors since ^3He has a large capture cross section for thermal neutrons and a negligible sensitivity to γ-rays. For this reason for decades they have been the preferred solution to obtain high neutron/gamma-ray discrimination. ^3He reacts by absorbing thermal neutrons and producing the $^3_1$H(0.191MeV)+p(0.574MeV) ions. Because ^3He is a noble gas, no solid compounds can be fabricated and it must be used in gaseous phase. Figure 2.7 illustrates the working principle of a ^3He counter.

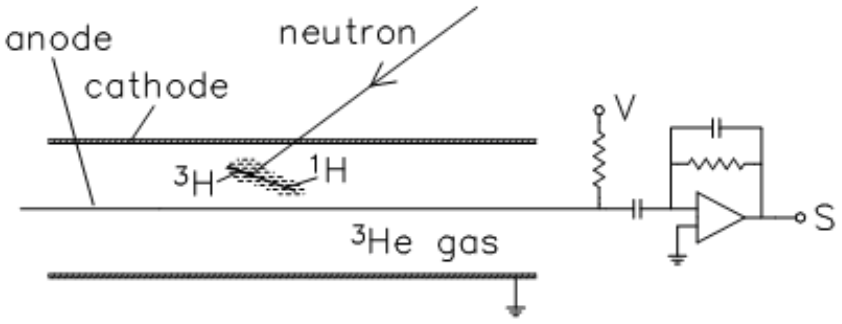

Figure 2.7: Working principle of a ^3He counter - Sketch of a gas-filled chamber with a wire anode.

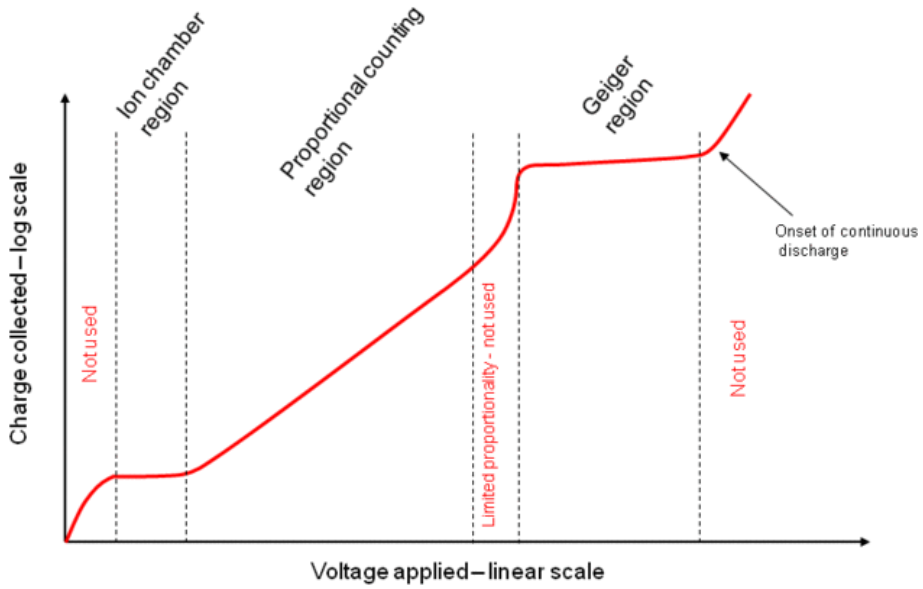

Figure 2.8: Regions of a gaseous ionization detector - Charge collected as a function of the applied voltage for a wire cylinder gas detector.

A proportional counter uses a combination of the Geiger-Muller tube and an ionization chamber, operating in an intermediate voltage (Figure 2.8), in the proportional mode such that the ionization produced by the reaction products initiate the multiplication process that leads to detection. This intermediate process of charge amplification improves the signal-to-noise ratio and reduces the electronic amplification needed. ^{3}He tubes usually operated in the range of 1200 to 1800 V.

These detectors work in the pulse-readout mode where neutron and gamma-ray signals are distinguished by their amplitude. The pulse height spectrum from the interaction of a thermal neutron in a typical ^{3}He neutron detector is shown in Figure 2.9. This presents three different areas: (left) the area which comes from noise and piled-up γ-ray events, which can be discriminated with an adequate threshold; (intermediate) events produced by interactions with the walls of the detector tube ('wall effect', which hinders the n-γ discrimination); and (right) one full peak which corresponds to the Q-value of the reaction, 0.765 MeV[1], provided both reaction products are collected. In order to reduce the wall effect there are three possible ways:

[1]Note that this Q-value is approximately a quarter of that of the ^{10}B reaction.

(i) increasing the diameter or the detector such that the ratio of reaction products colliding with the wall and the events that have completely deposited their energy in the gas volume is reduced as much as possible; (ii) increasing the gas pressure to reduce the range of the daughter products in the gas volume; (iii) including an amount of a heavier gas (typically krypton or carbon dioxide[1]) in the mixture to increase the stopping power of the gas, although this may also increase the gamma sensitivity of the detector (this is usually the best option when the size or pressure is fixed). Note that whereas in a solid such as silicon the ranges of the proton and tritium, coming from the n + ^3He reaction, are 6 and 5 μm respectively, in a common gas their ranges are of few mm (1000·$Range_{solid}$), so large surfaces/volumes (comparing to solid-state detectors) of gas detectors are required for comparable performances. In addition, the lower Q-value of the neutron capture with ^3He compared to ^{10}B makes the neutron/gamma-ray discrimination more difficult with ^3He.

Furthermore, the last few years the amount of ^3He available for use in detectors has become more restricted due to the ^3He reserves are foreseen to be consumed in the coming decades [3]. Besides, the supply of ^3He is limited to production as a byproduct from the decay of tritium (which has a 12.3 year half-life) which is produced either as part of weapons programs as a booster for nuclear weapons or as a byproduct of reactor operation. Therefore other alternative neutron detectors are being investigated. Nowadays one of the replacement technology options for ^3He-filled tubes are the boron-lined proportional counters detailed in Section 2.4.1.3.

2.4.1.2 Boron Trifluoride (BF_3) proportional tubes

Since natural boron is not gaseous, neutron gas detectors containing boron may alternately use boron trifluoride (BF_3), which is a gas. A BF_3 tube detector consists of a cylindrical tube (copper or brass with 2-5 cm diameter) filled with a BF_3 gas at a pressure of 0.2–2.0 atm (Figure 2.10). The cathode is typically an aluminum wall and the anode a single thin wire running down the axis of the tube. In this device the BF_3 works as target for slow neutron capture and proportional gas at the same time. In order to improve the detection efficiency of this device the BF_3 is frequently enriched in ^{10}B.

[1]Krypton gives best neutron spectroscopy and carbon dioxide gives a lower sensitivity to gamma-rays.

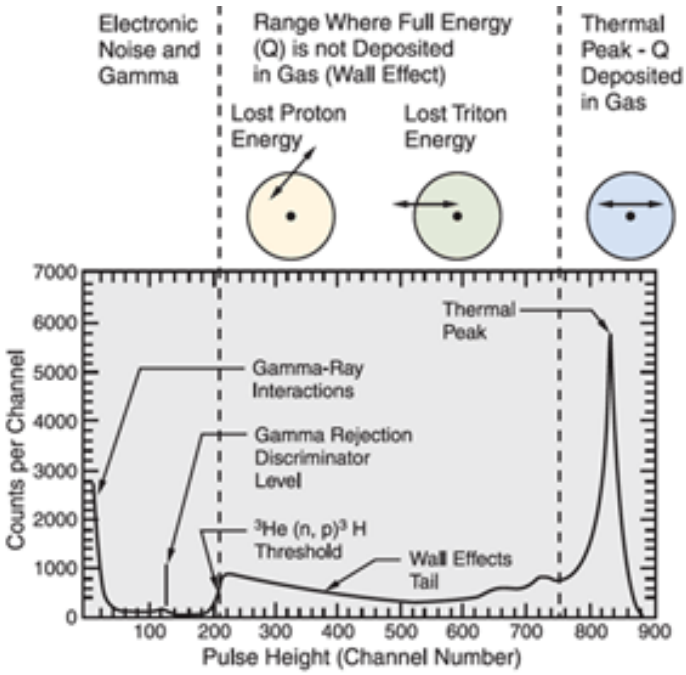

Figure 2.9: Pulse height spectrum in a ^3He-filled gas proportional counter - The three main characteristic regions of the spectrum in a ^3He counter are distinguished (from left to right): (i) an electronic noise and γ-ray interactions region, (ii) a intermediate region where the full energy of the reaction products is not deposited, and (iii) the last region where is displayed the full peak.

Figure 2.10: Image of a typical BF3 tube - Model G-10-2A. Active Length: 60 mm and diameter: 2.54 cm.

When a neutron is absorbed by the ^{10}B component of the gas, an alpha particle and a recoil ^{7}Li nucleus are produced and travel in opposite directions. The movement of the alpha particle and the ^{7}Li nucleus creates primary ion pairs in the gas. The size of the resulting pulse depends on whether the lithium nucleus was left in the ground state or an excited state. When the lithium nucleus is left in the ground state (about 6% of the time), the pulse is larger than if the nucleus were left in an excited state (about 94% of the time) because the alpha particle and ^{7}Li nucleus have more kinetic energy (2.792 MeV vs 2.310 MeV) with which to create ion pairs. In a large diameter detector all the kinetic energy from the reaction products is deposited inside the detector and then the pulse height spectrum has two peaks at 2.792 and 2.310 MeV. Nevertheless, this kind of detector may also present the wall effect which occurs when either the size of the tube is too small compared with the range of the reaction products from $^{10}B(n,\alpha)^{7}Li$ or if the neutron interaction takes place in the gas close enough to one side of the tube. Then, if one of these particles strikes the chamber wall, the distance to the other side of the tube would be greater than the range of the particle heading towards it and a small pulse is produced causing a additional continuum spectrum as is shown in Figure 2.11. As in the case of ^{3}He detectors, increasing the size of the tube reduces this effect.

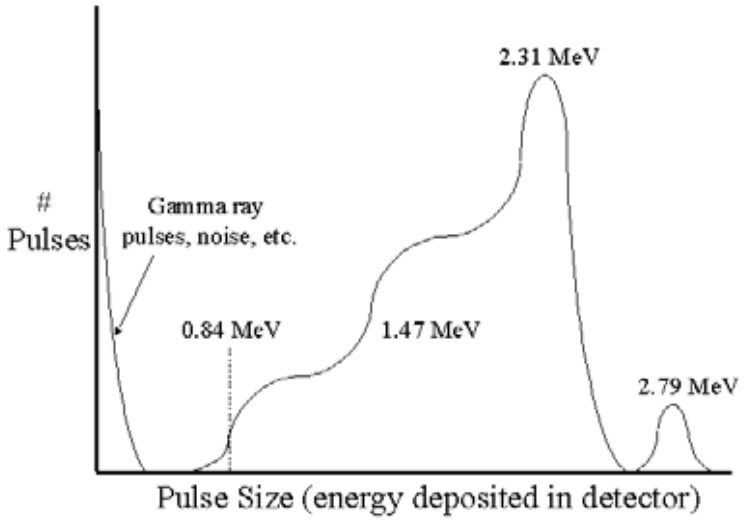

Figure 2.11: Pulse-height spectrum for a BF_3 proportional counter - The shape of the spectrum is due to the hits of the reaction products into the wall of the tube.

The detection efficiency for thermal neutrons can be up to 90% for a BF_3 tube (96%

enriched in ^{10}B) of 30 cm longitude and 80 kPa pressure. Nevertheless, these detectors have some undesirable operation conditions such a high operational voltage, between 1500 to 3000 volts, which can cause electronic noise and pulses due to background gamma rays that may exceed the threshold setting and generate spurious counts; they are bulky, and the BF_3 gas is not ideal as a proportional counter gas so it has to be manufactured with a mixture of a more suitable gas such as Argon. Besides, BF_3 is extremely toxic and when these detectors are exposed to high γ-ray fluxes, the BF_3 gas suffers chemical degradation problems. These disadvantages narrow their range of application.

Compared with the ^3He proportional counters, these can operate at higher pressures with good gas-multiplication behavior so for applications in which the maximum efficiency is necessary the ^3He counter is preferred to the BF_3 one. Nevertheless the high Q-value of the BF_3 reaction (2.79 MeV), versus ^3He (0.7 MeV), allows a better γ-discrimination by BF_3 based detectors. BF_3 gas is less expensive than ^3He, but in contrast, this is toxic whereas the ^3He is an inert gas.

2.4.1.3 Boron-lined Proportional Counters

Boron-lined proportional counters react similarly to BF_3 gas filled proportional tubes but incorporate the boron as a solid coating in the interior walls of an conventional proportional tube, as is shown in Figure 2.12. These detectors usually have a diameter roughly 3 cm, length ≈40 cm or even larger, and high work voltage ≈2000 V. With this design and since the reaction takes place on the tube surface, only one of the two particles will escape into the proportional counter so the pulse height spectrum consists of two distinguished areas, as it is shown in Figure 2.13. This is one of the most extended methods used in Radiation Portal Monitors (RPM) which are used for interdiction of illicit materials at borders [29]. Nevertheless, this type of detector has not achieved widespread popularity due to its enormous size, demanding operating conditions, and its worse γ-ray discrimination ability than the BF_3 tubes.

2.4.2 Scintillators

Scintillators operate by absorbing incident radiation that raises electrons to excited states. After the subsequent de-excitation, which usually takes from ns to tens of ns,

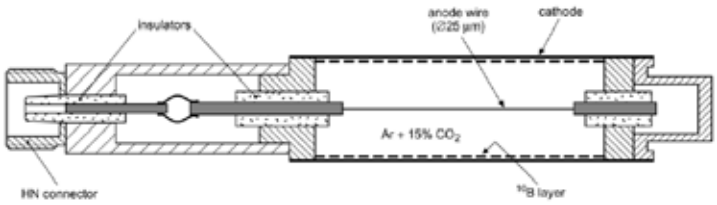

Figure 2.12: Sketch of a boron-lined counter - Boron is a coating in the interior of the walls.

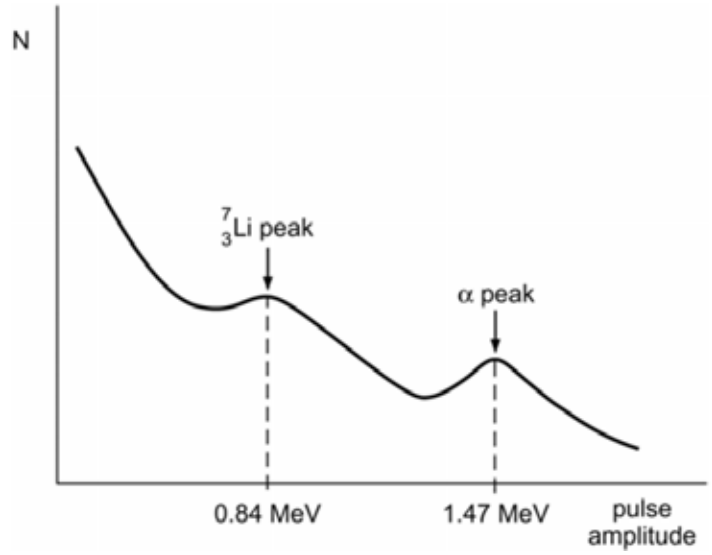

Figure 2.13: Pulse Amplitude Spectrum from a boron-lined proportional counter -

the scintillator emits a photon in the visible light range (see Figure 2.14). The light emitted from the scintillator interacts with the photocathode of a photomultiplier tube (PMT) or a photodiode, releasing electrons via the photoelectric effect. These electrons are guided, with the help of an electric field, towards the first dynode[1], which is coated with a substance that emits secondary electrons. The secondary electrons from the first dynode move towards the second, and so on. Each dynode in the chain is at a more positive electrical potential than its predecessor, such that the secondary electrons are accelerated from dynode to dynode. The final amplification is approximately 10^6 or higher. Scintillator detectors include: liquid organic scintillators, crystals, plastics, and scintillation fibers [28].

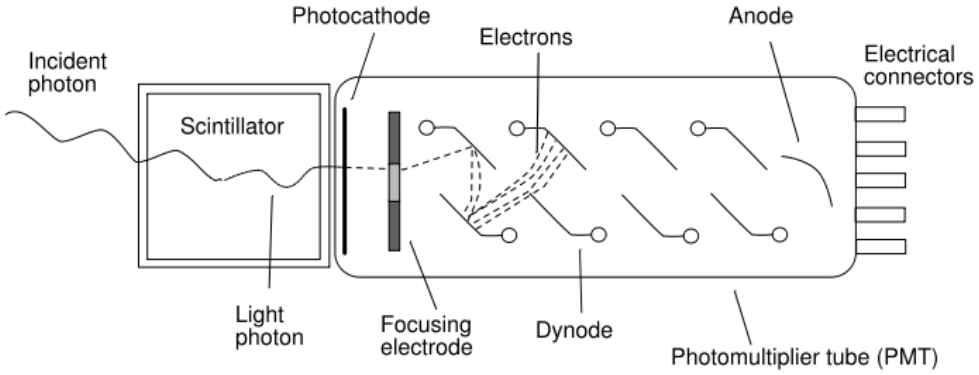

Figure 2.14: Schematic diagram of a scintillation detector - Sketch of a scintillation material (left) coupled to a photomultiplier tube (right)

Fast neutrons can be detected in any organic (plastic or liquid) scintillators that contain a large concentration of hydrogen atoms by means of elastic scattering. The energy of the neutron is partially transferred to the protons which on their turn can produce scintillation light. The visible light is collected in the PMT optically coupled to the scintillator and converted to an electronic pulse. Organic scintillators are often used for fast neutron detection because of their relatively fast response times and modest cost. Similarly, thermal neutrons may be detected by means of a nuclear reaction with ^6Li atoms in ^6Li-containing scintillation materials (loaded scintillators). ^6Li is normally used through ^6LiI doped with Eu [30]. The highly enriched ^6LiI(Eu) crystals

[1] A dynode is one of the electrodes within a photomultiplier tube and acts as a middle point between the photocathode and the anode.

(96% ^6Li) exhibit high thermal neutron detection efficiency (50%) and low gamma ray sensitivities comparable to ^3He. Figure 2.15 illustrates the working principle of one such neutron scintillator detector.

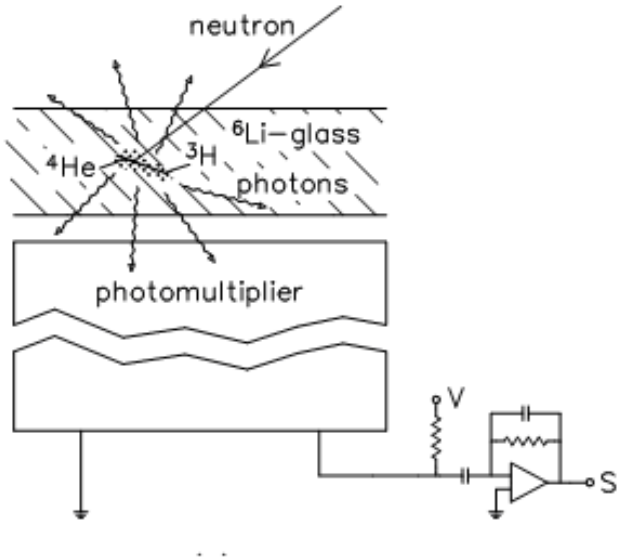

Figure 2.15: Working principle of a scintillator detector for neutrons -

Scintillators have a wide variety of applications. They are generally portable and have fast response times (tens to hundreds of nanoseconds). However, scintillator detectors have some undesirable characteristics as well: they contain photomultiplier tubes which are fragile, require a well-regulated power supply of hundred of volts, represent a shock hazard, and operationally degrade over time. Moreover, the PMT is affected by magnetic fields, adversely affecting the instrument response. Additionally, ^6Li-based scintillators for neutrons need hermetic assembly due to the hygroscopic nature of LiI(Eu) crystals, and like ^3He face difficulties in material supply as ^6Li requires special authorizations for export. These features do not allow for the versatility required by some environments.

2.4.3 Semiconductor detectors

Semiconductor detectors were historically conceived as solid-state ionization chambers [31, 32]. But since the density of semiconductors is high, they have a greater stopping power. As a consequence, a semiconductor may collect the charge carries delivered

by the radiation in a much smaller volume than those needed by gas o scintillation detectors. Therefore, they are more compact in size than the other two types of radiation detectors.

A semiconductor detector is usually a silicon or germanium diode of p-n or p-i-n type operating in reverse bias mode to detect charged particles or photons (see Figure 2.16). A p-i-n (PIN) diode consists in a wide and lightly doped ($\approx 10^{12} cm^{-3}$) intrinsic semiconductor between p-type and n-type extrinsic semiconductors, which are highly doped ($\approx 10^{18} cm^{-3}$). Both p-type and n-type regions are used for ohmic contacts with the metallization. When a particle passes through a semiconductor, it ionizes the matter, thereby creating free electron-hole[1] (e-h) pairs. The average energy necessary to create an e-h pair is 3.62 eV in silicon at 300 K, and 2.95 eV in germanium at 80 K. These values are 10 and 100 times smaller than that required for gaseous and scintillation detectors respectively.

The total number of e-h pairs created is proportional to the energy transmitted by the radiation to the semiconductor. At room temperature, the barrier created at the junction reduces the leakage current to low values, and when an electric field is applied, the charge carriers created by the radiation can be collected in the electrodes. These e-h pairs induce an image charge on the electrodes that is integrated, resulting in a pulse that is processed in an external preamplifier and its readout electronics, and thus the energy of the incident radiation can be found [2]. Details about the readout electronics used in this work are explained in Appendix B.

Diode particle detectors are usually manufactured with a shallow highly doped junction side and the other side is lightly doped in order to minimize the dead layer that the radiation has to cross before entering in the depletion region itself, as it is visualized in Figure 2.16. The lightly doped bulk favors a large depletion region that should match the range of the particles that have to be detected. The depletion width in a p-n junction is given by:

$$W_{dep} = \sqrt{\frac{2\varepsilon}{q}\left(\frac{1}{N_a} + \frac{1}{N_d}\right)(\phi_{bi} - V_a)} \tag{2.25}$$

[1]Electrons are transferred from the valence band to the conduction band of the semiconductor. Equally, the same number of holes are created in the valence band.

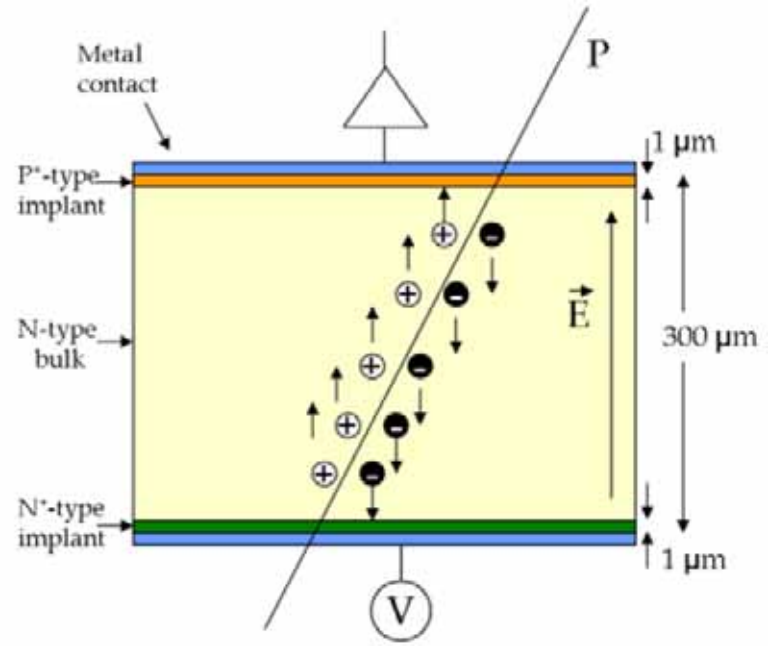

Figure 2.16: Schematic of a PIN diode - Sketch of a PIN diode that is transversed by a particle (P), which creates e-h pairs into the diode bulk. The diode is reversely biased to separate the e-h pairs and drift them to their respective electrodes [33].

where q is the charge of the electron[1], ϵ the product of the vacuum permittivity ϵ_0[2] and the relative permittivity of the semiconductor ϵ_r (ϵ_r=11.8 for silicon), ϕ_{bi} is the built-in voltage of the diode, V_a the bias applied, and N_d and N_a are the concentrations of donors and acceptors respectively[3].

The depletion voltage (V_{dep}) of the diode is given by (considering negligible the built-in voltage):

$$V_{dep} = \frac{q\,|N_{eff}|\,d^2}{2\varepsilon} \tag{2.26}$$

being N_{eff} the effective density, N_{eff}= N_d-N_a, and d the full depletion width [34]. In this simplified configuration, the diode may be assimilated to a capacitor where the

[1] q=1.602·10^{-19} C.

[2] ϵ_0=8.854·10^{-12}F/m.

[3] The dopants from Group III, e.g. boron, are *acceptors* and from Group V, e.g. phosphorous, are *donors*.

depletion region is the dielectric and the highly doped regions are the electrodes. With this assumption, the relation between the capacitance of the device and the depletion voltage is given by the next equation:

$$\frac{1}{C^2} = \frac{W^2}{\varepsilon^2} = \begin{cases} \frac{2\epsilon}{q|N_{eff}|} V_{bias} & \text{if } V_{bias} < V_{dep} \\ \frac{d^2}{\varepsilon^2} & \text{if } V_{bias} \geq V_{dep} \end{cases} \tag{2.27}$$

The $1/C^2$ curve presents two regions: (i) for $V_{bias} \leq V_{dep}$, $1/C^2$ increases linearly with the bias voltage up to V_{dep}, (ii) for $V_{bias} \geq V_{dep}$, $1/C^2$ remains constant independently of the voltage applied. The depletion voltage depends on the thickness of the depletion region. Measuring the $1/C^2$ values and fitting the curves of both regions, it is possible to calculate the depletion voltage as the interception point between the fitted curves. This value let us know the optimal voltage to operate the diode equal or higher than V_{dep}. More details about how the electrical characterization has been carried out in this work are explained in Appendix C.1.

Traditionally semiconductor detectors have been used to detect charged particles and photons, but prototypes for neutron detection have been developed in recent years. This has been prompted, on the one hand, by the need to replace the ^3He tube detectors because of the exhaustion of the ^3He gas reserves, and due to their difficult operating conditions, including size, elevated gas pressures (≈10 bar), and high voltage power supply (≈10 kV). On the other hand, there are several environments which require features that only semiconductor devices possess, such as low weight and size, compactness, robustness and low battery consumption for transportability, as well as a fast response [35]. Moreover, the compactness of semiconductor detectors, originated from the high density of the material, allows a short range of the neutron reaction products, but also increases the probability of interaction of the γ-rays. Silicon has an atomic number 14, which is lower than the Z of other semiconductors used as particle detectors like Ge (Z=32), CdTe (Z=48/52), or CdZnTe (Z=48/30/52). Therefore, the ideal semiconductor candidate for neutron detection with the higher γ-rejection rate is silicon, which provides a relatively low Z for moderate γ-ray interaction probability and above all a high technological know-how thanks to the microelectronics industry which makes it a material of choice as active sensor. These are the reasons for what the detectors developed in Chapter 4 are manufactured with a silicon substrate.

The adaptation of a semiconductor-based detector (SD) to detect neutrons entails the complexities inherent in the particular neutron physics. The basic detection mechanism of a SD neutron detector is shown in Figure 2.17.

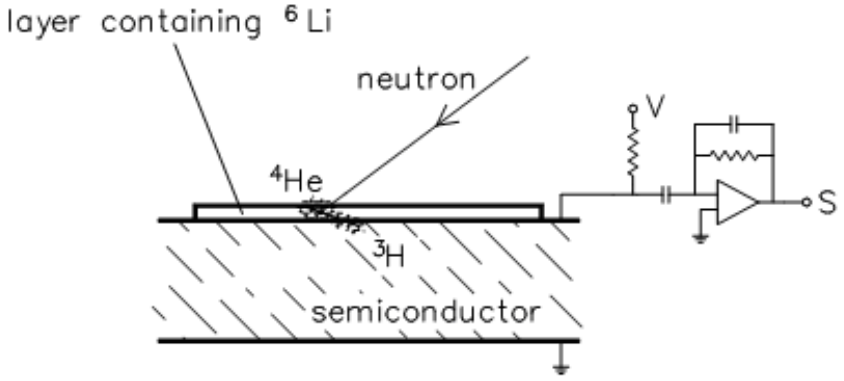

Figure 2.17: Working principle of a planar semiconductor detector for neutrons - The converter layer (^6Li in this example) is covering the semiconductor detector.

Semiconductor neutron detectors may be classified into three big groups, depending on how the converter is incorporated into the semiconductor [36]:

- The first group is constituted by detectors with planar configurations, i.e. a SD side is covered by one of the converters listed in Table 2.4, as Figure 2.18.a shows. This configuration is detailed in subsection 2.4.3.1.

- The second group is formed by 'bulk neutron detectors' which are detectors whose bulks themselves are sensitive to neutrons since they are made with a neutron converter [37, 38, 39, 40, 41], e.g. BP, BAs, BN, BxC, HgI_2, CdTe, CdZnTe, GaAs semiconductors. These detectors could be able to extract neutron signal directly from their bulk, without additional converter layers. Although they potentially could reach 100% thermal neutron efficiency, in fact these detectors have big limitations: they are usually very thick bulks with need high voltage bias (300–1000 V) and what is more important, the charge carrier transport properties of these materials are very bad, and there is trapping, severely limiting the detector signal. Thus, the collected charge is very low, with the risk of being confused with the noise level. In order to discriminate signal from noise, it is necessary to

increase threshold levels, and then the detection efficiency is dramatically reduced, being comparable to that of standard planar devices.

- The last group, the 'backfilled' SDs, is formed by detectors with perforations, holes or trenches, filled with a converter. Figure 2.18.b displays one of the possible structures. They are explained in subsection 2.4.3.2. Although many neutron detector designs might be considered as possible theoretically, most of them are not technologically realistic since they are not sometimes manufacturable with standard MEMS techniques in a clean room facility. Some 3D designs carried out in the framework of this thesis, which are in principle feasible technologically, are presented in subsection 3.5.

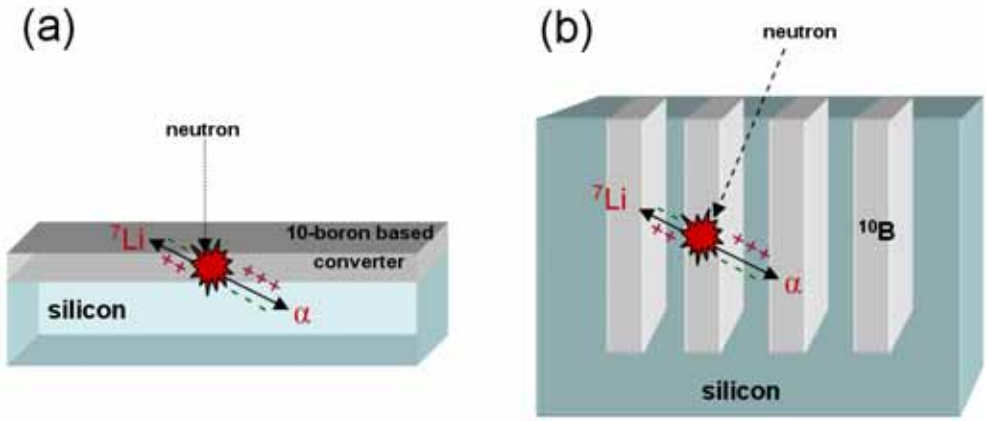

Figure 2.18: Schematic of the standard 2D and 3D design for silicon neutron detectors - (a) 2D design of a planar silicon neutron detector. (b) sketch of one of the 3D designs with silicon bulk.

2.4.3.1 Planar silicon neutron detectors

Planar detectors covered with a neutron converter have been the simplest design used to adapt semiconductor devices for neutron detection for years [42]. They consist of a planar diode detector, preferably with thin contact layers[1], and a layer of converter deposited on its surface (Figure 2.18.a) [7, 43]. The planar diode may be either a PN junction parallel to the detector surface or another detector configuration more complex

[1]The thinner the contact layers and detector entrance window are, the lower is the energy loss of the reaction products coming from the converter layer.

where the converter is equally deposited over one of its sides. With this layout, neutrons may be captured in the converter when they interact with the device such that if their reaction products reach the sensitive detector volume, these neutrons may be detected [44].

Nevertheless, the planar configuration has an unavoidable geometric restriction because the neutron interaction probability in a planar detector depends strongly on the thickness of the converter layer. The probability of the neutron interaction increases with the thickness of the converter layer, but at the same time this reduces the probability that the reaction products reach the sensitive volume of the silicon detector due to the self-absorption energy loss within the converter itself. When a neutron is absorbed the probability that the reaction products enter the detector depends on the solid angle subtending the surface within the average range of the particles, as Figure 2.19 shows. Note that in this planar configuration, not all the reaction products are able to reach the sensitive detector volume. For each converter material there is an optimal thickness to achieve the most efficient planar configuration (this item is discussed in subsection 3.4).

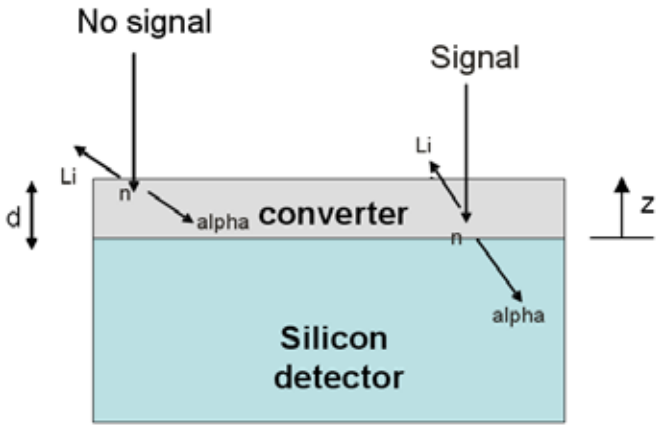

Figure 2.19: Sketch of planar detector irradiated by neutrons. - Schematic representation in a planar detector of a couple of possible directions of the reaction products for a ^{10}B based converter layer.

There are four factors that influence the efficiency of a planar silicon detector with a converter layer: (i) neutron interaction probability, (ii) ranges of the emitted charged particles and density of the converter, and (iii) thickness of the converter layer. A

compromise between these factors is crucial. In the following, we briefly analyze each of these parameters:

(i) Neutron interaction probability

If a normally incident collimated flux of neutrons (I_0) passes through a layer of converter material, the neutron flux is attenuated as:

$$I(x) = I_0 e^{-z/\lambda} \tag{2.28}$$

and therefore the fraction of thermal neutrons absorbed by the converter is described as [24]:

$$\frac{I_0 - I(x)}{I_0} = 1 - I(x)/I_0 = 1 - e^{-z/\lambda} \tag{2.29}$$

where λ is the mean-free-path of the neutrons in the material defined in equation 2.10 and z is the depth or thickness reached by the incident neutron. Table 2.5 contains the mean-free-path for thermal neutrons in the main neutron solid converters[1] listed in Table 2.4.

Table 2.5: Mean-free-paths of thermal neutrons into solid converters.

Converter	$\lambda(\mu m)$
^{10}B	17.58
^{6}Li	198.46
^{113}Cd	10.47
^{155}Gd	5.36
^{157}Gd	1.30

Figure 2.20 shows the fraction of thermal neutrons absorbed by these neutron converters as a function of their thicknesses, according to equation 2.29. This figure shows how the thermal neutron capture probability is higher if the mean-free-path is lower. For example, 3 mean-free-path lengths (54 μm) of ^{10}B can absorb nearly 95% of the incident thermal neutrons, whereas almost 600 μm of ^{6}Li thickness is necessary to reach such percentage of absorption. This reason, together with those established

[1] For this basic case, the calculations were done taking the converter densities from NIST database [45].

in subsection 2.3.1, made us choose the ^{10}B isotope as the converter to be used in this work. Therefore the following analysis will be done only for this isotope hereafter.

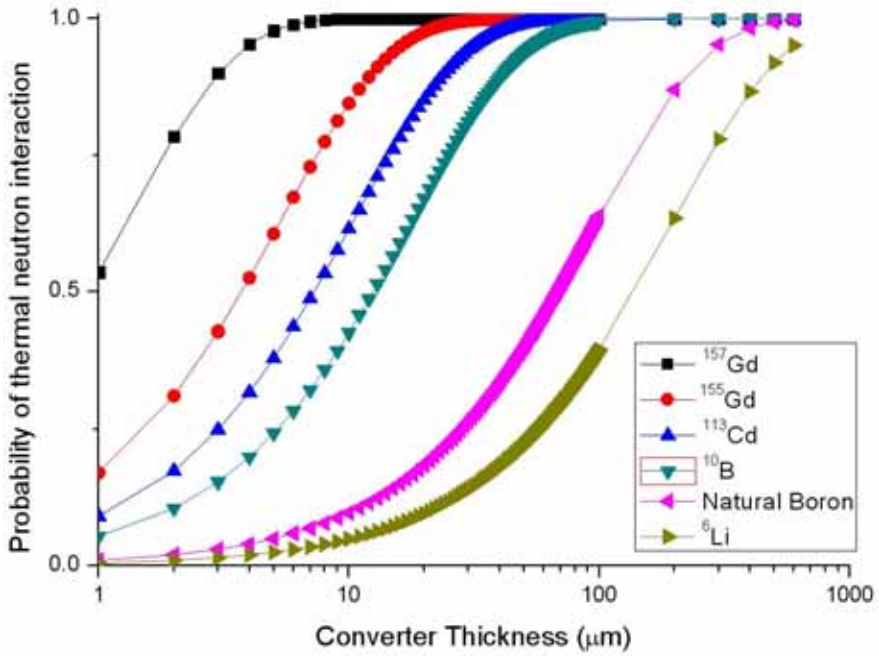

Figure 2.20: Thermal neutron absorption probability in solid converters - .

It is important to note that this calculation is true only if experiments or simulations are carried out with a narrow neutron beam. This does not usually happen since in most cases neutrons are either not collimated or the shielding causes scattering. In fact, neutrons may scatter several times before they are absorbed. The behaviour of non-collimated neutron fields is very complex to evaluate without the computational support of simulations.

(ii) Ranges of the $^{10}B(n,\alpha)^7Li$ reaction products

Apart from the converter layer, the reaction products also have to transverse other layers that make up the neutron detector: the metal contacts (usually Al), and the silicon bulk itself. Table 2.6 shows the average ranges[1] of the $^{10}B(n,\alpha)^7Li$ reaction products in silicon and aluminium as well as in different boron-based converters: ^{10}B

[1]Note that the density of ionization is not linear with the penetration distance since this is described by the Bragg ionization distribution [24].

and natural boron (20% ^{10}B), both with the nominal density of 2.46 g/cm^3, and a novel mixture of o-carborane ($C_2B_{10}H_{12}$) and adhesive, which was used in some of the tests reported in Chapter 5. The values given in this table were estimated by means of the SRIM software [46]. The total range of these reaction products limits the minimum size of the sensitive detector volume necessary to capture completely the full energy of such particles.

Table 2.6: Range of reaction products from neutron capture in different materials.

Material	Density (g/cm^3)	Alpha Range (μ)	^7Li Range (μ)
^{10}B	2.46	3.27–4.05	1.69–1.90
Natural Boron	2.46	3.53–4.38	1.83–2.05
$C_2B_{10}H_{12}*^1$	1.37	5.13–6.35	2.71–3.03
$C_2B_{10}H_{12}*^2$	0.5	14.06–17.40	7.44–8.30
Silicon	2.32	5.15–6.36	2.46–2.80
Aluminium	2.70	5.15–6.36	2.46–2.80

($C_2B_{10}H_{12}*^1$ is mixed with a cyanoacrilate matrix and $C_2B_{10}H_{12}*^2$ is mixed with a PVC matrix, as is explained in Appendix A.1)

As is indicated in Table 2.6, the range of charged particles produced in the o-carborane compounds is higher than in ^{10}B or natural boron mainly due to a lower density of the material, according to the Bragg-Kleeman rule[1] [2], given by:

$$\frac{R_1}{R_0} \simeq \frac{\rho_0\sqrt{A_1}}{\rho_1\sqrt{A_0}} \tag{2.30}$$

where ρ and A are the density and atomic weight respectively of the material.

Therefore there are two competing effects as a high bulk density of the converter increases the neutron interaction probability but at the same time decreases the range of the reaction products. In order to optimize each possible design and the converter used, Monte Carlo simulations are needed, as is explained in Chapter 3. Hence, the density of the converter has a direct impact on two parameters: the mean-free-path

[1]The Bragg-Kleeman rule is a semiempirical formula used to scale the range of charged particles in a compound provided its range is known in other material.

and the range of the neutron capture reaction products emitted inside the converter, as was explained above. First, given that λ^{-1}=N·σ, and N=$N_A \cdot \rho$/A, the mean-free-path is inversely proportional to the density, as Figure 2.21 illustrates. The second influence is discussed next.

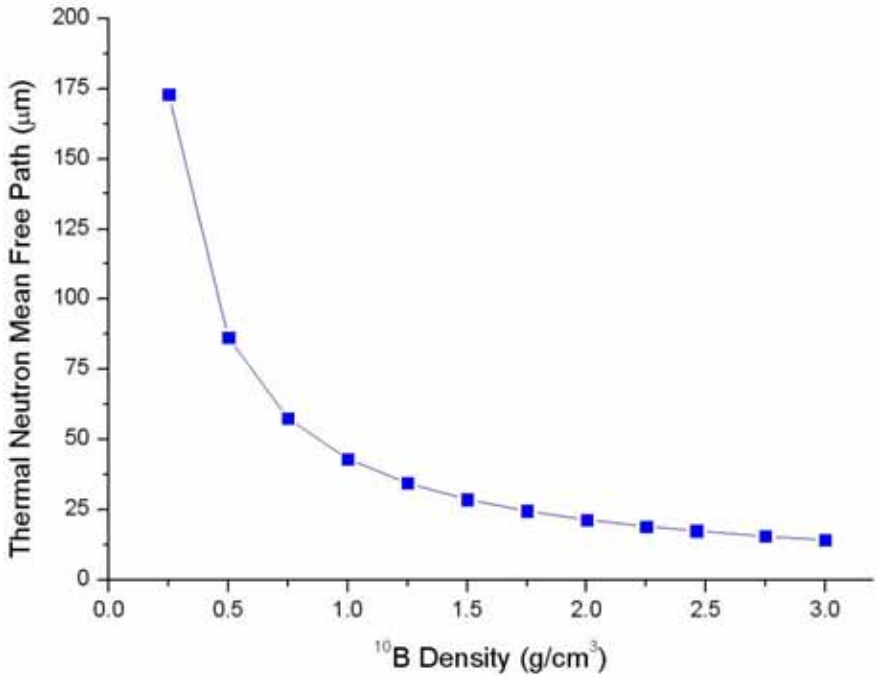

Figure 2.21: Thermal neutron mean free path as a function of the ^{10}B density - The mean-free-path for thermal neutrons drops markedly when the ^{10}B density increases.

When considering fragmented, microcrystalline solids, one has to distinguish between *bulk* density and *particle* density. Bulk density is a property of granulated solids or powders and is defined as the average density of a large volume of the powdered substance, whereas particle density refers to the internal density of the particles that make up the powder. In particular, the particle density of boron is 2.46 g/cm^3 while the bulk density depends of the compacted state of the crushed powder and may be as low as 0.45 g/cm^3 for a particle size $\prec$56 μm [47]. Most deposition techniques used for filling 3D structures with neutron converters make use of the powdered material so the real packing densities achieved could be lower than the intrinsic particle density of the material (see Appendix A.2.2).

Table 2.7 summarizes the main average range values of the ^{10}B(n,α)^7Li reaction

Table 2.7: Ranges of the $^{10}B(n,\alpha)^{7}Li$ reaction products in ^{10}B.

Isotope	Bulk density (g/cm^3)	Alpha Ranges	^{7}Li Ranges
^{10}B	2.5	3.1–3.8	1.6–1.8
	2.0	3.8–4.8	2.0–2.2
	1.5	5.1–6.3	2.7–3.0
	1.0	7.7–9.5	4.0–4.5
	0.5	15.4–19.0	8.0–8.9

products (estimated with the SRIM software) for different ^{10}B densities belonging to different compacted states of this converter. The calculations assume that the inter-particle space is vacuum and not air, but the effect of the air molecules in the ranges is negligible. Table 2.7 shows that the ranges of the reaction products are doubled when the substrate density is halved. This means that the density of the converter has a direct impact on the range of the neutron capture reaction products inside the converter itself. This fact is plotted in Fig.2.22 for theoretical layer of ^{10}B with different densities.

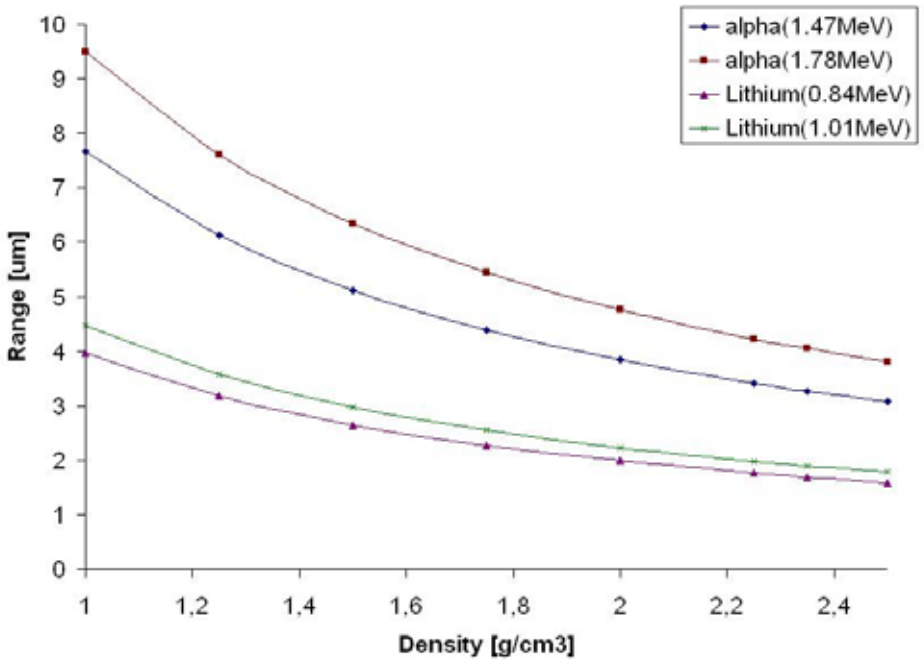

Figure 2.22: Range of the reaction products of ^{10}B - Ranges of the reaction products, ^{7}L and α particles, inside a ^{10}B layer of variable density.

(iii) Device geometry

As an overall rule, a proper configuration of the Si detector design will enhance its sensitivity for thermal neutrons. As seen above, the neutron interaction probability in a planar detector depends enormously on the thickness of the converter layer (d) (Fig. 2.19). The probability of a neutron interaction increases with a thicker converter layer, but at the same time this reduces the probability that the charged reaction products reach the sensitive volume of the silicon detector due to the energy loss within the converter itself. For each converter material an optimal thickness has to be found to achieve the most efficient planar configuration.

In order to analyze briefly how the converter thickness influences the neutron detection efficiency, a simple analytical model can be used to examine the physics and to serve as a guide for the posterior simulations needed for the study of the phenomenon (presented in subsection 3.4). We will consider here the simplest model to grasp the phenomenology of neutron detection for the front side irradiation case and a ^{10}B converter:

The detection efficiency of a planar neutron detector with a converter layer can be derived basically from the product of two probabilities: the probability of neutron interaction at a depth z within the converter, P_n(z), and the probability that the subsequent reaction products reach the semiconductor detector from the neutron interaction point z, P_{prod}(z). No dead zone between the converter and the semiconductor is considered. These two probabilities are governed by the two parameters introduced above: the neutron mean-free-path and the range of the $^{10}B(n,\alpha)^7Li$ reaction products in the converter material. The branching ratio B of the neutron reaction has to be added when more than one interaction of the neutron with the nucleus is possible. The efficiency can then be written as:

$$\varepsilon = \int_0^d P_n(z) B P_{prod}(z) dz \tag{2.31}$$

The probability P_n(z) of neutron interaction at a depth z follows an exponential decay governed by the neutron mean-free-path in the converter:

$$P_n(z) = \frac{exp\left(-\frac{d-z}{\lambda}\right)}{\lambda} \tag{2.32}$$

To calculate the probability $P_{prod(z)}$, we will consider separately each one of the $^{10}B(n,\alpha)^7Li$ reaction products. The detection efficiency is obtained by summing the

contributions from both reaction products. These particles are emitted at 180 deg and have a defined range R within the converter. Therefore, two cases have to be considered, depending on d (^{10}B layer thickness):

- $\mathbf{d \prec R}$: one reaction product can reach the semiconductor sensitive volume. The probability is given by the solid angle of the cone of aperture $2\theta_R$ (subtended from the neutron capture point to the detector):

$$P_{prod}(z) = \frac{\Omega(z)}{4\pi} = \frac{2\pi(1 - cos\theta_R)}{4\pi} = 0.5\left(\frac{R-z}{R}\right) \tag{2.33}$$

  with $\cos\theta_R$ = z/R

- $\mathbf{d \succ R}$: because for z$\succ$R no reaction products can reach the semiconductor, the probability can then be written with a step function H(R-z):

$$P_{prod}(z) = 0.5\left(\frac{R-z}{R}\right) H(R-z) \tag{2.34}$$

The detection efficiency is then calculated by integration of Eq. 2.31, given:

- For $\mathbf{d \prec R}$:

$$\varepsilon = 0.5B\left\{\frac{R+\lambda}{R}[1 - exp(-d)] - \frac{d}{r}\right\} \tag{2.35}$$

- For $\mathbf{d \prec R}$:

$$\varepsilon = 0.5B\left\{\left\{\frac{R+\lambda}{R}[1 - exp(-d/\lambda)] - 1\right\} exp\left(\frac{R-d}{\lambda}\right)\right\} \tag{2.36}$$

These results show that the efficiency depends on the charged particle range and the mean-free-path (and therefore implicitly on the ^{10}B density), and the converter thickness. Fig. 2.23 shows the estimated efficiency with the equations 2.35 and 2.36. For planar silicon-based neutron detectors covered with ^{10}B the maximum efficiency for thermal neutrons remains below 4.5%[1]. The best efficiency is reached at 0.75 mg/cm^2, i.e. for example for the particle boron density of 2.46 g/cm^3, the optimum thickness is 3

[1]It is important to hightlight that this value is for an ideal device, i.e. without dead layers, and for a thermal neutron beam focused on the detector side that is covered by converter. Other more complex options from more realistic considerations are discussed in subsection 3.4.

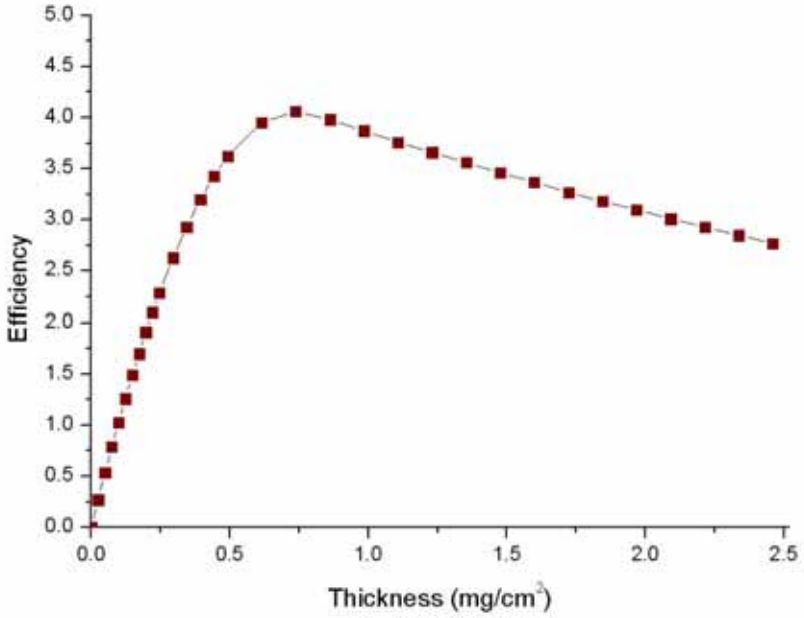

Figure 2.23: Calculated planar detection efficiency for thermal neutrons - Estimated efficiency with an analytic model as a function of the ^{10}B converter layer thickness, plotted as density-independently, and for front-side irradiation.

μm. That thickness is comparable to the range of the alpha particle in the ^{10}B converter (see Table 2.6). In addition, it is observed that for thickness thicker than this optimum value, the efficiency decreases since the charged particles capture probability in the sensitive detector volume declines due to the energy loss in the converter itself. What is more, the thicker the converter layer, the higher the number of low-energy counts in the spectrum is, and hence the measured efficiency could suffer with increased lower level discriminator (LLD)[1]. An extensive analytic study can be found in [48], where all the factors that have influence on the overall efficiency for ^{6}Li and ^{10}B converters [48] are analysed, producing similar results. This type of planar structures are the focus of part of the work developed in this thesis, detailed in Chapter 4 and whose results are discussed in Chapter 5.

Summarizing, the ideal planar semiconductor-based neutron detectors would have a maximum efficiency of 4.5% in the best of the cases. This value is low compared to other technological solutions such as perforated detectors, which overcome the planar-

[1]In a measurement, a LLD setting is used to discriminate signal pulses from background and low level noise.

geometric restriction by increasing the contact surface between the converter and the silicon detector with perforated-patterns, as is explained in the next subsection. Nevertheless, planar semiconductor layouts are relatively easy to manufacture, so they are very useful in some types of test and applications, as it will be expounded in Chapter 4.

Finally, it is important to emphasize that although obviously the optimum converter material would be a layer of pure ^{10}B, this is not easy to achieve at a technological level. In recent publications, several converter deposition techniques have been tried by other research groups (ranging from CVD [49] to simply applying pressure [50] or similar manual methods [36]), but they are either complex or not easily reproducible. In this work we propose some optimized methods for the deposition of the converter layer through three viable techniques: spinning, evaporation, and sputtering, all of them extensible to complete wafers, in order to facilitate a controllable and repeatable industrial process. These proposals are detailed in Appendix A.

2.4.3.2 Microstructured neutron detectors

Twenty-five years ago, R.A. Muminov and L.D. Tsvang pointed out that neutron detection efficiency would increase to 40%, and higher, if rectangular channels (microstructures) filled with ^{10}B were distributed into the SD volume [6]. In principle, a microstructured neutron detector works on a similar way as the planar neutron detector explained above, but it has perforations inside the sensitive detector that increases the surface area of the converter in contact with the sensitive semiconductor volume (see Figure 2.18.b). On the one hand, this fact would increase the neutron interaction probability and, on the other hand, it would raise also the probability of reaching of the reaction products into the sensitive detector.

Similar to the case of planar silicon detectors, a theoretical analysis of the microstructured detectors may be done to see the factors that have influence on the performance of the design of a prototype: (a) neutron interaction probability and (b) perforated geometry.

(a) Neutron interaction probability in perforated designs

The interaction probability of a particle in matter was shown in subsection 2.4.3.1 for the 2D simplest case, which limits the absorption due to its planar configuration, as

was argued above. In contrast, filling perforated trenches with a converter has several effects (Figure 2.24): First, for normally incident neutrons, the absorption thickness

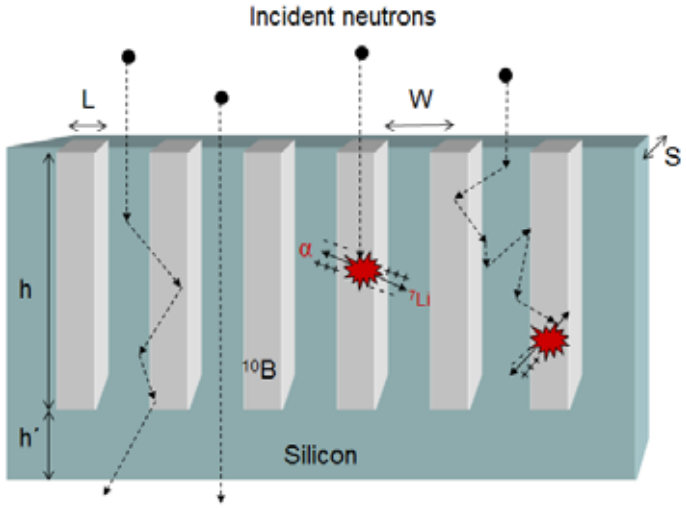

Figure 2.24: Schematic of a 3D design - Cross section of a 3D-pattern with microchannels etched in the silicon bulk and filled with ^{10}B converter.

may become as large as the trench depth (h), and if such trench depth is at least 3 mean-free-paths (54 μm for the ^{10}B case), it absorbs nearly 95% of the incident thermal neutrons. Secondly, the space between trenches (W), i.e. the sensitive silicon volume, surrounds the trenches that contains the converter, so the reaction products coming from the converter have more probabilities of reaching the silicon than in the planar case. Third, with multiple trenches along the detector, there is more probability that neutrons that have suffered scattering are finally captured. The inter-space should be higher than the averange range of the reaction products in silicon, but at the same time as low as possible technologically since this region does not capture neutrons. Therefore, for the ^{10}B converter, W should be $\approx$ 6.36 μm (see Table 2.6), whereas for example W should be $\approx$ 40 μm for ^{6}Li, which means up to six times more silicon volume that is insensitive to neutrons and receptive to γ-rays.

(b) Perforated design geometry

The neutron interaction probability depends strongly on the design of the device. If the prototype is a planar silicon detector, the neutron absorption will depend only on the thickness of the converter layer, but if the 3D design consists of for instance an

array of microchannels, there will be other parameters such as the trench width (L) and depth (h), the silicon wall width between channels (W), and the converter density (ρ). These parameters are defined in Figure 2.24. As it is explained in the item (a), the neutron capture probability of the 3D device is higher if the volume backfilled with the converter is large so both h and L should be maximized. At the same time, if L is too large the probability of the charged products reaching the sensitive silicon volume decreases due to their energy loss in the same converter. In addition, the width of the silicon walls between channels, W, should be as small as possible as they are not sensitive to the thermal neutron radiation but they can contribute unnecessary background signals from the photon radiation that normally accompanies neutrons. Hence, the detection efficiency of the SD is conditioned by the volume fraction V_f of the converter (see Figure 2.25):

$$V_f = \frac{V_{channel}}{V_{channel} + V_{Si}} = \frac{S \cdot L \cdot h}{S \cdot L \cdot h + S \cdot (L + W) \cdot (h + h')} \approx \frac{L}{L + W} \tag{2.37}$$

assuming h≻h'

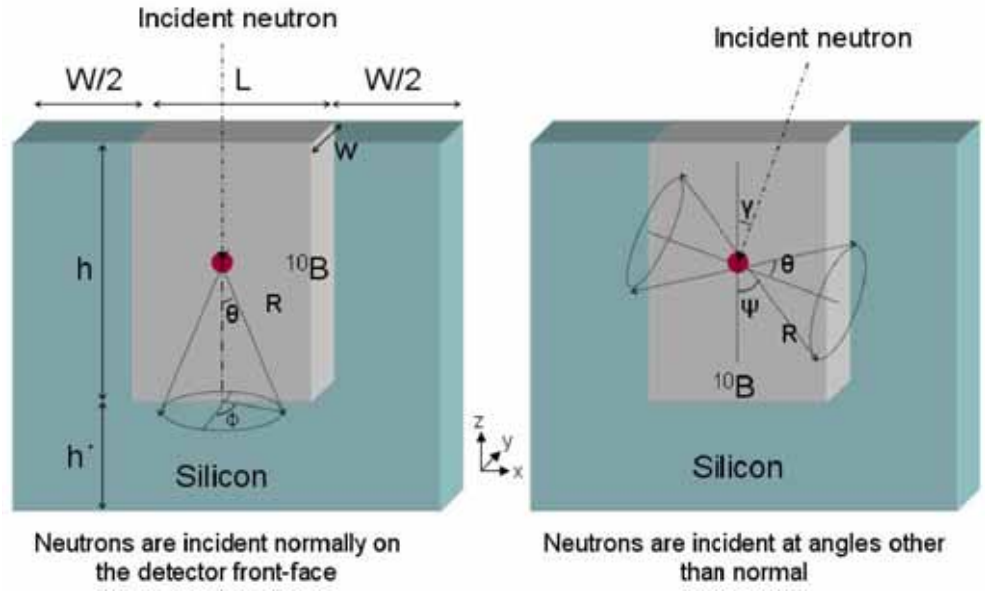

Figure 2.25: Schematic diagram of a perforated semiconductor detector - Sketch of the geometric parameters which intervene in the interaction process into a microchannel etched in the silicon bulk and filled with ^{10}B converter

In order to analyze briefly how V_f affects the neutron detection efficiency, we can use a simplified model of a microchannel as follows: the thermal neutron detection efficiency for a microchannel backfilled with ^{10}B is given by the product of the volume fraction V_f, the branching ratio B of the neutron reaction with ^{10}B, the probability of neutron interaction, $P_n(x, y, z)$, and the probability that $^{10}B(n, \alpha)^7Li$ reaction products reach the SD from the initial interaction point, $P_{prod}(x, y, z)$. Thus, the efficiency is written as:

$$\varepsilon = \int_{x_1 y_1 z_1}^{x_2 y_2 z_2} P_n(x, y, z) B V_f P_{prod}(x, y, z) dx dy dz \tag{2.38}$$

If the reference system is centered in the bottom of the channel the probability can be estimated as follows:

$$P_n(x, y, z) = \frac{e^{\frac{-r}{\lambda}}}{\lambda} \tag{2.39}$$

which relies on the neutron path r and on the state of the absorber through mean-free-path λ. And:

$$P_{prod}(x, y, z) = 2\frac{d\Omega}{4\pi} \tag{2.40}$$

where:

$$d\Omega = cos\psi tan\theta d\theta d\phi \tag{2.41}$$

is the solid angle subtended from the neutron capture point to the sensitive silicon bulk delimited by the range of the reaction product, and

$$cos\psi = cos\gamma cos\theta + sen\gamma sen\theta cos\phi \tag{2.42}$$

γ being the angle of the incident neutron with respect to the normal direction normal to the detector surface and ψ the angle between the direction of the ejected $^{10}B(n, \alpha)^7Li$ reaction products and such a normal direction. P_{prod} has been multiplied by two to take into account both trench walls through which the reaction products can exit the converter.

These analysis demonstrate that the detection efficiency depends on the neutron path (r) when it is captured within the converter, and therefore, this depends on the incident neutron direction and how much converter it crosses. Hence, the measured

efficiency relies on the kind of neutron beam we use, i.e. the incident neutron direction. There are three main layouts of neutron beams: a front-face irradiation (Fig. 2.26.a), i.e. the detector and beam are in front of each other such that a monodirectional neutron beam points toward the upper-face of the detector as it occurs approximately in collimated beams of research nuclear reactor facilities (used in subsection 3.4); a lateral irradiation (Fig. 2.26.b) where the neutron beam is transverse to the front-back sides of the detector; and an isotropic irradiation (Fig.2.26.c), i.e. the neutron beam is around the device, sufficiently far so there is an increase in uniformity in response to varying incident neutron directions, as for example it was used in the case of the neutron spectra coming from a medical linac (see subsection 5.3.1).

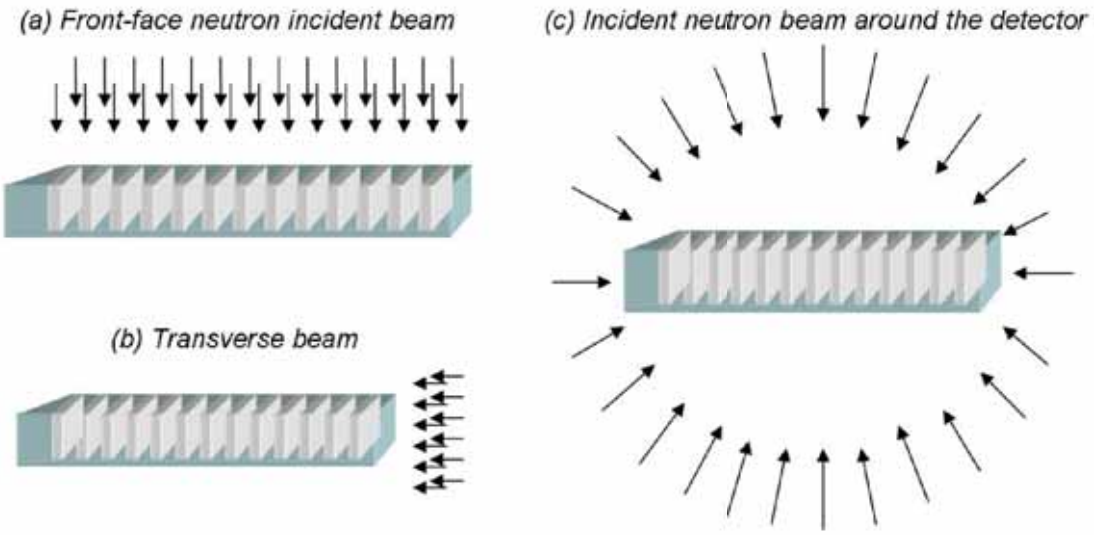

Figure 2.26: Schematic of possible incident beams. - Possible simplified distributions of incident neutron beams taking the detector as the system of reference.

All these analytical considerations display that the neutron efficiency relies mainly on four parameters of the microstructured SD: $\lambda(\rho)$, L, W and h, and on the direction of the incident neutron beam. Therefore they are considered as the starting-point parameters to be optimized by means of Monte Carlo simulations in Chapter 3.

Very few research groups have been able to manufacture a microstructured SD adapted for neutron detection, leaving this field still open. Depending on the perforated design, some few studies have been already reported encouraging values for thermal neutron detection, for example:

- The first operational perforated neutron detector was presented by McGregor in 2002 [51]. Thereafter, his group has continued working intensely on this topic, using a ^6LiF converter, with considerable improvements [52, 53]. They have reported a thermal neutron efficiency of 12% [54] for devices with sinusoidal trenches and up to 37% but using stacked detectors [55]. In 2010, W.J. McNeil estimated by simulation thermal neutron counting efficiencies for hole, straight, and sinusoid designs (with ^6LiF, 200 μm deep trench and including 26 μm thick coating additionally) of 12%, 20%, and 25% respectively [56]. Experimentally they reported measured efficiencies up to 9.7%, 12.6%, and 16.2% for each perforated design, with maximum a 10^6 n/γ discrimination rate, using a monoenergetic neutron beam coming from a nuclear reactor neutron beam-line facility, which constitutes an ideal testing configuration. Figure 2.27 shows two SEM[1] images of McGregor's designs filled with ^6LiF powder. In 2011, S.L. Bellinger reported the higher thermal neutron detection efficiency for silicon detectors with straight trenches[2]: 42% of measured thermal-neutron detection efficiency for a detector with 1 cm^2 and 10^6 n/γ ratio [57].

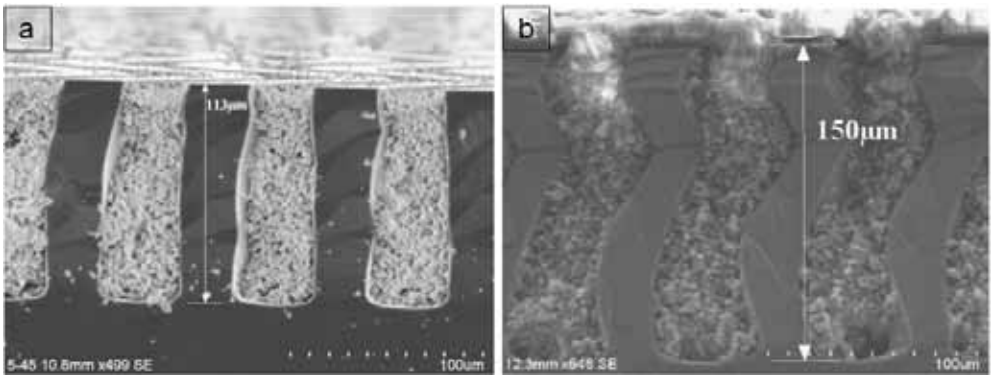

Figure 2.27: Cross-section details of two perforated silicon neutron detectors. - SEM images of (a) trenches of 100 μm deep and 40-50 μm width filled with ^6LiF powder, (b) sinusoidal trenches of 150 μm deep. All devices from D.S. McGregor's group [52, 56].

- Since 2005 the researchers led by R.J. Nikolic and A. Conway have been working

[1] Scanning electron microscope.

[2] Although perforations with sinusoidal and chevron patterns have a preferable angularly unresponsive design, the straight trenches showed a fabrication and a subsequent stacked much easier than those other designs.

with a device processing based on etching pillar structures and conformal coating, as Figure 2.28 shows [49, 58]. They have got a 20% thermal neutron efficiency with a pillar array with 2 μm silicon pillar width, 2 μm width between channels filled with boron, and 26 μm pillar height, with a 10^5 n/γ discrimination rate [59].

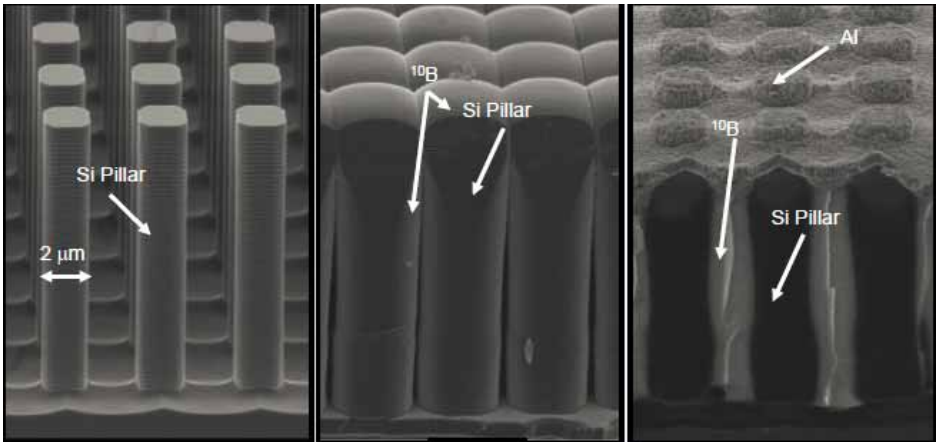

Figure 2.28: Silicon neutron detector with etching pillar structure. - From left to right: (i) deep reactive-ion etching (RIE) by inductively coupled plasma (ICP), (ii) conformal boron deposition by chemical vapor deposition (CVD) by thermal decomposition of decaborane ($B_{10}H_{14}$), (iii) plasma etching of boron and deposition contacts by sputter (Al electrodes). All from R. Nikolic's group [49, 58].

- In 2007, J. Uher predicted simulated thermal neutron efficiencies for square and cylinder pores (with 230 μm depth and silicon walls of 10 μm) of 32% and 28% for ^6LiF (enriched at 89%) and 22% and 20% for ^{10}B (enriched at 80%) respectively. These values are the maximum for variable converter densities [36].

- At the end of 2011, J. Clinton reported an experimental testing of an array of etched hexagonal holes filled with natural boron (see Figure 2.29 with B_4C), obtaining maximum intrinsic efficiencies of 4.5% for thermal neutrons [60].

Nevertheless, for years it has been suggested that the efficiency could reach 50%, highlighting that this issue remains incompletely resolved and novel designs may bring improvements. In recent years the Radiation Detectors Group at IMB-CNM has developed a new '3D' silicon detector technology developing columnar

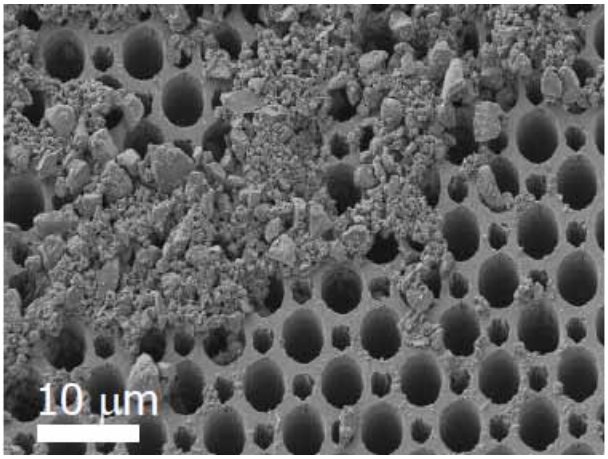

Figure 2.29: Image of etched hexagonal holes filled with B_4C. - SEM images of B_4C particles to fill the holes etched in the device. From J. Clinton [60].

electrodes through the semiconductor bulk [61]. Using high-aspect ratio deep etching techniques based on the advances depeloped in our research group, it is possible to etch microstructured patterns into the silicon bulk and make up the p-n junctions into such material [62]. Section 3.5 deals with the development of novel and feasible prototypes for neutron silicon detectors of high efficiency.

Like the above mentioned case of planar detectors, the filled of the perforations with converter material is a unresolved issue still. Encouraging developments with ^{10}B converter in this line have been done and they are presented in Appendix A.2.2.

3

Monte Carlo simulations

3.1 Monte Carlo method

The Monte Carlo (MC) method was introduced as a stochastic[1] mathematical technique based on the use of sequences of random numbers and probability statistics. It was developed in the 1940s by John von Neumann and Stanislaw Ulam [63] to solve with statistical approximations complex integro-differential equations that appear in several fields of Mathematics and Physics. With the advances in computer technology and power, this method has become widely used since computers are able to perform millions of simulations quickly. Hence, MC methods have been applied to simulate problems that are difficult, or with a large number of coupled degrees of freedom, and consume too much time to be resolved with classic analytic methods (a simulation can involve hundreds of thousands of evaluations of a model).

[1] A stochastic process is such that its behavior is non-deterministic, i.e. the subsequent state of the studied system is defined by predictable actions of the process and by random elements.

Monte Carlo methods are implemented as computational algorithms that depend on random sampling to compute their results. The huge computational capacity used by the MC methods allows to sample a large system in a number of random configurations such that with these data it is possible to describe the whole system. This method is frequently used in computer simulations of Nuclear Physics systems when it is not feasible to compute an exact result with a deterministic algorithm. It is also applied in Computational Biology, Chemistry, Engineering, Telecommunications, Economics, among others [64, 65, 66]. The way in which the MC method is used depends on the application area, but all them work following a general pattern as is explained below.

The results obtained have been published in [67, 68] and and as a consequence of the studies developed a patents has been filed [69].

3.1.1 Method and applications

A computer simulation uses models to reproduce real processes which have a certain number of input–variables and a few equations that use these inputs to give a set of output–response variables with deterministic results, i.e. it gets the same results each time that a re–calculation is done. In contrast, a MC simulation evaluates iteratively a deterministic model using a set of random numbers as inputs. Generally the MC method is used when the model is complex, nonlinear, has several uncertain parameters, or a large number of (interrelated or not) variables whose value may be reproduced by a probabilistic distribution.

The Monte Carlo method involves performing many simulations using random numbers and probabilities to get an approximation of the solution to the considered problem. Since this method provides an approximation, the analysis of its statistical error is a fundamental factor to ponder the accuracy of the outcome. In fact, there are many different MC methods to attempt to minimize this error. In general, the MC method can be summarized in few steps:

1. Define a domain of possible inputs x_{i1}, x_{i2},..., x_{iq}.
2. Create a parametric model y = f(x_{i1}, x_{i2},..., x_{iq}).
3. Generate a set of random inputs (x_{i1}, x_{i2},..., x_{iq}) from a probability distribution over the domain.

4. Evaluate the model on these inputs and store the results as y_i.

5. Repeat the previous steps for i= 1 to n.

6. Analyze the results using histograms, confidence intervals, etc.

During a MC simulation the values are sampled from the input probability distribution. Each set of samples is an iteration, and the outcome is recorded. A MC simulation does this process thousands of times so that the final result is a probability distribution of possible outcomes. Hence, MC is categorized as a 'sampling method' since the inputs are randomly generated from probability distributions to simulate the process of sampling. The MC simulations present several advantages over the deterministic methods:

- Probabilistic results: The MC simulations allow to know the outcomes as well as how likely each of them are.
- Analysis: with MC simulations is easier to see which inputs have the biggest effect on results than in deterministic models where different combinations of input–values entail a high computing time.
- Correlation of inputs: in MC is possible to model interdependent relationships between inputs.

The *Central Limit Theorem (CLT)*[1] states that the relative error, which represents the statistical precision, associated to an estimated value, is proportional to $\frac{1}{\sqrt{N}}$, being N the number of iterations. Therefore, if N increases, the error decreases, but in consequence the time needed for the simulation increases as well.

Using the Monte Carlo method, the result of a studied magnitude or variable (x) is the average value of the all contributions (x_i) of the N simulated events, i.e. it is an approximate solution of such magnitude. Therefore, for any variable x its estimated value by MC calculation is:

$$\bar{x} = \frac{1}{N} \sum_{i=1}^{N} x_i \tag{3.1}$$

[1]CLT is a theorem in probability theory that states that, given certain conditions, the mean of a large number of independent random variables (each of them with a variance) is approximately normally distributed.

with an associated variance $S^2 = \frac{1}{N-1}\sum_{i=1}^{N}(x_i - \bar{x})^2 \approx \bar{x^2} - \bar{x}^2$. The estimated variance for $\bar{x}$ is:

$$S_{\bar{x}}^2 = \frac{1}{N}S^2 \tag{3.2}$$

In the MC code the statistical precision is given in each out–file by means of the relative error:

$$R = \frac{S_{\bar{x}}}{\bar{x}} \tag{3.3}$$

considering acceptable $R < 0.1$, and being R proportional to $1/\sqrt{N}$. Therefore, the relative error decreases when the number of events N goes up (which consumes more time of calculation). In Section 3.1.2, some useful variance reduction methods to reduce the computing time without increasing the statistical precision are presented.

A quantity that is used to characterize the performance of the MC method is the Figure of Merit (FOM), calculated as:

$$FOM = \frac{1}{TR^2} \tag{3.4}$$

being T the calculation time (CPU time). R^2 is inversely proportional to the simulated particle number N (as Equation 3.3 shows). When N increases, R^2 decreases, but T goes up at the same time, and therefore the FOM remains roughly steady. The larger value of the FOM indicates a better performance of the calculation. Hence, FOM can be also used to compare the performance of different calculation methods or programs.

3.1.2 Variance reduction

Variance reduction is a procedure used to increase the precision of an estimated value. First of all, the variance reduction may be achieved increasing the number of particles simulated, but this increases the time of calculation as is explained in Section 3.1.1. Secondly, there are techniques that allow the user either to dispense with some simulation details or to change the probability of certain interaction processes. Thus, in this case, the user does not to simulate totally the 'reality' of the set–up, but still evaluates the physical processes. Some of these variance reduction techniques are based on the following techniques: Splitting/Russian roulette, Weight Windows, Control Variates, Importance Sampling, Common random numbers, i.a [65].

In this work two techniques have been mainly applied in both MCNPX and GEANT4 simulations:

- Delimiting the main volumes in which the simulated physical processes take place. In the MCNPX code this is managed through the IMP card (Section 3.2.4), whereas in the GEANT4 code this is applied defining the called 'sensitive detectors' (Section 3.3).

- Defining a cutoff energy (i.e. energy below which the transport of the particle is discarded) for each type of particle either equally for all the regions or with a different value for each volume.

Note that whereas the precision of a result deals with how close the measured values are to each other, the accuracy gives how close a measured value is to the true value. A MC simulation allows the user to know the statistical uncertainty due to the simulation of N particles, but it does not consider other possible uncertainties such as inaccuracies in the cross–section, in the physical models, in the description of the geometry or material compositions, or in the initial particle direction, i.a. Hence, the user must take care that all the data implemented in the code are correct.

3.1.3 Monte Carlo codes for Nuclear and Particle Physics

The interaction of particles with matter entails physical processes such as absorption, scattering, capture, i.a., which are random phenomena with a probabilistic distribution. In fact, the origin of the Monte Carlo method can be traced to the research of the propagation of the radiation in the matter, specifically in neutron processes. Hence, this method is widely applied to study the radiation transport through matter in Nuclear and Particle Physics. Specifically, the MC method is widely used in the study of the radiation transport in Medical Physics to assess magnitudes of dosimetry, brachytherapy, and treatment planning. In addition, it is very useful to simulate experimental set–ups and device designs, reproduce radiation sources, estimate out parameters in a measurement, etc. In all these possible situations of scientific interest, MC simulations allow to optimize the experimental conditions to save computing time and cost of design, manufacture, setting, and assembly of the experiment.

In particular, neutron transport is difficult to determine due to the large number of interactions possible in materials, which can change frequently along the path of the neutron. Instead of trying to anticipate what an single neutron can do, with MC methods is possible to predict what fraction of a large number of neutrons will undergo

each type of interaction. Millions of simulated neutrons can be started with certain energies and directions, such that they travel distances according to their mean–free–path lengths (depending on the materials crossed) with random variations from the expected mean (see final of section 3.3). Along the neutron path, the implemented MC method must take decisions to simulate one or another interactions in function of the cross–sections for the interactions, material, and energy neutron. When a interaction is selected, the consequences of such interaction are followed (e.g. secondary particles, changes in direction, energy, etc). This process is iterated until that neutrons and the secondary particles generated are absorbed, escape from the simulation boundaries, or their energies are below than their energy cut–offs. Keeping tallies of the physics parameters of interest, the average behavior can be deduced.

There are several well–known MC codes used in nuclear and particle physics:

- ETRAN (Electron TRANsport): code for the electron and photon transport (from 1 keV to 100 GeV) in the matter [70].
- PTRAN (Proton TRANsport): code for the proton transport (from 50 MeV to 250 GeV) [70].
- EGS (Electron Gamma Shower): code for coupled transport of electrons, photons, and positrons (from 1 keV to 10 GeV). It was developed at SLAC[1] [71].
- FLUKA (FLUktuierende KAskade): general purpose tool for particle transport and interaction of electrons and photons (from 1 keV to 1000 TeV), neutrons, hadrons (up to 20 TeV), and heavy ions. It is developed at CERN[2] and INFN[3] [72].
- PENELOPE (PENetration and Energy LOss of Positrons and Electrons): code for coupled transport of photons, electrons, and positrons (from 100 eV to 1 GeV), which has been developed by professors of the University of Barcelona (UB) [73].
- PHITS (Particle and Heavy Ion Transport code System): code for the transport of hadrons with energies up to 100 GeV/u [74].

[1]Standford Linear Accelerator Center.
[2]European Organization for Nuclear Research.
[3]National Institute for Nuclear Physics.

- BEAMnrc: code for modeling radiotherapy sources developed at NRC[1] [75].
- SRIM (Stopping and Range of Ions in Matter): software that calculates the features of the transport of ions (up to 2 GeV/u) [76].
- MCNP(Monte Carlo N–Particle): general purpose code for the transport of neutrons, photons, and electrons. It is developed at LANL[2] [77].
- MCNPX (Monte Carlo N-Particle eXtended): extended version of MCNP [78].
- GEANT4 (Geometry ANd Tracking): toolkit for the simulation of the passage of all kind of particles trough matter (from 250 eV to 10 TeV). It is developed at CERN [79].

In this work, most of the MC simulations have been developed using both GEANT4 and MCNPX codes in a complementary way because, as is widely known among the neutron physics community, in some energy ranges there are undeniable discrepancies between the results obtained by both codes. In addition, GAMOS, PENELOPE, and SRIM have been also used occasionally. MCNPX and GEANT4 are briefly presented in the following sections. The versions used in the framework of this work were MCNPX 2.6.0 and GEANT 4.9.2.

3.2 MCNPX simulation code

The Monte Carlo N–Particle code (MCNP) is a general purpose MC transport code developed in the 1940s in Los Alamos for the study of the interaction and transport of neutrons, photons, and electrons. The advanced version of MCNP is known as Monte Carlo N–Particle eXtended (MCNPX)[3], is written in the Fortran90 code, and allows to simulate 34 fundamental particles (nucleons and light ions) and heavy ions with energies from meV to GeV, contains up–to–date library data of cross sections, improved physical models and new variance reduction techniques. In addition, MCNPX is able to combine the use of nuclear library data with physical models [80].

[1] National Research Council Canada.
[2] Los Alamos National Laboratory.
[3] MCNPX can be obtained from the Radiation Safety Information Computational Center (RSICC).

In the next sections the basic components of a MCNPX program are outlined briefly. Extensive details about the rules to use this code may be consulted in the user manual [81].

Note that the main units of measurement used in MCNPX code are: centimeters for length, MeV for energy, barns for cross sections, and g/cm^3 for mass density.

3.2.1 Geometry, materials, source

In MCNPX the geometry of the simulated device consists of *cells*. Cells are volumes fitted by means of the intersection or union of surfaces which are defined either by analytic equations or by boolean operations with preestablished solid geometries (planes, spheres, cones, cylinders, hyperboloids, etc). A material has to be associated to each cell. Additionally, a particle source must be defined containing not only the type of incident particle but also its energy, position, direction, and area distribution, i.a. A brief description of the *cards*[1] used to define the simulated geometry, materials, and source is presented below. There is a 2–D plotting routine that lets the users check their simulated geometries in two–dimensions to debug them quickly (for example to check if there is overlapping or gaps between cells).

Cells

Each cell must be made up by a material which is defined by its density and composition, i.e. the cell-card should have a cell identifier (ID_cell), the identifier of the material of such cell ($ID\_material$), its density (d), and the surface-identifiers ($ID\_surfaces$) that delimit the cells. Thus, the input file of the cell-card is implemented with the following input parameters:

$$ID\_cell \qquad ID\_material \qquad \text{d} \qquad ID\_surfaces$$

Surfaces

The surfaces are specified with the surface-identifier ($ID\_surface$), the type of surface (plane, sphere, cylinder, cone, i.a.), and the values of the parameters that define the analytic equation of such surfaces. Therefore, the surface-card is implemented as:

$$ID\_surface \qquad \text{Type of Surface} \qquad \text{Parameters (of the surface)}$$

[1] A *card* is a line (an input option) in the MCNPX input file.

Materials

The cells are constituted by numbered materials (m) which are made up by isotopes, elements, or compounds extracted from data libraries (with their corresponding cross sections) that are described through a identifier (ZZZAAA.ID), and the appropriate mass or atomic fractions of the isotopes for each compound. Hence, the material-card specification is:

m ZZZ.AAA.ID Mass or Atomic Fractions

Some of the materials used in this study are specified in Table 3.1 and their use is clarified in Sections 3.4, 3.5, 5.1.2, 5.2, and 5.3.1.

Furthermore, before running the code, it is possible to display in 3–D the whole geometry to test the correct definition, position, and fitting together of the volumes and materials using visualization programs as Visual Editor (VISED). Figure 3.1 shows a LINAC machine simulated with MCNPX.

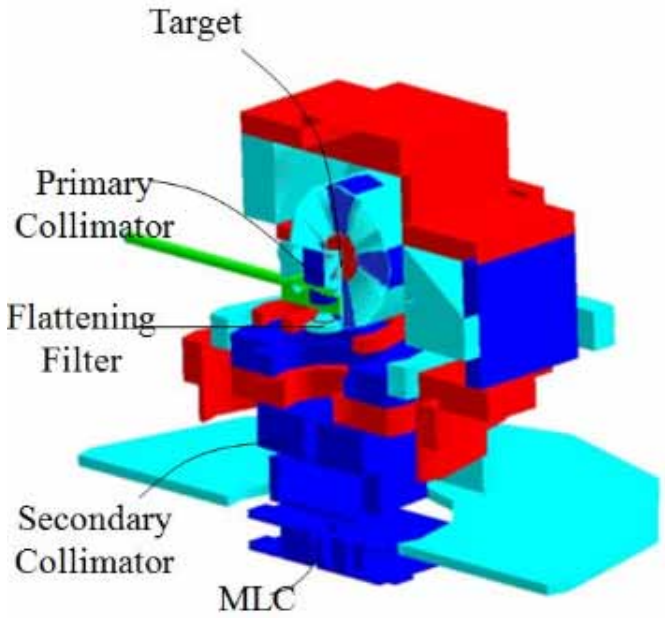

Figure 3.1: Varian LINAC modeled in MCNPX - Detailed model of the Varian LINAC head simulated with MCNPX for in–field and out–of–field dose calculations [82].

Table 3.1: Materials used in this study in the MCNPX code.

Isotopes	**ZZZAAA.ID**
$^{10}Boron$	005010
Elements	**ZZZAAA.ID**
Silicon	014000
Aluminum	013000
Boron	005000
Compounds	**Material-card**
Silicon Oxide	014000 1 008000 2
Air	007000 -0.755 008000 -0.232 018000 -0.013
Water	001000 1 008000 2
Polyethylene	001001.60c 0.67 006012.50c 0.33
O-carborane+Cyanoacrylate	001000 0.0753 006000 0.287 005010 0.53 007000 0.0329 008000 0.0752
O-carborane+PVC	001000 0.0708 006000 0.2433 005010 0.4853 017000 0.2006

Source

The simulated source implements the type of the particles that interacts with the setup as well as its position, direction, energy spectra, shapes, i.a. For instance, a thermal neutron source positioned at (x,y,z)=(0,0,0) with direction $\vec{r} = (0, 0, 1)$ is implemented with the following source-card:

SDEF pos=0 0 0 dir=1 vec=0 0 1 par=1 erg=$0.0253 \cdot 10^{-06}$

3.2.2 Particle transport: neutron, gamma, and electron transport

MCNPX allows to simulate 34 types of fundamental particles and hundred of heavy ions with energies up to several GeV depending on the particle. Using the MC method, each particle is tracked from the source by sampling all its possible random interactions. Tracking ends either when the particle undergoes a terminal event like absorption or capture, or when it leaves the geometry boundaries of the simulated setup. In order to sample these interactions according to the probabilities of each mechanism, the MC code needs to use cross–section databases and physical models. MCNPX contains not only a large number of library data but also physical models, which can even be combined with each other. MCNPX supports cross section data libraries that are continuous in energy. The MCNPX code uses mainly these libraries for neutrons, photons, electrons, protons, and photonuclear reactions, whereas for pions, mesons, and kaons this code makes use of physical models.

Table 3.2 shows some nuclear data libraries used by the MCNPX inner code for each type of particle. These libraries are in ASCII format. More information about these libraries can be found through the NEA [83] and LANL [84] nuclear data. The energy range of application of some of these data libraries is worth commenting:

- **Neutrons**: the Evaluated Nuclear Data File (ENDF) library contains neutron reaction data that are periodically evaluated by the LANL research organization. There are several types of ENDFs: (i) the ENDF/B–iV data library contains neutron reactions for 90 materials in the energy range from 10^{-5} eV to 20 MeV; (ii) The ENDF/B–V covers physical processes like fission product yields, or activation, among others; (iii) the ENDF/B–VI groups several data sublibraries about radiative decay, thermal scattering, photo–atomic interaction, incident charged–particle, activation, and neutron and proton reactions up to 1 GeV

Table 3.2: Particle libraries in MCNPX.

Particle/Interaction	Data Library
Neutrons	ENDF/B–IV, ENDF/B–V, ENDF/B–V.0, ENDF/B–VI.1 LA150N, Thermal S(alpha,beta)
Photons	MCPLIB02, ENDF, EPDL
Electrons	EL01, EL03
Protons	LA150H
Photonuclear	LA150U
Photoatomic	MCPLIB04

incident energy, as well as a general purpose library. MCNPX contains also the LA150N library that is a nuclear database for high energy neutrons. Moreover, the thermal neutron data libraries are contained in the S(alpha,beta) data.

- **Photons**: the MCPLIB02 library covers from 1 keV to 100 GeV for Z=1–94, and is based on data obtained from the ENDF for photons with energies up to 100 MeV, and on the Livermore Evaluated Photon Data Library (EPDL) for photons up to 100 GeV.

- **Electrons**: the EL01 library covers electron energies from 1 keV to 1 GeV for Z=1–94, and the EL03 is its improved extension (from the EPDL data library).

In this work only the physical processes related with the interaction of neutrons, photons, electrons, alphas, and heavy ions have been considered.

3.2.3 Input file

To run a MCNPX simulation, the user has to provide an input file where the whole simulation is described. The input file consists of four main blocks (Figure 3.2): (i) a message block (optional) where the program can be described, (ii) a second block where the cell–cards are defined, i.e. it constructs the geometry of the system, (iii) a third one in which the surface–cards which constitute the cells are implemented, and (iv) a last block where other data such as materials, type of source, physical models, variance reduction techniques, cross section libraries, tallies, number of histories, and other conditions to carry out the run (e.g. cut energies, physics parameters, etc), are

specified. It is created with MCNPX–style predefined commands. A brief explanation of each item is presented below. A detailed description of the MCNPX files can be found in the code manual [80].

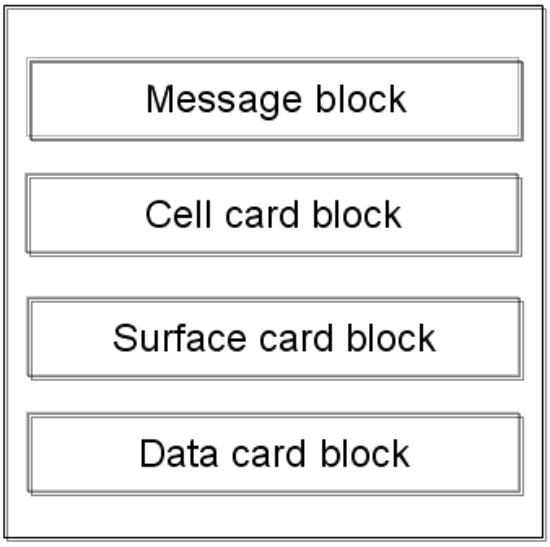

Figure 3.2: Initial run file in MCNPX - Card blocks that forms the input file in a MCNPX program.

Both the cell and surface blocks have been outlined is section 3.2.1. The data block contains several important items to control the execution like the number of histories to be run in the problem (NPS tag), the computer time cutoff (CTME tag), or the variance reduction (using the IMP and ELPT cards). The two first cards are indicated as follows and the two latter are explained in the next section:

NPS N

being N the number of histories to be simulated. In all the simulations developed in this work the NPS were such that the uncertainties are lower than 1%. And:

CTME time

with *time* as the maximum amount of computer time in minutes to be spent in the simulation.

3.2.4 Variance reduction in MCNPX

In order to improve the out results it is advisable to use variance reduction with the IMP or ELPT cards: on the one hand, IMP is applied to define the calculation regions as:

$$\text{IMP:pl} \qquad \text{C1} \quad \text{C2}\ldots \quad C_n$$

where C_i represents each cell of the geometry. There is a IMP card for each particle that is indicated by means of the 'pl' tag. Each of these C_i cell tags can take two values: 0 means that there is no transport in that cell for the pl–particle and 1 the opposite. This card is specially useful to save computing time because it is possible to exclude the particle transport inside cells where there is no interest. On the other hand, ELPT manages the minimum energy of the transported particle pl, using the following card:

$$\text{ELPT:pl} \qquad \text{E1} \quad \text{E2} \quad \text{E3}\ldots \quad E_n$$

where E_n is the particle cutoff energy in the n–th cell. Thus, ELPT allows to discard the transport of particles with E below the cut–off, reducing the computing complexity.

3.2.5 Out File: tallies and analysis

The estimation of the magnitudes evaluated by the MCNPX code is obtained by means of the Tallies, which are built–in calculations. They are out–files which give information about magnitudes like the current integrated over a surface (Tally F1), the average flux over a cell (Tally F4), or the energy distribution of pulses created in a detector (Tally F8), i.a. Tallies are normalized per unit of source emitted particle. Hence a tally estimates a mean value ($\bar{x}$) of a scored quantity (x), with a relative standard uncertainty of statistical origin ($R = \frac{S_{\bar{x}}}{\bar{x}}$), as is detailed in Section 3.1.1.

The role of the main tallies as well as their corresponding magnitudes are listed on Table 3.3. Depending on the information that is needed, we can take out one of them as is or even use one or several of them to calculate another magnitude like the absorbed dose, kerma, etc. In the framework of this work, F1, F2, F4 and F8 were used.

The tally results can be displayed by means of the MCPLOT tool which allows to visualize the distribution of the calculated magnitudes as a function of the particle energy.

Table 3.3: Tallies in MCNPX.

Tally	Description	Fn units
F1:< pl >	Current integrated over a surface	[particles]
F2:< pl >	Flux averaged over a surface	[particles·cm^{-2}]
F4:< pl >	Flux averaged over a cell	[particles·cm^{-2}]
F5:< pl >	Flux at a point or ring detector	[particles·cm^{-2}]
F6:< pl >	Energy deposition averaged over a cell	[MeV·g^{-1}]
+F6:< pl >	Collision heating	[MeV·g^{-1}]
F7:< pl >	Fission energy deposition averaged over a cell	[MeV·g^{-1}]
F8:< pl >	Energy distribution of pulses created in a detector by radiation	[pulses]
+F8:< pl >	Deposition	[charge]

Through a card tagged as PRINT, MCNPX out–files give a detailed summary of the particle tracks, results and statistical analysis, position and direction of the first events, activity for each cell, and tallies, i.a. These out data are collected after a simulation is finished in a binary file (runtime information) and in a text file (simulation results), named by default RUNTPE and OUTP respectively.

Finally, it is important to emphasize that MCNPX has a major disadvantage: it is not able to track heavy charged particles (i.e. particles with Z>2) entirely well. Even although this shortcoming has been addressed in the latest release of the code (MCNPX v.2.6), there are still problems with its implementation. For instance, the lower tracking threshold for heavy ions is 5 MeV, value below which all energy is deposited locally; this obstacle may limit the simulation accuracy for, for instance, the thermal neutron detection using ^{10}B as converter since the energy of one of its reaction products, ^{7}Li, has an energy below 1 MeV. In contrast, the GEANT4 toolkit, presented in the next section, is able to reduce that tracking threshold up to a few keV in energy. However, the GEANT4 code presents other disadvantages, mentioned at the end of Section 3.3.

This is one of the reasons for what both codes are used alike, depending on the accuracy required for each simulation case.

3.3 GEANT4 simulation toolkit

GEANT4 (GEometry ANd Tracking) is an *Application Programming Interface* (API)[1] to simulate the passage of particles through matter, developed at CERN by an international collaboration of various institutions and universities around the world [85, 86]. The first GEANT4 version appeared at the end of 1998 and thenceforth it has had continuous improvements and updated versions. It is a free software implemented in the C++ programming language, according to the Object Oriented Programming (OOP)[2]. Unlike the other MC codes, GEANT4 is not an executable program, but it is a set of predefined C++ classes with which the users must write their own C++ code and compile it to generate an executable file.

GEANT4 uses the MC method to evaluate the physical models, recreate complex geometries with a large number of system parameters, study in–depth the passage of radiation in detection devices, and process large amounts of data to analyze. Initially GEANT4 was designed to develop simulations for processes in high energy ranges. Later it implemented physical models for the low energy range. Currently, GEANT4 covers a wide energy range of meV up to the TeV region: from processes of low energies, such as interactions of optical photons and thermal neutrons, up to high energy reactions like heavy ions collisions, cosmic ray experiments, etc. GEANT4 also covers all the types of particles: leptons, hadrons, bosons, resonances, and any type of heavy ions. GEANT4 is a powerful toolkit and it is applicable in numerous fields, such as Nuclear and Particle Physics, High Energy Physics, Medical Physics (Figure 3.3), Space Astrophysics, Radiation Protection, Dosimetry and Radiobiology, i.a. This MC package allows user to simulate from complex particle detectors, e.g. ATLAS and CMS detectors (Figure 3.4), to medical setups such as hadron therapy facilities or

[1] An API is a set of methods that has certain libraries to be used by other softwares and allows the communication between software components by means of *calls* to such libraries.

[2] Thanks to the modular structure of the OOP, GEANT4 allows users to debug, optimize, and update the G4–code frequently, improving it constantly.

tomographic emission machines (by means of the specific GATE application[1] [87] or the GAMOS application[2] [88]).

The GEANT4 functionality and models continue to be refined and extended, with the expansion of existing libraries and the creation of new more precise ones. Moreover, GEANT4 acts as a repository of models and information about the interaction of radiation and particles in a wide range of applications, thanks to the extensive international collaboration which supports this simulation code. Thereby frequent physical database updates are guaranteed. The GEANT4 software and source code are freely available from the project web site [89].

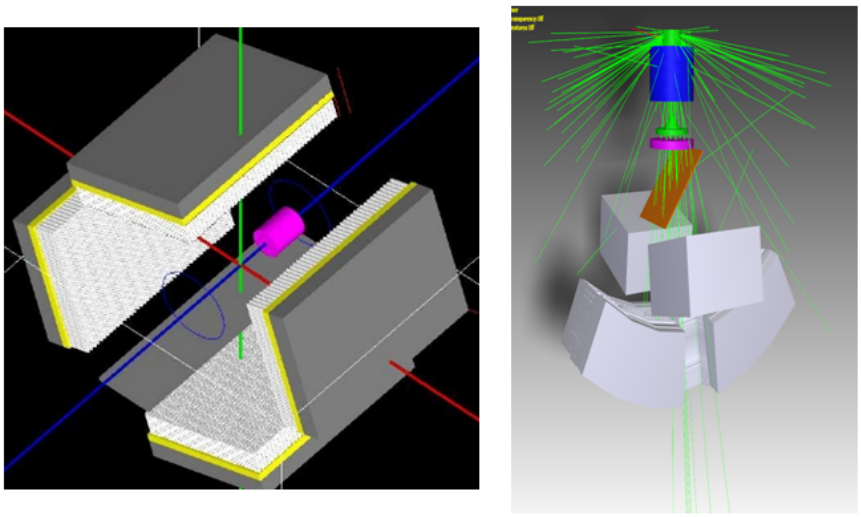

Figure 3.3: Examples of GEANT4 simulations with GATE and GAMOS architectures - Left: Image of a SPECT system using GATE [90]. Right: Simulation of a VARIAN accelerator using GAMOS [88].

A GEANT4 simulation can be broken down in the following items:

- System geometry.
- Materials that compose the geometry.
- System response through *Sensitive Detector* (SD), which consists of one or several volumes of which extract data.

[1] Geant4 Application for simulations of preclinical and clinical Scans in Emission Tomography.
[2] Geant4-based Architecture for Medicine-Oriented Simulations.

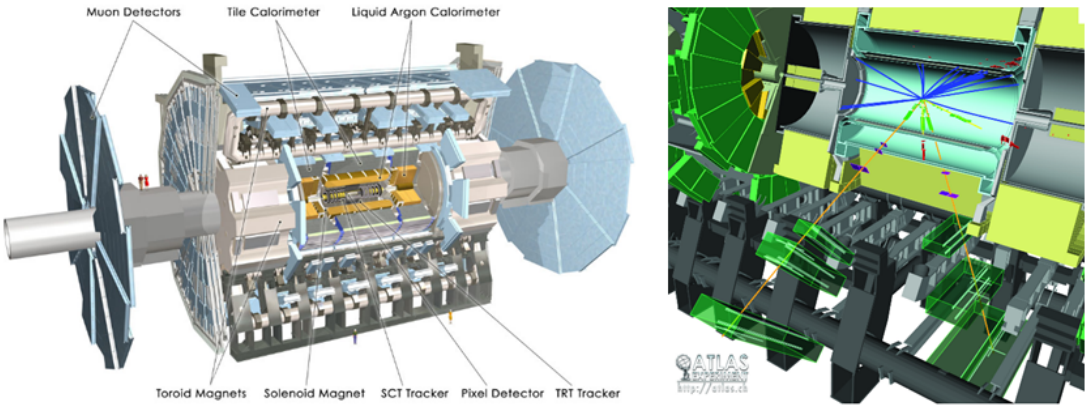

Figure 3.4: ATLAS detector simulated with GEANT4 - Left: Sketch of the ATLAS detector. Right: Section of the ATLAS geometry and interactions simulated with GEANT4.[91]

- Generation of primary particles or source.
- Particles of interest.
- Models and physical processes that manage the interactions.
- Trajectory of the particles through the materials.
- Storage and trace of events.
- External electromagnetic fields.
- Setting the *run*.
- Displaying the detector and particle trajectories.
- Data Analysis.
- Interfaces to external work environments.

This code division allows users: (i) to design systems of complex geometry with any type of materials or compounds, (ii) to choose the incident particles and the secondary ones as well as to monitor the trajectory of these particles in their interactions with the system; (iii) to identify the processes that each particle undergoes in the matter and the energy deposited through it; (iv) to create radioactive sources, specifying their

distributions in energy and position; (v) to recreate electromagnetic fields; (vi) to restrict the types of physics processes to be simulated, i.e. to include only the relevant processes for each geometric area; (vii) to extract information (Hits) to reproduce the detector response (Digitisation) and to choose what physical processes take into account. Finally, the graphical interfaces allow the users to visualize the geometry and traces and to analyze the whole simulation.

The modularity of GEANT4, the fact that the physical implementation is transparent to the user, and the ability to select only the necessary components, reduces the computing time. This package allows not only the selection of the parameters of interest in our experiment but also of physical processes, energy range, and models of interest. When simulations involve a large number of particles (millions of particles or even hundred of millions), this is crucial to reduce the CPU time.

The overall structure of GEANT4 consists of 17 *categories* since the large size of the code requires a partition into smaller units [89]. The categories are clusters of *classes*[1], which are the smallest logical unit defined in the software, connected with other clusters. A *class category* consists of a group of classes with a close relationship between classes of the same category, but almost without relationship with classes of other categories, i.e. there are strong relationships between classes that belong to the same category and weak relationships between classes of different categories. This hierarchy lets users have a high control over the system of the code and lead their own simulations with high level of direction. Further, that arrangement enables a hierarchical structure of sub-domains connected by an unidirectional flow dependency which is represented by the GEANT4 Class Categories as is shown in Figure 3.5[2]. The user has to write several interconnected classes, i.e. C++ classes. The tasks that are performed by each class category are:

- The *Overall category* covers all classes, structures, types and constants of general use. It also defines the interface for the CLHEP[3] [92] and STL[4] libraries. This

[1] In the C++ programming code, a class is an expanded concept of a data structure: instead of holding only data, it can hold both data and functions.

[2] Classes which are below are used for the classes above in the flow diagram.

[3] CLHEP (Class Libraries of High Energy Physics) is a set of class libraries containing large amounts of basic classes for the use of high energy physics.

[4] STL (Standard Template Library) is a general purpose library that contains generic algorithms and data structures. It is part of the standard library of C++.

covers also the system of units, physical constants, and random numerical values of GEANT4.

- *Material category* directs the creation of materials that make up the simulated geometries: isotopes, elements, and composite materials. It defines from simple elements and molecules to complex compounds: in the first case by introducing the main features of the elements, and in the second one making use of GEANT4 databases. GEANT4 supplies all the elements of the periodic table and complex compounds through the NIST[1] database [93].

- *Geometry* controls the definition of the geometry of the setup. The design of the simulated geometries can be developed through GEANT4 classes with (i) modelers such as constructive solid geometry (CSG), wherein volumes are described by a collection of boundaries, or boundary represented solids (BREPS) that are a collection of 3-D volumes, or (ii) adapting complex geometries designed in CAD (Computer Aided Design) programs to C++ through an adaptation program.

- *Particle category* manages the definition of all the kind of known particles: leptons, mesons, baryons, bosons, short-lived resonant particles, and ions.

- *Track category* contains classes used to direct the path by analyzing the steps and applying the physical processes.

- *Tracking* controls the evolution of the state of the tracks during their transport, providing information on the Sensitive Detector (SD) for Hits and Digitisation.

- *Physics category* manages the physical processes involved in the interactions of particles with matter, including physical models as well as evaluated data to reproduce the electromagnetic and hadronic interactions. The models used in the program are selected by energy range, particle type, and material. The same process can take several models, i.e. the user must distinguish between the process (the initial and final state with a cross section or well-defined half-life) and the model that adds the production of secondary particles with such physical process.

[1]NIST (National Institute of Standards and Technology) is a database that contains the definition of the classes of all elements of the periodic table and some common compounds used in medicine, high energy physics, and detectors among others.

- *Hits + Digitization categories* control the construction of: (i) Hits which are snapshots of the interaction of trace particles in the SD detector that store information, and (ii) Digits which are created using information from the Hits for the reconstruction of the detector response. In the simulation, all Hits are saved in Hit-collections that are logical readouts of the SD.

- *Event category* controls the overall event which is made up by all the generated particles from an primary particle. Therefore, the events are an initial set of particles. When a setup launches several particles, each of them is identified as an individual event and is processed individually. The Event is the main unit of the simulation. This class stores the flux of information of hits, digits, and trajectories generated during all the simulation process.

- *Run* carries out a sequence of events which come from the same generator of primary particles and geometric configuration.

- *Readout category* gives the output data.

- *Visualisation* connects the previous categories and also allows the use of external tools for displaying of solids, trajectories, and hits. This interacts with graphical libraries as the VRML[1] software. Thanks to this it is possible to visualize in 3-D the geometry, paths, steps, and hits.

- *Intercoms* provides a means of interaction with GEANT4 through the user-interface and enables communication between modules.

- *Inteface* deals with the creation of Graphical User Interfaces (GUIs)[2] and the relations with other external softwares.

All these tools may be customized as GEANT4 is built based on the OOP features. Thus, GEANT4–classes let the user define physical models, fundamental particles, sensitive detectors, geometries, and track visualization, as well as allowing a high control over the input–parameters and in the out–information.

[1] VRML (Virtual Realiy Modelig Language). Available from: http://cic.nist.gov/vrml/vbdetect.html

[2] A GUI is a graphical user interface, i.e. a type of interface that uses a set of images and graphic objects in order to represent information and actions available. These actions are usually performed by the user directly over the program.

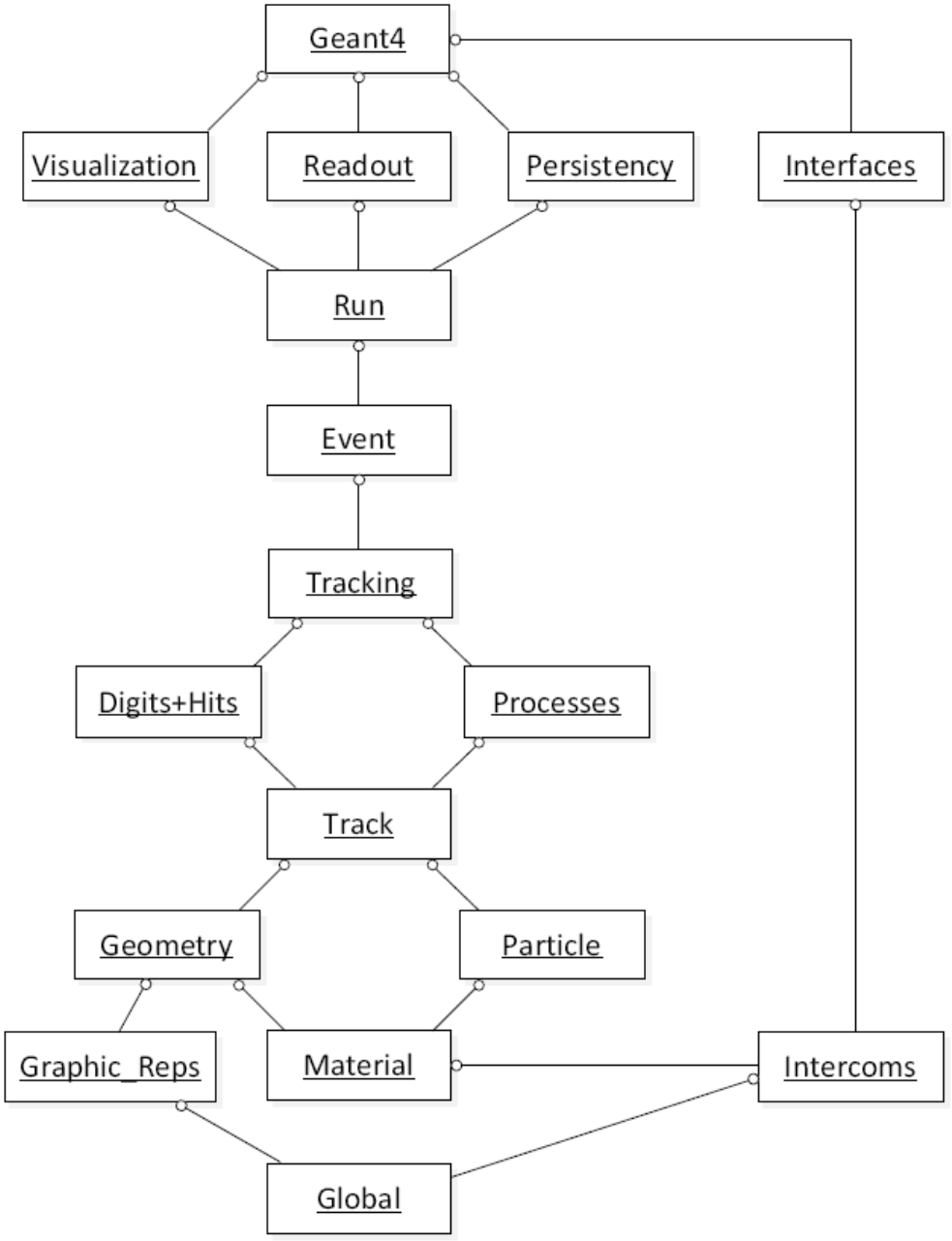

Figure 3.5: GEANT4 class categories - Each box represents a class category and the lines between them represent which is the type of relationship between them: the circle at an end of the line means the class category that has this circle uses the other category [89].

The commands that control the interaction of the user with the interface are led by the *G4UIsession class* (*Intercomand category*). In this work, the following have been used:

- *Batch* for reading and executing the command ranks.
- A terminal *tcsh* for interactive sessions.
- A type adapted of GUI, GAG, which reproduces the states of the user programs. It is a Java application that allows the user to run GEANT4 interactively.

Other commands that the user can use to interact with the interface, built in GEANT4, are:

- Other Graphical User Interfaces (GUI), via the interactive commands.
- Macros, via: /control/execute < *command* > in the main program.
- Methods *ApplyCommand* of G4UImanager, coded in C++.

It is important to emphasize that GEANT4 is not really an application itself, but that the users must create their own code using the large libraries supplied and coordinate all the programs created for each aspect of the simulation within a main program. The libraries have to include: shells, routines of the program flow control, user interfaces, operating controls over all the system, events, particle transport, visualization, analysis, and coordination of all these particles, i.a. Hence, running a GEANT4 simulation requires that the user sets up a *main()* method which includes all the outstanding classes, known as *Main* file, where the simulation begins. The *main()* method is compulsory and it is the file from which all the other classes are called and used. Equally, it is necessary to write several compulsory classes (the Mandatory User Classes) and other optional (Optional User Classes). Afterwards, the user must compile the collection of GEANT4 files and then the GEANT4 kernel creates an executable file to be run to start the simulation. To this end, the G4-simulation framework has to be in a directory which contains: (i) a *GNUmakefile* file which stipulates the compilation method for the simulation, (ii) a *tmp* subdirectory that receives the files produced by the compilation and that are called by the G4 kernel when the simulation code is

executed, (iii) the *bin* subdirectory which contains the executable files produced by the compilation, (iv) the *main() file* where the main() method is set up, (v) the *include* subdirectory where are all the *header files* [1], and (vi) the *src* subdirectory where are all the user defined classes that are *source files*[2].

Finally, the execution of a GEANT4 simulation consist of four components: (1) The *Step*, which is the minimum path of a particle between interactions, (2) *Track* or sum of all the Steps of the particle, (3) *Event*, which is the track history of a single incident particle (including the tracks of all its secondary particles), and (4) *Run*, collection of all the events that share the same geometry, physics list, and primary particle generator. Thereafter, GEANT4 divides the particle trajectories into series of Steps with a certain length λ (the mean–free–path), which represents the average distance that the particle travels before undergoing an interaction. The mean–free–path is calculated according to:

$$\lambda = \frac{1}{\sum \sigma_i(E)N} \tag{3.5}$$

being σ_i the cross section for the physical process that takes place and N the atomic density of the material, as was explained in section 2.2. To achieve a simulation as real as possible it is necessary to have accurate cross–sections. GEANT4 calculates the cross–sections by formulas, parameterisations, or interpolation of databases depending on the particle type, material, and energy. Along the trajectory of a particle, the program will take one or another value of the effective section from the corresponding libraries as a function of the energy that the particle has in each Step and depending on the material in which it is located. Thereby, the probability distribution of the traveled distance before interaction (l) is:

$$f(l) = (\sigma_i \cdot N) \cdot e^{-\sigma_i \cdot N \cdot l} \tag{3.6}$$

and the interaction distance l_i is sampled for each process as:

$$l_i = -ln(\xi) \cdot \lambda_i \tag{3.7}$$

being ξ a random number uniformly distributed in the range (0,1). Next, the code selects the process with the smallest length from all possible. At the end of the Step,

[1] *Header files* are the G4–files where the user defines the classes which use in the simulation. These files end with the .hh extension.

[2] *Source files* are the G4–files where the user defines what to do with the classes which have been defined. They end with the .cc extension.

which entails changes in energy and trajectory, the state of the particle is updated and a new Step is calculated. The particles are transported Step by Step. Over the selected process, the code takes the actions defined to carry it out. This chain is iterated until that the particle is absorbed, escapes from the simulation boundaries, or its energy is below than its energy cut-off. The size of the Step is usually small because the continued loss of energy makes the cross sections change. The shorter is the interaction length, the higher is the accuracy of the simulation, but the CPU time is also higher. Therefore the user has to balance these two purposes through the imposition of limits.

Finally, to run a GEANT4 simulation, it is required that the user defines at least three mandatory classes (subsection 3.3.1), and depending on the complexity of the simulated system, it is also necessary to implement other action and optional user classes (see 3.3.2 and 3.3.3 respectively). All these user classes are explained in the following subsections.

3.3.1 Mandatory user classes

The main classes indispensable to define a GEANT4 simulation are called *Mandatory User Classes*. They are derived[1] following the *Abstract Base Classes* provided by the G4 kernel. The Abstract Base Classes and their functions are presented as follows:

- The ***G4VUserDetectorConstruction*** *class* is used to define the set–up (materials and geometry) of the simulated devices, and to define the SD and display attributes. In this work the CSG geometries mentioned above are used, constructing the geometries via Boolean operations (intersection, union, and subtraction). Figure 3.6 shows an example of basic boolean operations on CSG.

  Note that when a compound requires particular specification of its density, physical state, or constituent ratios, the user can create the pure elements to make up the concrete material. For example, to compose a material in terms of isotopic concentrations the first step is to define the isotopes needed for each element using the atomic and mass numbers (Z,A) and their respective atomic weights; secondly, the isotopes are combined by % abundance to define the element. Finally, the user has to specify other material parameters such as its density.

[1] What this means is that the users have to create their own class from that G4–class.

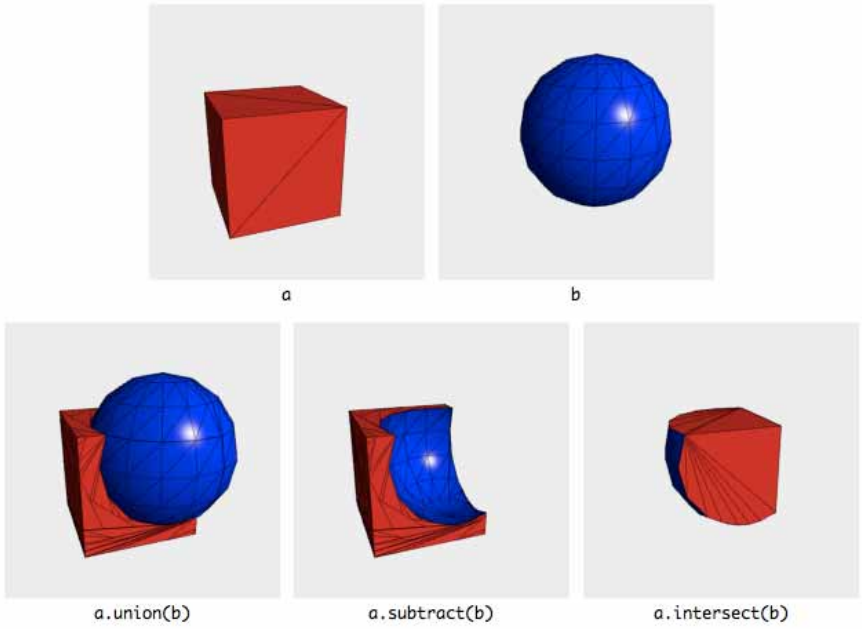

Figure 3.6: Boolean operations on CSG - Example of constructed geometries with boolean operations: starting from a cube (a) and a sphere (b), it is possible to create other combined volumes via union, subtraction, and intersection [94].

It is worth mentioning that even although technically any material can be defined in GEANT4, when simulating neutrons, the user has to ensure that both cross–section data and physics models are updated, and with a correct performance, for the simulated elements at the energy range of interest. This is a crucial point in the simulation process since a lot of the disagreements obtained between Monte Carlo simulation codes can be due to some of those shortcomings.

- The ***G4VUserPhysicsList*** lets the user define all the physics models that take place in the simulation and the energy cut–offs. There are seven main categories of physics processes [89], two of which apply for the simulations developed along this work: Electromagnetic (EM) and Hadronic physics models.

  – *Electromagnetic class* includes: (i) standard EM processes, such as photon interactions (Compton, pair production, etc.), electron/positron processes, Coulomb interaction of charged particles (ionization, scattering), and processes for simulation of X-rays production by charged particles, i.a.; and

(ii) low energy EM processes, like photo-electric effect, Rayleigh scattering, Bremsstrahlung, Ionisation and delta ray production, etc.

– *Hadronic* class controls both high and thermal neutron interactions, nucleus-nucleus scattering, photonuclear and electronuclear interactions, and various high-energy processes up to GeV. As said above, there are may physics models implemented in GEANT4 about the hadron production and its transport. Depending how much detail is needed (weighing the detail against CPU performance), the user has to construct the physics list using the lists offered or modifying any of them. There are four families of lists:

  * LHEP: low and high energy parameterised modeling of hadronic interactions.
  * QGS: lists based on a modeling using Quark Gluon String model for high energy hadronic interactions of protons, neutrons, pions, and kaons.
  * FTF: lists based on a modeling using the FTF model for high energy hadronic interactions of protons, neutrons, pions, and kaons.
  * Other more specialized lists.

For neutrons, it is recommended to use the $QGSP_BERT_$HP and $QGSP_BIC_$HP lists [95].

It should be noted that the GEANT4 objects associated to hadronic process may have one or more cross–section data sets, i.e. these objects are made up with methods and data that can be derived from simple equations to sophisticated parameterisations that use large data tables. These cross–section data are used for the calculation of the physical interaction length λ, as said above, for a given particle, material, and to a certain energy range. The default hadronic cross–sections include inelastic, elastic, fission, and capture processes, having each model a range of applicability. Nevertheless, the cross–section data for low energy neutron transport (capture, elastic, fission, and inelastic data) have to be specifically set by the user. The cross section data set classes for low energy neutron transport are G4NeutronHPCaptureData, G4NeutronHPElasticData, G4NeutronHPFissionData, G4NeutronHPInelasticData. The modeling is based on data of ENDF/B–VI libraries, covering from thermal energies to 20 MeV.

- The ***G4VUserPrimaryGeneratorAction*** *class* requires the user to define the initial event state or radiation source via an event generator, i.e. this class has to generate the primary particles in the simulation. The radiation source has to be modeled as realistic as possible since the simulation results depend strongly on the irradiation configuration.

From these classes the users must derive their own classes, adapting them to their simulation conditions since GEANT4 does not provide any setup by default. Then, the *G4RunManager* class checks that the three previous classes are provided correctly by the user. Next, the Initialize() and BeamOn() methods, inside of the Main() file, start the Run.

It is important to emphasize the fundamental role that the Physics List plays in the overall simulation process: GEANT4 does not provide any particle or physical process by default, and therefore the user has to specify (i) all the particles, (ii) type of interactions for all the preceding defined particles, and (iii) energy cut-offs for secondary electrons, photons, and positrons. Many modules can be modified to eliminate the production and transport of particles and processes without relevance for our study. In the GEANT4 User's Guide for Application Developers details on how to proceed to implement correctly these items may be consulted [89].

3.3.2 User action classes

The User Action Classes are used to gain control over the data in the simulation. The main ones are:

- *G4UserRunAction* controls the actions in the beginning and end of each run. It has three virtual methods that are invoked through the *G4RunManager* class for each run: *GenerateRun()*, *BeginOfRunAction()*, *EndOfRunAction*.

- *G4UserEventAction* is executed in the beginning and end of each event. Its virtual methods are called through the *G4EventManager* class for each event: *BeginOfEventAction()* and *EndOfEventAction()*. It is normally used to initialize and fill histograms at this level.

- *G4UserSteppinAction* controls the progress of each step. It is useful to control concrete physical processes that take place in specific positions (surfaces, volumes, regions or SD).

- *G4UserTrackingAction* controls the actions in each particle trace.

- *G4UserStackingAction* allows to give priority to selected secondary particles in which the user is interested.

3.3.3 Optional user action, initialization, and analysis classes

There are other Optional User Classes that allow to control some phases or levels within the simulation. They may be of type (a) action, (b) initialization, and (c) analysis:

(a) Optional User Action Classes:

- *G4VUserEventInformation*: abstract class from which the users can refer their specific classes to store information related to a G4Event class object.

- *G4VUserTrackInformation* is an abstract class for deriving your own to store information associated with a G4Track class object.

- *G4VUserPrimaryVertexInformation*: like the previous ones, is an abstract class to add the information regarding the primary vertex.

- *G4VUserPrimaryTrackInformation* reports on the primary particle.

- *G4VUserRegionInformation*: it can attach information on the region where the users are interested and therefore identify the components which cross the detector.

(b) Optional User Initialization Classes:

- *G4UserSensitiveDetector*.

- *G4UserHit*.

Both classes let define the sensitive detectors (SD) which can be done in two ways: (i) using the *G4UserSensitiveDetector* class and associating a specific SD for each region that requires to be analyzed, or (ii) using the *G4MultiFunctionalDetector* that lets pre–define scorers of a collection of regions at the same time.

(c) Optional User Analysis Classes:

- *G4UserAnalysisManager* is used to access the information from *hitcollections* and to make up an output-file with the simulation results.

3.3.4 Execution and out-files

In order to carry out the whole GEANT4 simulations developed in this work, several technical requirements were necessary, such as:

- A Linux operating System on PC with g++[1].
- The CLHEP library which contains the basic physics classes derived from events generated by Monte Carlo in C++.
- The native STL library of general purpose which contains generic algorithms and data structures.
- A GNU–make[2] system: located in each directory, defines guidelines for building a library, a set of sublibraries, or an executable.
- 'Environment variables', i.e. set of dynamic values[3] that allow the performance of the infrastructure of the GEANT4 GNU–make.
- Source code of the GEANT4 toolkit that can be downloaded from [79].
- The input–files of the user's code.
- A display program.
- A data processing program like ROOT and other common data analysis softwares.

[1] GNU C++ compiler.

[2] Make is the utility software that builds executable programs and libraries from source code by reading the makefiles where is indicated how to carry out the main program.

[3] Values that affect the behavior of the running processes in a PC.

Finally, it is important to note that although GEANT4 code has a lot of advantages, as is discussed in the beginning of this section, there are some disadvantages that it is worth mentioning: first of all, the GEANT4 complex structure and the huge quantity of G4–options affects directly the learning time of the user, in contrast with other specific-use Monte Carlo codes that are much simpler to use. Secondly, GEANT4 requires more computational resources that other codes which are particularly designed for some concrete application. Third, the modeling of interactions at low energy for neutrons and electromagnetic interactions is still under debugging and development, hence GEANT4 could occasionally provide results that do not agree with others obtained by other MC codes with high experimental backup (for example MCNP, which has a high validation for neutrons). This issue will be reviewed in Section 3.4.

3.4 Simulation results for planar designs

In section 2.4.3.1 was concluded that the neutron detection efficiency in planar detectors depends on the charged particle range, the ^{10}B density, and the converter thickness. On the basis of that analysis, and in order to adapt the planar neutron sensors adequately, a set of Monte Carlo simulations were carried out with the MC packages detailed above, GEANT4 and MCNPX. The two packages were used to compare their performance for neutrons. First of all, the main characteristics of the design simulated with each simulation package are summarize below:

(a) Simulation parameters with MCNPX:

- The geometric structure consists of a silicon volume with a thickness of 300 μm and a square area of 25 mm^2 with a layer of a neutron converter material on one surface. The outside region of the structure is vacuum. The variable parameters in the simulations were the thickness of the converter layer and its composition. Fig. 3.7 shows a sketch of the simulated geometry. In MCNPX, materials are created employing their percentages by fraction mass, with isotopic compositions and densities. The simulated materials were: ^{10}B, natural boron, and two o–carborane/cyanoacrylate mixtures, one with ^{10}B and the other with natural boron. The specific compositions are shown in the Table 3.4[1].

[1]These compounds will be used in the experimental tests carried out in Chapter 5.

Table 3.4: Converter composition

Materials	**Mass Fraction** (%)	**Density** (g/cm^3)
^{10}B	100%	2.46
Natural Boron	19.9% ^{10}B & 80.1% ^{11}B	2.46
o-carborane	81.9% o-carborane + 18.11% cyanoac.	
H	7.5%	
C	28.7%	
^{10}B	53.0%	1.37
O	7.5%	
N	3.3%	

- Models for low energy neutron tracking were implemented from the latest version of the continuous-energy data libraries JENDL, and the evaluated nuclear data file (ENDF), explained in section 3.2.2.

- The neutron source was created like an expanded beam in a plane disk perpendicular to the beam direction and parallel to the plane defined by the front detector face (see Figure 3.7). The plane disk radius matches the half–size of the detector. In each simulation run 10^7 thermal monoenergetic neutrons, 0.025 eV, were uniformly directed over the detector surface, focused towards the detector entrance face. The statistical uncertainties were less than 0.05%.

- The simulated temperature was 300 K. The energy cut–off, i.e. the energy below which the transport of the particles is discarded ('tracking cut'), was 10 keV for heavy ions and alphas.

- The inbuilt tally cards F4 (particles/cm^2) and F8 (pulses) were used to obtain the fluence from the ^{10}B(n,α)^7Li reaction, and the energy deposited in the detector, respectively. The subsequent analysis was carried out with a conventional mathematical software.

(b) Simulation parameters with GEANT4:

- The simulated structure was the same as with MCNPX above. GEANT4 does not allow to use 'vacuum' as a material so 'interstellar air' (air with very low density,

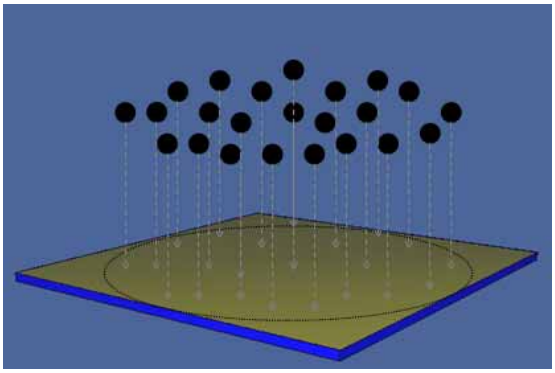

Figure 3.7: Planar silicon detector simulated with MCNPX. - The neutron beam is a parallel monoenergetic (0.025 eV) beam with normal incidence over the detector.

10^{-25}g/cm^3) was used instead. Like in the MCNPX simulations the parameters were the converter materials and their thicknesses. The materials were either created or taken from the GEANT4 database, derived from the NIST database. The simulated converter compounds are listed in the Table 3.4.

- The physical processes implemented in Geant4 were: (i) Standard electromagnetic, hadronic and transportation models; (ii) for neutrons, the low energy processes were implemented using the Evaluated Neutron Data Library G4ENDL, based on the ENDF/B-VI cross-section evaluation. The elastic, inelastic and capture processes were considered by means of the G4NeutronHP-dataset (renamed in the code system as ThermalScatteringData, ElasticData, InelasticData and CaptureData); (iii) The LHEP Physics List (based on parameterized modeling of hadronic interactions) was used as well. This combines the High Energy Parameterized (HEP) and the Low Energy Parameterized (LEP) models.

- The General Particle Source (GPS) tool, available in the GEANT4 distribution, was used to define the neutron source. It was an user–adaptation with the following features: the simulated structure was irradiated by a monoenergetic broad thermal neutron beam focused on the detector surface, sufficiently far in such a way that the irradiation direction can be considered normally incident on the detector device (see Fig.3.8). In each simulation run, the source emitted 10^6 incident thermal monoenergetic neutrons, 0.025 eV, towards the entrance face of the detector. The statistical relative uncertainties were less than 0.1%.

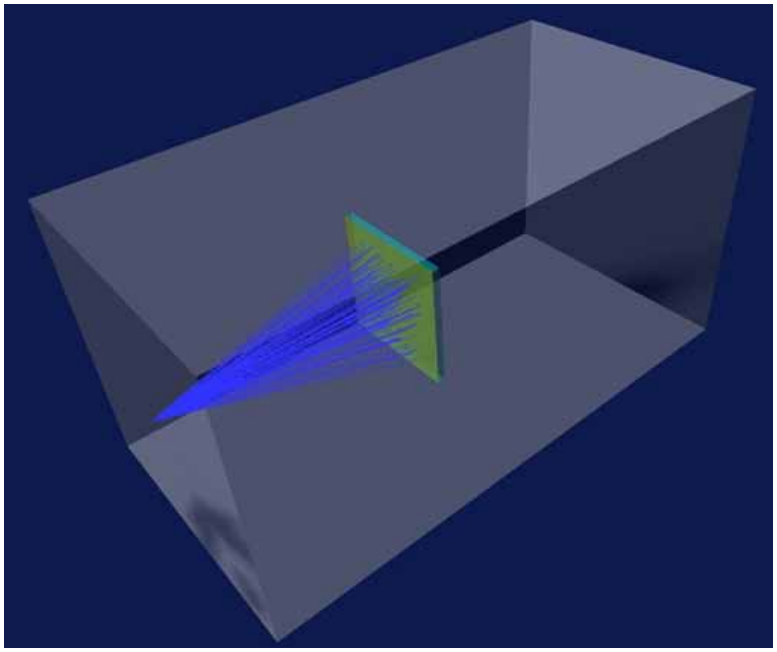

Figure 3.8: Planar silicon detector simulated with GEANT4. - The neutron beam is a monoenergetic broad thermal neutron beam (0.025 eV) focused on the detector.

- The default temperature used for the simulation was 273.15 K. For GEANT4 the energy cut–off is a value that must be set in length units and that is converted into energy for each material. Below this value, the energy is deposited locally and secondary particles will not be transported. The cut–off was set for all particles at 100 nm.

- For all tracked particles, several methods were used to verify that the charged particles, products of the $^{10}B(\mathrm{n},\alpha)^{7}Li$ reaction, reached the detector sensitive volume. Then, for each event, the energy deposited by them inside this volume was saved. For this purpose, several G4–methods like 'GetEnergyDeposit' were used. Both the spectra and the efficiencies were calculated using the 'UserSteppingAction' class, which belongs to an user action class 'G4UserSteppingAction'.

3.4.1 Simulated thermal neutron detection efficiency

To quantify the goodness of the different prototypes the detection efficiency has been established as the key parameter, which is defined as the ratio of registered neutrons in

the sensitive silicon bulk, Σn_{det}, divided by the number of incident neutrons ($\Phi_{incident_n}$) on the devices, i.e:

$$\varepsilon = \frac{\Sigma n_{det}}{\phi_{incident}} \cdot 100[\%] \tag{3.8}$$

Fig. 3.9 shows the simulated efficiency for thermal neutrons in a planar silicon detector as a function of the thickness of a ^{10}B layer for several densities and calculated with MCNPX. These results agree well with the values previously reported by [96] and [48]. Note that the tendency of these curves is similar than those obtained in the analytic discussion (section 2.23). This figure shows the influence of the converter density on the efficiency: as it was discussed in section 2.4.3.1, the lower the converter density, the higher is the range of the charged particles, but at the same time there is a lower number of ^{10}B target atoms per unit volume, resulting in a smaller number of neutron captures. Hence, for converters with higher density the efficiency rises faster than for those with lower density and, once peaked, decreases more rapidly (these trends can also be derived from equations 2.35 and 2.36). Nevertheless, according to Fig. 3.9, the highest possible detection efficiency, independently of the density of the ^{10}B layer, is about 4.7%.

Figure 3.10 compares the thermal neutron efficiencies obtained with MCNPX and GEANT4 for a planar detector as a function of the converter layer thickness considering a ^{10}B material. A surprising result is found when the results of both simulation packages are compared: the discrepancies are evident for this case independently of the converter density: whereas the efficiencies calculated with MCNPX reach a maximum of 4.7%, those calculated with GEANT4 do not exceed 3.3%.

Similar calculations were carried out for two other compounds, the mixture of o-carborane and cyanoacrylate from Table 3.4, both with natural boron and with ^{10}B. In the case of natural boron, plotted in Fig. 3.11, the efficiencies are similar for both codes. However, the discrepancies are obvious again in the case of the o-carborane compound with ^{10}B: MCNPX indicates a maximum detection efficiency of 2.5% but with GEANT4 only 1.5% is obtained.

The MCNPX efficiency curves of the detectors from Fig. 3.10 and 3.11 show that the total efficiency for thermal neutrons can be up to 4.5% for a 5 μm layer of pure ^{10}B and 2.5% for a 5 μm layer of the $C_2B_{10}H_{12}$/cyanoacrylate compound fabricated with

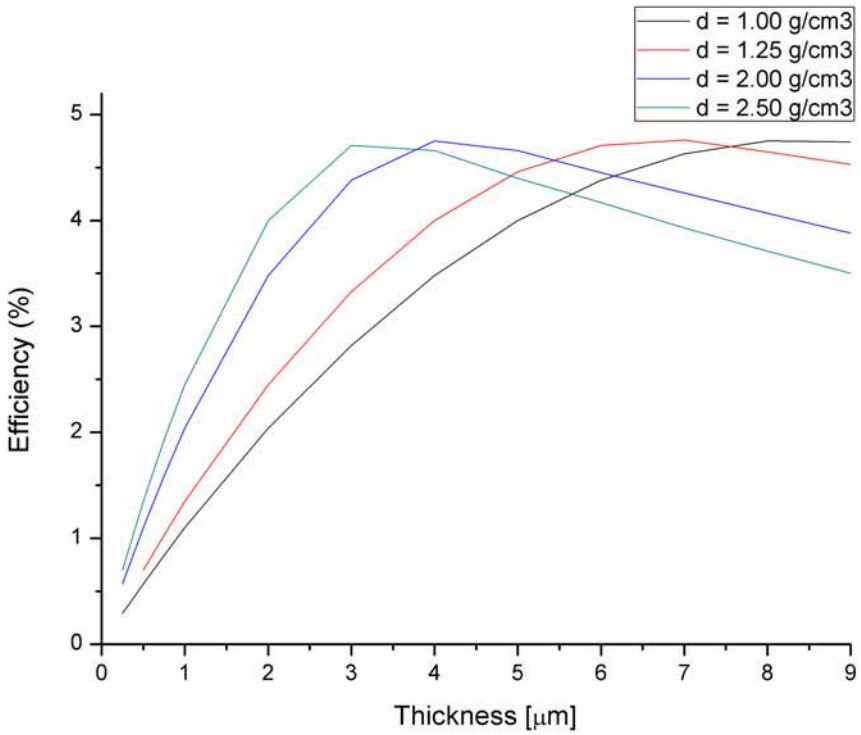

Figure 3.9: Simulated thermal neutron detection efficiency with MCNPX in a planar detector covered with ^{10}B for several densities.

^{10}B, or 0.5% for the same layer with natural boron. The efficiency decreases gradually with higher thicknesses. It is worth noting that the MCNPX simulated maximum efficiency for $C_2B_{10}H_{12}$/cyanoacrylate with ^{10}B, 2.5%, is half the simulated value of ^{10}B, 5%. This result is coherent with the relative content (53%) of ^{10}B in the materials, as can be seen in Table 3.4.

Although there are not many published studies about the propagation of thermal neutrons with GEANT4, some reports have already verified discrepancies between GEANT4 and MCNPX for the thermal neutron capture [97]. However, there are other few papers that report a reasonably agreement for low energy neutron propagation [98, 99, 100], or variable agreement depending on the neutron energy range [101]. In some of these works the authors pointed that the differences found in their studies between GEANT4 and MCNPX or experimental data could be due to the fact that the physics is encoded in a different way in the core of each software package. Never-

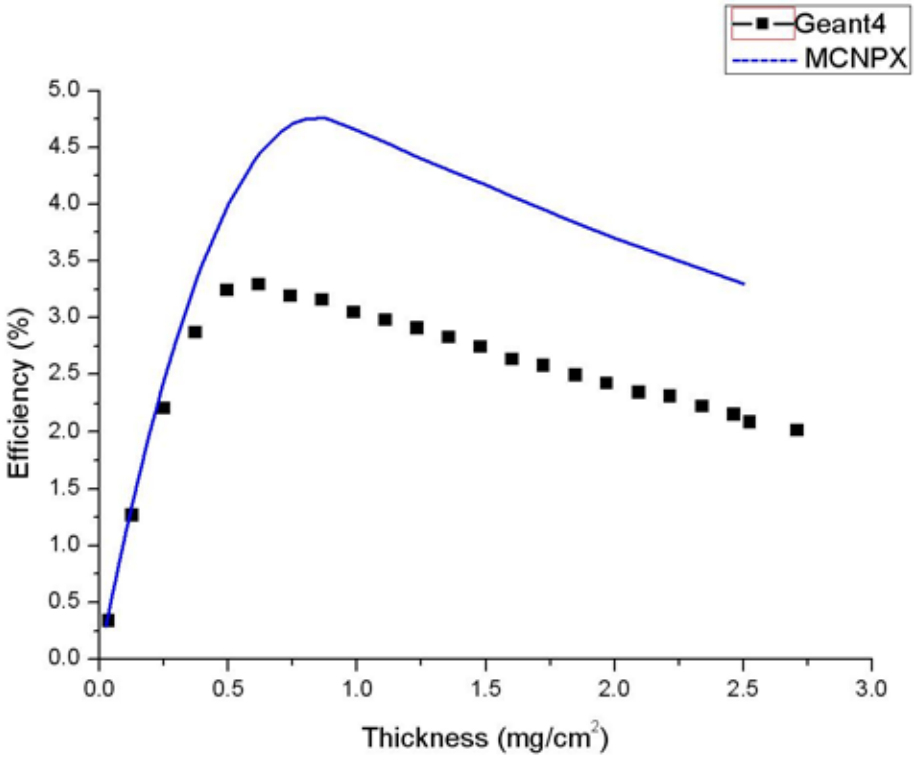

Figure 3.10: Simulated thermal neutron detection efficiency for planar silicon detectors covered with ^{10}B with MCNPX and GEANT4 codes.

theless, it is important to notice that in these cases the simulated materials (and the corresponding geometries) are different. i.e. their neutron cross-section libraries, which are specific for each element, may have had different associated physical processes, depending also on the version of the codes. Therefore, it is likely that for some elements the low energy neutron propagation is working properly, but in other cases it is not. This could explain the discrepancies found in the results of our simulations, as seen in Fig. 3.10 and 3.11: there is consistency between the codes for the simulated efficiency using o-carborane with natural boron, whereas for the same compound, with ^{10}B, the disagreement is obvious.

One of the main differences in the physics implementation between GEANT4 and MCNPX, when comparing thermal neutron interactions, is that GEANT4 only includes a free gas treatment for thermal neutrons whereas MCNPX is also able to account for the chemical binding in solids and liquids. This may affect both the energy and angular distributions of the incident neutrons mainly after their local elastic scatterings. In

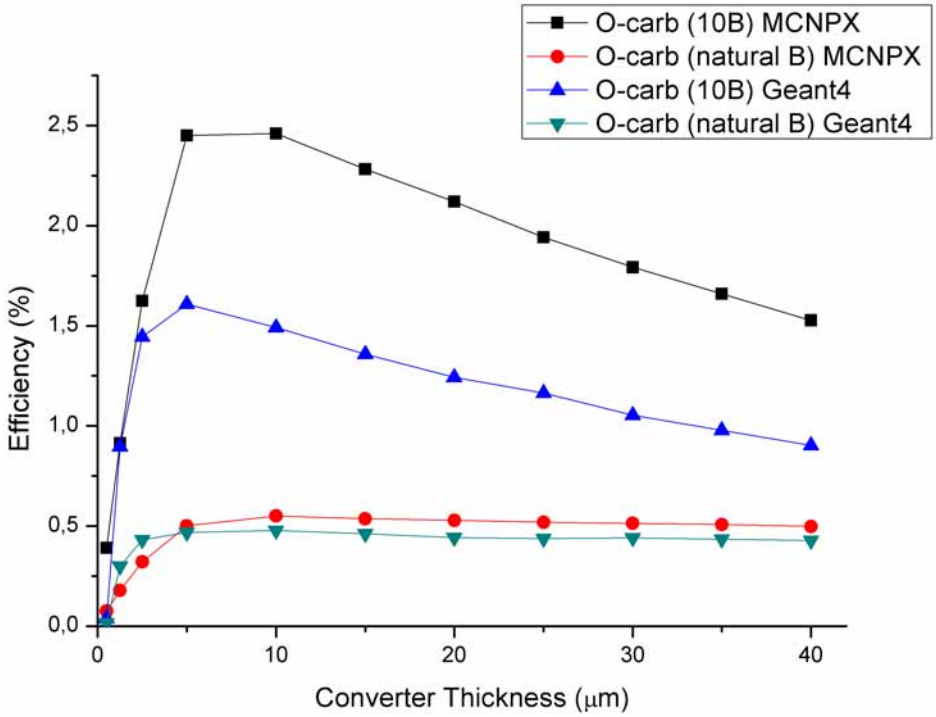

Figure 3.11: Simulated thermal neutron detection efficiency for planar silicon detectors covered with o-carboranes using MCNPX and GEANT4 codes.

addition, for neutron energies below 20 MeV the physics is implemented in MCNPX through the evaluated ENDF cross-section library, while in GEANT4 can be implemented through data libraries or with nuclear models, called *parameterization driven models*. Therefore, the cross-sections databases and the interpolation techniques in each code might disagree. Besides all this, both toolkits handle the energy cut-off in a different way. This concept can be applied either as a *tracking cut*, for which the transport of particles below this parameter is not considered and their energy is lost for the simulation, or as a *production cut*, i.e. the particles with energy below this value are not generated as secondary but their energies are deposited locally. While MCNPX has the option of choosing between the two methods for each type of particle, for GEANT4 only the second one is possible, and each particle has its own production cut, which is introduced by the user.

GEANT4 was initially developed for high-energy physics, so its implementation

to transport high-energy particles is well established, but the treatment of thermal neutrons in its version 4.9.2 still has limitations and data from literature are scarce. However, the neutron cross sections implemented in GEANT4 are constantly updated by the GEANT collaboration. Furthermore, since the models must be validated experimentally, there are continuous refinements of the code as discrepancies with experimental data are reported. On the other hand, neutron transport in MCNPX is widely used for any neutron energetic range and has been compared with experimental data showing a good agreement for its versions 2.6.0 and older.

This differences between the simulation results made us continue in the next simulations with MCNPX code, until the debugging of such mistakes in GEANT4.

3.4.2 Simulated reaction product spectra

The pulse–height spectra of deposited energy allows us to discriminate the neutron signal, i.e. the signal created by the ^{10}B(n,α)^{7}Li reaction products, from background signal that is usually present in the neutron sources/beams. Herein it is considered that all the energy deposition of the reaction products coming from the ^{10}B(n,α)^{7}Li contributes to the pulse–height signal. The LLD setting is fixed at 0 keV as a first approximation. Later, in the experimental tests, this will be included in the simulations (see subsection 5.3).

Figures 3.12 and 3.13 show the simulated energy with MCNPX deposited in planar silicon detectors covered with ^{10}B with two possible values of the density of such isotope, d=1 g/cm^3 and d=2.5 g/cm^3 respectively. It is observed:

- As said in section 2.4.3.1, the quantity of energy deposited in the sensitive silicon detector depends on the depth where the neutron capture takes place as well as the out–angle of such reaction. Therefore, the pulse–height distribution of the deposited energy is a continuous spectrum.

- There are two main edges that correspond to the energy deposited by the alpha particles coming from the excited state of the ^{10}B(n,α)^{7}Li capture reaction, i.e. 1470 keV and 1780 keV.

- The thinner is the converter layer, the better is the resolution of the peaks due to a lower straggling of the nuclear reaction fragment energy when it reaches the silicon.

- The thicker is the converter layer, the spectrum shows less sharp edges/peaks because the ^{10}B(n,α)^{7}Li reaction products have to pass through more material with larger loss of energy.

- Alpha particles and ^{7}Li ions fly in opposite directions and, hence, they never reach the silicon at the same time. As a result, there are no counts above the maximum energies of these particles.

- There are marked dips in the spectra at low energies when the thicknesses of the ^{10}B layer are thin, which could help to discriminate the signal from background without losing many neutron counts if the LLD setting had to be fixed relatively high.

- The thicker is the converter layer, the higher is the total number of counts, up to the maximum efficiency thickness: 8 μm of ^{10}B coating provided the boron density is d=1 g/cm^3 (Fig. 3.12) and 3 μm with d=2.5 g/cm^3 (Fig. 3.13).

- For the optimum thicknesses in each case, the discrimination thresholds have to be set as low as possible to keep a high efficiency because the counts at low channels are high.

Note that these results are obtained under ideal conditions. In an experiment there are several adverse effects, which are difficult to reproduce in Monte Carlo, that reduce the calculated efficiencies, for example: leakage currents that raise the whole noise of the system, physical defects into the silicon bulk, unavoidable 'dead layers'[1], random spurious signals, background radiation, etc. These unwanted effects cause a widening to lower energies that, depending on the LLD setting, affect negatively the counting efficiency. Some of these distortions will become patent in the experimental results shown in Chapter 5.

In view of the remarks above and since most of the energy deposition takes place near the ^{10}B layer/silicon interface, it is strongly advisable that the 'dead layer' of the detector is as thin as possible. To this end, it is necessary that: (i) the contact metallic layers, which are between the ^{10}B and the sensitive silicon bulk (see Figure 2.16), are as thin as possible; (ii) if there is a p^{+}n junction, the p^{+} should be highly doped to reduce

[1]Herein it is denoted as dead layer whatever layer that is insensitive to neutron capture.

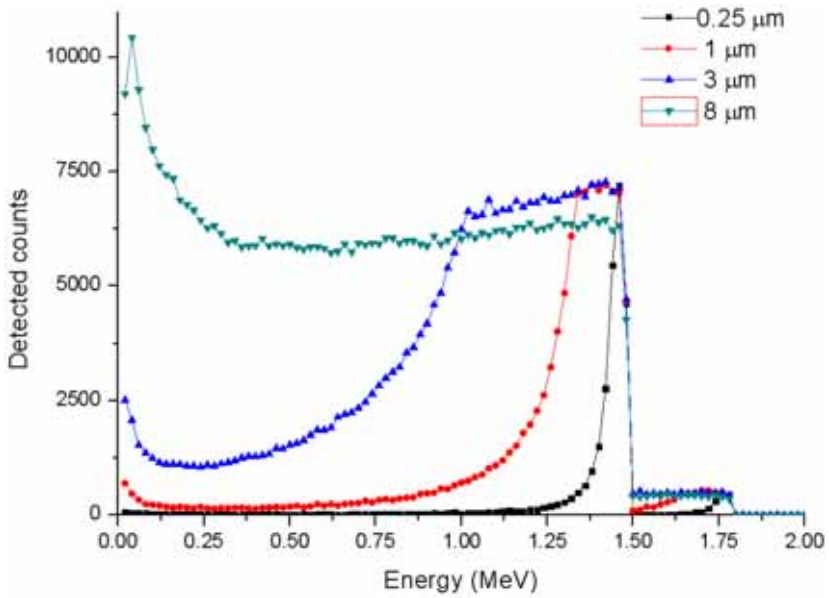

Figure 3.12: Simulated spectra of energy deposited in a planar silicon detector covered with ^{10}B of d=1 g/cm^3 - Detected counts for thermal neutron detection with a planar silicon detector covered with 0.25, 1, 3, and 8 μm thicknesses of ^{10}B of density 1 g/cm^3. The optimum thickness is 8 μm of ^{10}B with d=1 g/cm^3.

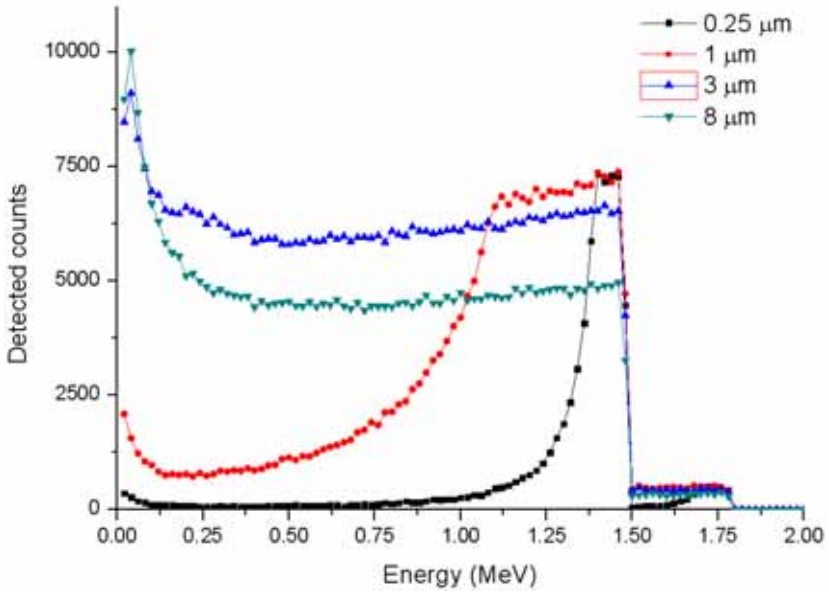

Figure 3.13: Simulated spectra of energy deposited in a planar silicon detector covered with ^{10}B of d=2.5 g/cm^3 - Detected counts for thermal neutron detection with a planar silicon detector covered with 0.25, 1, 3, and 8 μm thicknesses of ^{10}B of density 2.5 g/cm^3. The optimum thick is 3 μm of ^{10}B with d=2.5 g/cm^3.

the interface of the p–n junction (because it is not sensitive detector bulk and is a region where the charged particles may lose energy). Additionally, the neutron/γ-rays discrimination needs to be high to favor a low LLD setting and thus a higher counting efficiency. All these considerations are taken into account for the designs presented in Chapter 4.

3.5 Prototypes of 3D silicon neutron detectors

As said in the introduction, microstructured devices could reach high neutron detection efficiency. Based on the theoretical analysis presented in section 2.4.3.2, it is studied a general case of perforated/microstructured detector: the first simulated device consisted of an array of micro-channels etched inside a sensitive silicon bulk and filled with a pure ^{10}B converter. Figure 3.14 shows three versions of a (*unit–cell*[1]) of the same prototype that could be filled with liquid boron-based compounds.

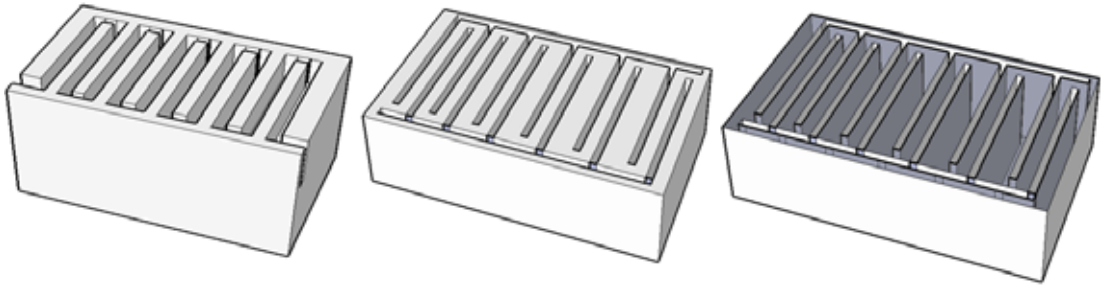

Figure 3.14: Schematic of a 3D design of trenches - Sketch of three possible designs of trenches etched into the silicon bulk to be filled with liquid boron-based converters: note that the microchannels are distributed in a slightly different arrangement.

The p–n junctions that turn this prototype into a particle detector would be located in the trench walls. Previously to the simulations, it is important to take into account the realistic technological restrictions in order to limit the range of the simulated parameters. Hence, it was decided that the proposed designs should be reproduced with standard MEMS techniques in a clean room facility. The choice of MEMS technologies ensures the repeatability, mass–producibility and low cost of the fabricated detectors.

[1]Minimum volume of a simulated geometry that is representative of the system geometry, i.e. its simulated results can be scaled.

These restrictions are listed below. These devices are going currently manufactured in the IMB–CNM clean room facilities.

3.5.1 Simulations of Microstructured Designs

Although prototypes with very high aspect ratio holes would give the highest efficiencies (as shown by the previous analytical considerations), there are technological limits to what is reliable and easy to fabricate. For instance:

- The aspect-ratio of microstructures in the silicon substrate obtained by the DRIE etching process remains roughly steady at 20:1 for holes or 28:1 for trenches, conditioning the *h:L* ratio. Other techniques such as laser drilling, electrochemical etching or wet chemical etching, could give higher aspect ratios but they are not easily integrated into a standard MEMS process.

- The width of the silicon walls can not be reduced indefinitely for reasons of mechanical stability, so W lower than 10 μm will not be considered in the simulations.

- The possible values for the converter density (ρ) should cover a feasible range. In the simulations a density of 0.9 g/cm^3 has been assumed as valid lower limit for the tapped boron powder as has been discussed above. The upper limit is the boron particle density, 2.34 g/cm^3.

- Dimensions lower than 2.5 μm are difficult to obtain with contact and proximity lithography techniques and will not be considered. Additionally smaller dimensions make the filling of the microchannels with converter increasingly difficult.

Moreover the following assumptions were made in the simulations (the first three to reduce computing times):

- There is no air between the converter and the SD. This is a valid assumption if the deposition technique allows for a good adherence of the converter.

- There are no dead layers on the front face of the devices. Although real devices would have metallic contacts and/or passivation layers that would slow down the charged particles and hinder their detection in the silicon bulk, these are not taken into account in the simulation. The assumption is valid if the prototypes are

designed such that these layers are very thin (in the order of hundred nanometers) and therefore their effects over the overall detection are negligible.

- Similarly, there are no dead layers on the etched walls of the devices. In order to achieve this, the prototypes should be fabricated with shallow junctions.

- The energy cut-off, which can be understood as equivalent to the lower limit of detection (LLD), was fixed as 10 keV in the simulations. In the experimental measurements the LLD of the readout system depends on the electronic noise. It is important to note that when the LLD increases, the measured range (or effective range) of the reaction products from $^{10}B(\mathrm{n},\alpha)^{7}Li$ drops. For a LLD setting below 100 keV the actual and effective ranges differ little.

Note that although the dead layers can be reduced to some extent, in real devices they are inevitable so there is always a loss of energy of the reaction products when they go through the different interfaces. This means that, even though the simulation is a powerful tool in order to evaluate the performance of novel prototypes and compare between designs, the overall measured efficiency will be lower than the simulated.

Simulation results

Figure 3.15 shows the simulated geometry with MCNPX which consists of a silicon volume as the sensitive SD bulk with an array of 40 microchannels backfilled with the ^{10}B converter.

The physics processes were implemented using cross-section libraries for low energy neutron tracking from the evaluated nuclear data file ENDF/B-VII. In addition, the device was irradiated by a thermal neutron beam (0.025 eV) around the device, modeled as a sphere positioned sufficiently far from the detector (sphere radio > size device) in such way that the irradiation is independent of the incident angle, on all sides of the device at all possible angles (Figure 2.26.c). Therefore, this way neither neutron beam direction is given priority. Based on the analytical considerations discussed, the parameters of the proposed design that have been optimized by the simulations are: the trench depth (h) and width (L), the silicon wall width (W), and the ^{10}B converter density (ρ). Note that, although as explained above in this Section the aspect-ratio of the etched trenches is fixed around 28:1, in the simulations this aspect ratio has been

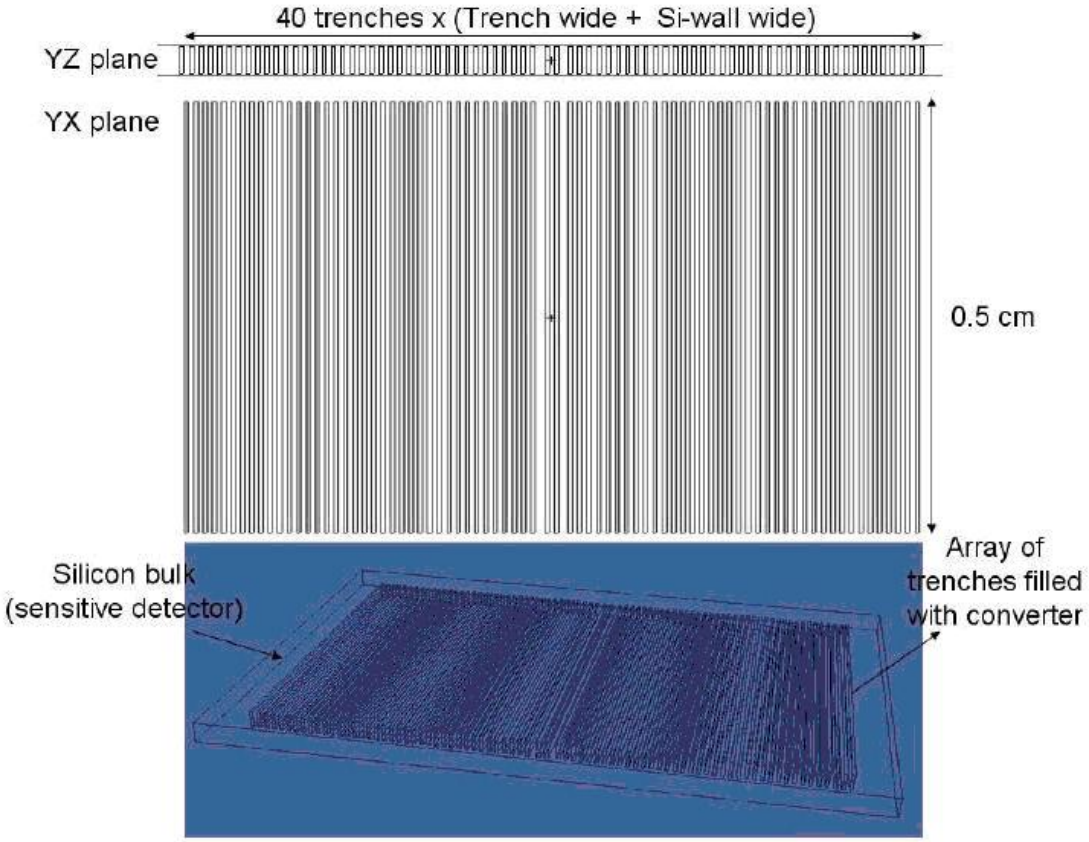

Figure 3.15: Sketch of the 3D-pattern with microchannels filled with ^{10}B

split in (L, h) in order to show the overall behavior of the dependence of the efficiency with the simulated variables. The simulations have been performed fixing at least two of the parameters, and varying the other two each time. Two general cases have been considered: total number of channels fixed (Figures 3.16 to 3.18), and total area of the detector fixed (Figures 3.19 and 3.20).

Constant-array design: fixed microchannels

Figure 3.16 shows the simulated efficiency for thermal neutrons as a function of the trench width (L) for an array of 40 microchannels with 250 μm depth (h) and silicon walls of 40 μm width (W) between channels. It displays the effect of the converter density on the efficiency, that can be as high as 50%. As was discussed, the lower is the converter density, the higher is the range of the charged particles, but at the

same time there are a lower number of ^{10}B target atoms per unit volume, resulting in a smaller number of neutron captures. Therefore, for ^{10}B converters with a higher density, the efficiency raises faster than for those with a lower density and, once peaked, it drops more rapidly. It is important to notice that as L increases, above 5 μm, a lower density gives higher efficiencies. Considering only the lowest density (0.9 g/cm^3), the

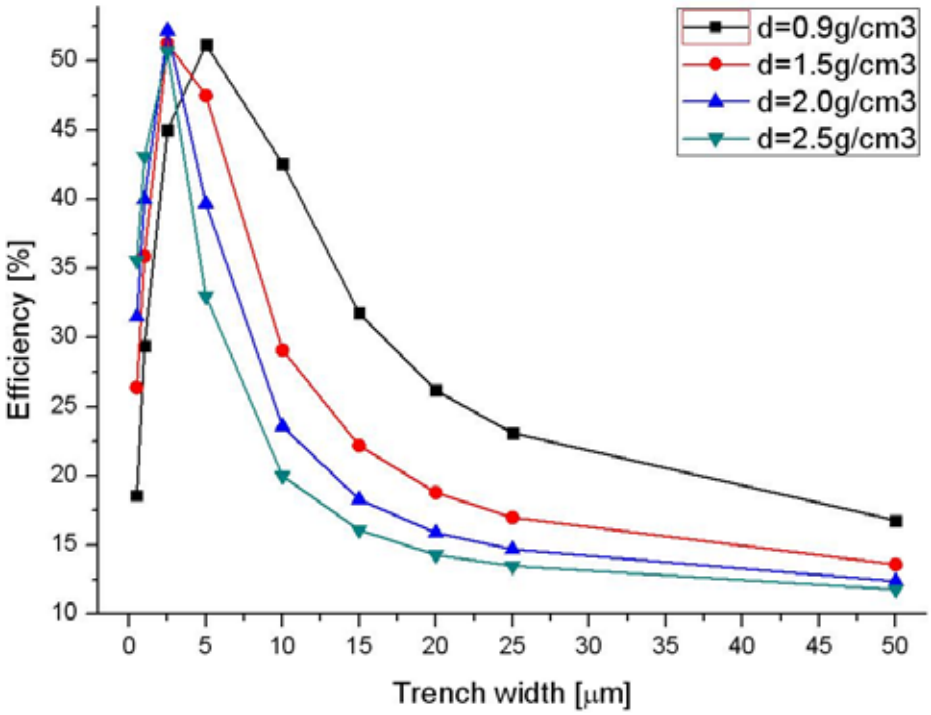

Figure 3.16: Dependence of the simulated efficiency versus trench width for several ^{10}B densities - Design with silicon wall width (40 μm) and trench depth (250 μm) as fixed parameters.

simulations were repeated for different values of the wall width (W). The results are shown in Figure 3.17, which demonstrates that as W decreases the efficiency improves. This effect is more marked if $W$is reduced to 10 μm, in which case the efficiency can be higher than 75%. Nevertheless, in order to design a technologically viable device, we need to limit some of the parameters. Thus, we will focus on the lowest density, 0.9 g/cm^3, and silicon walls between channels with a width of 40 μm to ensure a viable further process as these provide enough mechanical robustness still assuring high efficiency, not much different than the 30 μm walls.

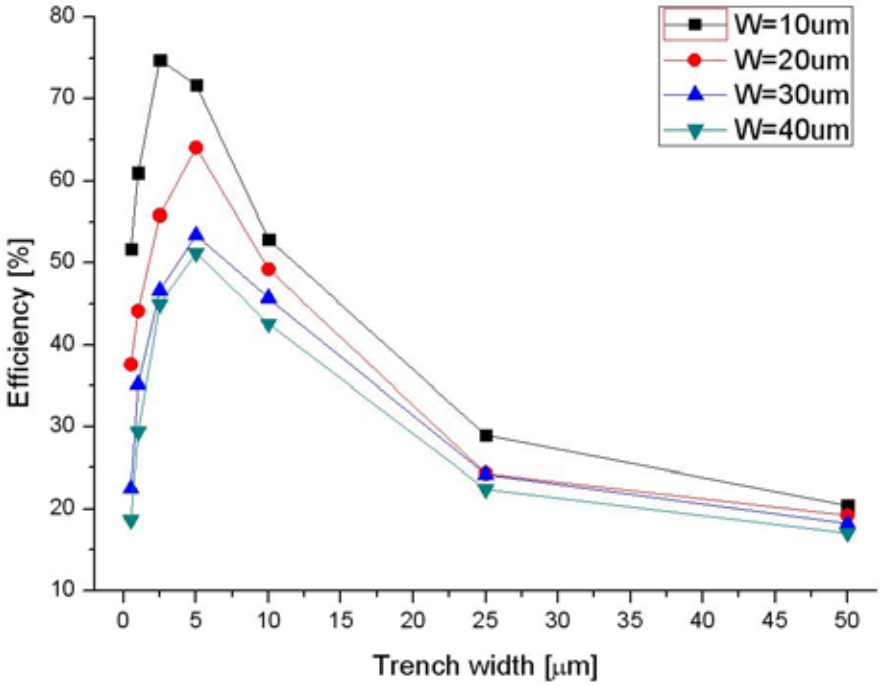

Figure 3.17: Dependence of the efficiency versus trench width for several silicon wall widths - Fixed parameters: ^{10}B density 0.9 g/cm^3 and trench depth 250 μm.

Figure 3.18 compares the simulated efficiency as a function of the trench width for several depths of the channels, with the converter density fixed as 0.9 g/cm^3 and the silicon wall width as 40 μm. The plots show that the efficiency increases when the channel depth h rises and it saturates for h higher than 250 μm.

These results point out that, for technologically feasible parameters (d= 0.9 g/cm^3, W=40 μm and h=250 μm), the thermal neutron efficiency is maximized for L=5 μm as >50%.

Variable-array design: fixed detector area

Similar simulations were carried out for the same design changing the total number of channels and keeping the total detector area, i.e. normalizing the sensitive area of the devices for all the cases. The first simulations were executed with the following fixed parameters: d= 0.9 g/cm^3, h = 250 μm, S = 0.25 cm^2. Figure 3.19 shows the dependence of the simulated efficiency versus channel width for four silicon wall widths. The simulated efficiency reaches 65% for a design with W = 20 μm and L = 5 μm.

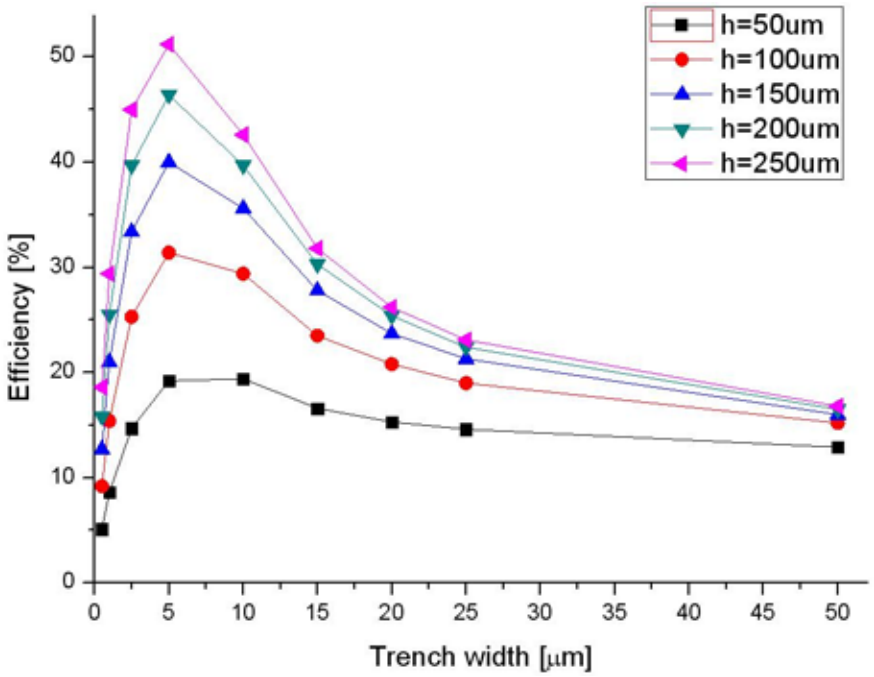

Figure 3.18: Dependence of the efficiency versus trench width for several channel depths - Fixed parameters: ^{10}B density 0.9 g/cm^3 and silicon wall width 40 μm.

The dependency of the efficiency with the silicon wall width is displayed in Figure 3.20. In this case, for one fixed W, the efficiency increases markedly when the channel width is reduced. For instance, if the silicon wall width is 40 μm, for channels with L = 25 μm the efficiency reaches 25% but for an array of channels with L = 5 μm the efficiency can be as high as 55%.

The detection efficiencies for thermal neutrons of a 3D–patterned silicon sensor backfilled with ^{10}B were simulated with MCNPX. The design parameters used in the simulations have been chosen so the detector can be fabricated with MEMS fabrication techniques in order to obtain repeatable, cheap and mass-producible sensors. The simulation results prove that the thermal neutron detection efficiency of such 3D sensors may be higher than 50% for a device fabricated with realistic parameters, an order of magnitude higher that the efficiency of a common planar detector. The conclusions of the simulations have been used to design a neutron detector prototype that is currently being manufactured in the clean room facilities of the Instituto de Microelectrónica de Barcelona with good prospects.

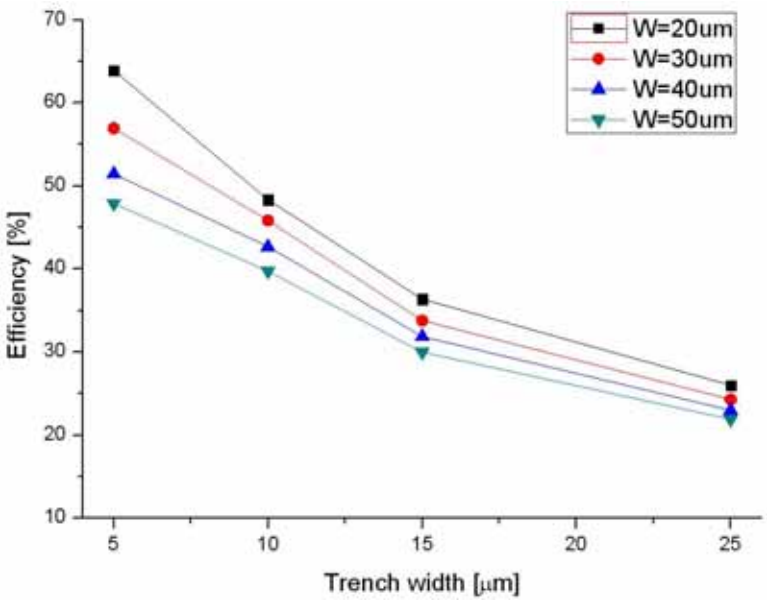

Figure 3.19: Dependence of the efficiency versus channel width for several silicon wall widths - Fixed parameters: ^{10}B density at 0.9 g/cm^3, channel depth 250 μm and detector area 0.25 cm^2.

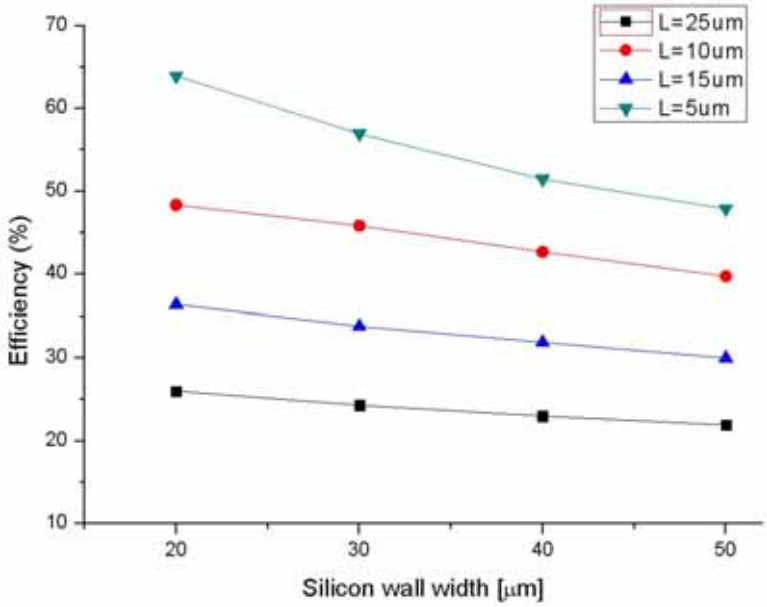

Figure 3.20: Dependence of the efficiency versus silicon wall width for several channel widths - Fixed parameters: ^{10}B density 0.9 g/cm^3, channel depth 250 μm and detector area 0.25 cm^2.

4

Silicon sensors for neutron detection

The production of semiconductor devices is based on the microelectronic technology which makes use of wafers[1]. The wafers are altered by means of a series of processing steps like doping, chemical etching, oxidation and deposition of materials, among others, in the facilities of a clean room [102]. Nowadays the technology employed in semiconductor radiation detectors is based on this technology.

Most of the radiation sensors fabricated at IMB–CNM are based on PIN diodes made on very high resistivity silicon substrates [103]. They may be fabricated using very large areas and can be segmented into strips or pixels for position sensing [33] for applications like imaging and particle tracking. In recent years the Radiation Detectors Group at IMB–CNM has developed a new '3D' technology for silicon detectors that

[1]Thin slices of a semiconductor material that is usually silicon (Si) or germanium (Ge).

exploits the capability of such processing steps to develop columnar electrodes through the semiconductor bulk. This alternative 3D technology adds many advantages in comparison with the standard planar designs that are explained in section 4.2. The versions fabricated at IMB–CNM for neutron detection are explained in the following subsections.

As it was detailed in section 2.4.3, a solid-state neutron detector consists in a semiconductor radiation sensor covered or filled by a neutron converter. In this work we focus on thermal neutron detection using ^{10}B as neutron converter and silicon as sensor for the reasons explained in subsections 2.3.1 and 2.4.3. This chapter is divided in two sections:

- First of all, section 4.1 deals with two type of planar silicon detectors adapted to neutron detection: one standard p-i-n detector that will be used as a first proof-of-concept, and Schottky diodes with thin entrance windows. Experimental results are shown in sections 5.1.1 and 5.1.2 respectively.

- Secondly, section 4.2 is about the design, optimization, fabrication, and characterization of the novel ultra-thin 3D silicon detectors proposed to detect neutrons in radiotherapy rooms, main goal of this thesis. The experimental tests carried out with these devices are detailed in sections 5.2 and 5.3.

All the presented detectors were produced at the clean room facilities of the IMB–CNM and were adapted with boron-based compounds (o-carboranes, $^{10}B_4C$, and ^{10}B). Both the synthesized compounds and deposition methods used in those detectors are described in Appendix A. It is worth mentioning that the deposition of these converters is not easy to achieve at a technological level and thus it represented technical challenges that, in the end, were solved successfully.

Part of the results obtained have been published in [62] and as a consequence of the studies developed another patent has been filed [69].

4.1 Planar silicon detectors

4.1.1 P-i-N planar silicon detectors

The simplest configuration of a silicon particle detector is a reverse biased diode, as said in section 2.4.3. The devices used for the first proof–of–concept were P–i–N (PIN) detectors (see Figure 4.1) with an active area of 5×5 mm^2, and a total area of 7.11×7.11 mm^2. These consist in a wide and lightly doped ($(1.1\pm0.1)\cdot10^{12}cm^{-3}$) <100> silicon bulk between p^+-type and n^+-type highly doped regions ($10^{20}cm^{-3}$ and $2\cdot10^{19}cm^{-3}$ respectively). Both p^+–type and n^+–type regions are used for ohmic contacts with the metallization that is usually done with aluminium. A circular window in the center of the detector area is opened in the metal to allow the pass of laser light to carry out measurements of charge collection efficiency. The full depletion voltage of these detectors is 30 V.

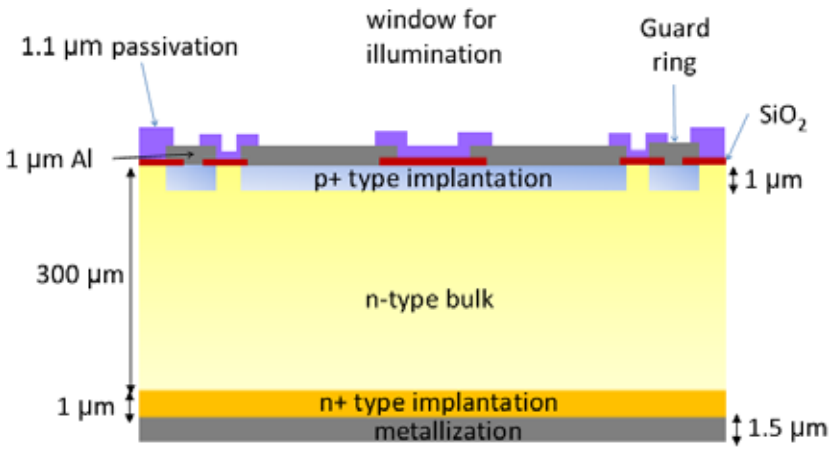

Figure 4.1: Sketch of a p–i–n PAD detector - Schematic of a p–i–n PAD detector fabricated in the clean room facility at IMB–CNM. The total area including guard rings is 7.11×7.11 mm^2, with an active area (defined by the central p–type implantation) of 5×5 mm^2.

These detectors were covered with the converter and moderator films that are typically used in CR–39 dosimeters [104]. As said above, this test was carried out with these devices only as a proof–of–concept. They are not optimized for neutron detection since: (i) they have an active volume of 300 μm, i.e. low γ rejection is expected (this can be improved by operating the sensor underdepleted, although at the cost of a higher

noise due to the elevated capacitance. More about this issue in section 4.2.), (ii) they have a thick entrance window (1 μm Al + passivation layer), and (iii) their entrance window is non-uniform (see Fig. 4.1). Despite those drawbacks, these detectors were useful to understand better the experimental issues associated with neutron sources. Results are shown in section 5.1.1.

4.1.2 Schottky barrier silicon diodes

Taking into account the considerations mentioned in section 2.4.3.1, the design of a planar silicon neutron detector should have the minimum number of entrance layers (between the converter coating and the sensitive silicon) and moreover they should be as thin as possible. Consequently, the first prototype considered was a Schottky barrier silicon diode adapted with an o–carborane compound. These devices consist of a metal–semiconductor junction that creates a Schottky barrier, with almost nonexistent depletion width in the metal, instead of the semiconductor–semiconductor junctions as in convectional diodes. Thus, the charged particles coming from the $^{10}B(\mathrm{n},\alpha)^{7}Li$ reaction would lose less energy in their paths. This device has rectifying characteristics[1] that make it suitable to work as a diode.

The metal and the semiconductor used to make the junction in this work were aluminium and high resistivity n–type silicon. The metal acts as the anode and the n–type silicon acts as the cathode. What this means is that if the semiconductor bulk is doped n–type, only the n–type carriers (electrons) domain the operation of these devices since they are quickly injected into the conduction band of the metal to become free moving electrons, allowing the conduction to be faster. Moreover, the reverse recovery time of a Schottky diode is faster than for a p–n diode, in the order of hundreds of nanoseconds, while for the Schottky is in the order of 100 ps (because there is no charge carrier depletion region at the junction). However, it is important to take into account that the Schottky diodes have an important limitation: they usually have a high reverse leakage current, what will be discussed at the end of this section. Nevertheless, these

[1]Depending on the characteristics of the metals and semiconductors, the junction can provide a rectifying Schottky junction or ohmic contacts. In the ohmic contact the charge carriers can move freely from the metal to the semiconductor and vice versa, whereas in the a rectifying barrier they find a barrier potential between both components.

devices have the advantage of being fast and simple to manufacture to carry out the first tests before moving on to more complex designs.

Figure 4.2 shows the structure of a Schottky diode manufactured in the IMB–CNM clean room facilities. The devices are 285 μm thick with an active area of 5×5 mm^2. They were made-up on high resistivity n-type silicon with an Al layer of 100 nm (24 g/cm^2) for the Schottky contact. This thin aluminium layer has a minimal effect in terms of energy loss of any charged particle passing through it before reaching the silicon. A n^+ implant with an Al layer of 1 μm in the backside acts as the ohmic contact. Note again that the entrance window is non–homogeneous with a maximum thickness of 100 nm Al/Cu because the masks used for the fabrication were not optimized for neutron detectors. However, the fabrication process was specifically designed so that the entrance window was as thin as possible, unlike the PIN sensors of the previous section. The fabrication process is detailed in the next subsection.

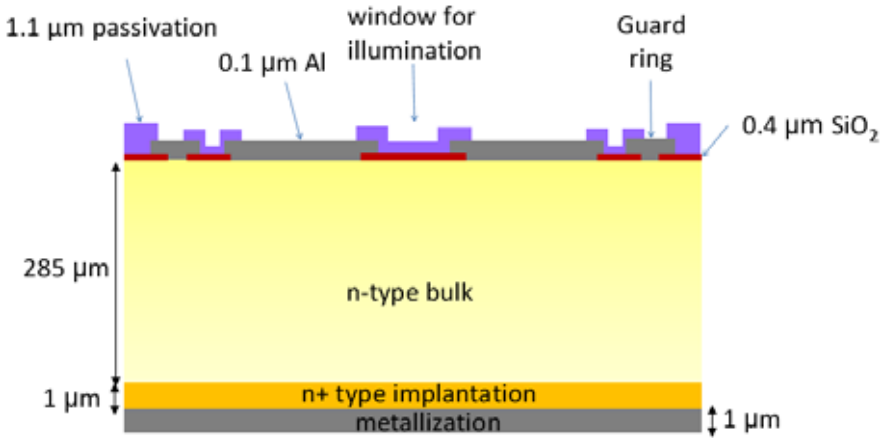

Figure 4.2: Schottky diode structure fabricated at IMB–CNM - Sketch of the section of the Schottky diode whose entrance window is 100 nm of Al/Cu.

4.1.2.1 Fabrication process of Schottky diodes

Four silicon wafers of Schottky diodes were manufactured making use of CMOS microfabrication processes [105]. The main steps followed are summarized in the following paragraphs:

1. Selection of silicon wafers of high resistivity n-type silicon (>5 kΩ·cm) of ∼285 μm thickness that are polished by both sides.

2. Cleaning with H_2SO_4 (95–97%) and H_2O_2 (30%) to remove organic and metallic remains.

3. Wet oxidation (Si + $2H_20 \rightarrow SiO_2$) of 8000 $\mathring{A}$ on both wafer sides to remove possible defects on the surface of the wafer.

4. Etching of the previous oxide with a reactive compound (a commercial mixture, 'SiOEtch', formed by HF(6%) and NH_4F (25%)).

5. Cleaning with H_2SO_4 (95–97%) and H_2O_2 (30%) to not only remove organic and metallic remains but also to eliminate native oxide layers that might grow on the surface of the wafer.

6. Dry oxidation of 38 nm gate oxide at 950°C.

7. Ionic implantation n^+ (phosphorous at 100 keV, $4.2{\cdot}10^{15}$ at/cm^2) on the wafer back–side.

8. Wet oxidation, 400 nm at 1100°C. It is the field oxide (FOX) of the detectors.

9. Photolithography (first mask on wafer front–side) to define the p^+ region in the central diode and the guard ring (see Figure 4.2).

10. Selective etching of 400 nm of oxide (with 'SiOEtch') in the unmasked regions, including backside.

11. Oxygen plasma cleaning of the photoresist residual.

12. Metalization of 100 nm Al/(0.5%)Cu on wafer front-side.

13. Photolithography (second mask) to define the region to be metalized.

14. Chemical metal etching.

15. Oxygen plasma cleaning of the photoresist residual on the front–side.

16. Metalization of 1 μm Al/Cu thickness on all the wafer back–side (without mask) by RF sputter.

17. Cleaning with H_2O.

18. Annealing of Al/Cu at $350°C$ or $550°C$.

19. Cleaning with H_2O of wafers.

20. Passivation layer by PECVD[1], 400 nm of SiO_2 and 700 nm of Si_3N_4, on wafer front–side with PECVD (not in all wafers).

21. Photolithography (third and last mask) to define the passivated region on the front–side.

22. Etching by RIE[2] of the passivation layer in the regions defined by the previous mask.

23. Oxygen plasma cleaning of the photoresist residual on the front–side.

Figure 4.3 shows a picture of a whole wafer that contains these Schottky detectors and Figure 4.4 shows a photograph of one of these devices.

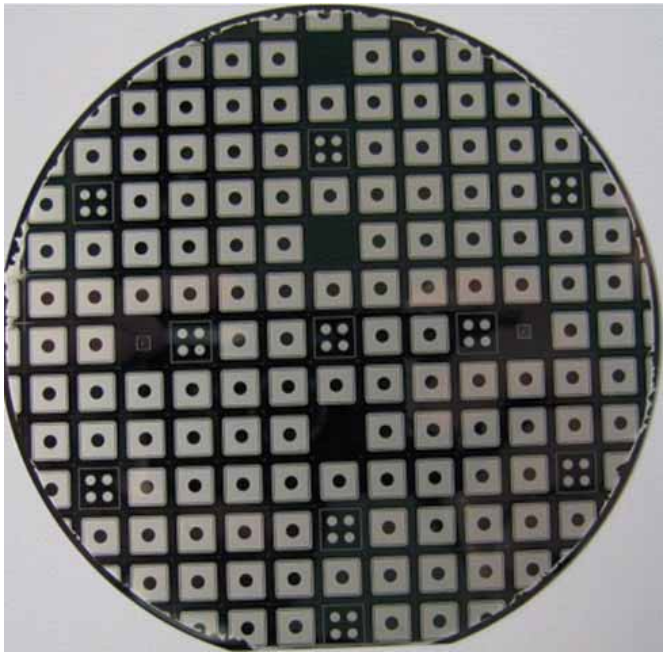

Figure 4.3: Photo of a wafer of Schottky detectors fabricated at the IMB–CNM clean room facilities.

[1]Plasma-enhanced chemical vapor deposition method.
[2]The reactive-ion etching (RIE) uses chemically reactive plasma to remove material over wafers.

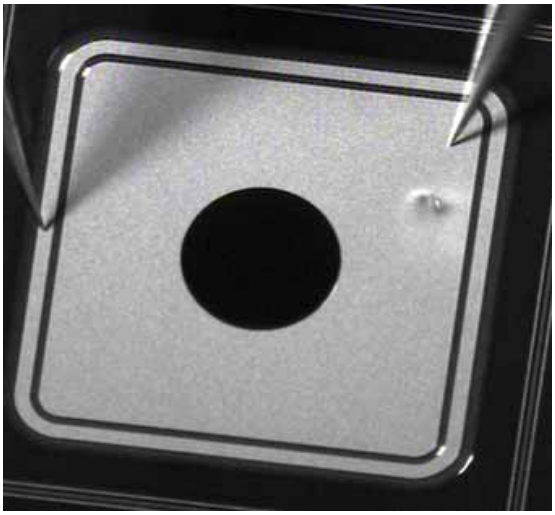

Figure 4.4: Image of a Schottky diode fabricated at IMB–CNM - Front-side image of a Schottky diode whose entrance window is 100 nm of Al/Cu. The hole in the middle of the diode is the window for illumination with laser to carry out the measurements of charge collection efficiency. It has an active area of 5×5 mm^2.

It is worth noting that in order to test different technological options, some wafers were annealed at 550°C instead of 350°C or not passivated, but their electrical performance resulted to be worse as is seen in the next section.

4.1.2.2 Characterization of Schottky diodes

The electrical characterization of all the Schottky detectors was carried out as is explained in Appendix C.1. In this case, a shielded KarlSuss PA200 probe station was used for the electrical probing. The I–V curves of each detector were obtained with a HP4155 Semiconductor Parameter Analyzer and the thermal chuck kept at 21°C. The I–V curves when the devices are reverse biased are shown in Figure 4.5.

Surprisingly and contrary to predictions [106, 107], the devices that were annealed at 550°C had a higher leakage current than those annealed at 350°C. Besides, there is not substantial difference in the I–V curves between the wafers with passivation layer and those without it, although it is stressed that the performance of non-passivated devices may degrade with time due to external agents (e.g. humidity, incorrect handling). Then, the Schottky detectors with lower leakage current, i.e. those of the the wafer #4, were selected to be used in the experiments explained in section 5.1.2. The average

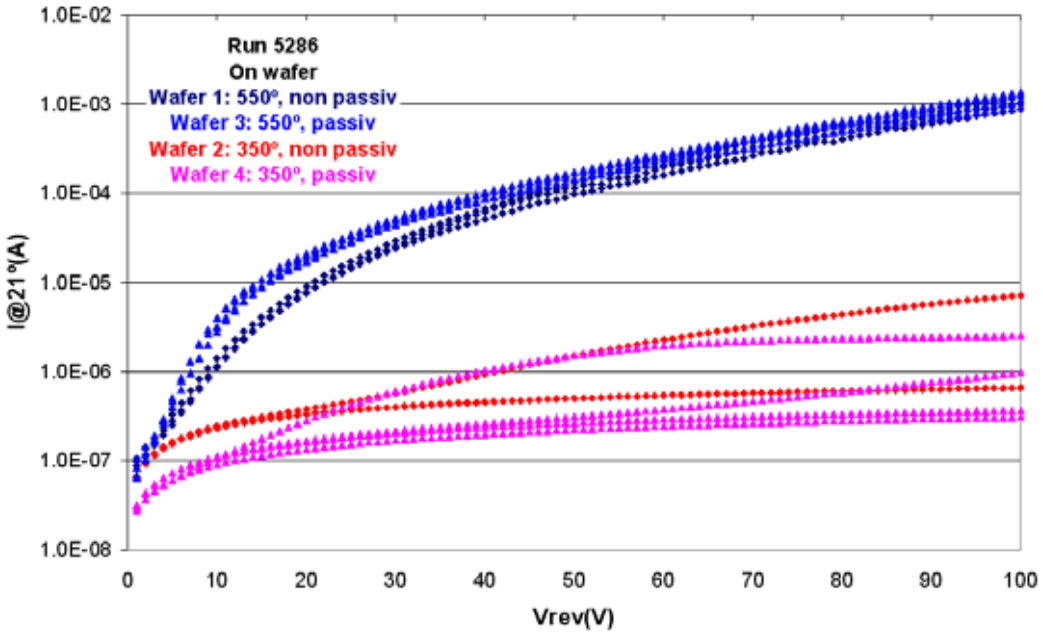

Figure 4.5: I–V curves for Schottky diodes - Current versus reverse voltage up to 100 V of some Schottky diodes measured for the manufactured wafers.

current at 10 and 100 V of the sensor in this wafer are indicated in Table 4.1.

Table 4.1: Average Current @10V and @100V for wafer #4.

Voltage (V)	Average Current (μA)	StdDev	Median (μA)
@10 V	-0.123	0.018	-0.127
@100 V	-0.414	0.056	-0.424

The full depletion voltage of the devices, obtained from capacitance-voltage measurements (see Figure 4.6), was (16±1) V. This corresponds to a doping of $2.6{\cdot}10^{11}$ cm^{-3} that is, a resistivity of 17 kΩ·cm for n–type wafers.

Thereafter, these devices were calibrated in energy with the setup presented in Appendix C.2. With this system, the detected signal by the surface barrier Si detector with no converter layer has a conversion factor of 1.5 V/MeV, a noise level of 40 keV (peak–to–peak) and a FWHM of 8.74 keV. Hence, the signal pulse that results from a 1.47 MeV alpha particle has a voltage amplitude of 2.2 V.

Finally, the Schottky diodes were adapted for neutron detection by spinning an

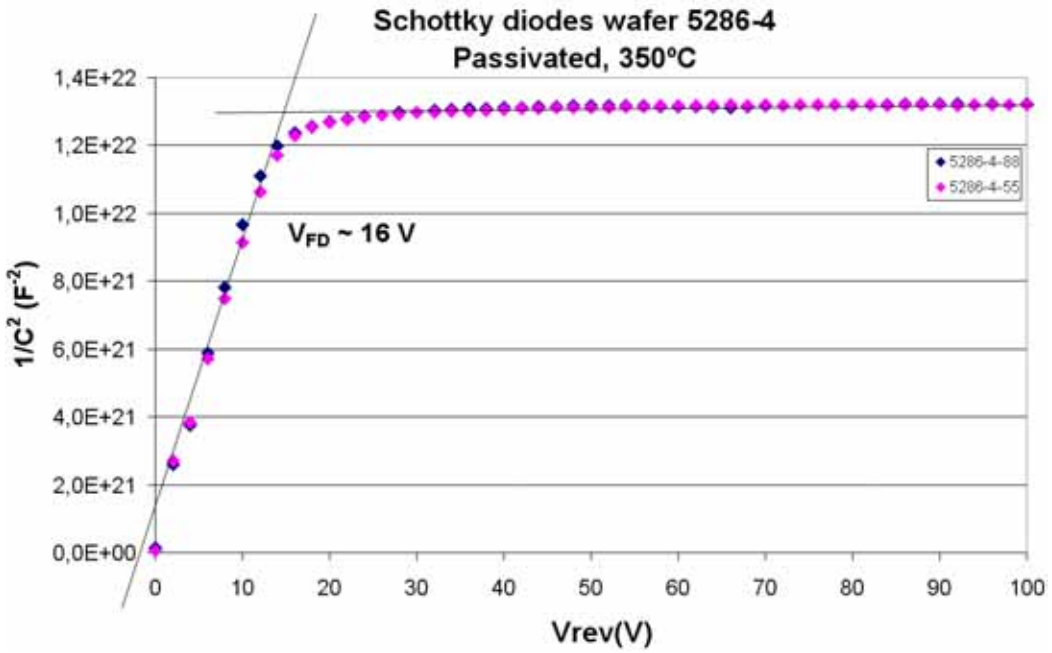

Figure 4.6: C–V curve for Schottky diodes - Capacitance versus reverse voltage up to 100 V for Schottky diodes. The full depletion voltage is 16 V.

o-carborane layer over their surface (see Appendix A.1). The optimum thickness of this o–carborane layer was obtained by Monte Carlo simulations, which are detailed in section 3.4. Thus, these devices were the first adapted detectors used in this work to try to detect neutrons emitted by an $^{241}AmBe$ source. The experimental results of these measurements are presented and discussed in section 5.1.2.

4.2 Ultra-thin 3D silicon detectors

In order to satisfy the requirements established at the end of section 3.4, it is necessary a new design with the following guidelines:

- The silicon thickness should be the minimum possible to ensure a good n/γ discrimination, i.e. the ideal active thickness should match exactly the range of the reaction products in silicon, on the order of few microns.

- It is should have an entrance window of a few hundred of nanometers. This might be led by means of two arrangements: (i) the metallic layer could be segmented

in strips that reduce the surface occupied between the converter and the silicon, and (ii) it could be used the '3D' technology carried out at IMB-CNM to develop columnar electrodes through the silicon bulk, in such a way that the planar p–n junction is avoided.

All these characteristics have been joined to lead a novel detector, the ultra–thin detector based on the 3D technology, that is detailed as follows.

First of all, in order to ensure a good neutron-gamma ray discrimination, a compromise in the active thickness of the sensor has to be found. As said above, ideally the active thickness should match the range of the reaction products in the material, on the order of few microns in silicon for the reactions listed in Table 2.4. However, in the usual parallel plate geometry for silicon detectors (i.e. they deplete vertically from the surface), such a low thickness comes usually at the expense of a high capacitance and therefore large electronic noise. In fact, the use of silicon sensors with thin active layers for neutron detection applications is already well known [108], [109], [110] but all these devices are based on a planar geometry and thus suffer from a high electrode–to–backplane capacitance that decreases the signal to noise ratio. In contrast, the ultra–thin 3D detector (U3DTHIN) is based on the new 3D architecture for solid–state radiation detectors proposed by Parker, Kenny and Segal [111] in 1997 and on the thin membrane fabrication process [112, 113]. The result of such combination is a novel detector with a thin sensitive volume with low capacitance and therefore with low electronic noise. The ultra–thin active volume allows for a high gamma-ray rejection, a key requirement in order to discriminate the signal coming from the neutrons in a mixed neutron-gamma ray environment.

In the next subsection the operating principle of the 3D technology for silicon detectors is first explained. Next their layout, fabrication process and characterization is detailed. Experimental results are detailed in sections 5.2 and 5.3.

4.2.1 3D architecture for silicon detectors

3D detectors have p– and n–type columnar electrodes which penetrate the sensitive silicon bulk instead of being implanted on the device surface like in planar structures [111]. Figure 4.7 displays this fact: the depletion region between the planar electrodes

(W_{2D}) grows vertically until the whole wafer thickness is depleted, whereas such region grows laterally as a cylinder between columnar electrodes (W_{3D}), i.e. the depletion region is independent of the substrate thickness and is instead proportional to the distance between electrodes [114].

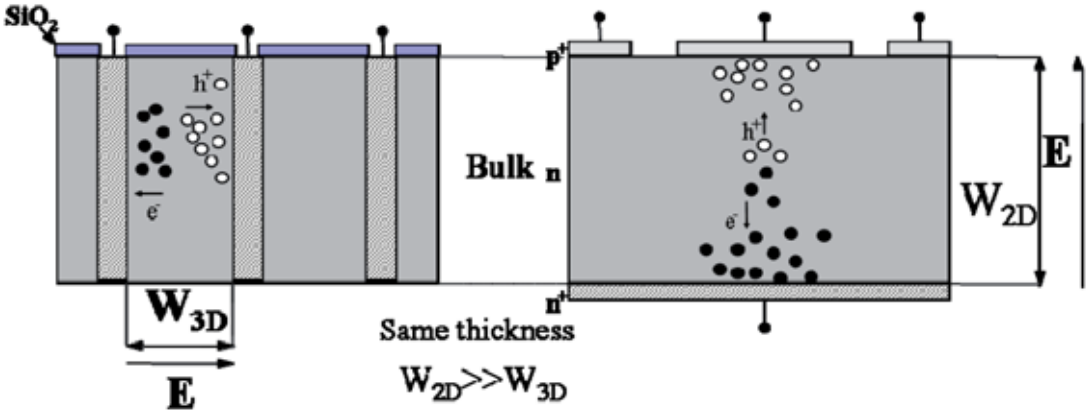

Figure 4.7: Cross sections of 3D and planar geometrics - Schematic cross section of the 3D (left) and planar (right) geometrics with same thickness (W): in the planar detector the electrodes are implanted on the top and bottom surfaces, whereas in the 3D detector the electrodes are etched as columns into the bulk.

Figures 4.8 and 4.9 show this design where a type of electrodes is connected to the readout electronics and other ones are used to bias the detector: when a particle goes through the device, it ionizes the sensitive semiconductor bulk generating electron–hole pairs that are swept horizontally to the neighboring electrodes.

Considering the approximation of a coaxial–cable capacitor, the associated capacitance of a columnar electrode can be written as:

$$C = 2\pi\varepsilon \frac{l}{ln(\frac{r_d}{r_c})} \tag{4.1}$$

being l the column length, r_d the radius of the depleted region, and r_c the radius of the columnar electrode. Whereas the capacitance for a planar detector, C=ϵ/d (equation 2.27), depends on the thickness of the sensor (d), the capacitance for a 3D columnar electrode depends only on the column length and radius and on the distance between columnar electrodes of different type. An extensive study about the simulations of the electric behaviour of these detectors can be found in [114].

3D detectors have the following advantages:

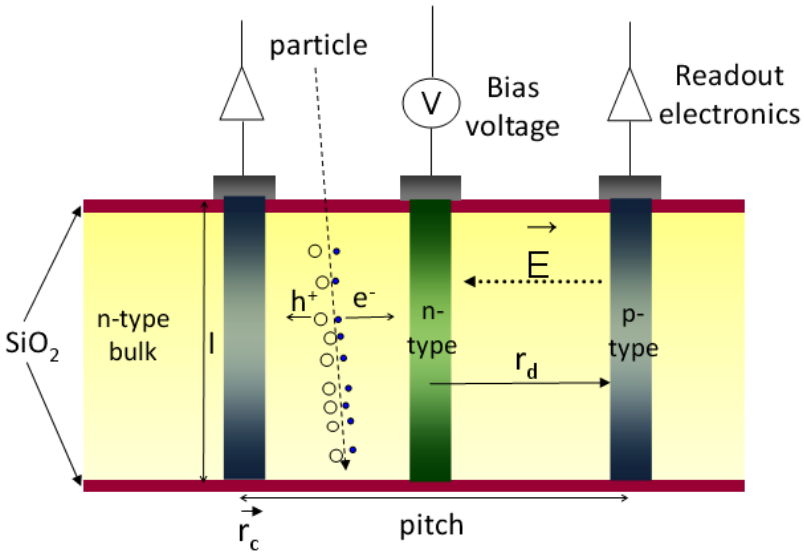

Figure 4.8: Schematic cross section of a 3D semiconductor detector - Sketch of the 3D architecture for solid–state detectors where the electrodes are columns p- and n-type passing vertically through the substrate bulk and they are connected out on the front surface. The SiO_2 grown creates decoupling capacitors between the electrodes and the metal contacts.

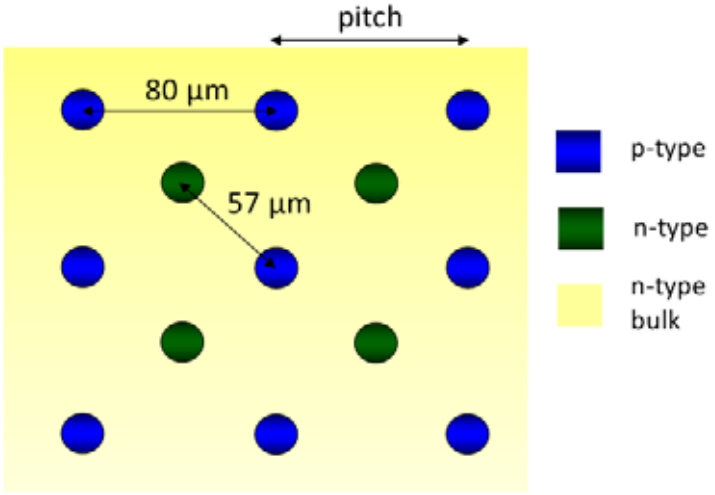

Figure 4.9: Front side 3D pattern - Layout of the 3D arrangement: the distance between columnar electrodes of the same type (pitch) is 80 μm and the p–n distance is 57 μm.

- The 3D detector structure achieves small electrode spacing without reducing the sensitive thickness.

- The depletion region is not determined by the substrate thickness, but by the electrode spacing.

- The capacitance depends only on distance between electrodes, not on wafer thickness. This is advantageous for manufacturing thin devices with low capacitance.

- They are extremely radiation hard: IMB–CNM's 3D detectors have been proven to work well for a fluence of $> 2{\cdot}10^{16}$ 1 MeV neutrons equivalent particles/cm^2[115].

- Thanks to the fast collection time the carriers diffuse less outwards and therefore the charge sharing between neighboring electrodes is negligible.

- They lead to smaller depletion voltage and collection time than standard planar detectors.

Nevertheless 3D detectors have two main disadvantages: (1) they are difficult to manufacture because the fabrication of the holes of the columnar electrodes requires delicate etching processes; (2) the electrode columns are an inactive volume inside the detector itself, and therefore they should be fabricated as narrow as possible. Both restrictions are related each to other since the aspect ratio (rate between the depth and diameter of holes) of the etching process is fixed. This fabrication process is not trivial and implies a technological challenge that is detailed in the section 4.2.3.

The Radiation Detector Group at IMB–CNM has developed their own 3D technology for the last years with significant progress [62], drawing on the work that Pellegrini started more than ten years ago [61].

[1]This value corresponds to the fluence expected for the inner pixel detector layers at the High-Luminosity LHC.

4.2.2 Ultra-thin 3D layouts

Figure 4.10 compares the capacitance of a standard silicon detector with that of the 3D structure (with 80μm pitch[1]), using the coaxial cable and parallel plate approximations above. For a silicon thickness of 10 μm and 80 μm pitch, the U3DTHIN capacitance is two orders of magnitude smaller than a planar silicon detector with the same thickness and surface area. Nevertheless, it is important to note that when the thickness increases, the capacitance increases to match the planar case. In this case (80 μm pitch), the U3DTHIN structure is advantageous for thicknesses lower than 50 μm. As said at the

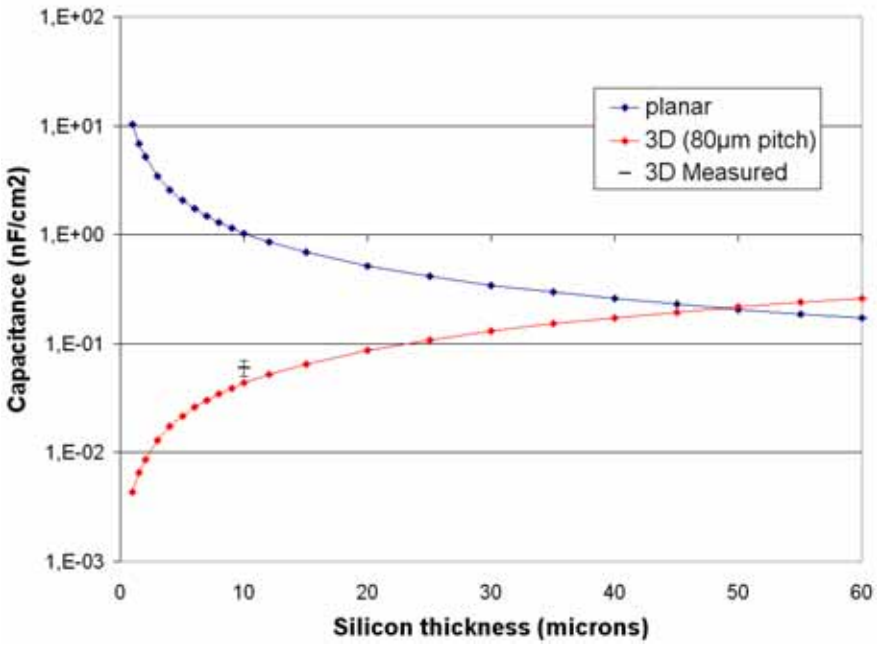

Figure 4.10: Capacitance of the 3D and planar detectors versus silicon thickness

beginning of the section, to detect neutrons in environments with a mixed n/γ field, it is necessary to have a silicon thickness as small as possible. Since the capacitance of 3D detectors does not depend on the substrate thickness, a 3D detector with an ultra–thin silicon thickness was proposed by IMB–CNM for such type of radiation environments. All the same time, following the requirements listed at the end of section 3.4.2, these detectors were manufactured with a thin entrance window to reduce the energy loss of the reactions products coming from the $^{10}B(\mathrm{n},\alpha)^{7}Li$ reaction.

[1]Value used in the detectors at the ATLAS Semiconductor Tracker (SCT) at CERN.

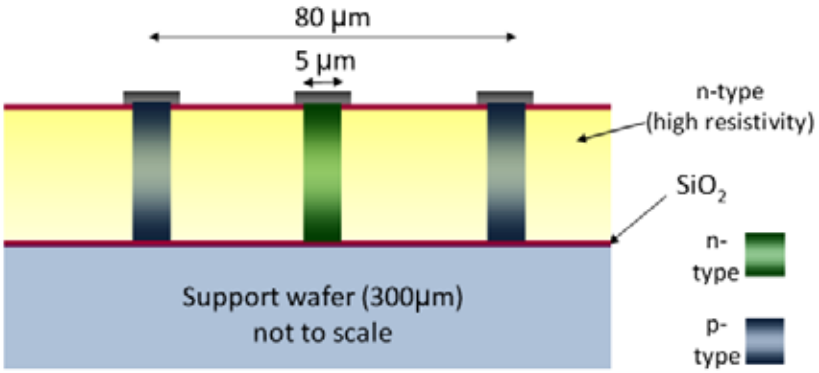

Figure 4.11: Cross-section of the ultra–thin 3D design. - Lateral layout of the U3DTHIN detector. The converter layer is not shown in the sketch, but this would be deposited over the detector front–side

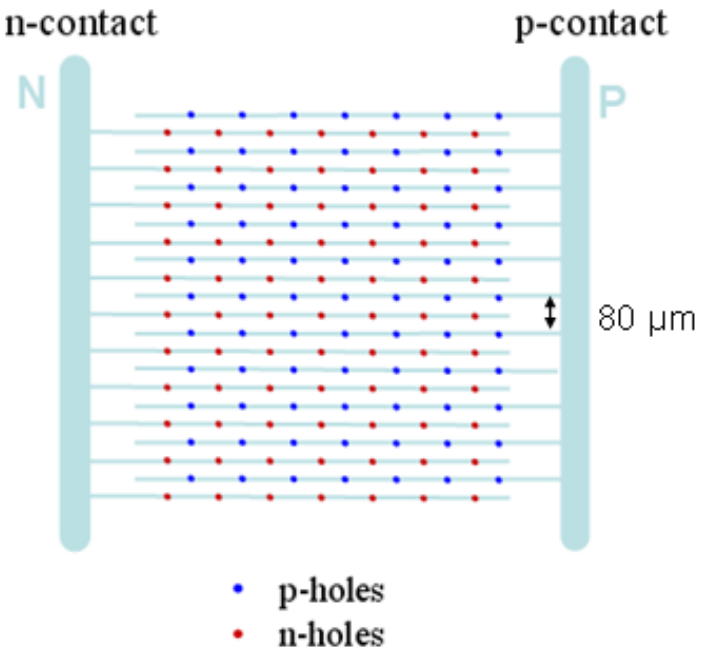

Figure 4.12: Schematic of the ultra–thin 3D detector front-side - Layout for the U3DTHIN where the electrodes/strips which connect the p–holes and n–holes with the p and n–contacts respectively are shown (this sketch is for a pad configuration, i.e. the strips are shorted to one electrode).

Figures 4.11 shows the layout of the U3DTHIN sensors manufactured for this work. They have an active thickness of only 10 or 20 μm. This ultra–thin 3D detector is fabricated on a Silicon–on–Insulator (SOI) n–type wafer with a 10 or 20 μm–thick Si layer and a 1 μm–thick buried silicon oxide layer over a 300 μm–thick silicon handle wafer (mechanical support[1]). Figure 4.12 displays the front–side of such layout where the same type of electrodes are connected together by metal lines for electrical contact.

Two designs of U3DTHIN detectors were manufactured, whose fabrication processes are specified in the next subsection:

1. Design–A: four wafers which had sensors of 4.8×4.8 mm^2 area and 10×10 mm^2 (Figure 4.13 a&b).

2. Design–B: eight wafers with sensors of 7.52×7.52 mm^2 area each one. This second batch implied substantial improvements with respect to the previous one: the detectors had a much thinner entrance window as they were specifically design for neutron detection. Also, the active/total area ratio was increased in this new design. Figure 4.14 displays the layout of the aluminium strips in the first design (a) and in the second one, (b). Details are given in the next section. This design contained four wafers of 10 μm–thick and 20 μm–thick.

The main features of these layouts are summarized in Table 4.2.

Table 4.2: Layout features of the ultra-thin 3D detectors.

Design–A	**Design–B**
59/128 strips 4.8×4.8 mm^2 and 10×10 mm^2 area	92 strips 7.52×7.52 mm^2
80 μm pitch distance 5 μm hole diameter DC coupled	

[1]This support can be removed using chemical solutions which stop at the silicon oxide interface of the SOI wafer. These 'membrane' sensors could be used to measurements with high energy particles, e.g. for particle therapy, in order to avoid backscattering contributions (see Appendix D.1)

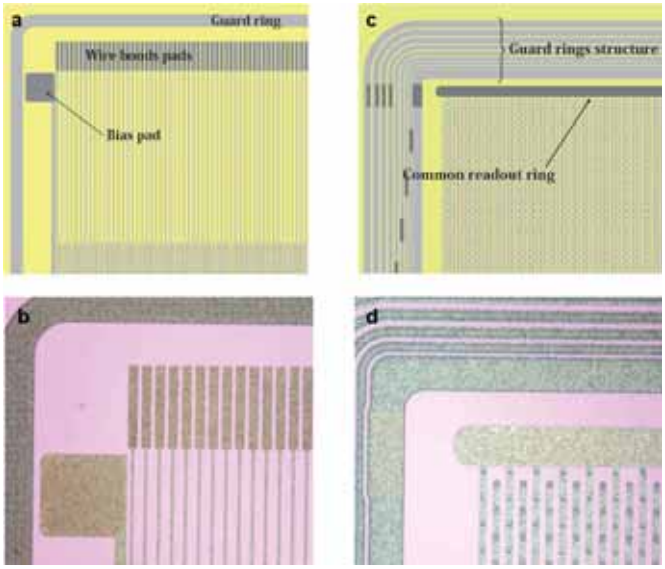

Figure 4.13: Microscope images of the first ultra-thin 3D detectors - Layout and pictures with optical microscope corresponding to the design–A (a and b) and design–B (c and d) configurations. The guard-structure surrounding the detector stops currents from the edge and defines the limit of the active area of the detector, guaranteeing a defined homogeneous potential within the detector. These guard-structures are implanted rings of the same doping type as the readout electrodes.

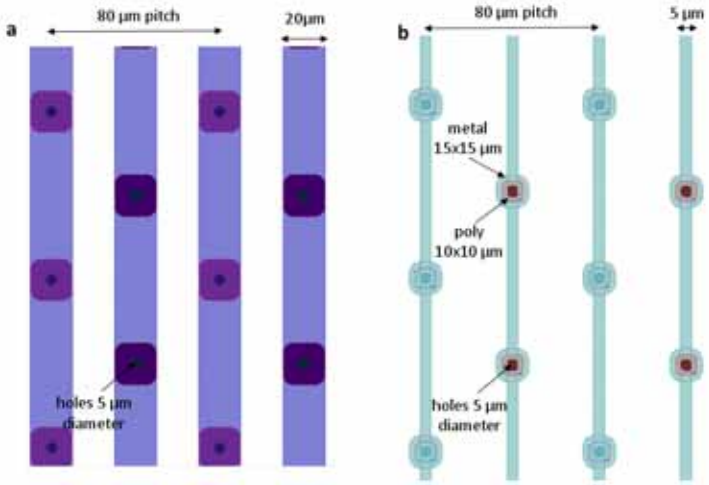

Figure 4.14: Improvement of the ultra-thin 3D designs - (a) Electrode design of A. (b) Improved design–B: the metal strips are narrowed from 20 to 5 μm width in order to have as much active area as possible (area covered by metal is considered not active as the metal thickness is 1 μm for design–A and 500 nm for design–B, although in this case some low energy signals can still be collected).

4.2.3 Fabrication process of ultra-thin 3D detectors

Previously to introduce the full fabrication process, it is worth describing in detail the biggest technological challenge: the hole etching.

Hole etching

The etching process allows to remove material selectively using imaged photoresist as a masking template. Plasma (dry) etching involves the generation of chemically reactive neutrals (e.g. F, Cl) and ions (e.g. SF_x^+) that are accelerated under the effect of an electric field toward a target substrate. The reactive species are formed by the collision of such molecules in a reactant gas (e.g. SF_6, CF_4, Cl_2). If the ion bombardment of the silicon surface plays a synergistic role in the chemical etch reaction, the process is called reactive ion etching (RIE). In RIE, the ion SF_x^+ motion is nearly vertical. In order to get vertically high–aspect–ratio trenches (Deep RIE, i.e. DRIE), the traditional plasma etching is combined sequentially with cycles of passivation. Figure 4.15 shows such cycle: (a) the gas for silicon etching is SF_6, which has both vertical and isotropic character; (b) C_4F_8 gas depositions create the passivation layer; (c) the next etching step removes the protective polymer at the bottom of the trench, while part of the polymer remains intact along the sidewalls, preventing the lateral etching. This time–multiplexed alternating process results in a very directional etching. Figure 4.16 displays the aspect ratio at several etching times created by a Deep Reactive Ion Etching–Inductively Coupled Plasma (DRIE–ICP) using Alcatel–601E machine located at IMB–CNM clean room facilities.

Fabrication process

All the wafers used for the fabrication process were SOI wafers of 10 μm or 20 μm thickness of high resistivity n-type active silicon (ρ>1 kΩ·cm) and a 1 μm–thick buried silicon oxide layer over a 300 μm–thick silicon handle wafer. In short: first, one type of columnar electrodes are patterned in a square geometry with 80 μm pitch, following the arrangement shown in Figure 4.14. Then, they are etched by DRIE–ICP following the procedure described above. Next, the columns are partially filled with polysilicon and doped with boron (p^+) or phosphorous (n^+) to form the p–n junction and the ohmic contact respectively, and are passivated with a thin oxide layer. These steps are

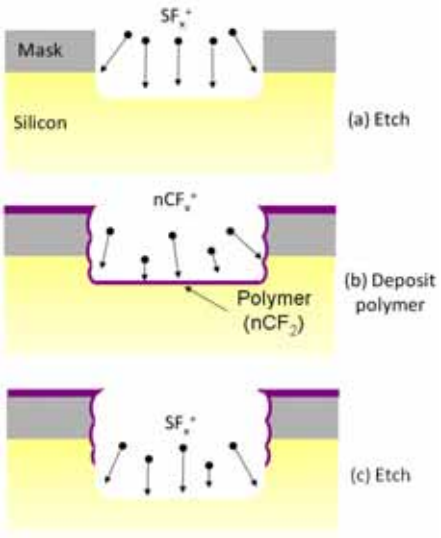

Figure 4.15: Steps of a DRIE etching of a trench.

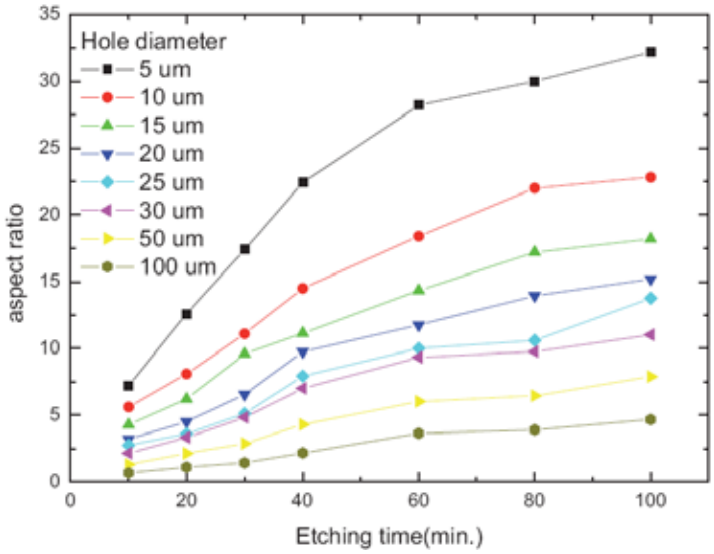

Figure 4.16: Aspect ratio for hole as a function of the etching time - Aspect ratio for several hole diameters as a function of the etching time with an ALCATEL–601E machine located in IMB–CNM Clean Room facilities [116].

repeated for the other type of electrodes. Finally, the p^+ and n^+ columnar electrodes of the same type are connected together using aluminium strips to provide the electrical contact. The whole fabrication process consists of 76 CMOS-steps [105], and the main stages are shown in Figures 4.17—4.20, using the masks display in Fig. 4.21.

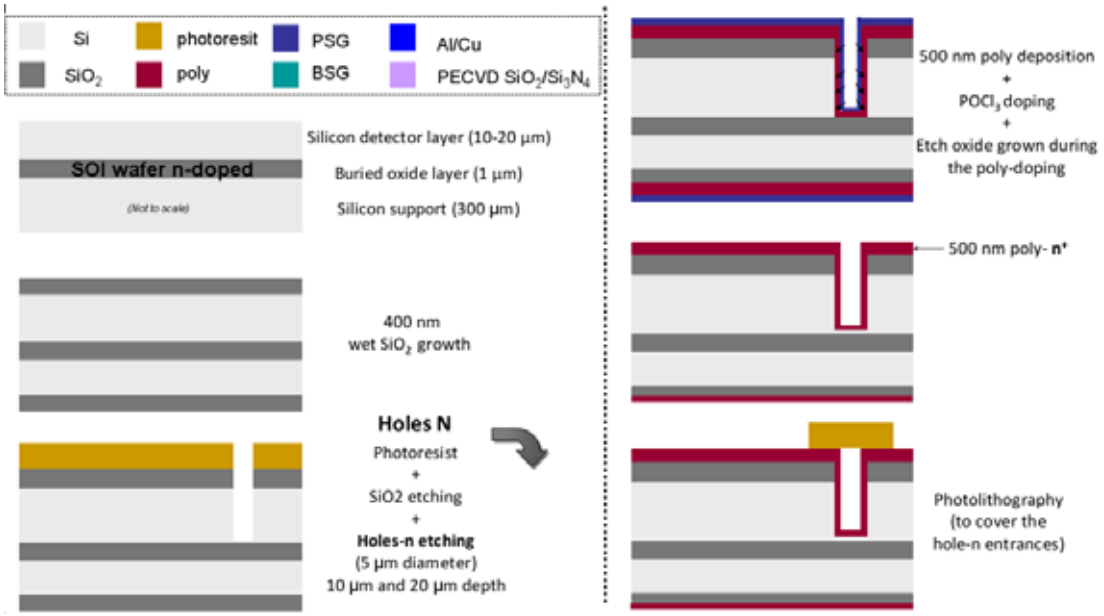

Figure 4.17: Fabrication process of the U3DTHIN: Holes N -

Figure 4.22 shows a front view of a manufactured wafer of the U3DTHIN design–B. Details of the detector top pattern are shown in Figure 4.23. Figure 4.24 and 4.25 contain SEM images of an U3DTHIN where the dimensions of its components are shown. Tables 4.3 and 4.4 summarize the percentages that each material takes up over the total area for each design: (i) the metal strips in the new design occupy a 6.24% instead of 37.5% of the area with less than the half the layer thickness; (ii) the thickness of the field oxide layer and metal around the holes have been reduced by more than half; (iii) the hole area has been reduced to a sixth.

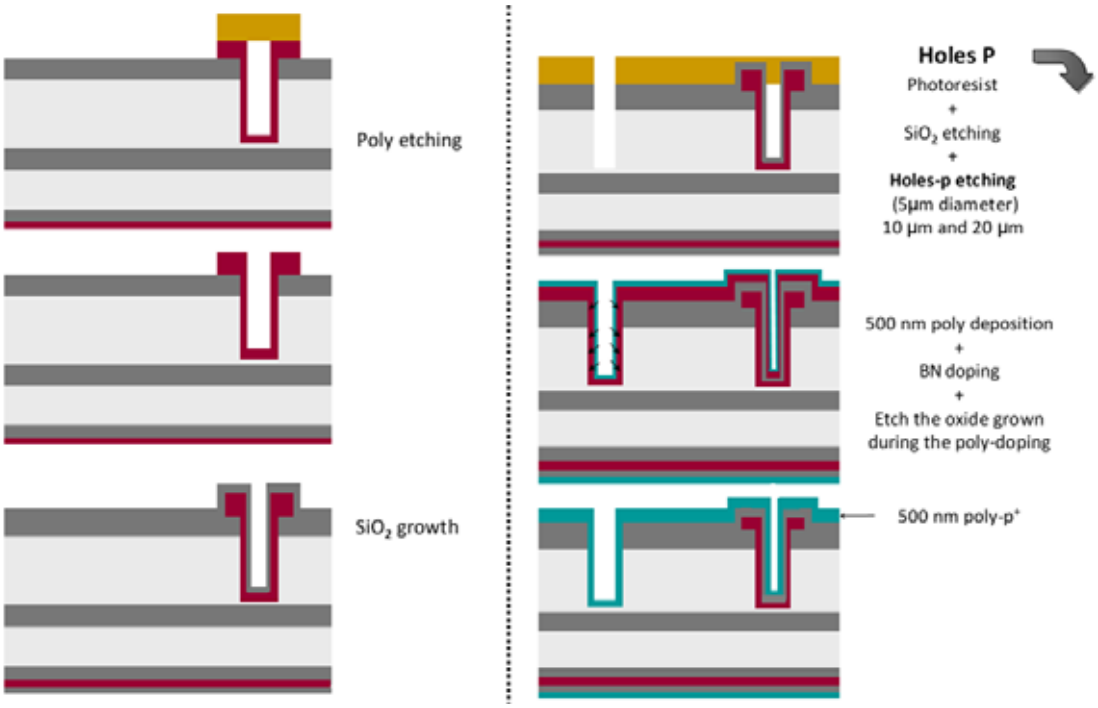

Figure 4.18: Fabrication process of the U3DTHIN: Holes P -

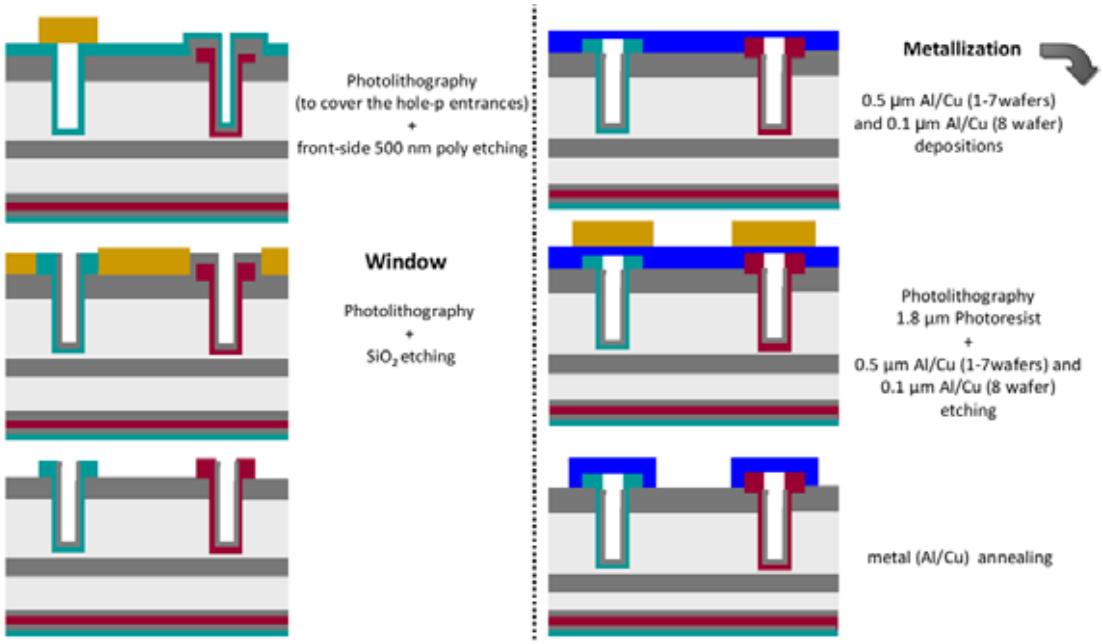

Figure 4.19: Fabrication process of the U3DTHIN: Metallization -

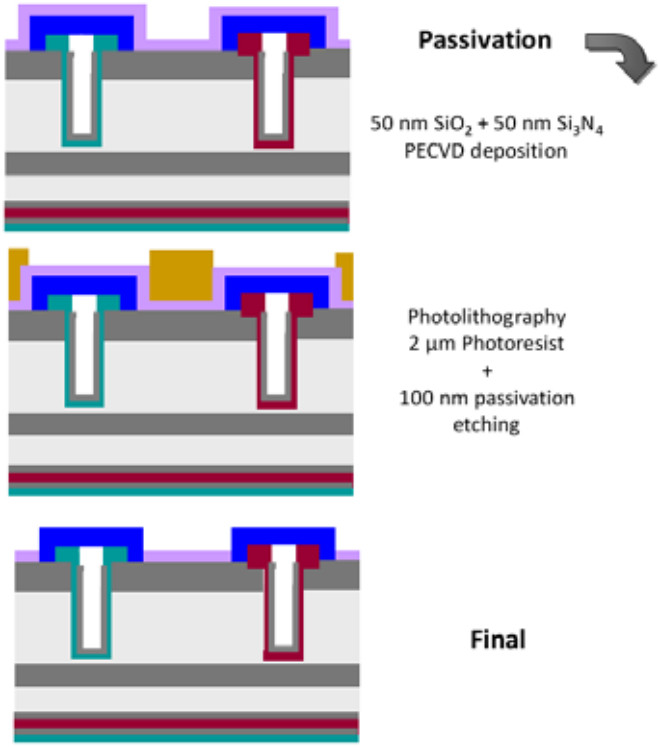

Figure 4.20: Fabrication process of the U3DTHIN: Passivation -

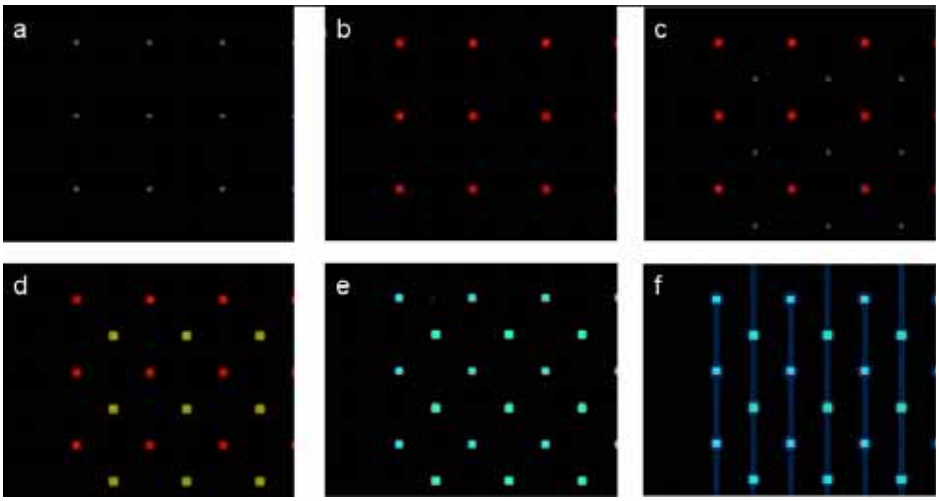

Figure 4.21: Pattern masks used for the U3DTHIN fabrication process - (a) Holes-n. (b) Poly-n. (c) Holes-p. (d) Poly-p. (e) Window. (f) Metallization.

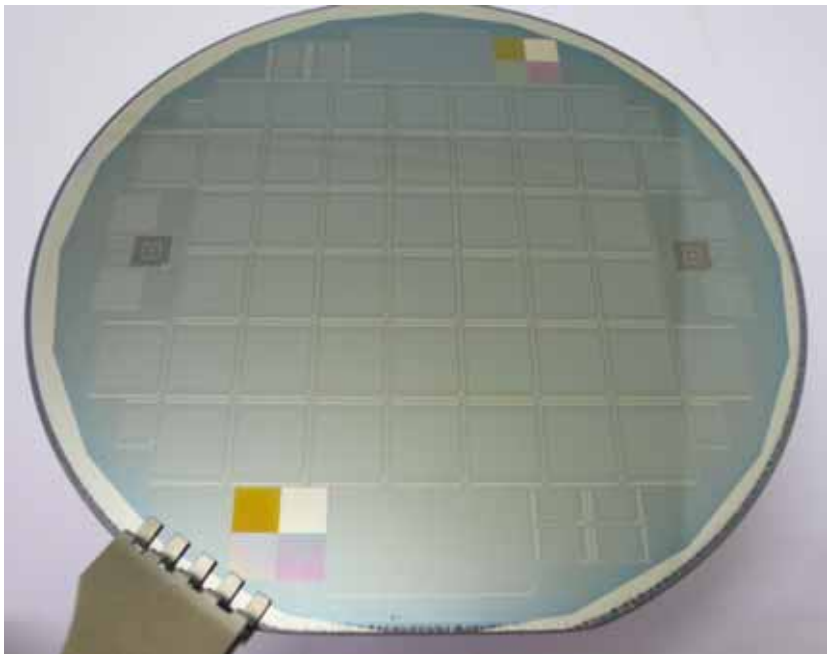

Figure 4.22: Photograph of manufactured wafer with ultra-thin 3D detectors - The central area contains an array of 46 7×7 mm^2 ultra-thin 3D detectors.

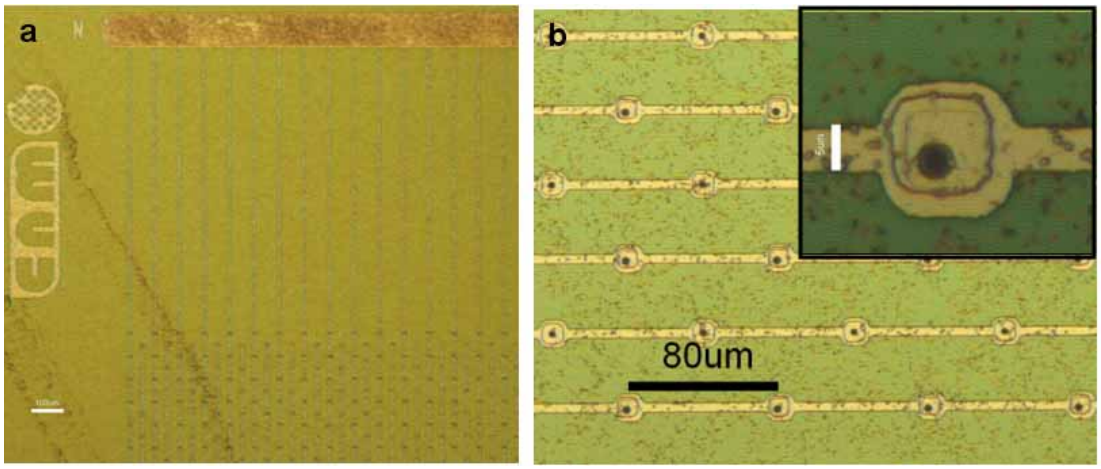

Figure 4.23: Optical microscope images of an ultra-thin 3D detector - Images of different areas of the front side of one U3DTHIN: (a) zone of n-contact. (b) active area with the connected electrodes and zoom of a hole.

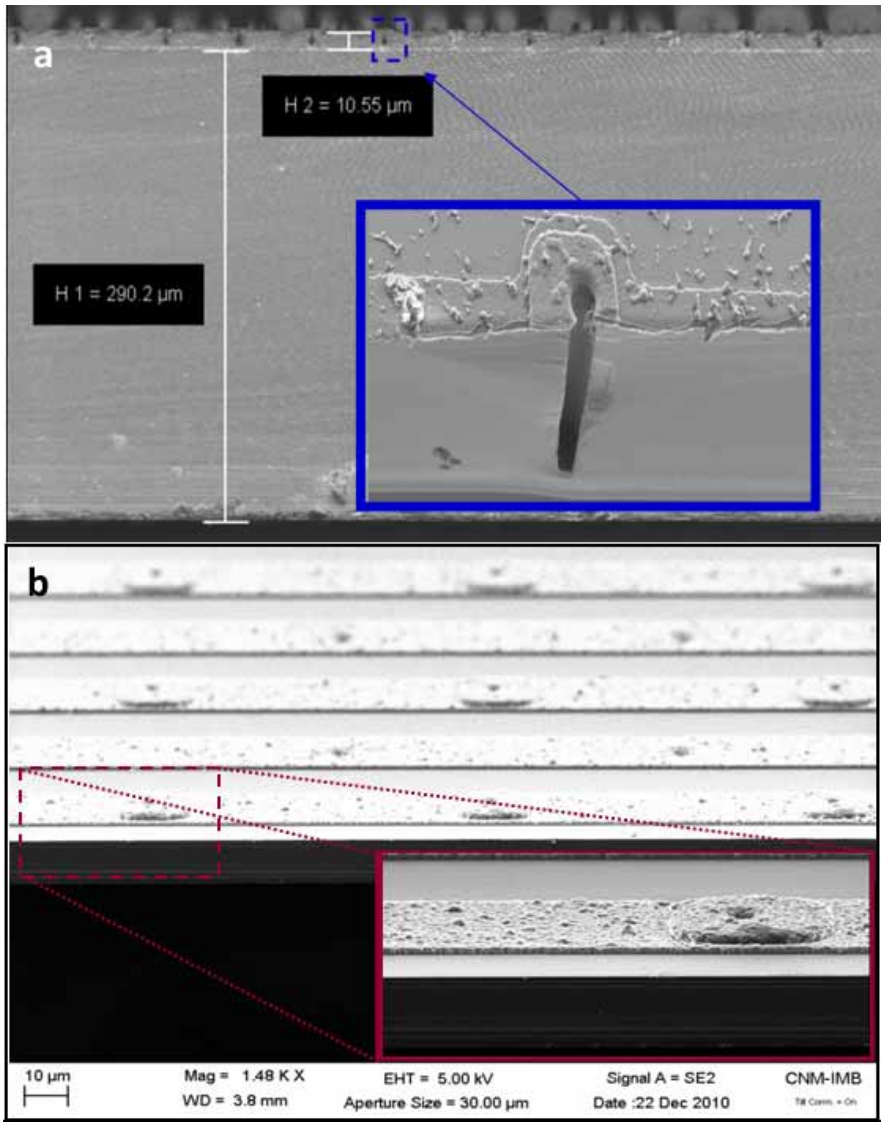

Figure 4.24: SEM images of the cross-section of the U3DTHIN detector - (a) cross-section of 290 μm-thick support wafer and the $\sim$10 μm-thick high resistivity n-type active silicon with the columnar electrodes distributed along the top surface. (b) view of the front–face with the metal strips that connect the columnar electrodes of the same type.

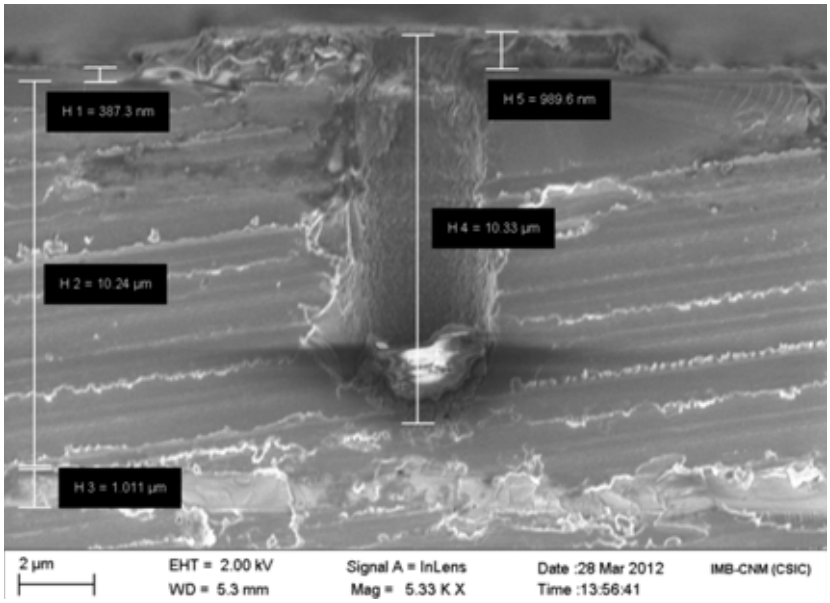

Figure 4.25: SEM image of the columnar electrodes of the U3DTHIN detector - Detail of a hole that forms a columnar electrode (from the bottom up): ∼1 μm-thick buried silicon oxide layer, ∼10 μm–thick high resistivity n-type active silicon, ∼400 nm field oxide, ∼10 μm-thick hole, and ∼1 μm–thick aluminium metal plus polysilicon.

4.2.4 Characterization of ultra-thin 3D detectors

The electrical characterization of all the ultra-thin 3D detectors was carried out as is explained in Appendix C.1. Figures 4.26 and 4.27 show the I–V and C–V characteristics of U3DTHIN design–B detectors for one representative wafer. Summarizing:

1. Design–A: leakage currents < 10 nA/cm^2 and capacitances around ∼10 pF/cm^2 at 10 V (lateral depletion voltage achieved at 5 V).

2. Design–B: leakage currents of 70±10 nA/cm^2 and capacitances of 70±10 pF/cm^2 at 10 V (lateral depletion voltage is 5 V).

Figure 4.28 shows two photographs of the as-fabricated ultra–thin 3D detectors diced and attached to PCBs without depositing the converter layers. The remaining step, the deposit of boron–based compounds is carried out according to the values obtained in the Monte Carlo simulations as is explained in section 3.4. The methods used are detailed in Appendix A. The experimental results with neutron sources are presented in sections 5.2 and 5.3 for design–B and –A respectively.

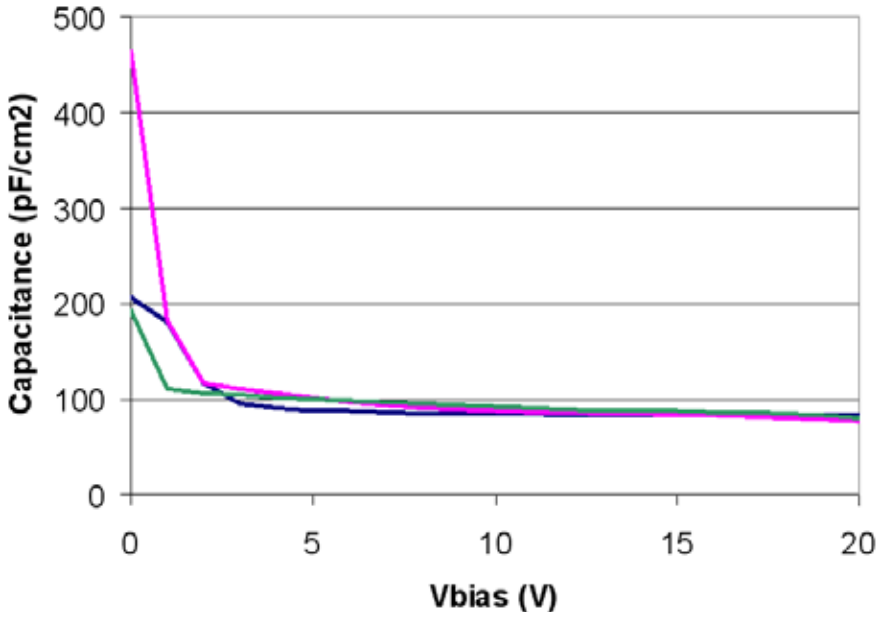

Figure 4.26: I–V curves of ultra-thin 3D detectors - .

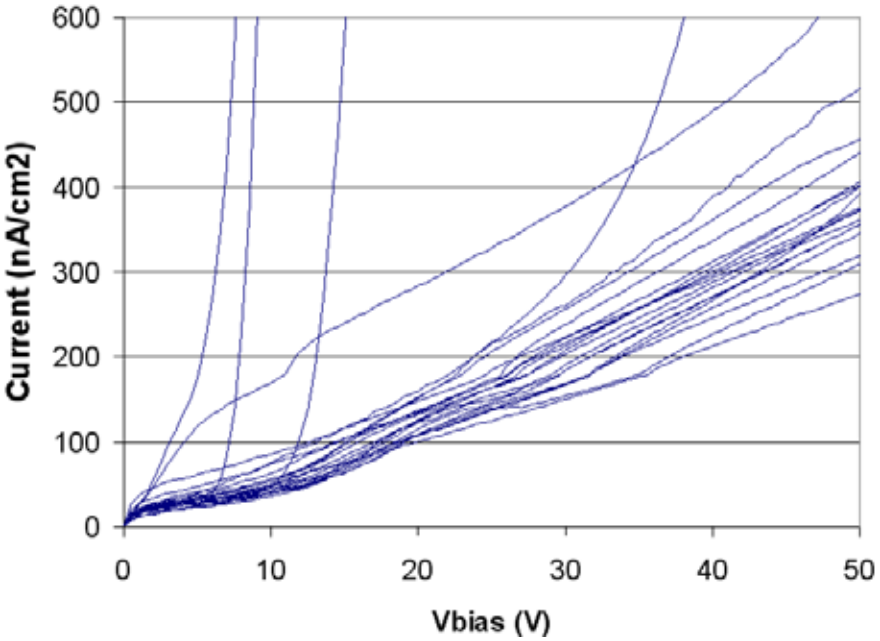

Figure 4.27: C–V curves of ultra-thin 3D detectors - .

Table 4.3: Characteristics of the U3DTHIN design-A.

Zone	**% of area**	**Area (mm^2)**	**Layers**
field oxide (active zone)	50%	50	≈1μm SiO_2
metal strips	37.5%	37.5	1μm SiO_2 1μm Al/(0.5%)Cu
metal&poly*	10%	10	1μm SiO_2 1μm poly 1μm Al/(0.5%)Cu
Holes (inactive zone)	2.5%	2.5	ø

Table 4.4: Characteristics of the U3DTHIN design-B.

Zone	**% of total area**	**Area (mm^2)**	**Layers**
field oxide (active zone)	92.2%	52.14	400nm SiO_2
metal strips	6.24	3.53	400nm SiO_2 500 nm Al/(0.5%)Cu
metal, poly	1.17%	0.66	400nm SiO_2 500 nm poly 500 nm Al
Holes (inactive zone)	0.39%	0.22	ø

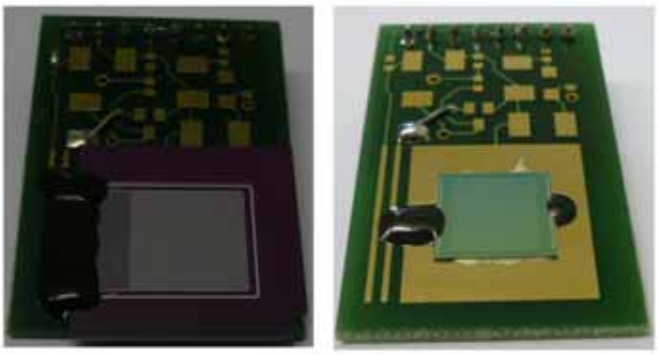

Figure 4.28: Photographs of two U3DTHIN detectors on PCB - Photographs of ultra–thin 3D detectors of the design–A (left) and design–B (right) stuck to a board with silver lacquer in their backsides. Detectors have 25 μm-thick wires from metal electrodes of the detector to the PCB for readout (Appendix B).

5

Experimental validation of the silicon neutron detectors

In this chapter the experiments performed in n-γ radiation fields with the silicon detectors developed in Chapter 4 are presented. Initially, two preliminary tests were carried out: the first one is a proof–of–concept to demonstrate that with silicon planar devices manufactured in IMB–CNM neutron detection is viable; the second test was carried out with Schottky barrier silicon diodes with thin entrance window covered with a new boron–based converter, o–carborane, to test the performance of this compound. Third, the ultra–thin 3D detectors proposed as novel silicon detectors and covered by different test converter layers are tested with a ^{137}Cs γ–ray source, an $^{241}AmBe$ neutron source, and with a thermal neutron beam generated in a nuclear reactor. Fourth, these detectors are covered with coatings of $^{10}B_4C$ and ^{10}B, which supposed two additional technical challenges, to be tested in a radiotherapy treatment room, main objective of this thesis.

The results obtained herein have been published in [117, 118, 119]

5.1 Preliminary tests

5.1.1 Proof–of–concept with planar PIN diodes

A preliminary test with silicon detectors covered with neutron moderators/converters was carried out in the laboratory of the Radiation Physics Group of the Universitat Autònoma de Barcelona (UAB) with an $^{241}AmBe$ neutron source. Figure 5.1 displays the neutron flux in terms of lethargy[1] of this source.

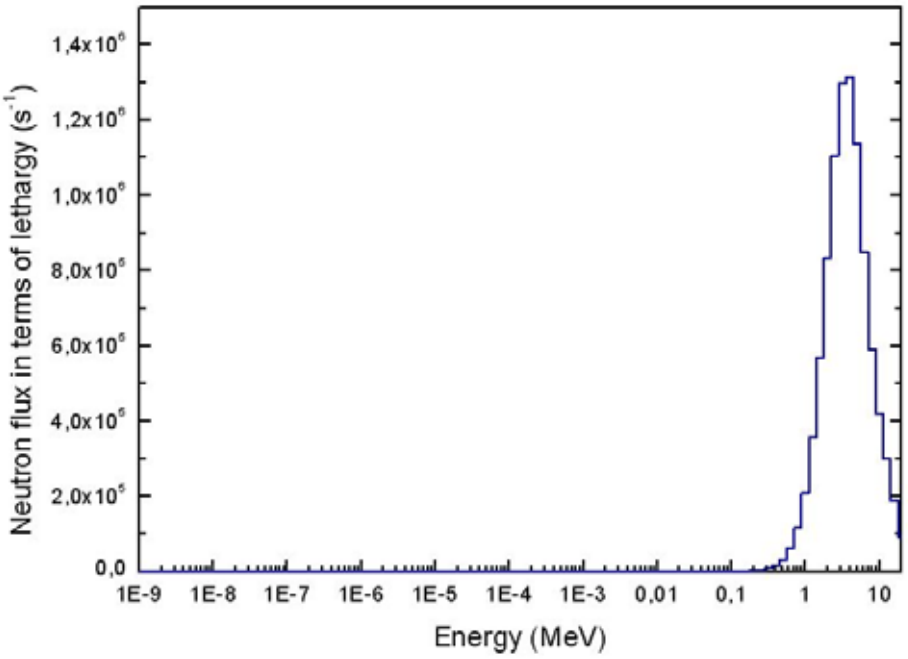

Figure 5.1: Neutron spectrum from a $^{241}AmBe$ source - Neutron flux in terms of lethargy versus neutron energy for the $^{241}AmBe$ source located in UAB.

The devices were standard planar 300 μm thick silicon PIN pad detectors like the shown in Figure 4.1 with an area of $5 \times 5\ mm^2$ covered with layers of nylon, makrofol[2], and polythene, as Figure 5.2 shows. These layers are commonly used in CR–39 fast

[1]The lethargy is the logarithm of neutron kinetic energy, defined as u=ln(E_{ref}/E), where the choice of E_{ref} is arbitrary.

[2]Makrofol-ED polycarbonate.

neutrons dosemeter [104]. The layer of polyethylene and makrofol, which are hydrogen–rich materials, were used to moderate the fast neutrons from the source through the elastic reaction n + p → n + p, generating protons with several energies, and a layer of nylon was used to capture the slow neutrons. Nylon contains nitrogen that produces the following reaction:

$$^{14}N + n \rightarrow ^{14}C + p(620keV)$$

So in this case the signal in the silicon is produced by protons. Table 5.1 shows the characteristics of both moderator and converter films.

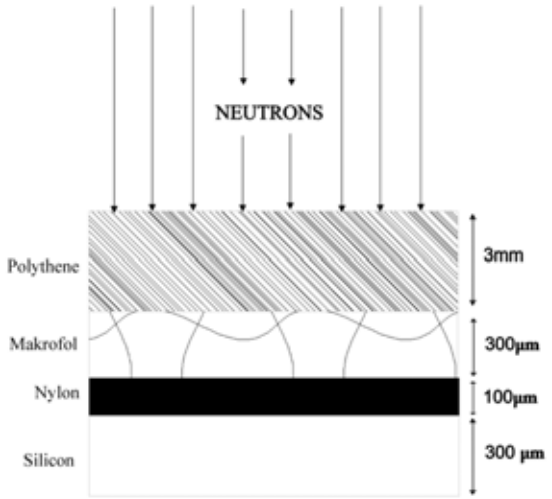

Figure 5.2: Silicon PIN pad covered by moderation/conversion layers - Sketch of a silicon pad detector covered with polyethylene (moderator) and nylon (converter) layers.

Table 5.1: Moderator and converter characteristics

Layer	Isotopic composition	Density (g/cm^3)	Thickness
Polyethylene	H4 C2	0.94	3 mm
Makrofol	H14 C16 O3	1.2	300 μm
Nylon	H11 C6 N1 O1	1.13	100 μm

Figure 5.3 displays a schematic of the setup used which contains the silicon PIN diode with the moderator/converter layers (SS detector) inside a metal box. The diode is connected to an electronic reading system that consists of a charge sensitive

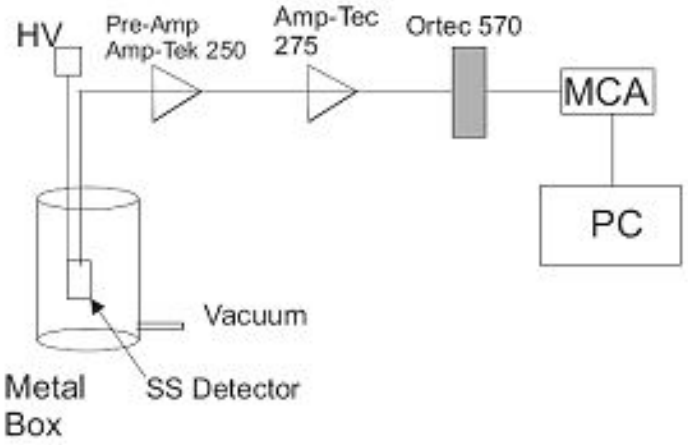

Figure 5.3: Diagram of the first experimental setup - Simplified sketch of the setup made up to carry out the first preliminary neutron tests with a silicon diode.

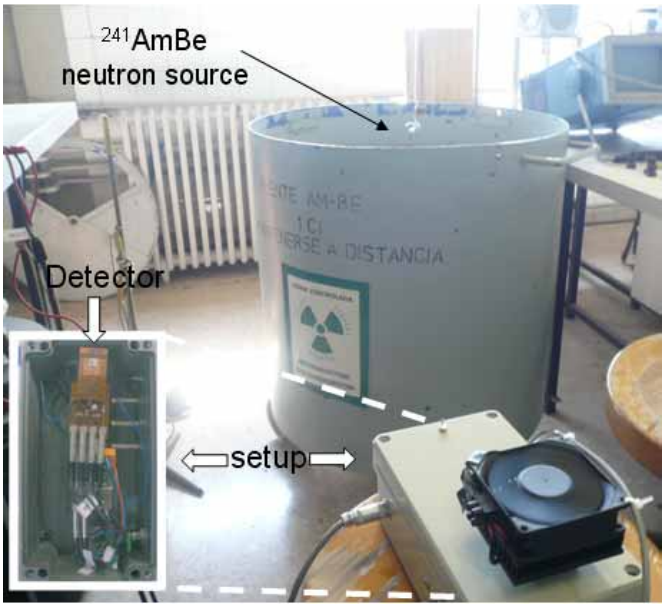

Figure 5.4: Experimental test configuration - The photo displays the $^{241}AmBe$ source with 1 Ci activity at 1 m distance of the setup. The metal box contains the detector connected to an electronic reading system.

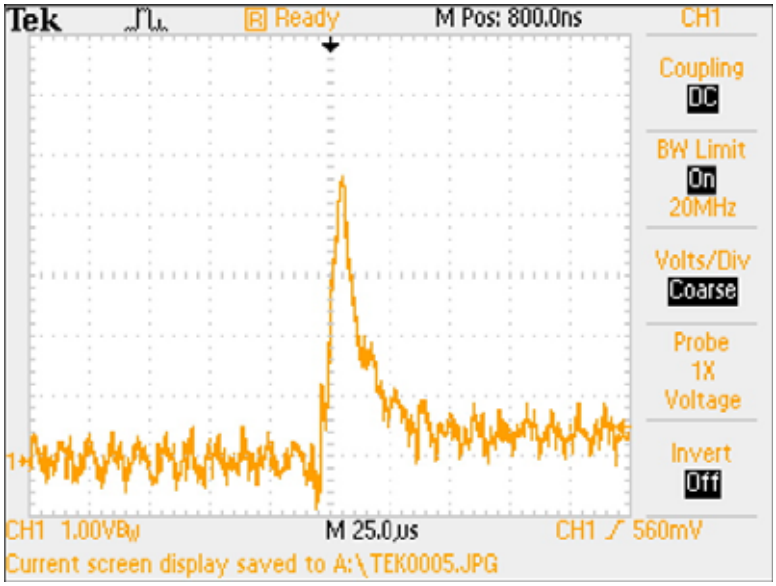

Figure 5.5: Oscilloscope signal for the preliminary experiment with $^{241}AmBe$ - Oscilloscope signal of the charged particles (protons) produced after neutron capture inside the nylon.

preamplifier (Pre–Amp Amp–Tek250) and a pulse amplifier (Amp–Tek275), combined with a computer–controlled multichannel pulse–height analyzer (MCA) (see Appendix B.1). Figure 5.4 shows the experimental test configuration: The $^{241}AmBe$ source was located at 1 m distance of the detector. Figure 5.5 displays the signal (as seen in an oscilloscope) coming from the experimental setup when a measurement is carried out. The signal corresponds to the voltage pulse produced by a proton.

5.1.2 Neutron detection with Schottky diodes

Schottky surface barrier silicon detectors (explained in section 4.1.2) were used to test the first converter layers synthesized in this work, carboranes (see Appendix A.1). The Schottky diodes were 300 μm thick with an active area of 5×5 mm^2 and were adapted for neutron detection by spinning a carborane layer over their surface. For these tests an o–carborane ($C_2B_{10}H_{12}$) was dissolved in a PVC matrix (81.9% and 18.11% mass fractions, respectively), within tetrahydrofuran (THF). This dilution was chosen because of its high boron concentration and low density. The THF is volatile and evaporates easily, leaving an adhesive matrix of PVC and o–carborane with a

measured density of 0.5 g/cm^3. As indicated in Table 2.6, the range of the neutron reaction products created inside the o–carborane/PVC matrix is higher than in the ^{10}B powder (2.46 g/cm^3) for the reasons argued in subsection 2.4.3.1. At the same time this compound is low cost, adaptable, and compatible with silicon devices. Furthermore, it can be easily deposited on whole wafers. The dilution was deposited onto the surface of the devices and spun at 800 rpm during 5 minutes (see Figure 5.6, as it is explained in Appendix A.1. After the evaporation of the THF, adhesive films with thickness of 20 μm were obtained (according to the MC simulation results presented in section 3.4).

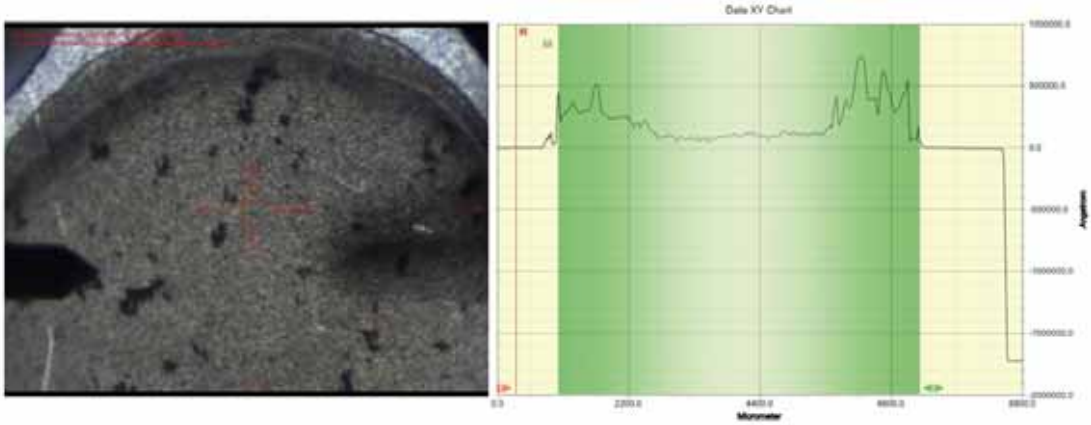

Figure 5.6: Deposit of O-carboranes - Left: Photo of the o-carborane coating deposited over the Schottky diode by spinning. Right: Measurement of the thickness with a Dektak-150 profiler.

The electronic setup used for the readout of the detector signals consists of a charge sensitive preamplifier Amptek–250 with an external FET, a pulse amplifier Amptek–275 and an Ortec–570 amplifier with 2.5 μs shaping time combined with a computer-controlled multichannel pulse–height analyzer MCA8000A (see Figure 5.3 and Appendix B.2). With this setup, the signal detected by the surface barrier Si detector with no converter layer has a conversion factor of 1.5 V/MeV and a noise level of 40 keV. Hence, the signal pulse that results from a 1.47 MeV alpha particle has a voltage amplitude of 2.2 V [120].

The neutron source used to test the detectors was the $^{241}AmBe$ source of the UAB facility. As said above (Figure 5.1), this source has a neutron spectrum covering a wide range at high–energies (from 100 keV up to 12 MeV). Therefore, the neutrons emitted by this source should be thermalized in order to produce a maximal thermal

neutron flux and therefore to test the performance of the boron converter. For this purpose, the detector was placed inside a cylindrical polyethylene (PE) block used as a neutron moderator. In order to optimize the full thickness of the moderator, MCNPX simulations were performed to study the variation of the moderated inner spectrum considering different diameters for the PE cylinder. PE was defined as CH_2, with 0.92 g/cm^3 density, and the MCNPX–supplied S(α,β) scattering law data[1] were included in the simulations. The flux averaged over the detector surface, tally F2 (Table 3.3), was calculated to assess the optimum geometry of the moderator. The results obtained are given in Fig. 5.7 and summarized in Table 5.2. According to these simulations, the highest flux for thermal neutrons occurs at a polyethylene depth $\geq$10 cm. This is in agreement with previous reports for similar moderator configurations [121, 122, 123]. However, due to the practical question of the moderator weight and that at high depth within polyethylene absorption of the thermal neutrons becomes much more important, a cylindrical polyethylene block of 10 cm radius is considered optimal. It is worth noting that despite the moderation of the PE block the spectrum continues to have a high ratio (around 80%) of fast neutrons that may contribute significantly to the detector signal. Hence, the devices were exposed to moderated

Table 5.2: Moderation effect of the neutrons emitted from an $^{241}AmBe$ source within polyethylene cylinder.

Polyethylene radius (cm)	**Thermal** E≤0.5 eV	**Intermediate** 0.5 eV≤E≤10 keV	**Fast** 10 keV≤E≤20 MeV	n_t/n_i × 100%
2.5	2.5%±0.1%	5.1%±0.2%	92.4%±1.3%	30.0%±0.3%
5.0	12.1%±0.3%	6.2%±0.2%	81.7%±1.2%	34.8%±0.4%
10	15.9%±0.4%	6.0%±0.2%	78.1%±1.1%	36.5%±0.4%
15	16.0%±0.4%	6.0%±0.2%	78.0%±1.1%	36.6%±0.4%
20	16.1%±0.4%	6.0%±0.2%	77.9%±1.1%	36.6%±0.4%
30	16.1%±0.4%	6.0%±0.2%	77.9%±1.1%	36.6%±0.4%

n_t/n_i is the quotient of the transmitted and incident neutrons.

neutrons from an $^{241}AmBe$ neutron source with a total emission rate of $2{\cdot}10^6$ n/s and the spectrum shown in Figure 5.7. Figure 5.8 shows the experimental setup used in

[1] S(α,β) is a model more accurately for the scattering of low energy neutrons from bound nuclei [81].

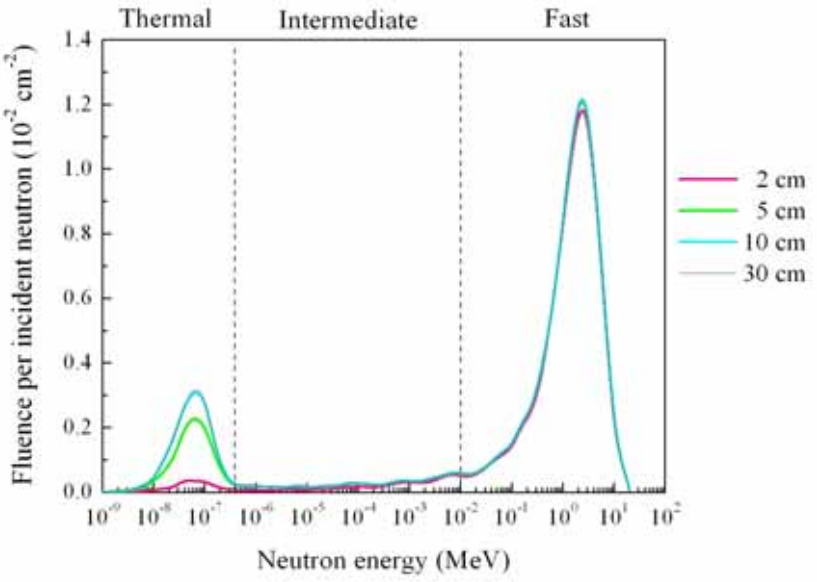

Figure 5.7: Fluence of moderated neutrons within polyethylene - Moderation effect of the incident neutrons within a polyethylene cylindrical block as a function of its radius.

this work. It consisted of a cylindrical polyethylene block with 10 cm radius containing an aluminium box with the detector and the front–end electronics. This was placed in front of the $^{241}AmBe$ source, at less than 1 cm of distance, and the measurements were carried out in a closed environment. The devices tested were a silicon detector with a 20 μm o–carborane/PVC (with natural boron) layer and a similar detector without any converter material. Both were biased to 0, 5, 20 and 40 V in order to test the dependence of the signal with the bias voltage and hence the depleted volume (full depletion voltage of these sensors is 16 V). The measurement time was 20 minutes for each setting. The spectral shape obtained is defined as can be seen in Fig. 5.9, which displays the pulse height distribution measured with the detector with o–carborane at 40 V. By applying an energy threshold of 161 keV, to avoid the intrinsic electronic noise and other unavoidable effects (e.g. background radiation), a count rate of (0.87±0.03) counts/s was obtained. Figure 5.10 displays the image of an oscilloscope signal during the experiment. The signal corresponds to the voltage pulse produced by one of the charged particles coming from the $^{10}B(\mathrm{n},\alpha)^{7}Li$ reaction, depositing around 1.5 MeV,

Figure 5.8: Experimental test configuration with Schottky diodes - The polyethylene cylindrical container consists of parallel cylindrical sheets with 20 cm diameter. The $^{241}AmBe$ source was fixed at less than 1 cm distance near the container and at the same height as the inner silicon detector. The inset shows the box containing the silicon detector and the front-end electronics inside the aluminium box.

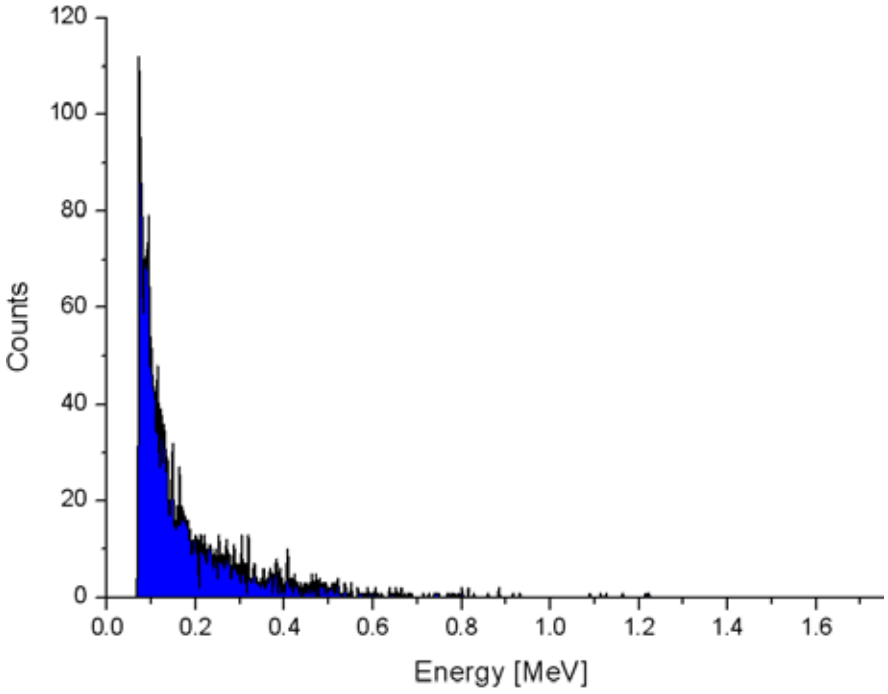

Figure 5.9: Pulse height distribution of the Schottky detector - Pulse height distribution of the Schottky detector covered with the o–carborane converter. The $^{241}AmBe$ neutron spectrum was moderated with the polyethylene cylindrical block (see Fig. 5.8).

Figure 5.10: Oscilloscope signal of neutron detection with a Schottky diode - Image of oscilloscope signal produced by a charged particle (α or ^7Li) in the silicon.

i.e. it is probably an alpha particle of the excited state of the neutron capture.

Figure 5.11 provides the total count rate, by fixing the same energy threshold of 161 keV, for both detectors (bare and with o–carborane converter) at the different voltages. The uncertainty bars shown correspond only to those of statistical origin. It must be stressed that the results change if the energy threshold is varied up or down. When the threshold is lowered, a larger number of reaction products from the converter material may be able to reach the sensitive volume detector increasing the final count rate. Conversely, if the threshold is varied up the count rate will decrease.

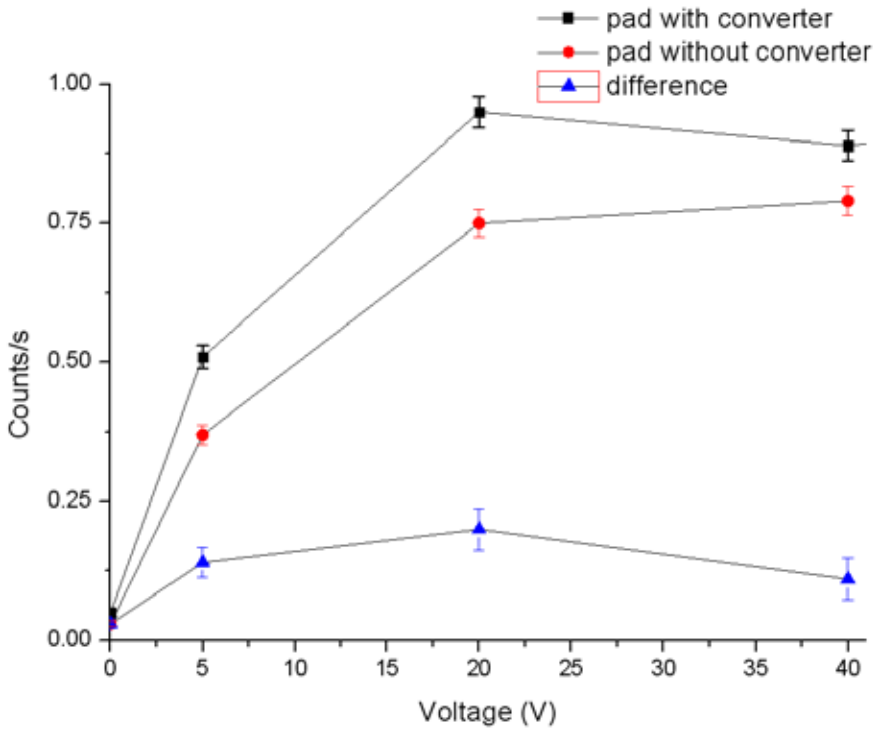

Figure 5.11: Count rate of the Schottky detector - Count rates of the Schottky detector with and without carborane converter. An energy threshold of 161 keV was applied to avoid electronic noise.

Fig. 5.11 also gives the difference in counts between the detectors with and without converter due to the charged particles produced by the capture reaction, $^{10}B(\mathrm{n},\alpha)^{7}Li$, of slow neutrons within the o–carborane converter. This difference increases with the applied voltage form 0 to 5 V, when the depleted volume in the silicon is enough to collect the entire charge created by both the emitted alpha and lithium ions. Although

the full depletion voltage is (16±1) V for these silicon detectors, 5 V is quite sufficient to deplete a volume thick enough so the ^{10}B(n,α)^{7}Li reaction products leave all their energy because their ranges within silicon (see Table 2.6) are few micrometers only. For higher voltages, the count rate difference remains constant within the uncertainty bars and the detector with o–carborane presents (0.11±0.04) counts/s more than the bare one at 40 V bias. This demonstrates the feasibility of the o–carborane material for the detection of slow neutrons with silicon sensors.

There is an additional signal contribution in both detectors that increases from 0 to 20 V, past full depletion, and then remains constant. For the bare detector at 40 V, the total measured count rate is (0.76±0.03) counts/s. It is clear that the extra count rate comes from the silicon detector itself. Several processes might contribute: a) the γ–rays emitted from the $^{241}AmBe$ source [124]; b) the recoil protons produced as a consequence of n–p elastic scatterings inside the PE block [125]; c) the charged particles released from the Si(n_{fast},α) and Si(n_{fast},p) reactions or even from elastic and/or inelastic scattering of fast neutrons with silicon nuclei [126], [127], [128]; and, finally, d) the contributions of the background radiation and other contamination effects [129]. These processes are considered in detail in the following paragraphs:

- The $^{241}AmBe$ neutron source produces γ–rays with energy peaks at 59.54 keV, 662.4 keV, 722.01 keV and 4.438 MeV. Table 5.3 summarizes the relative intensities for these photon peaks [124]. At 59.54 keV there is a high probability of emission but these photons cannot be considered because they are below the applied energy threshold (161 keV). At 4.438 MeV, although the probability of emission is considerable (0.591 gamma/neutron ratio), this energy is so high that low net signal is expected to occur within the sensitive volume of the Si detector. The other γ-rays have very low emission probability, so that their contributions to the detector reading are also fully negligible.

- Recoil protons can be emitted inside the PE cylindrical moderator as a result of elastic scatterings of neutrons at whatever energy with local hydrogen nuclei. These protons will have comparable energies to that of the incident neutrons but the thickness (2 mm) of the Al box enclosing the silicon detector is enough to absorb all of them so this contribution can be also ruled out.

Table 5.3: Gamma and Neutron emission per 10^6 alphas of $^{241}AmBe$ source.

Particle **emitted**	**Emitter**	**Energy**	**Intensity** (particles/10^6 α) 40 mCi AmBe
n/s	$^{9}Be(\alpha,\mathrm{n})^{12}C$	Spectrum $[0.2 - 11]$ MeV	60
	$^{241}Am \rightarrow {}^{237}Np + \alpha$	26.3 keV	$2.4{\cdot}10^4$
		33.2 keV	$1.3{\cdot}10^3$
		59.5 keV	$3.59{\cdot}10^5$
γ/s	$^{237}Np \rightarrow \gamma + {}^{237}Np$	125.3 keV	40.8
		146.6 keV	4.6
		208 keV	7.9
		335.4 keV	5
		368.7 keV	2.2
		662.4 keV	3.64
		722.01 keV	1.96
	$^{9}Be(\alpha,\mathrm{n})^{12}C^*$	4.438 MeV	35.46
		7.654 MeV	7.91

- As shown in Table 5.2, a high amount of the fast component persists in the transmitted $^{241}AmBe$ neutron spectrum despite the moderation within the PE cylindrical container. These fast neutrons could contribute to the detector reading via Si(n_{fast},α) and Si(n_{fast},p) reactions as well as elastic and/or inelastic scattering with silicon nuclei. This possibility was verified with Monte Carlo simulations. As MCNPX show limitations in its estimations of the heavy ion ranges below 1 MeV, which is higher than the energy range of some of the charged particles to be analyzed (^{7}Li, 0.84MeV), GEANT4 was used instead. In this code, the energy cut-off can be defined by the user as low as required but we cannot forced it to track ion particles below 100 keV because at this energy overestimations in the range calculations higher than +10% with regards to data given in the ICRU Report 73 [130], may appear. The first set of simulations examined the impact of the moderated neutrons from the $^{241}AmBe$ source by elastic scattering in the sensitive silicon detector area. The neutron spectrum used as input was the reference one emitted by the $^{241}AmBe$ source (Figure 5.1). The experimental configuration, including the moderator and the geometrical conditions, were also simulated and the result was normalized to the total experimental time. A considerable contribution to the count rate, 0.5 counts/s, was found and this amounts to an extra 0.32% to the total detection efficiency. Furthermore, by considering the Si(n_{fast},α) and Si(n_{fast},p) reactions, additional 0.014 and 0.01 counts/s were obtained but they represent only $9{\cdot}10^{-3}$% and $6.4{\cdot}10^{-3}$% to the detection efficiency, respectively. We can observe in Fig. 5.12 that the GEANT4 reproduces the measured pulse height distribution of the bare Schottky detector at nearly all the energy range of interest.

- All the experiments done in this work were carried out in the enclosed environment of the laboratory, i.e. the set–up is also exposed to the background radiation mainly due to natural γ–ray sources. There is also another unavoidable contribution generated either by those photons emitted from (n,γ) radiative capture reactions in all the materials around the devices and/or by the H(n,γ)D reaction, Q=2.22MeV, in the PE block used to moderate them. In addition, the closed environment in which the measurements were carried out, might contribute with neutrons scattered back from from the lateral walls, floor and ceiling as well

as from any furniture or equipment present in the experimental room. This unwanted scattered neutron field is very complex and very difficult to take into account in the simulations.

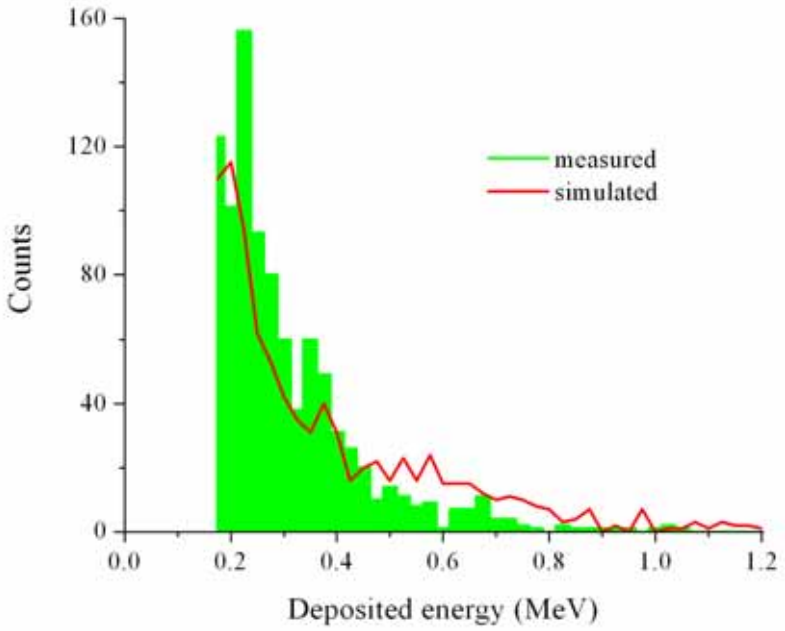

Figure 5.12: Simulated pulse height distributions of the Schottky - Comparison between the simulated (GEANT4) and measured pulse height distributions of the bare Schottky detector.

The results support the fact that both the Schottky barrier silicon diode and the o–carborane compound are suitable to detect neutrons. But the main contribution of the signal came from elastic scattering of fast neutrons in the thick depleted silicon bulk (300 μm). This problem will be avoided with the ultra–thin 3D structures.

5.2 Experiments with ultra–thin 3D detectors

As said in Section 2.4, to validate the performance of the ultra-thin 3D detectors developed in this thesis (section 4.2) as neutron detectors, it is necessary to assess three coefficients: γ–rejection factor, n/γ discrimination, and neutron efficiency. The

first two are particularly important due to the fact that, in a mixed gamma–neutron field, the output signal of the neutrons can be indistinguishable of those due to the γ–background/field. Each of them is evaluated in the next sections. All the experiments presented in this section were carried out with U3DTHIN detectors of the design–A (see subsection 4.2.2).

5.2.1 Gamma–ray rejection factor

A monoenergetic γ–ray ^{137}Cs source was used to evaluate the gamma rejection factor of the bare ultra–thin 3D detectors. Table 5.4 shows the characteristics of the source.

Table 5.4: ^{137}Cs source characteristics

Nuclide	**Half-life (y)**	**Energy γ-ray (keV)**	**Activity (Bq)**
^{137}Cs	30.17	662	$3.3{\cdot}10^{9}$

The ultra–thin 3D detector was located 1 m distance from the ^{137}Cs source which emitted isotropically. An energy threshold of 100 keV was applied to the readout system to avoid electronic noise. This low energy threshold was possible thanks to the low capacitance of the U3DTHIN detector (see section 4.2.2). In these conditions, only one count was measured for the 10 μm thickness detector for a measuring time of 10 minutes. This means that the gamma rejection factor of the ultra–thin 3D detectors for the 662 keV photons and an energy threshold of 100 keV is higher than 10^{-8}. This value is the highest γ–rejection factor for silicon neutron detectors reported so far. Under the same experimental conditions, standard silicon detectors with thicknesses 300 μm and 800 μm registered total count rates of (29.0±0.2) counts/s and (204.0±0.6) counts/s respectively.

Figure 5.13 shows the spectrum obtained in this conditions, where the photopeak ($\sim$ 662 keV), the Compton edge, and the Compton plateau can be seen. For silicon and photons of 662 keV energy emitted by this ^{137}Cs source, the Compton scattering dominates above photoelectric from around 60 keV. Few photons are completely absorbed (photopeak) due to the low silicon thickness of the silicon. Note that photoelectrons and Compton electrons with E $\geq$ 60 keV have an average path length higher than 33 μm in silicon (value estimated with ESTAR software [131]). Figure 5.14 shows the spectra simulated with MCNPX when planar silicon devices are irradiated

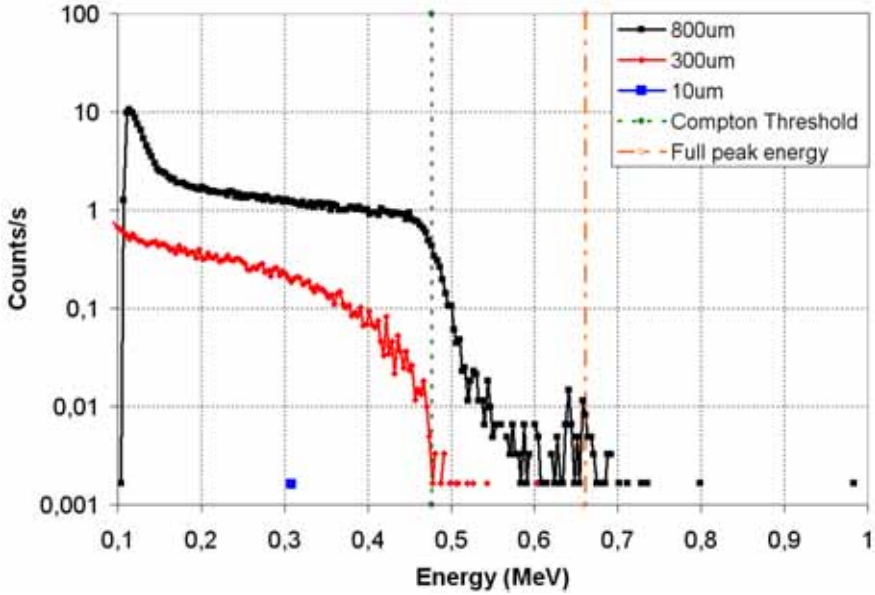

Figure 5.13: Spectrum of ^{137}Cs in silicon detectors - Counts per second measured with a ^{137}Cs gamma source at 1 m distance of silicon detectors of 10, 300, and 800 μm thick with 100 keV LLD.

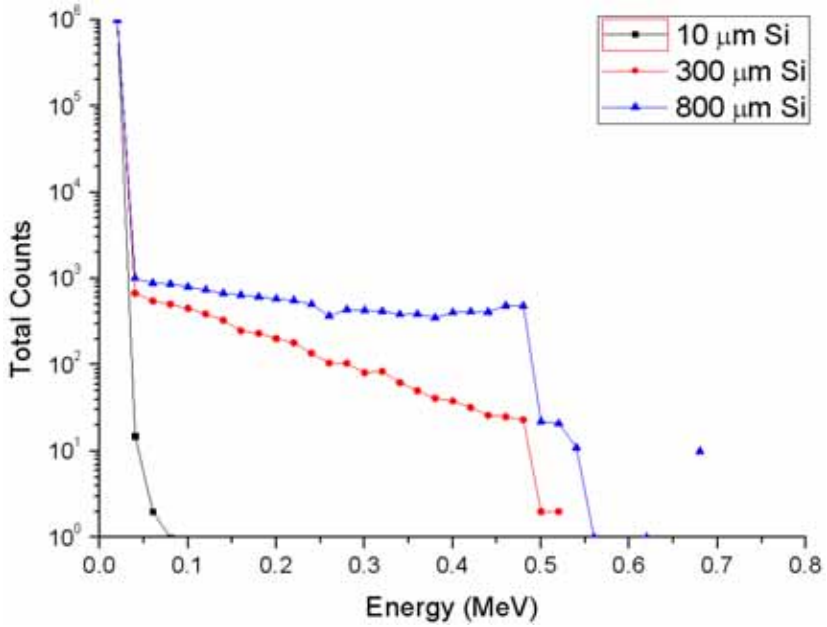

Figure 5.14: Simulated spectra of energy deposited in planar silicon detectors irradiated with ^{137}Cs gamma source - Total counts deposited within silicon planar detectors with 10, 300, 800 μm thick when these are simulated with MCNPX code, for 662 keV photons without energy threshold.

with 662 keV photons. If the LLD setting was above 100 keV, there would not be counts expected in the detector with 10 μm thickness.

5.2.2 Neutron-gamma ray discrimination

The ultra–thin 3D devices were exposed to an $^{241}AmBe$ neutron source with an activity of 40 mCi, and a total neutron emission rate of $8.8{\cdot}10^4$ n/s·4π sr (i.e. 2200 neutrons/s per mCi of ^{241}Am, with neutron average energy of approximately 4.5 MeV). The $^{241}AmBe$ source also produces photons with energy peaks at 22.3 keV, 33.3 keV, 59.54 keV, 662.4 keV, 722.01 keV, 4.438 MeV and 7.654MeV. Although there are other gamma peaks, their probabilities are very low, so they are not taken into account in this analysis (see Table 5.3). The source also contained 8 mCi of ^{137}Cs emitting gamma–rays at 662 keV but, as it has been demonstrated in the previous section, this is not expected to contribute to the pulse height distribution measured by the detector.

The neutron spectrum of the $^{241}AmBe$ source covers a range of energies from 0.2 MeV to 11 MeV, with a maximum at 4.5 MeV. In order to better test the performance of the converter, with higher cross–section in the thermal neutron range, the neutrons from the source were thermalized with a polyethylene block 10 cm thick placed between the $^{241}AmBe$ source and the detector. The distance from the center of the source to the silicon detectors was 25 cm. For this experiment, the same o–carborane ($C_2B_{10}H_{12}$) tested in the first preliminar experiment (see 5.1.2) was used, but dissolved in another matrix adhesive: cyanoacrylate within tetrahydrofuran (THF). After this solution is deposited, the THF evaporates, leaving an adhesive matrix of o–carborane/cyanoacrylate with a density of 1.37 g/cm^3. The composition of this compound is shown in the Table 5.5. This cyanoacrylate matrix was chosen as it is not only easy to deposit on devices but also because it is more adhesive than the PVC matrix. The thickness of the deposited converter layer was previously optimized with MCNPX simulations (see 3.4).

Both an adapted ultra–thin 3D thin with neutron converter and a bare one were tested at the same time so the difference in counts between them should be due to the charged particles produced by the capture of neutrons within the converter. The detectors were biased to 10 V and the measurement time was 26 hours. Figure 5.15 shows the count rate distributions obtained by the detectors with an applied threshold of 180 keV to avoid counts from the electronic noise.

Table 5.5: Converter composition

Materials	**Mass Fraction** (%)
o-carborane and cyanoacrylate	81.9% o-carborane + 18.11% cyanoac.
H	7.5%
C	28.7%
^{10}B	53.0%
O	7.5%
N	3.3%

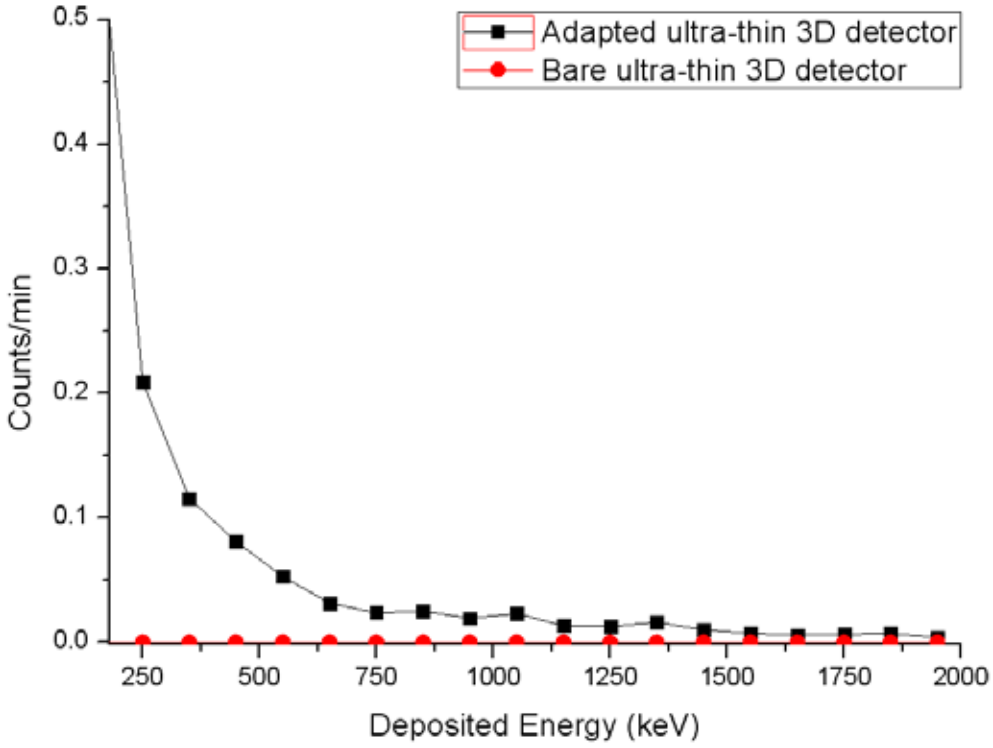

Figure 5.15: Pulse height distribution measured using a $^{241}AmBe$ γ-n source. - Charged particle pulse height distribution measured by an adapted and a bare ultra-thin 3D detector. An energy threshold of 180 keV was used in the readout system to avoid electronic noise.

The bare ultra–thin 3D detector obtained (181±13)·10^{-5} counts/s. These counts may come from: (i) the natural γ–ray background, (ii) photons produced from (n,γ) reactions in the materials around the devices, (iii) γ–rays from the neutron capture reaction in the polyethylene block H(n,γ)D, Q=2.22 MeV, (iv) the 4.438 and 7.654 MeV γ-rays of the $^{241}AmBe$ source, with considerable emission rates although low absorption probability in 10 μm silicon, (v) energy deposited in the silicon volume by n–Si nuclear interactions (only the contributions with energies higher than the 180 keV applied threshold are considered here).

In the same measurement time the o–carborane adapted detector obtained a total of (218±5)·10^{-4} counts/s, i.e. this measured one order of magnitude higher than the background measured by the bare detector. This result demonstrates the feasibility of ultra–thin 3D detector with o–carborane for the detection of slow neutrons. According to the neutron emission rate from the $^{241}AmBe$ source, 8.8·10^4 n/s·4π sr, the percentage of moderated neutrons within the 10 cm thick polyethylene, and considering the simulated efficiency for thermal neutrons in our device (section 3.4), 2.5%, the expected count rate at 25 cm is (280±80)·10^{-4} counts/s which is in good agreement with the experimental value. Hence the neutron/background discrimination rate is 12 to 1 in the explained experimental conditions. The spectral shape of the signal distribution is mainly due to the energy loss for the reaction products from the ^{10}B(n,alpha)^7Li reaction either within the entrance window (1 μm SiO_2 for the U3DTHIN design–A, see Table 4.3) of the detector or inside the converter.

5.2.3 Neutron detection efficiency in a nuclear reactor beam

Finally, to assess the efficiency of the ultra–thin 3D detectors for neutron detection with the o–carborane boron-based converter, it is necessary to test them with a neutron beam as monoenergetic as possible. The nuclear reactor located at the Instituto Tecnológico e Nuclear (ITN) facilities (Lisbon, Portugal), was used for such aim.

Table 5.6 shows the available neutron fluxes as well as the linear dependence of these with the reactor power. As usually happens in most of the neutron fields, there is an inherent gamma field associated to the neutron one, which is necessary to take into account to fix the LLD setting.

Figure 5.16 displays the experimental setup in the ITN's nuclear reactor: the "beam port" for thermal neutrons delivers a 5 cm diameter well collimated neutron beam with

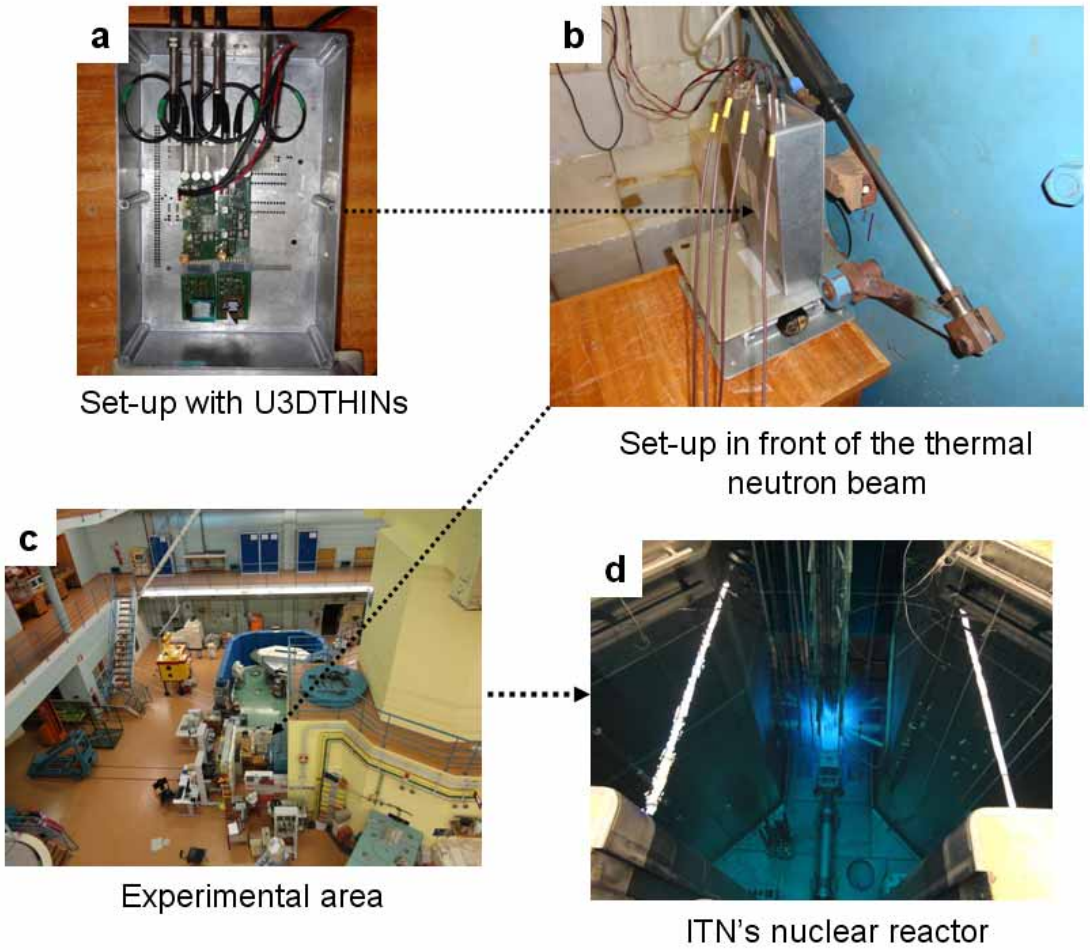

Figure 5.16: Experimental setup in the ITN's nuclear reactor - (a) Aluminium box that contains the ultra–thin 3D detector with the o–carborane converter coating, the bare one, and their respective readout electronics. (b) Set–up placed in front of the thermal neutron beam shutter, with the detectors in the center of the beam. (c) Experimental area for thermal neutron beams, adjoined nuclear reactor. (d) Nuclear reactor kernel where the Cherenkov radiation is visible.

Table 5.6: Neutron flux and gamma field powered in the ITN nuclear reactor.

Power kW	**Flux** (n/cm^2·s)	**Gamma field** (μSv/s)
1000	$2{\cdot}10^5$	5.5556
100	$2{\cdot}10^4$	0.5556
10	$2{\cdot}10^3$	0.0556
1	200	0.0056
0.1	20	0.0006

a flux of $2{\cdot}10^5$ with the reactor power at 1 MW. The detectors were located just in front of the beam shutter. The data acquisition system was placed at 3 meters, outside the biological shielding. Then, a set of measurements at 10 kW, 100 kW, and 1 MW was carried out at 220 keV LLD setting (fixed with the bare detector to exclude background signals). The results obtained are shown next:

- Figure 5.17 shows the total counts of an ultra–thin 3D detector covered with an o–carborane converter at different reactor powers. There are two results to highlight: first, there is linearity between the readout counts and the neutron fluence; secondly, there is not saturation effect in the detector system even for the highest neutron rate.

- Figure 5.18 shows the pulse height distributions of the signals obtained by the detector under those reactor powers. It is observed: (i) as a consequence of the linear response represented in Figure 5.17, the spectrum shape scales up with the reactor power; (ii) probably due to the non–uniform distribution of the o–carborane layer (see Appendix A.1) there are a high quantity of counts at low energies; (iii) the maximum energy observed in the spectra is lower than the energy from the $^{10}B(\mathrm{n},\alpha)^7Li$ reaction products because of the energy loss that they suffer when pass through the entrance windows of these ultra-thin 3D detectors. The devices used in this experiments were the first prototype of the ultra–thin 3D detectors (see Fig. 4.14 and Table 4.3) that had an entrance window of 1 μm SiO_2 in the active area, which may reduce the incident particle energies to some hundreds of keV.

- A bare detector was measured at 100 kW during 5 minutes. The signal–to–background ratio was 43 to 1. This value is reasonably good taking into account the gamma field associated to the measure (see Table 5.6).

- The measured efficiency result was 0.23% (assuming that the active area covered by o-carborane was approximately 0.5 cm^2). This value is one order of magnitude lower than that predicted by the simulations, around 2% (see 3.4). A visual inspection of the o–carborane layer after the measurement showed that this type of coating loses adherence and uniformity, and forms micelles with air which may well deteriorate its physical–chemical properties. Hence, although this neutron converter has been tested with reasonable results, unfortunately such deterioration over time of obliged us to continue working in the development of other reliable boron–based compounds.

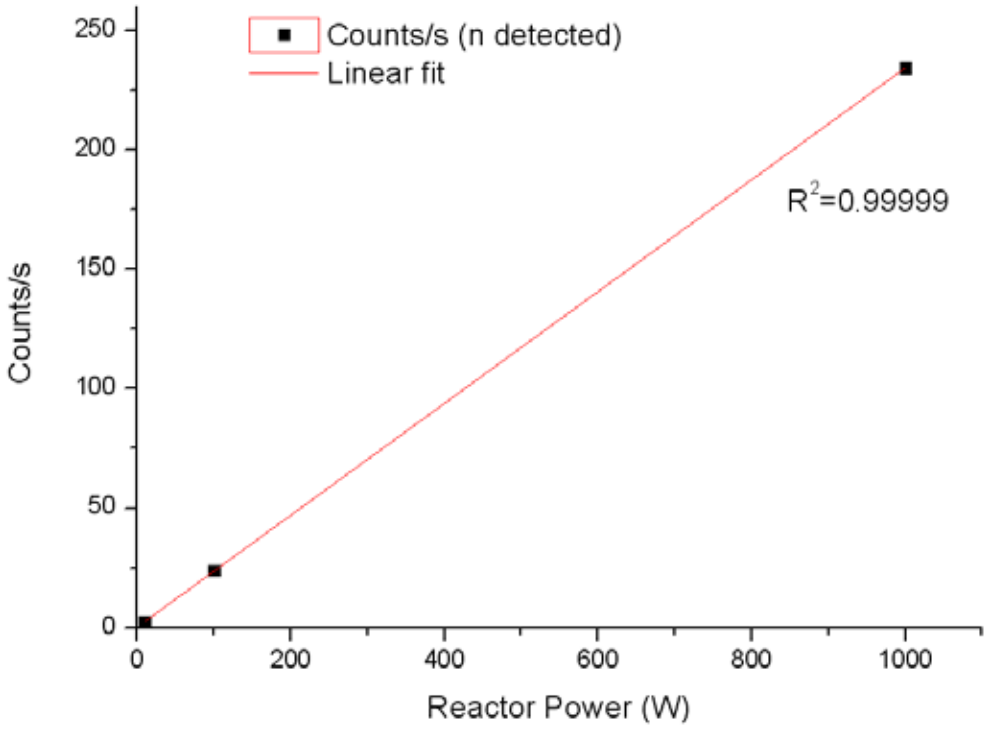

Figure 5.17: Linear response of the ultra-thin 3D detector tested with the ITN's nuclear reactor - Three measurements at 10 kW, 100 kW, and 1 MW (i.e. at $2{\cdot}10^3$, $2{\cdot}10^4$, and $2{\cdot}10^5$ n/$cm^2{\cdot}$s) were carried out with the ultra-thin 3D detector covered with o-carborane. LLD setting at 220 keV.

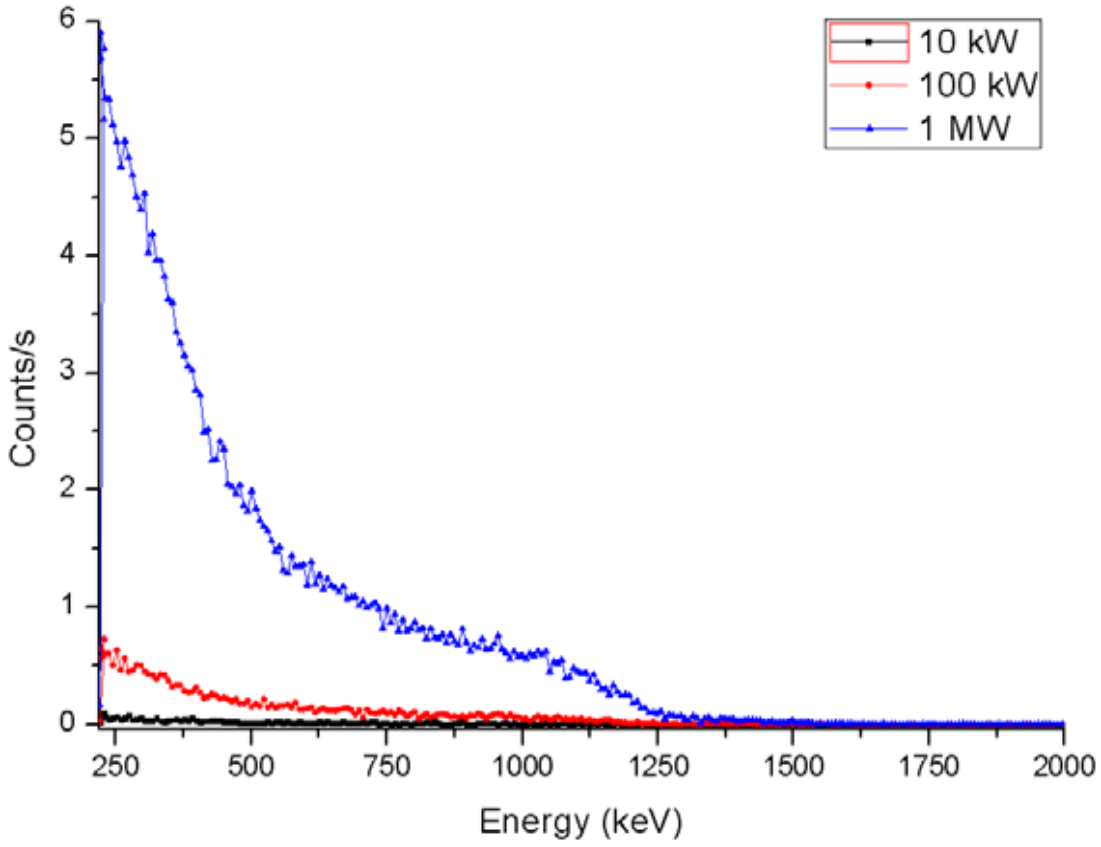

Figure 5.18: Measured pulse height distribution of the ultra-thin 3D detector with o–carborane - Spectra of the detector when it is applied a neutron collimated beam from a nuclear reactor working at 10 kW, 100 kW, and 1 MW. LLD setting at 220 keV.

From this result in this section it is clear that new boron–based coatings with good uniformity, adhesion, and durability are indispensable. Efforts have been done to get such boron coatings, which represented technical challenges since the deposit of these coatings with thicknesses higher than 1 μm is problematic and unstable (poor adhesion and peelings). Coatings with $^{10}B_4C$ and ^{10}B were achieved by RF-sputtering (Appendix A.3) and electron beam physical vapor deposition methods respectively (Appendix A.2). The final tests detailed in the next sections were obtained with the improved ultra-thin 3D detectors (see design–B in 4.2.2) with thin entrance (400 nm) windows and these optimized coatings.

5.3 Application at LINAC workplaces

As said at the beginning of the manuscript, the main aim of this thesis is the neutron detection in radiotherapy treatment rooms. To test the ultra–thin 3D detectors in RT rooms, experimental measurements in the Hospital Universitario de Santiago de Compostela (HSC) with a Siemens Primus LINAC used for oncological treatment, were carried out. The results are detailed in the next sections. All the experiments presented in this section were carried out with U3DTHIN detectors of the enhanced design–B (see subsection 4.2.2).

5.3.1 Simulated neutron fields in radiotherapy treatment rooms

Previously to performance the measurements, it is necessary to know the neutron spectral distribution inside the RT room as accurately as possible. Hitherto, this has been done by Monte Carlo simulations [132], [15], or with passive methods [11]. Hence, as a first approximation, the fluence spectral distribution simulated by Monte Carlo of the HSC room where the experiments were done will be used.

Neutron lethargy inside the treatment room is shown in Figure 5.19 in terms of fluence per MU photon dose. It was obtained from simulations with the Monte-Carlo MCNPX software for the Siemens PRIMUS at 15 MV at 2 meters from the isocenter in the gantry axis, where the test detectors are placed [132]. The spectrum displays two peaks: a direct component from neutron evaporation around 1 MeV of fast neutrons arriving from the LINAC head and another component of slow neutrons below 1 eV from the fast neutrons thermalized by the accelerator components and room walls. This

spectrum shows that most photoneutrons have energies whose biological effectiveness is high. In all the RT rooms the thermal neutron fluence is homogeneous and depends on the LINAC model and room volume. An extensive study can be found in [15].

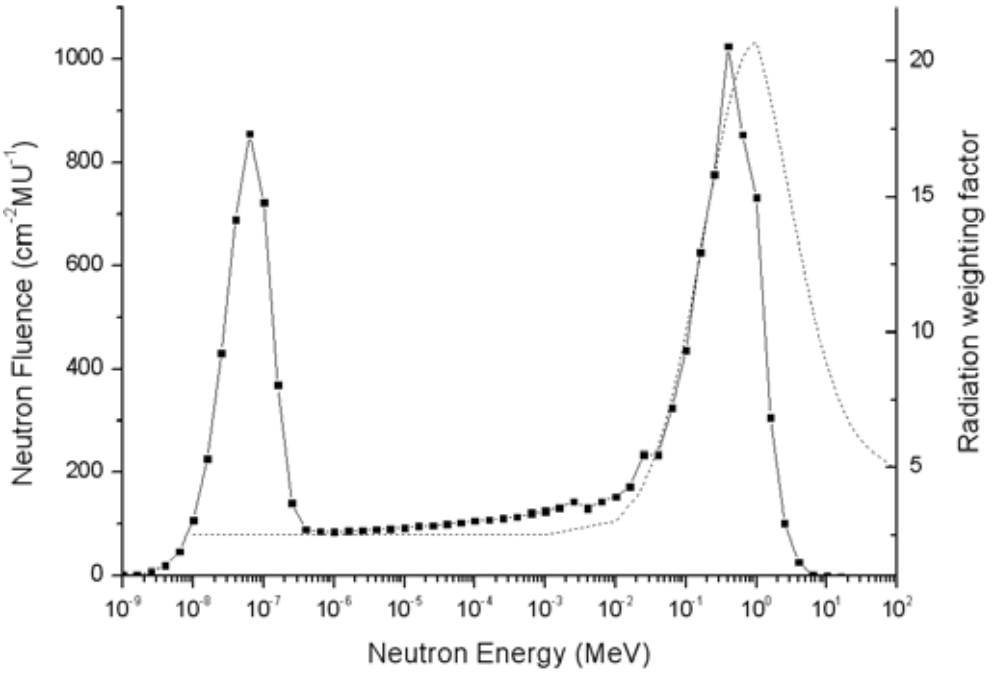

Figure 5.19: Simulated fluence spectral distribution inside a radiotherapy room - Fluence spectral distribution at 2 m distance from the isocenter inside the radiotherapy room for a Siemens Primus LINAC working at 15 MV, field 10×10 cm^2, gantry at 0°. The discontinuous curve corresponds to the neutron W_R.

Figure 5.20 shows the simulated efficiency for the ultra-thin 3D detector as a function of the ^{10}B layer thickness when it is subjected to the neutron irradiation with the spectral distribution specified in Figure 5.19. Albeit the behavior of these efficiencies tend to be similar to the shown in subsection 3.4, the value of the efficiency is reduced when the slow neutron field is arriving in a quasi isotropic angular distribution and has a energy with significant broadening in the thermal region. Figure 5.21 shows that the neutron detection efficiency is reduced by 0.8% with respect to the thermal front-face beam for 2 μm ^{10}B thickness with a 400 keV LLD setting (the reason for this high LLD is explained in subsection 5.3.2.1).

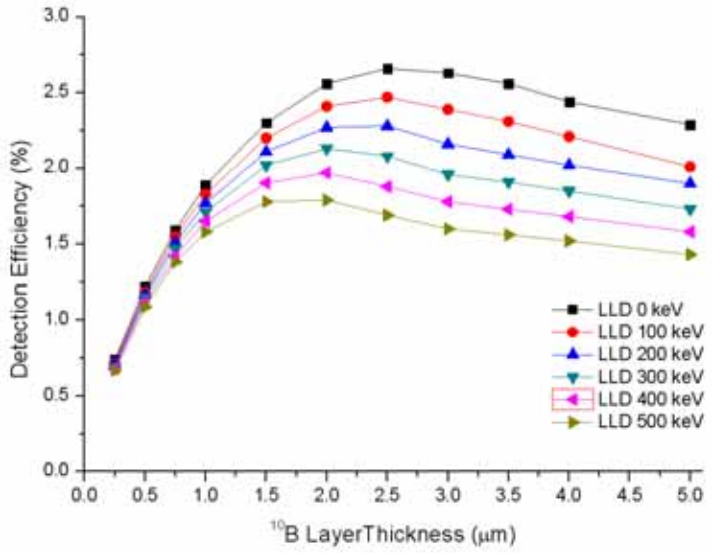

Figure 5.20: Simulated detection efficiency inside radiotherapy room. - Simulated detection efficiency in the ultra-thin 3D detector as a function of the ^{10}B layer thickness for several LLD settings. The simulated neutron beam comes from the spectral distribution in the point inside the RT room where the experimental setup is placed.

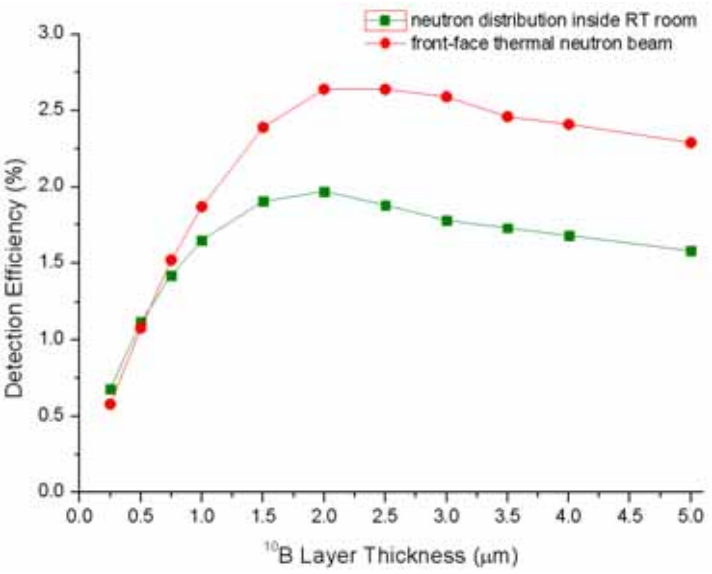

Figure 5.21: Comparison of the simulated detection efficiencies for two possible incident neutron beams - Simulated detection efficiency for irradiations of (a) a front-face thermal neutron beam and (b) the spectral distribution represented in Figure 5.19 over the ultra-thin 3D detector as a function of the ^{10}B layer thickness for 400 keV of LLD setting.

5.3.2 Measurements and results

The ultra–thin 3D detectors used here were those described in section 4.2.2: they have a considerable thinner entrance window in comparison with the first version (see Figure 4.14), which makes the charged particles lose less energy in the converter–sensitive detector interface. Moreover, two boron–based materials, ^{10}B pure and $^{10}B_4C$, were used as converters for the reasons stated at the end of the previous section. Table 5.7 summarizes the characteristics of the detectors used in this study: $^{10}B_4C$ and pure ^{10}B coatings were deposited by RF–sputtering and evaporation methods respectively. The $^{10}B_4C$ compound enriched in ^{10}B at 99% contains 78.6% ^{10}B and 21.4% C in weight. Details about the deposition methods developed in this work are summarized in appendixes A.2 and A.3.

Seven ultra–thin 3D detectors as those described in Section 4.2 were tested in the RT room of the Hospital Universitario de Santiago de Compostela. The experimental set-up consisted of: (i) a Siemens Primus LINAC which was collimated to a field of 10×10 cm^2 at the isocenter, 0° gantry angle, and working at 6 MV and 15 MV; (ii) detectors positioned in front of the LINAC in the gantry axis at a distance of 2 m from the isocenter; (iii) two readout electronics connected one with a bare ultra–thin 3D detector, i.e. without converter (sample C1, see Table 5.7), and another with an adapted ultra–thin 3D detector, i.e. with the boron–based compound (samples A1, A2, A3, B1, B2, and B3, Table 5.7). The bare ultra–thin 3D detector is used to measure the photon background. Thus, both an adapted detector with neutron converter and a bare detector are tested at the same time so the difference in counts between them should be due to the charged particles produced by the capture of neutrons within the converter. Figure 5.22 displays the experimental set–up inside that RT room.

5.3.2.1 Detector sensitivity to gamma-rays

A first measurement with the bare ultra-thin 3D detector was carried out to adjust the LLD setting. Figure 5.23 shows the response of the fully depleted bare sensor for background versus total irradiation fluence with different LLD settings. It is clear that a LLD setting of 200 keV is not enough to reject most of the gamma signals in the ultra-thin sensor and a higher LLD should be used. Below 200 total MU with a 400 keV LLD setting the detector showed only 8 counts. This radiation dose is taken as reference

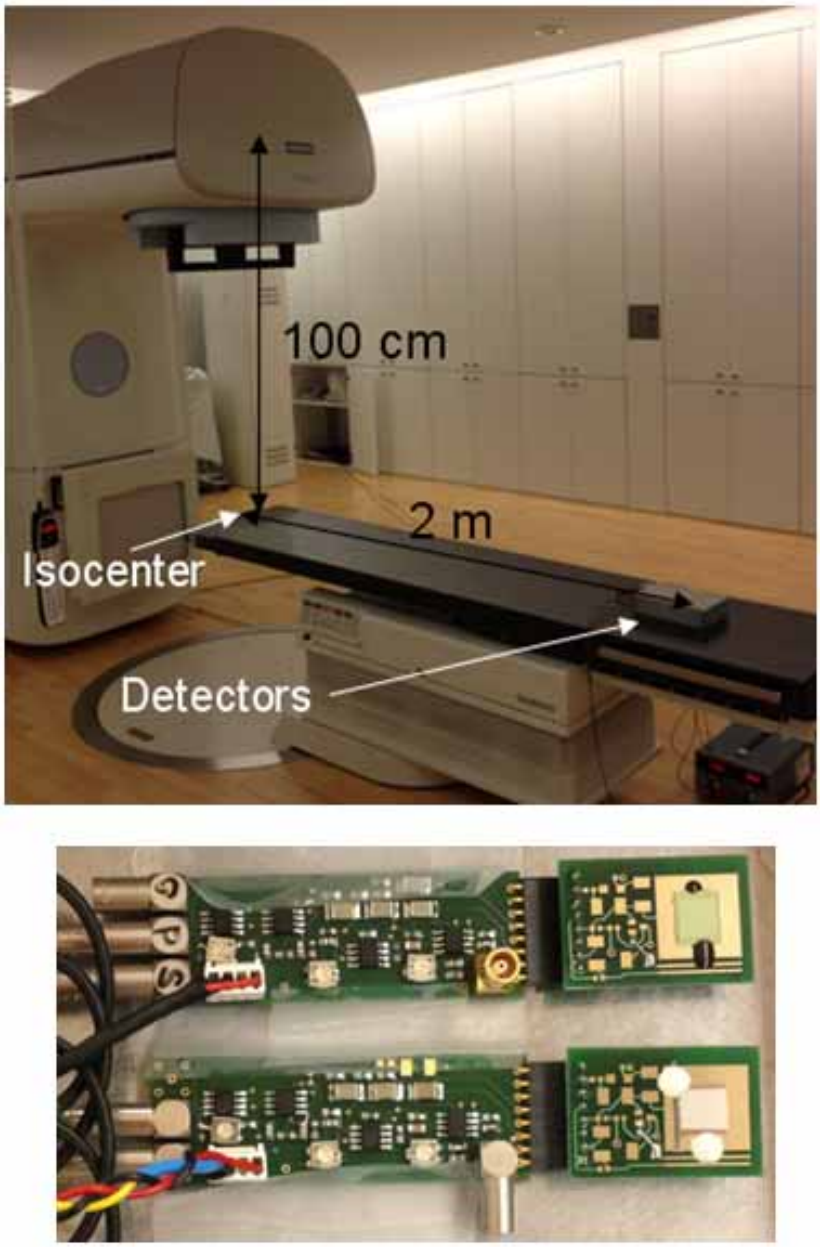

Figure 5.22: Experimental set–up in the Santiago de Compostela's Hospital - Top: Image of the experimental set–up in the Complexo Hospitalario de Santiago facilities. Bottom: Photograph of the detectors connected to the readout system: on the top there is a bare ultra–thin detector and on the bottom an ultra-thin detector covered with ^{10}B; both are mounted in printed circuit boards connected to a separated board to allow testing different detectors with the same system.

Table 5.7: Boron-based compounds on ultra-thin 3D detectors

Boron-based compound	Sample	Converter Thickness (μm)
^{10}B	A1	1.5
	A2	2.5
	A3	3.0
$^{10}B_4$C	B1	0.5
	B2	1.0
	B3	1.5
Bare detector	C1	$\oslash$

because, although the number of MUs per treatment depends on the type of tumor, its depth in the body, and the patient size, among other conditions, an orientative figure for the photon RT dose per session is around 200 MU (i.e. 2 Gy). Note that part of this undesirable noise is due to the long cables (15 m) used from the inside of the RT room where the detectors are placed to the data gathering area outside.

From the results in Figure 5.23 in the following measurements an energy threshold of 400 keV was applied to the readout system to, on one hand, ensure that for tests at a high number of MU the detector response to the γ–background would be roughly constant and very low (the detectors were tested under extreme, non–realistic RT session conditions). On the other hand, the high threshold minimizes the probability of spurious signals at low channels due to the electronic noise that might be caused by electromagnetic disturbances from the high EM field in the LINAC machine.

5.3.2.2 Closed field at 6 MV and 15 MV

Two runs of 800 total MU at 6 MV and 15 MV with closed gamma beam (i.e. with the LINAC head collimators closed) were undertaken. In these conditions, there is less than 1% of γ-rays in the room with respect to a standard 10×10 cm^2 field, so in this case any count registered by the detectors should be only due to neutrons.

- At 6 MV there are no neutrons since the photonuclear reaction appears at photon energies $\geq$ 8 MV. Thus the only contributions to the detector count rate would come from the possible interactions of leakage γ-rays around the room plus any other background radiation.

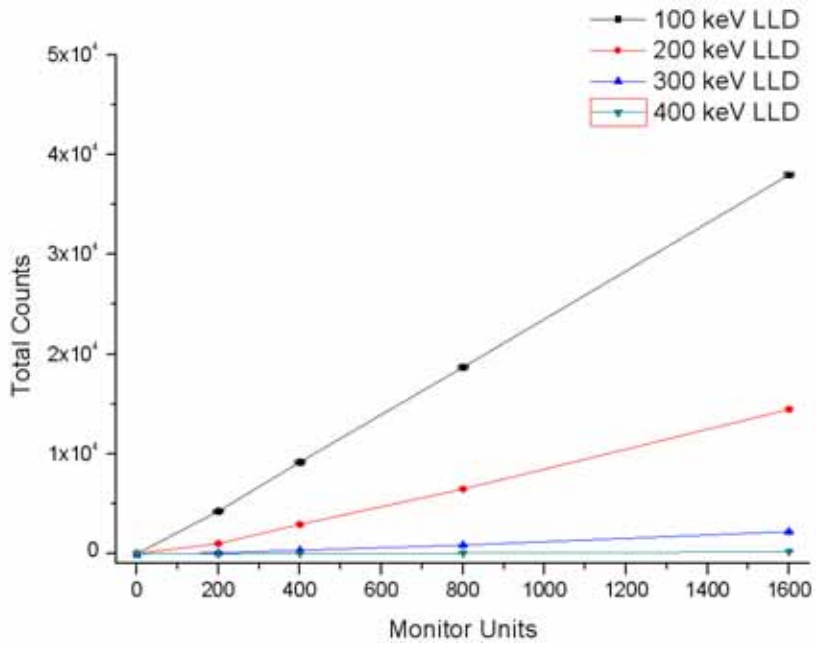

Figure 5.23: Total counts accumulated versus irradiation fluence for a bare ultra-thin 3D detector - Runs of 0, 200, 400, 800 and 1600 MU were carried out with the Siemens Primus LINAC model working at 15 MV.

- At 15 MV there is a double contribution to the detector measurement that is due to leakage γ-rays around the room (with a different spectrum than for the 6 MV case) plus the contribution due to the neutrons created by the photoneutron effect.

Note that the photon beam from LINACs is made up of a continuous energy spectrum whose maximum energy is equal to 6 MeV (first case) and 15 MeV (second case), but it has a mean γ-ray energy about a third part of such maximum energy, i.e. about 2 MeV and 5 MeV respectively.

Table 5.8 summarizes the results of that test with a LLD setting of 400 keV: (a) working at 6 MV there are no counts either for the 3.0 μm ^{10}B (A3) or the reference bare (C1) detector; (b) at 15 MV, when there are photoneutron reactions, the difference in counts between the C1 and A3 samples is clearly due to the charged particles produced by the capture of neutrons within the ^{10}B converter. The readout signal for the C1 sample at 15 MV, two orders of magnitude lower than for A3, is likely due to the charged particles released from the Si(n_{fast},α) and Si(n_{fast},p) reactions or even from

elastic and/or inelastic scattering of fast neutrons with silicon nuclei. Units in counts

Table 5.8: Spectra with closed field at 6 and 15 MV with 800 total MU.

Samples	6 MV $\leq 1\%$ γ-rays	15 MV $\leq 1\%$ γ-rays + n_{fast} + n_{slow}
C1	$\approx$0 c/MU	(198$\pm$5)$\cdot 10^{-3}$ c/MU
A3	$\approx$0 c/MU	(17.2$\pm$0.2 c/MU

per MU (c/MU). Both detectors have the same LLD setting (400 keV).

5.3.2.3 Detector sensitivity to fast neutrons

In order to test the detector sensitivity to fast neutrons a test was performed shielding the sample A3 from the slow neutrons with a cadmium sheet with a thickness of 1 mm. The cadmium foil absorbs most of the incident thermal neutrons with energies below 0.5 eV but transmits neutrons with energies higher than this value. Therefore, a reduction of the slow neutron counts is expected comparatively with the non-shielded sample. It was applied a radiation fluence of 1000 total MU with 500 MU/min rate. Table 5.9 summarizes the count rates obtained for the sample A3 in these conditions, with and without Cd foil. A reduction of 85% in total sensitivity was measured when the sample was shielded, showing that the main contribution to the signal readout is due to slow neutrons.

Table 5.9: Counts for Sample A3 with and without Cadmium shielding

	Cd shielding	**Without shielding**
Neutron Spectrum	γ-rays + n_{fast}	γ-rays + n_{fast} + n_{slow}
Count rate	(307$\pm$6)$\cdot 10^{-2}$ c/MU	(2008$\pm$14)$\cdot 10^{-2}$ c/MU

5.3.2.4 Detector response: Linearity

The dynamic range of the detector system was evaluated increasing the number of accumulated irradiation tests with the LINAC at 15 MV. Runs of 200, 400, 800 and 1600 total MUs were undertaken with the C1 and A3 samples. Figure 5.24 shows the linear

ultra-thin 3D detector response to the total irradiation fluence in the Siemens Primus LINAC. The A3 detector response showed linear proportionality between its readout counts and the neutron fluence and no saturation. This result complements the shown in Figure 5.17 for constant neutron fields and is expected since, first, semiconductor-based detectors show no saturation due to radiation damage up to very high radiation doses, and furthermore the detectors tested are based on the 3D detection technology which is radiation hard [62], and secondly the system has the advantage of having an electronic readout with a count limit higher than the detected neutron rate. As was discussed in Section 1, these features represent a great advantage because the detector system is not saturated or deteriorated with increasing particle doses.

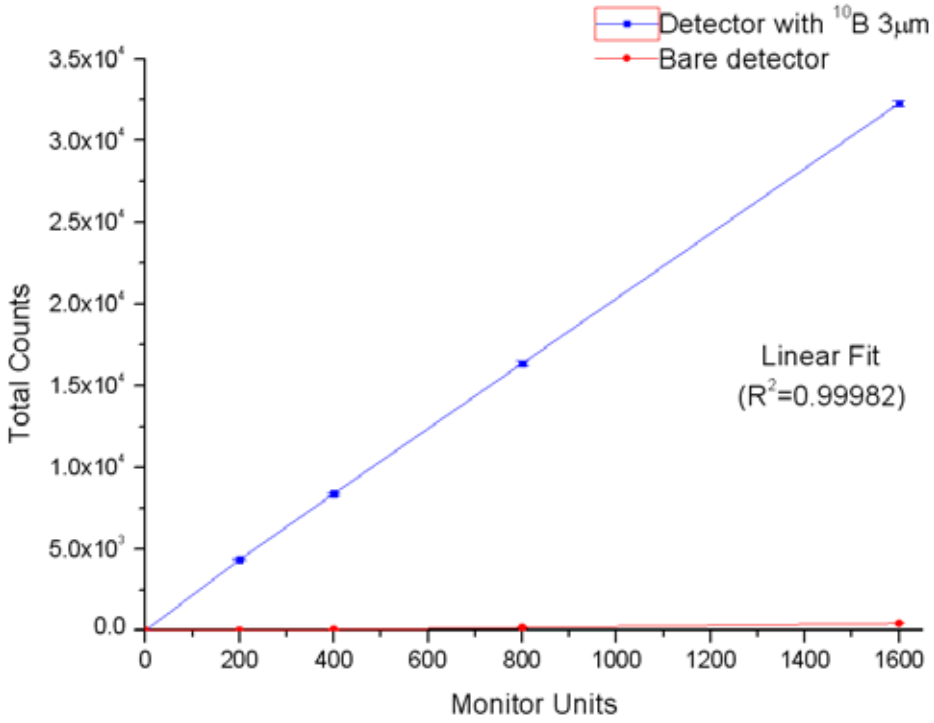

Figure 5.24: Linear response of the ultra-thin 3D detector covered with ^{10}B. - Linear response of the ultra-thin 3D detector covered with 3 μm ^{10}B (sample A3) and the bare detector (sample C1) versus total MU. Runs of 0, 200, 400, 800 and 1600 MU were carried out with the Siemens Primus LINAC model working at 15 MV. LLD setting at 400 keV.

Note that the slope of the detector response can change with the accelerator model and with the room volume: firstly, the accelerator model affects directly the neutron

production around the therapy room since the composition of the LINAC head materials and its design are different in each case. Secondly, the low-energy neutron fluence inside a RT room is roughly inversely proportional to room area, so for the same LINAC model these results can approximately be extrapolated taking into account the room volume.

5.3.2.5 Detector response versus irradiation rate: no-saturation effect

In order to assure the reproducibility and the statistical uncertainty grade of the detector, different irradiation rates (MU/min) were applied. Figure 5.25 shows the constant response of the A3 detector versus irradiation rate for 500 MU total when runs of 50, 100, 200 and 500 MU/min were carried out at 15 MV. This results show that there are no saturation effects, i.e. there is no signal pile-up in the detector readout with variations in the detection counts of 1SD in the range 50 to 500 MU/min.

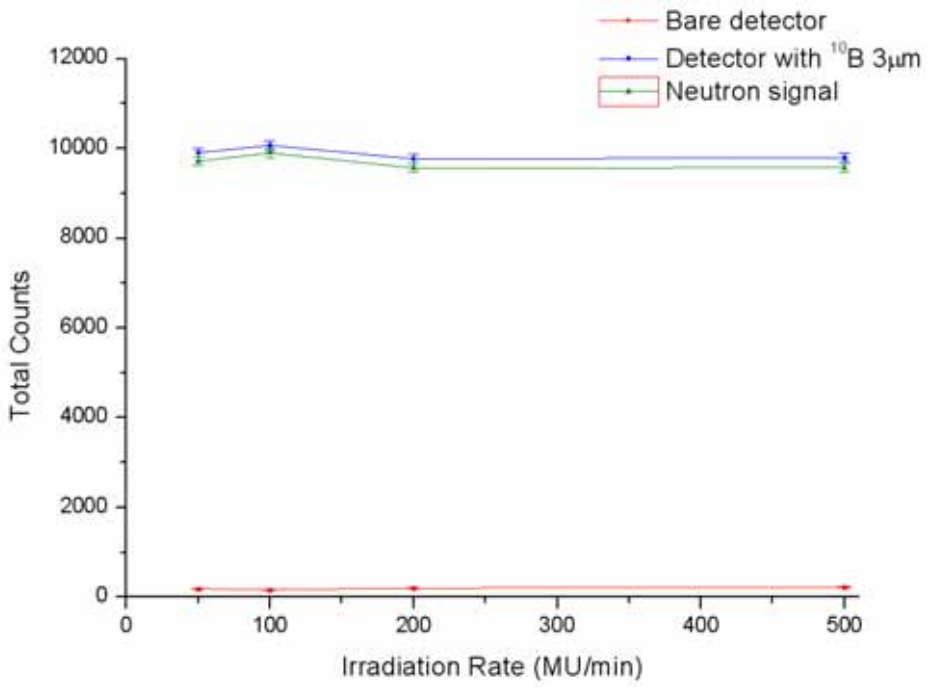

Figure 5.25: Response of the ultra-thin 3D detector versus irradiation rate. - Response of the ultra-thin 3D detector covered with 3 μm ^{10}B (sample A3) versus irradiation rate for 500 MU total. Runs of 50, 100, 200 and 500 MU/min were carried out with the Siemens Primus LINAC model working at 15 MV.

5.3.2.6 Detector sensitivity in RT rooms

In order to calculate the sensitivity of the ultra-thin 3D detectors covered with $^{10}B_4C$ and pure ^{10}B coatings, each of these samples was tested at 1000 total MU with an irradiation rate of 500 MU/min under the same experimental conditions. Figure 5.26 shows the measured and simulated total counts coming from neutrons as a function of the ^{10}B layer thickness. First, the results show a maximum thermal neutron detection efficiency around 2% at 400 keV LLD. Secondly, the measured data follow the behavior of the simulated function (Fig. 5.20). The agreement of the measured data with the simulated Monte Carlo data is acceptable taking into account that the successive approximations done to shape the experimental setup and the complex radiation field entail accumulated uncertainties not weighted in the simulations.

5.3.2.7 Energy spectra

Figures 5.27 and 5.28 show the pulse height distributions of the signals obtained by the ultra-thin 3D detectors with 0.5, 1, and 1.5 μm $^{10}B_4C$ (samples B1, B2, and B3) and with 1,5, 2,5, and 3 μm ^{10}B (samples A1, A2, and A3) at 1000 total MU with an irradiation rate of 500 MU/min.

The pulse height spectra for neutron detectors with converter coating do not reproduce the incident neutron energy, due to the intrinsic dispersion of the charge produced in the detector sensitive volume from the ionization slowing down mechanism of the neutron capture reaction particles. However, that spectral distribution lets us discriminate neutron signal from background, e.g. gammas and electrons that are usually present in neutron beams.

First of all, since the amount of deposited energy in the detector sensitive volume (space charge region) depends on the depth where the capture reaction takes place in the converter, the pulse height distribution is a continuous spectrum. Hence, for example, the 0.5 μm $^{10}B_4C$ spectrum shows a pronounced main edge that corresponds to the energy deposited by the alpha particles coming from the excited state of the $^{10}B(\mathrm{n},\alpha)^7Li$ capture reaction in the detector, i.e. with 1470 keV energy. There is another lower edge which corresponds with the alpha energy of the second decay of such reaction, at 1780 keV. On the other hand, the 3 μm ^{10}B spectrum shows such edges/peaks less sharply than in the 0.5 μm $^{10}B_4C$ case because the thickness of its layer

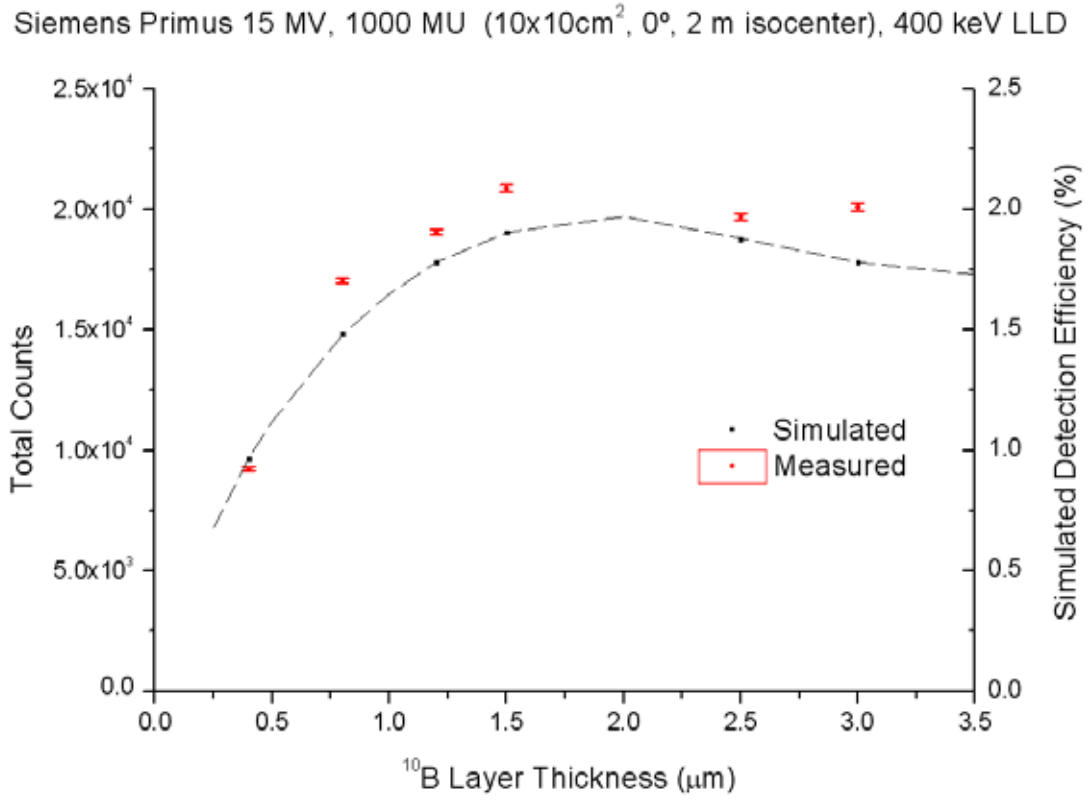

Figure 5.26: Measured total counts as a function of the ^{10}B layer thickness. - Measured and simulated total counts as a function of the ^{10}B layer thickness for all the samples: ultra-thin 3D detectors with 0.5 μm, 1.0 μm, and 1.5 μm of $^{10}B_4C$ coatings (78.6% ^{10}B) and 1.5 μm, 2.5 μm, and 3 μm of pure ^{10}B coatings, moving along the x-axis from left to right respectively. The line is a guide for the eye.

is much higher and therefore the $^{10}B(n,\alpha)^{7}Li$ reaction products have to pass through more material with larger loss of energy. But, because the 3 μm ^{10}B detector has a neutron efficiency higher than the 0.5 μm $^{10}B_4C$ detector (Figure 5.26), its measured pulse height distribution is proportionally higher.

In summary: (i) the thinner is the converter layer, the better is the resolution of the peaks due to a lower straggling of the reaction nuclear fragment energy when they reach the silicon depletion layer, (ii) The thicker is the converter layer, the higher is the total number of counts, up to the maximum efficiency point (which depends on the LLD setting).

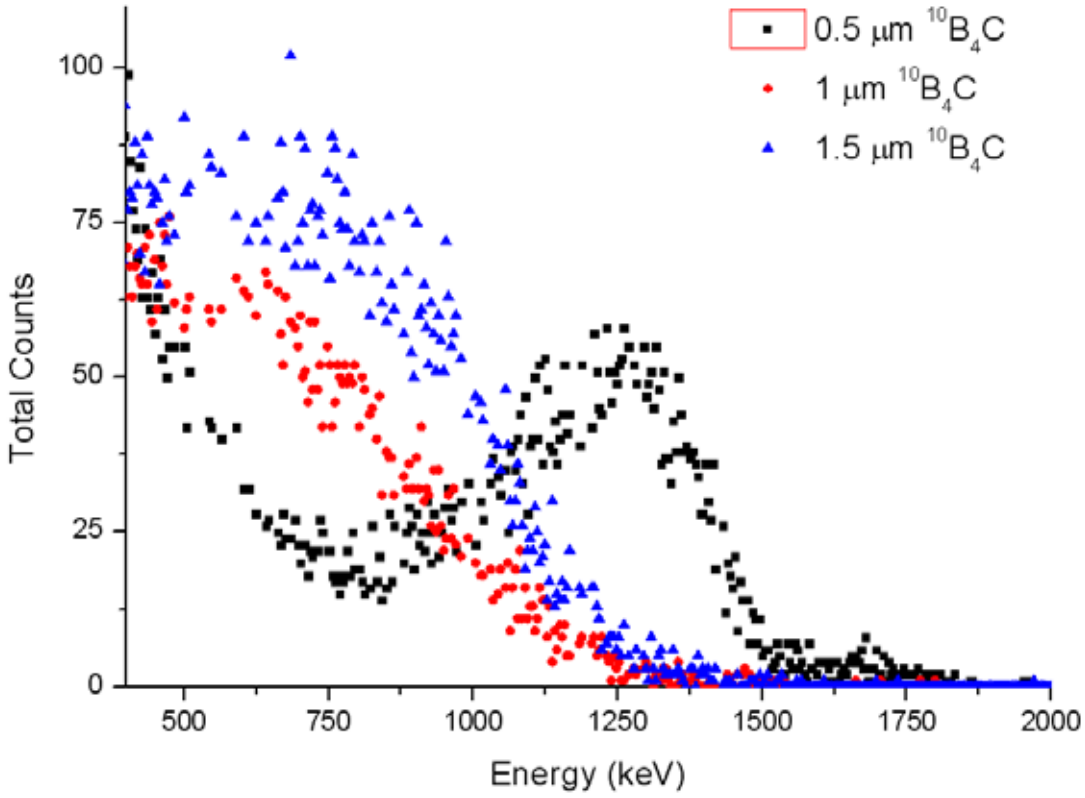

Figure 5.27: Measured pulse height distribution with $^{10}B_4C$ 0,5, 1, and 1.5 μm thick - Measured pulse height distribution of an ultra-thin 3D detector covered with a $^{10}B_4C$ coatings of 0.5, 1, and 1.5 μm thickness deposited by RF magnetron sputtering (Appendix **??**).

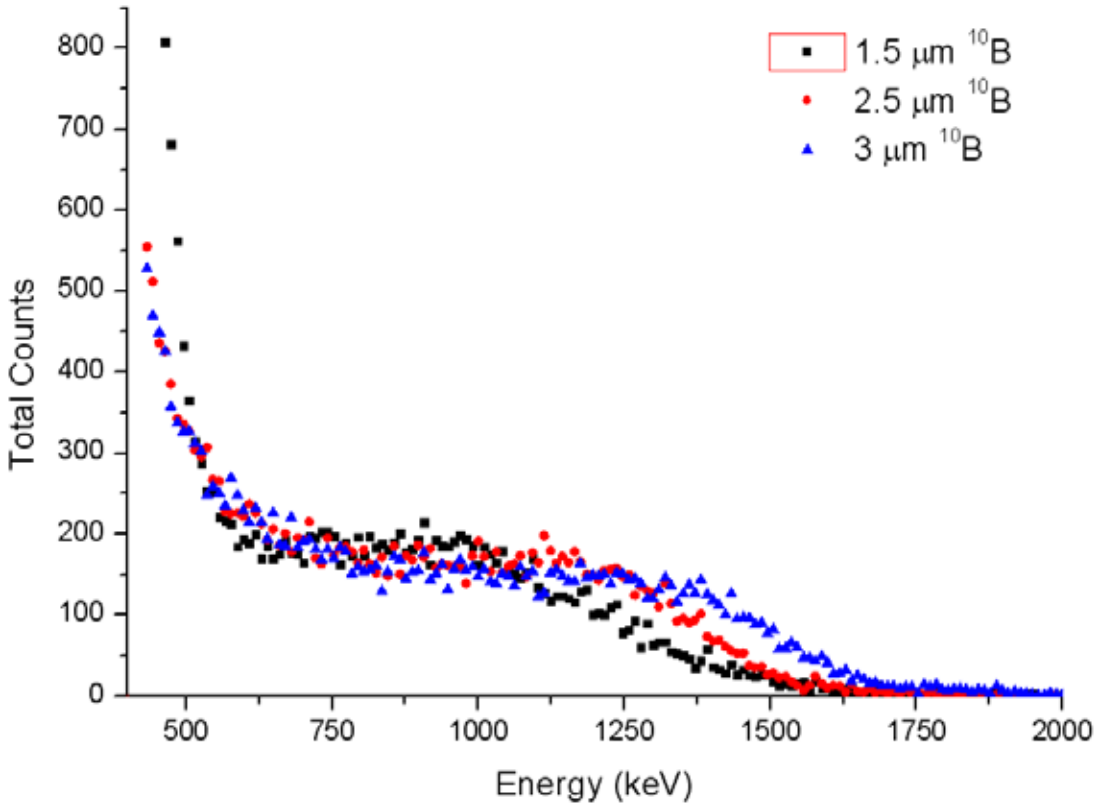

Figure 5.28: Spectra of an ultra-thin 3D detector with ^{10}B coatings - Measured pulse height distribution of an ultra-thin 3D detector covered with ^{10}B coatings of 1.5, 2,5, and 3 μm ^{10}B thicknesses deposited by EBPVD (Appendix A.2).

5.4 Discussion & Summary

This chapter has shown the results of the experimental work:

First, the preliminary measurements with planar PIN diodes showed the feasibility of neutron detection with simple silicon pad detectors covered with neutron converters [118].

Secondly, the measurements with Schottky diodes showed the feasibility of neutron detection with silicon detectors covered with a new boron compound, o–carborane [117]. The sensor and the experimental set–up were previously simulated with MCNPX and GEANT4. The detected count rate due to the slow neutron capture within the converter layer was consistent with simulation.

Third, for the measurements carried out with the first U3DTHIN detectors (design–A), it is deduced that: (i) the γ–rejection factor of the ultra-thin 3D detectors for the 662 keV photons and an energy threshold of 100 keV is higher than 10^{-8}; (ii) the signal/background ratio, or neutron/background discrimination rate, is 12/1 at LLD=180 keV inside the environment that the mixed n/γ source of $^{241}AmBe$ creates in the surrounding area, with a detector around 2% simulated efficiency. These first experiments with an ultra–thin 3D sensor showed the feasibility for neutron detection with these novel devices and their usefulness in complex mixed γ–neutron radiation fields [119]; (iii) the measurements in a nuclear reactor with the first ultra–thin 3D detectors showed linearity, not saturation effect, a signal–to–background ratio of 43/1 at LLD=220 keV, and a measured efficiency result of 0.23%, which is a order of magnitude lower than the simulated value; (iv) the first boron–based compound proposed for this work, o–carborane, showed deterioration over time and hence its long-term use is ruled out. New boron–based coatings had to be developed for the next tests.

Finally, improved ultra–thin 3D detectors (design–B) with thinner entrance windows and covered with ^{10}B pure and $^{10}B_4C$ were tested inside a radiotherapy room. The main results generated of such measurements were consistent with those commented in the previous paragraphs and furthermore: (i) the ultra-thin 3D silicon detectors were useful to detect the leakage radiation neutron field inside a RT room; (ii) there was no pile-up from 50 to 1000 MU/min for slow neutron detection inside a radiotherapy room and consequently the behavior of the detectors is linear even for the highest dose rates achievable in radiotherapy; (iii) the ultra–thin 3D silicon

detectors also showed good signal discrimination in a complex mixed gamma–neutron pulsed radiation field and therefore they can work without interference from the photon beam; (iv) the measured performance of the detectors proves their excellent gamma–rejection and high reliability; (v) they showed an excellent performance with a 2% neutron efficiency.

6

Conclusions and Future Work

6.1 Conclusions

The work developed in this thesis presents a novel neutron detector based on an innovative ultra–thin 3D silicon technology with high γ–ray rejection adapted to detect neutrons with ^{10}B–based converters. This study covers the simulations, design, fabrication, characterization and application of that neutron detector. This sensor is useful for mixed γ–n radiation environments, like radiotherapy rooms where active detectors can not be easily used due to the complex characteristics of the mixed and pulsed γ–n field. Therefore, the ultra-thin 3D silicon detector presented in this work is likely the first active silicon sensor for neutron detector specifically designed for that application.

The main conclusions of this work are:

- Monte Carlo simulations (with the GEANT4 and MCNPX codes) were developed

properly for several functions: first, MC simulations served as tool to optimize planar silicon neutron detector designs with boron–based compounds and to compare their performances. Secondly, MC was used to recreate measurement environments to better understanding of the phenomenology of the experiments. Third, feasible designs according to realistic MEMS microfabrication steps were simulated as alternative proposals at current high efficiency neutron detectors. MC simulations were also applied to help analyze experimental data. The well–use of both codes not only has assured the reliability of the detector prototype phase but also has allowed to verify the experimental results.

- The 3D architecture of columnar electrodes was implemented in ultra–thin silicon detectors, allowing to reduce the capacitance and the full depletion voltage considerably in comparison with planar silicon detectors with the same thickness. A comprehensive study, design, and fabrication of this sensor is presented.

- Two designs of ultra–thin 3D silicon detectors with a sensitive substrate of 10 and 20 micrometers were manufactured at IMB–CNM clean room facilities successfully. These thicknesses make them suitable for getting high γ–ray rejection, which is necessary to discriminate the neutron signal in the radiotherapy peripheral radiation field with a high gamma background, aim of this thesis.

- The first design of ultra–thin 3D detectors showed an extremely high γ–rejection factor higher than 10^{-8} for ^{137}Cs at LLD 100 keV. This value is the highest γ–rejection factor for silicon neutron detectors reported so far.

- Several techniques for depositing boron–based compounds (e.g. o–carboranes ($C_2B_{10}H_{12}$, $C_2^{10}B_{10}H_{12}$), ^{10}B pure, B_4C, $^{10}B_4C$) were developed and optimized along this work.

- The first U3DTHIN detectors were covered with o–carborane compounds and characterized with an ^{241}AmBe neutron source and in a nuclear reactor neutron beam. These campaigns showed that: (i) the neutron/background discrimination rate is 12/1 (using a $^{241}AmBe$ source and LLD=180 keV), with around 2% simulated efficiency; (ii) in the measurements in the ITN's nuclear reactor these sensors showed linearity, not saturation effect, a signal–to–background ratio of

43/1 (at LLD=220 keV) and a measured efficiency result of 0.23% (lower than the simulated value, ∼2% due to the deterioration of the converter coating). These measurements were carried out with the first neutron converter tested, $C_2^{10}B_{10}H_{12}$, and evidenced the deterioration that such converter suffers along time and hence its long–term use was ruled out. Hence other boron-based compounds (^{10}B pure and $^{10}B_4C$) had to be studied.

- New boron–based coatings of ^{10}B pure and $^{10}B_4C$ were successfully developed for the next tests. In particular, it was found a way of employing electron-beam physical vapor deposition to obtain boron coatings up to 3 μm thick, highly uniform, stable both in time and thermomechanically, and with good adhesion to the substrate, overcoming the tens of nanometer restriction of previous methods. This represents a landmark in the fabrication of efficient neutron detectors. These converters were employed in the second U3DTHIN design.

- The second U3DTHIN design was improved by implementing a much thinner entrance window, i.e. it was optimized so as to maximize the active area and minimize the energy loss of the charged particles coming from ^{10}B(n, α)^7Li reaction.

- Improved sensors (second design) covered with ^{10}B and $^{10}B_4C$ were tested inside a radiotherapy room and showed their usefulness in such complex γ–n pulsated radiation field. The LINAC used was a *Siemens Primus* working in conditions similar to those in realistic treatments. Sensors showed a very good performance for neutron detection and a very high γ-ray rejection, proving that they are an outstanding alternative to standard detectors for medical applications. For instance, they showed: (i) a linear behaviour even for the highest dose rates achievable in radiotherapy (1000 MU/min), (ii) an excellent γ-rejection, working without considerable interference from the photon beam, and (iii) a 2% neutron efficiency. This is the first active–silicon sensor for neutron detection used inside a radiotherapy room reporting such values.

In summary, the study carried out throughout this thesis lays the technological development of novel silicon sensors for neutron detection based on 3D silicon technology with thin membrane fabrication process. This device represents not only a significant

advance in active neutron detectors but also an interesting contribution, and yet to be explored, to the state-of-the-art of sensors for medical applications. Moreover, these sensors have small size, weight, and consumption, and hence they could respond to the increasing demand of portable systems for neutron detection.

6.2 Ongoing and future work

One of the most important issues to cover in the near future is to consolidate the ultra–thin 3D technology for neutron detectors in order to get a reliable implementation in workplaces that need it. For that, following the research begun and described in this thesis, a considerable number of procedures have been initiated. Some of the most highlights are commented below.

First of all, most of the facilities and radiation sources necessary for this research (hospitals, nuclear reactors, neutron sources, i.a.) are not directly accessible. An important experimental part of this work had to be done in short campaigns in collaboration with hospitals, where there is a restrictive and limited access. Therefore, insufficient campaigns were carried out and more batches of measurements are necessary to improve the statistical study with more experimental conditions. In order to carry out such pending tasks, a new research project has been requested in collaboration with national hospitals.

Secondly, albeit this research has been rather lead to the neutron detection issues, thereupon, and once it has been proved the well performance of the sensors in RT rooms, the next research steps will focus on neutron dosimetry. For that, moderators could be added over the detector surface to detect fast neutrons as well. In this way, if several U3DTHINs covered with moderators of different thicknesses are properly combined, a wide fast neutron spectrum could be detected. Then, from both slow and fast neutron contributions, one could convolute neutron energy correction factors, yielding an accurate dose. In this way, it is hoped that this work will help to quantify the radiological risk for patients in nuclear medicine workplaces.

Third, starting on the basis of the achievements obtained with the ^{10}B deposition in this work, the boron layer etching is being studied to be used on pixelated detectors for neutron imaging.

Fourth, other issue deals with the the integration of all the devices with the readout electronics in a small portable system. It is planned that all the neutron sensor system is miniaturized as much as possible without resulting in an increase in its cost.

Fifth, since the neutron efficiency obtained with ultra–thin 3D detectors in the RT room was relatively low (2%), multiple sensors could be stacked up to the needed overall efficieny. This solution is currently going to test for setting up detection systems that require high efficiency like those used in nuclear security.

Sixth, other options to increase the overall neutron efficiency are based on the microstructured designs explained in section 3.5.1. They are being currently manufactured in the IMB-CNM clean room facilities. Even though considerable improvements in the filled of dummy microstructures have been carried out along this work, this job is still in progress.

Seventh, a second generation of ultra-thin 3D sensors without mechanical support, as 'membranes' (with thicknesses comparable to the average cell diameter), could be potentially used in microdosimetry. In particular, the first tests of CCE and LET measurement for proton therapy applications are going to be carried out shortly.

Finally, from the author's point of view, it is especially hoped that this thesis will encourage to continue the opened research line in the development of innovative silicon radiation sensors for medical applications.

Appendix A

Coating methods of neutron converters

The aim of this appendix is to describe the work developed in order to overcome the issues related with the depositions of compounds based on boron. Getting boron coatings up to 3 μm thick (theoretical value to optimize the neutron efficiency in planar devices, see section 3.4) is one of the key requirements of the proposed neutron semiconductor detectors. These coatings should have not only good uniformity, but also good adhesion and stability over time. Moreover, it is desirable that the used technique for such purposes is repetitive, scalable, and economical. The lack of publications about stable boron coatings (boron films thicker than 1 μm tend to peel off) forced us to develop our own experimental conditions in deposition techniques to get reliable boron coatings. Since the neutron detection efficiency of the devices with boron converter depends directly on the quality of such layers, constant efforts were done in devising new coating methods. However, the goal of this thesis was not to carry out an analysis in depth since that is out of the scope of this work. Therefore, in the next sections only the main issues and achievements related to the deposition of boron-based compounds are described qualitatively, such as: (i) stability (adhesion and aging), (ii) homogeneity, (iii) topology, (iv) compatible substrates, (v) process safety, and (vi) repeatability.

The boron-based compounds studied were: carboranes, microcrystalline ^{10}B solids and boron carbides ($^{10}B_4C$ and B_4C).

A.1 Carboranes

The first boron–based compounds tested for this work were the carboranes, macromolecule clusters that are mainly composed by boron, carbon, and hydrogen. After the functional analysis of several cluster–compounds like $Na_2B_{12}H_{12}$, $B_{10}H_{14}$, and $C_2B_{10}H_{12}$ (see Figure A.1), the last one, known as o–carborane, was selected as the most feasible borane because the others presented problems of toxicity and reactivity.

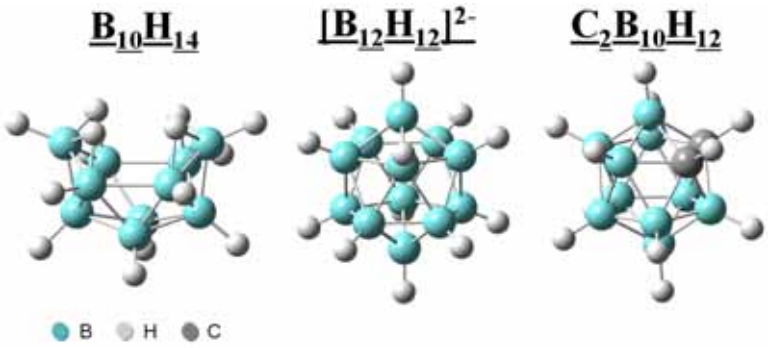

Figure A.1: Chemical structures of carboranes - Schematic of three carboranes synthesized in this work: $B_{10}H_{14}$, $Na_2B_{12}H_{12}$, and $C_2B_{10}H_{12}$.

These compounds were synthesized in collaboration with the Inorganic Materials and Catalysis Group which belongs to the Institute of Materials Science of Barcelona (ICMAB, CSIC) [133]. Boron and carbon are elements that have the ability to build molecules of unlimited size by covalent self-bonding [134, 135, 136, 137, 138, 138, 139, 140]. Carborane needs to be mixed with another compound that works as an *adhesive matrix* over the detector. On the other hand, a solvent is necessary to mix the solution adequately and keep it well–preserved until its deposition. Table A.1 shows the main adhesive matrixes and solvents tested during this work.

Table A.1: Main adhesive matrixes and solvents used with carboranes

Adhesive Matrix	Solvent
PVC	Tetrahydrofuran (THF), diglima (Eter-2-metoxietilo)
Cyanoacrylate	Acetonitrile, Dibromoethane

Tens of solutions were synthesized, changing their chemical concentrations,

densities, and combinations in order to obtain the most suitable. Both PVC and Cyanoacrylate showed good adhesion abilities over the devices. The first neutron measurements were carried out with an o–$C_2B_{10}H_{12}$/PVC mixture (see section 5.1.2). Although PVC presented a good behaviour in the first tests, the converter synthesized with Cyanoacrylate (see section 5.2.2) showed even better resistance to degradation when subjected to a chemical attack with hexane and water. Most of the samples were synthesized with the tetrahydrofuran (THF) solvent. THF is volatile and evaporates easily, leaving an adhesive matrix (PVC or Cyanoacrylate) and o–carborane with densities from 0.5 to 1.5 g/cm^3. Thus, boron–based solutions may be chosen with high ^{10}B concentration and the desirable density depending on the requirements of the design (the effect of the converter density is explained in subsection 2.4.3.1). These compounds are low cost, adaptable, compatible with silicon devices, and they can be easily deposited on whole wafers by the Spin–coating method, explained below. The parameters of two solutions used in the experiments carried out in sections 5.1.2 and 5.2.2 are summarized in Table A.2.

Table A.2: O-carboranes used as converter coatings

Boron Cluster	**Matrix**	**Solvent**	**Density (g/cm^3)**
$O-C_2B_{10}H_{12}$	PVC	THF	0.5
$O-C_2B_{10}H_{12}$	Cyanoacrylate	THF	1.37

A.1.1 Spin-coating method

Once that the o–carborane/adhesive mixture has been synthetized, it has to be deposited over the detector evenly and with a controlled thickness, according to the Monte Carlo simulations (see 3.4). Spinning is a simple process for the deposition of viscous materials, and for this reason the spin–coating method was used to deposit these carboranes. Figure A.2 shows the manual spinner[1] that was used for all the depositions of o–carboranes.

A drop of few μl of o–carborane has to be dispensed with a micropipette at the device center, the quantity depending on the detector size and desirable layer thickness. Then, the spinner accelerates up to spread the solution towards the edges of the device.

[1]WS-400A-6NPP/LITE Model

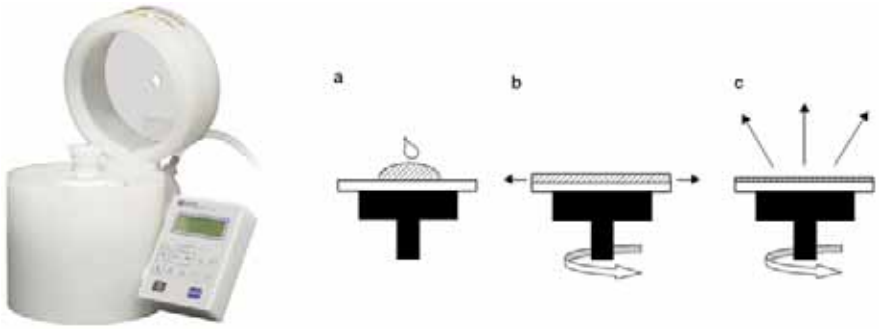

Figure A.2: Manual Spinner used to deposit O-carboranes - Left: Photo of the spinner, WS-400A-6NPP/LITE Model, used to deposit the O-carborane/Matrix mixtures, located in the microfabrication laboratory at IMB–CNM facilities. Right: Spin-coating process to deposit o-carboranes whose main steps are: (a) O-carborane/Adhesive matrix solution deposited on wafer, (b) acceleration, where the solution is uniformly coated over the wafer surface, and (c) Partial drying via evaporation of the solvent [141]

In order to correlate the spinning parameters (spin speed, acceleration, time) with the required coating thickness, and since the process is manual, many trials were done to optimize the resulting coatings. For instance, Table A.3 contains the final parameters used for the solution used in section 5.2.2. It was observed that: (i) most of the solvent evaporates during the first seconds, which changes drastically the viscosity of the sample that dries quickly; (ii) a rapid acceleration is needed to distribute evenly the material over the device; (iii) an error in the spin speed of ± 50 rpm might result in 10% thickness difference; (iv) due to the liquid quality of the o-carborane/adhesive mixture, the deposited layer may contain bubbles and micelles (created during the THF evaporation) or pinholes which are kept inside the matrix when this dries. Hence, the spin–coating is not entirely the ideal method to get highly uniform thicknesses.

A Dektak–150 profiler was used to measure the deposited thickness after each spin–coating. Figure A.3 shows one of the many samples done so, which the highly bumpy texture of the coating due to the reasons commented above is observed. Despite this, o–carboranes were useful to carry out the first tests, as demonstrated the good performance of the sensors shown in sections 5.1.2, 5.2.2, and 5.2.3.

Table A.3: Spin-Coating Parameters

Solution	20 μl $O-C_2^{10}B_{10}H_{12}$
Speed	800 rpm
Time	5 min
Average Thickness	20 μm

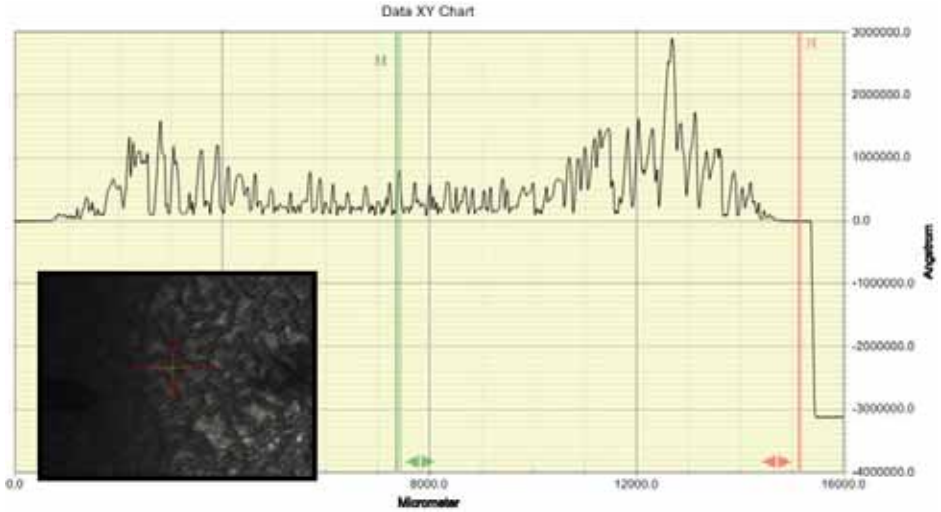

Figure A.3: Profile of an o–carborane/matrix deposition with spinner - Profile of a typical o–carborane/adhesive matrix coating deposited with a manual spinner. The inset shows the top view of such coating, where is observed a considerably pitted layer.

A.1.2 Filling of 3D structures

The o–carboranes used above to coat planar devices were also utilized to try to fill etched test structures, similar to those proposed as novel designs in section 3.5. Several methods were applied: (i) filling the 3D structures with micro–pipettes (Figure A.4); (ii) flooding the samples until the solvent evaporates; (iii) synthesizing a converter with low viscosity able to seep through the perforations and spread by capillarity. Figure A.5 shows some of the results obtained with these methods in silicon with drillings. These SEM images have been taken of cross–sections done with a diamond point scribe to avoid removing the converter filling. Even then, some parts of the fillings have jumped out, as it is visualized in the images. Moreover, it is evident that in some cases the fillings are partial, i.e. there are pinholes and hollows inside the columnar fillings. These results come from techniques that have not been optimized yet but can be easily

improved with fluidic methods.

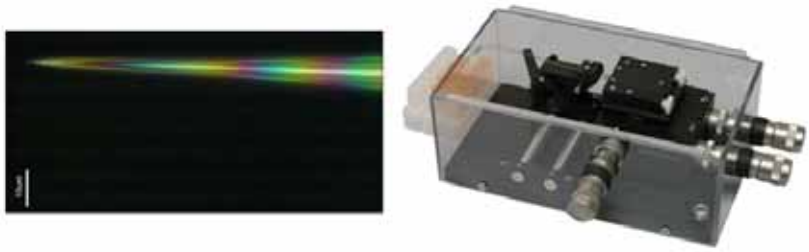

Figure A.4: Micro-pipettes used to fill 3D structures - Left: microscope photo of a pipette with an opening diameter of few micrometers. This was fabricated with borosilicate glasss modeled with a P-30 vertical micropipette puller. Right: Picture of the micromanipulator Cantisens FU-401 used to fill the liquid converter inside the perforations of the 3D structures.

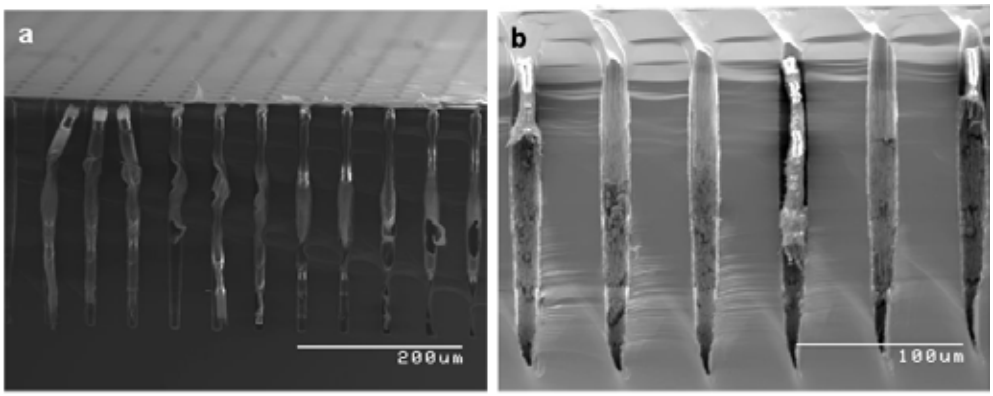

Figure A.5: SEM images of the columnar holes filled with o–carborane - (a) SEM image of one sample perforated with columnar holes (200 μm height, 10 μm diameter) flooded in liquid o–carborane. When the THF evaporates, the o–carborane solidifies slowly, adapting to the 3D-shape. (b) Detail of other 3D estructure that shows the carborane contained inside the perforation.

A.2 Microcrystalline ^{10}B solids

A.2.1 ^{10}B Coatings

The fabrication of boron coatings is difficult and unsafe since this element is brittle and under certain experimental conditions is hazardous. Table A.4 shows some of the main characteristics of boron.

Table A.4: ^{10}B Characteristics

Molecular Weight	10 g/mole
Density	2.34 g/cm^3
Boilg Point	2550 °C
Melting Point	2079 °C
Resistivity	10^5 Ω·cm
Thermal Conductivity	0.274 W/cm/K @20°C
Specific Heat	0.25 Cal/g/K @20°C
Heat of Fusion	5.3 Cal/g·mole

It is important to note that boron may present fire hazards, e.g. it is slightly flammable in presence of sparks, heat or flames, and is reactive with oxidizing agents and acids i.a. [142], although it is non-flammable in presence of shocks. In addition, boron in powder form is able to create a dust explosion. Therefore particular care must be taken when this element is used, as is indicated in the next paragraphs.

An important parameter to develop thin films is the sticking coefficient, which deals with the probability that an impinging particle remains on the surface, i.e. a high-sticking coefficient means that the particle stays at the point of collision, whereas a low coefficient involves that only the energetically favourable attached species will stick and the others will desorb. This coefficient is generally lower for the chemical vapor deposition (CVD) process than for the physical vapor deposition (PVD) process. Depositing boron with CVD makes use of diborane (B_2H_6) and hence various safety requirements and chemical handling regulations are necessary, whereas PVD is a widely used technique in semiconductor integrated circuit manufacturing, eliminating contamination and allowing high deposition rates and improved evenness and integrity. PVD may be done by means of two safe techniques: electron-beam evaporation and sputtering [102]. The evaporation technique used in the present study is PVD with an Electron-Beam-Gun (EBG), also so-called EBPVD.

The main variables to take into account when evaporation techniques are used are:

- Nature of the substrate.
- Temperature of the substrate during deposition.
- Rate of deposition.

- Deposition thickness.
- Angle of incidence of the vapor stream.
- Pressure and nature of the ambient gas phase.

All of these parameters must be combined adequately such that the final coating is stable.

In thin-film technology, other of the main concerns is the adhesion of the coatings, being poor adhesion the norm since in evaporation there is no inherent removal of bonded atoms. Boron tends to expand when the melted liquid is solidified after evaporation, and as a result the generated stress may well cause cracks and peelings in the coating, which make this film useless for being used as converter layer. In order to improve the adhesion of the deposited films some *adhesion layer* (additional film that improves the adhesion between the main film and the substrate) may be used provided that this layer does not affect on the operation of the device over which is deposited. That adhesion layer is usually in the range of few nanometers (from 10 to 100 nm typically) since that only its surface properties favour the adhesion, not its volume properties. The adhesion layer and the main film may be deposited one after the other in the same evaporation process. Some of the most common elements used as adhesion layers for their bond-forming abilities are Titanium and Chromium. This type of complementary layers is used in this study to make the deposition process robust and stable, as is explained below.

Another relevant issue in the thin films is the stress when they are deposited on the wafers, which is caused by the mismatch due to either the thermal expansion between the deposited film and the substrate (extrinsic stress), or the film nucleation and growth process itself (intrinsic stress) [105]. Stresses can be either compressive or tensile (by convention, negative stresses are compressive), as Figure A.6 displays. For example, there is a direct relation between the intrinsic stress and the film density, and as a result, the adhesion can be related to the density of the film that stays on the substrate. Note that if the atoms on the substrate are bombarded by energetic particles of the target, they can be squeezed densely to form a film that is more compact and united, and therefore tends to expand itself, creating compressive stress. In contrast, the thermal/extrinsic stress is caused by the substrate temperature change and the

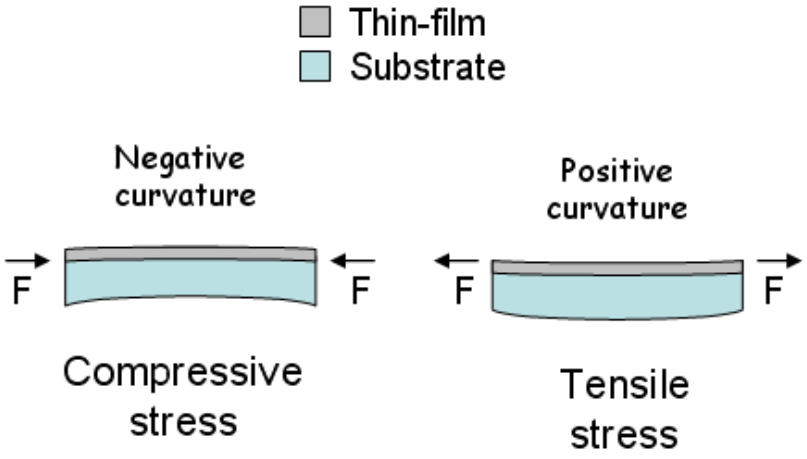

Figure A.6: Sketch of the type of stresses - Definitions of compressive (left) and tensile stress (right).

difference between the thermal expansion coefficient of the substrate and the film. Depending of the relation between both, the stress can be tensile or compressive. At the same time, if the coefficients of thermal expansion of substrate and deposited material are similar, the thermal strains are less likely between both. Both types of stresses must be take into account to understand the performance of these coatings and improve their features [143].

Equation A.1 displays the calculation of the extrinsic stress from differences thermal expansion coefficient:

$$\sigma = E_f \cdot (\alpha_f - \alpha_s) \cdot \frac{\Delta T}{1 - \nu} \tag{A.1}$$

being E_f the Young's modulus of the film, ΔT the temperature difference between the deposition and measurement (although the real situation is usually more complex, e.g. the stress relaxation can occur during deposition at high temperature), α_f and α_s the coefficients of thermal expansion for the film and substrate respectively, ν the Poisson ratio of the film. Table A.5 shows the coefficients of thermal expansion of boron and various substrate materials. After the deposition process, when the wafer is cooling down to room temperature, the silicon substrate shrinks and, depending on the film deposited on it, the stress can be manageable or so high that the wafer can even be broken. High tensile stress causes the film to peel.

Table A.5: Coefficients of thermal expansion of several materials at 300 K.

Material	**Expansion Coefficient** $(10^{-6}/°C)$
Boron	6.9
Silicon	2.6
Titanium	8.5
Chromium	6.2
Alumina	6.8
Aluminium	25
Silicon Oxide	2.5
Tantalum	6.5
Silicon Nitride	0.5

Few studies about boron coatings with EBPVD have been published: in 1985 Labov et al. [144] reported the evaporation of thin films of natural boron, up to 100 nm thickness; in 1989 G.E. Thomas proposed a technique for producing thin boron films [145] but without enough information to reproduce their coatings, and twenty years later, in 2008, M. Vidal–Dasilva et al. [146] presented a technique for thinner layers, of tens of nanometers. Additionally, two of the main neutron solid state detector research groups that have been working intensely in the field of boron deposition have bet on developing coatings by other techniques: R.J. Nikolic's group has worked to get boron backfillings with the CVD method [58], while D.S. McGregor's group reached 1.8 μm thick boron layers by evaporation in 2001 [147] but later changed to ^{6}LiF evaporation by condensation deposition [148]. No data were found in the literature on the evaporation of reliable thick ^{10}B layers with electron–beam.

In an attempt to overcome this issue, a batch of evaporations using silicon as substrate were carried out as is explained in the next paragraphs. This part of the work describes the technique used to deposit up to 3 μm thick ultrapure ^{10}B crystalline films by electron–beam evaporation over silicon with repeatability and stability. The films deposited on the substrate have been analyzed using a profiler, a Scanning Electron Microscope (SEM), X-Ray Spectrometry Analysis (EDX), climate chamber, and finally a Peel–Test. The results show that thicker coatings of ^{10}B may be deposited with the technique presented. Hence, electron–beam physical vapor deposition of ^{10}B thick films is presented as a reliable method for realizing coatings over planar substrates for

applications in MEMS–based neutron detectors.

Microcrystalline ^{10}B may be synthesized at high isotopic purity by enrichment in the raw crystalline natural boron. During this work, hot–pressed parts of 99% pure crystalline ^{10}B with a density of approximately 60% of its solid granular density, 2.46 g/cm^3, were prepared from ^{10}B powders and finally cracked in order to get granular pieces of size from 1 mm to 10 mm, as Figure A.7 shows.

Figure A.7: Image of ^{10}B hot–pressed chunks - (a) ^{10}B lumps manufactured how hot–pressed raw crystalline ^{10}B. (b) ^{10}B crystalline fracture parts with sizes ranging from 1 to 10 mm.

Figure A.8 shows the Univex-450B (Oerlikon) Electron-Beam Gun Machine for Physical Vapor Deposition, located in the IMB–CNM clean room facilities (Fig. A.8 (a)), and the design of its evaporation unit (Fig. A.8 (b)) with the ^{10}B granular pieces fitted inside a graphite crucible (inset). The substrate is at a distance of 210 mm from the boron source and is heated radiantly by an IR lamp, which raises the wafer/substrate temperature. The deposition rate is measured by a quartz crystal oscillator.

The used substrates were, in the first tests, pieces of a n-type polished silicon wafer, and finally were silicon detectors. One of the becoming options was done using some nanometers of an adhesion layer with an expansion coefficient close to the boron coefficient to reduce the stress between layers, as was explained above. Titanium was evaporated over the silicon substrate and then the ^{10}B was evaporated to the required thicknesses: sequential evaporation of 80 nm Titanium and 0.33 μm, 0.8 μm, 0.92 μm,

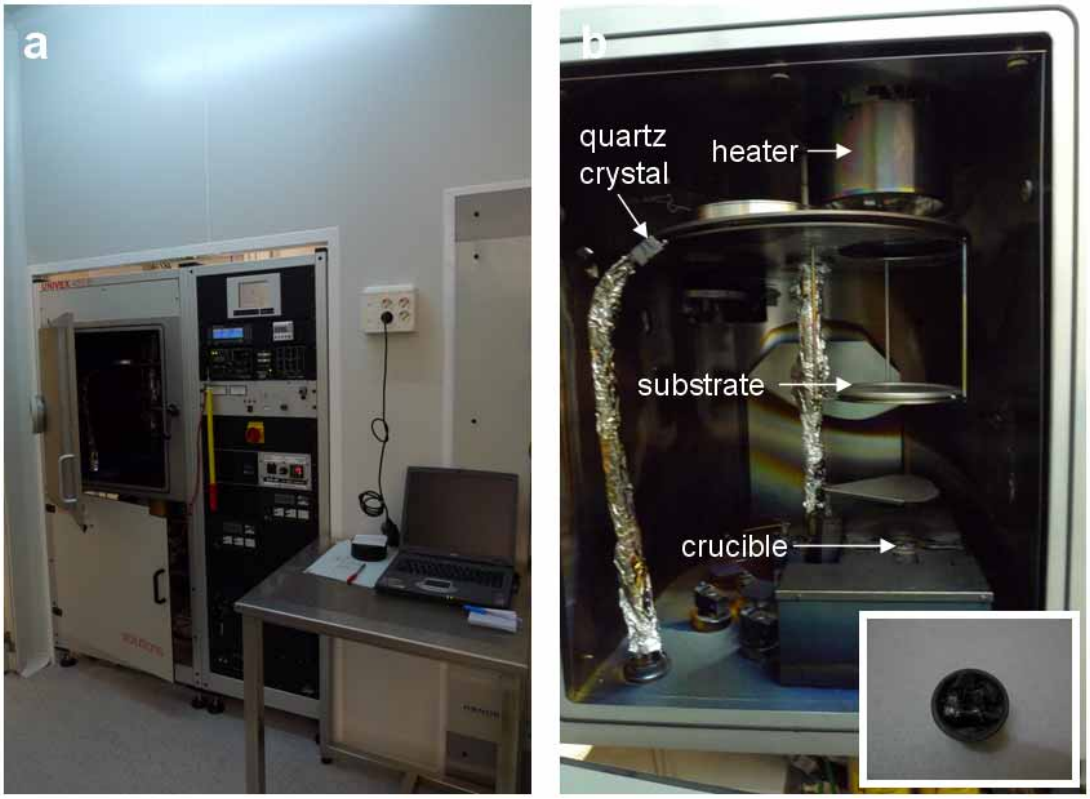

Figure A.8: Electron-Beam Gun Machine for Physical Vapor Deposition - (a) EBPVD in the IMB–CNM clean room facilities. (b) Interior of the EBGPVD chamber with the main pieces that control the process: (i) quartz crystal oscillator that measures the deposition rate, (ii) IR lamp which heats the substrate, (iii) substrate, where the wafer is placed a distance of 21 cm from the crucible, and (iv) crucible with the ^{10}B-lumps as target of the electron–beam gun. Note that a built–in holding system was used to bring the substrate nearer to the target.

and 1.08 μm of ^{10}B crystalline films (four samples) were deposited successfully. Table A.6 shows the thicknesses of the four samples developed in consecutive steps.

Table A.6: Samples with consecutive evaporation of Ti and ^{10}B.

Sample No.	Layers Ti/^{10}B	Ti (nm)/^{10}B(μm)	^{10}B average thickness
1	1/1	80/0.33	0.33
2	2/2	80/0.80	1.13
3	4/3	80/0.92	2.05
4	5/4	40/1.08	3.13

Table A.7 summarizes the experimental conditions found for ^{10}B depositions over silicon and detectors.

Table A.7: Experimental conditions used in the EBPVD for ^{10}B coatings

Item	Conditions
Heater Temperature	350°C
Initial Pressure	$3{\cdot}10^{-7}$ mbar
Pressure during the evaporation	$[1.2-6]{\cdot}10^{-6}$ mbar
Substrate-Source Distance	210 mm
Deposition rate (Quartz Crystal)	$[0.1-0.4]\dot{A}$/s
Deposition rate (measured)	$[0.13-1.2]\dot{A}$/s

The results of the deposition showed that ^{10}B coatings were well–adhered, uncracked, and had smooth profiles. Figure A.9 contains the front view of two samples with ^{10}B evaporated with good aspect. The colour of the ^{10}B coating varies from green to brown for the fine crystalline (amorphous state), to dark gray for the crystalline form. In some case the SEM images confirmed that one of the worse defects which can present the coating is caused by spitting of ^{10}B from the melt impacting the target. Additionally, in previous samples were observed that the roughness of silicon substrate can screen off the grain size of the deposited ^{10}B, and that coatings without voids or defects turn the coating less prone to react with gases of the atmosphere, improving their temporal stability.

The deposited films were analyzed checking their thickness, morphology, composition, adhesion, and thermomechanical stability. For the analytic study of the deposited

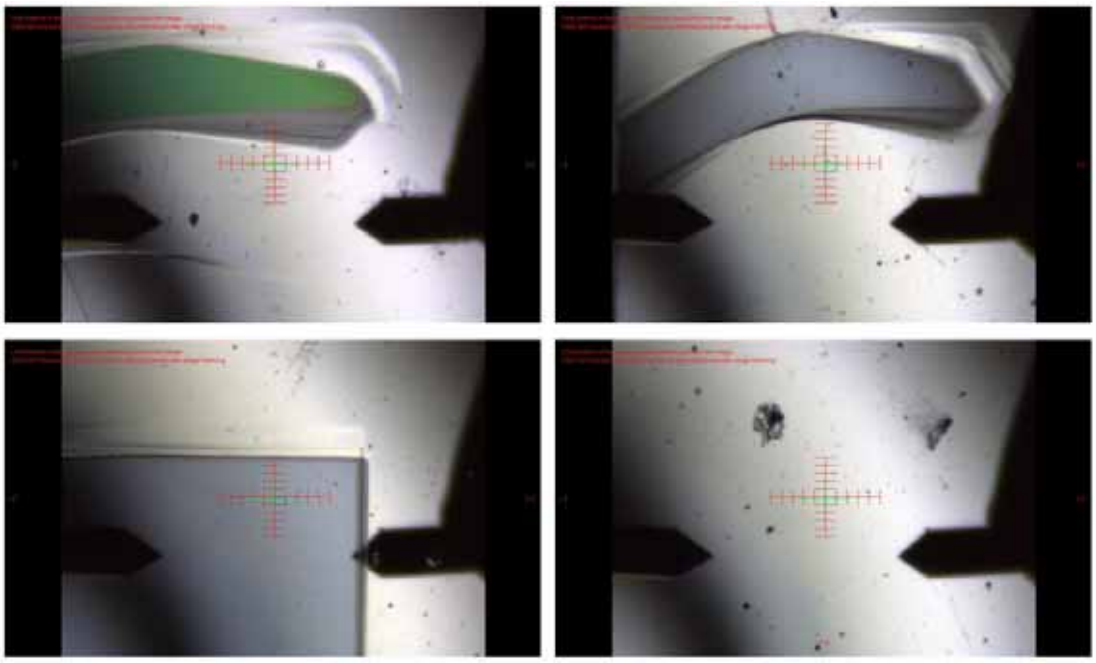

Figure A.9: Photos of the ^{10}B coating over silicon substrate - Photos with a Dektak-150 profiler for the deposited ^{10}B coatings on two silicon samples. Pictures show the nicks done before carrying out the deposition to measure the thickness. In the top, the nick of the first figure (left) shows a greenish tone colour of the first deposited layer (0.33 μm), whereas if the coating is thicker, that tone tends to get dark (right). In the bottom, the picture on the left displays a pattern well defined, distinguishing clearly two zones with different thickness; and on the right is shown the damaging effect on the layer of the target spitting.

^{10}B on the four samples, each of them were undertaken for profiler, Scanning Electron Microscope (SEM), X-Ray Spectrometry Analysis (EDX), and climate chamber analysis. Results are explained below.

A Dektak–150 profilometer was used to measure the thickness deposited after each evaporation. Table A.8 shows the average thicknesses for each of the silicon above developed sample. The profiles measured of these deposits were highly uniform, as Figure A.10 displays.

Table A.8: ^{10}B Thicknesses measured by profiler

Sample No.	Thicknesses ($\dot{A}$)
1	3357 ± 1
2	11502 ± 1
3	20512 ± 1
4	31306 ± 1

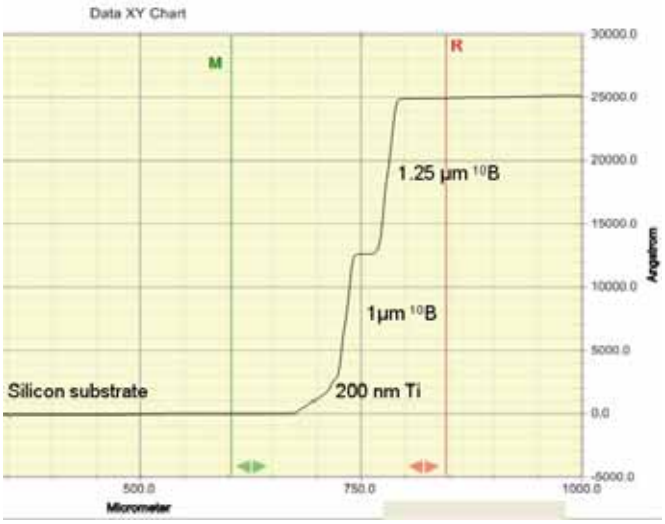

Figure A.10: Measured Profile of an evaporated coating by EBPVD - Profile image with a Dektak-150 Profilometer for the deposited ^{10}B coatings. Three zones are observed over the silicon substrate: the first deposition of 200 nm thick of the Titanium, roughly 1 μm of ^{10}B evaporated, and almost 1.25 μm of another ^{10}B coating.

The morphological details were measured by SEM studies with a *Zeiss Auriga* SEM placed in the IMB–CNM facilities. Figure A.11 shows the SEM images for all the four

substrates, where the Titanium coatings (bright bands) are differed from ^{10}B layers (dark bands).

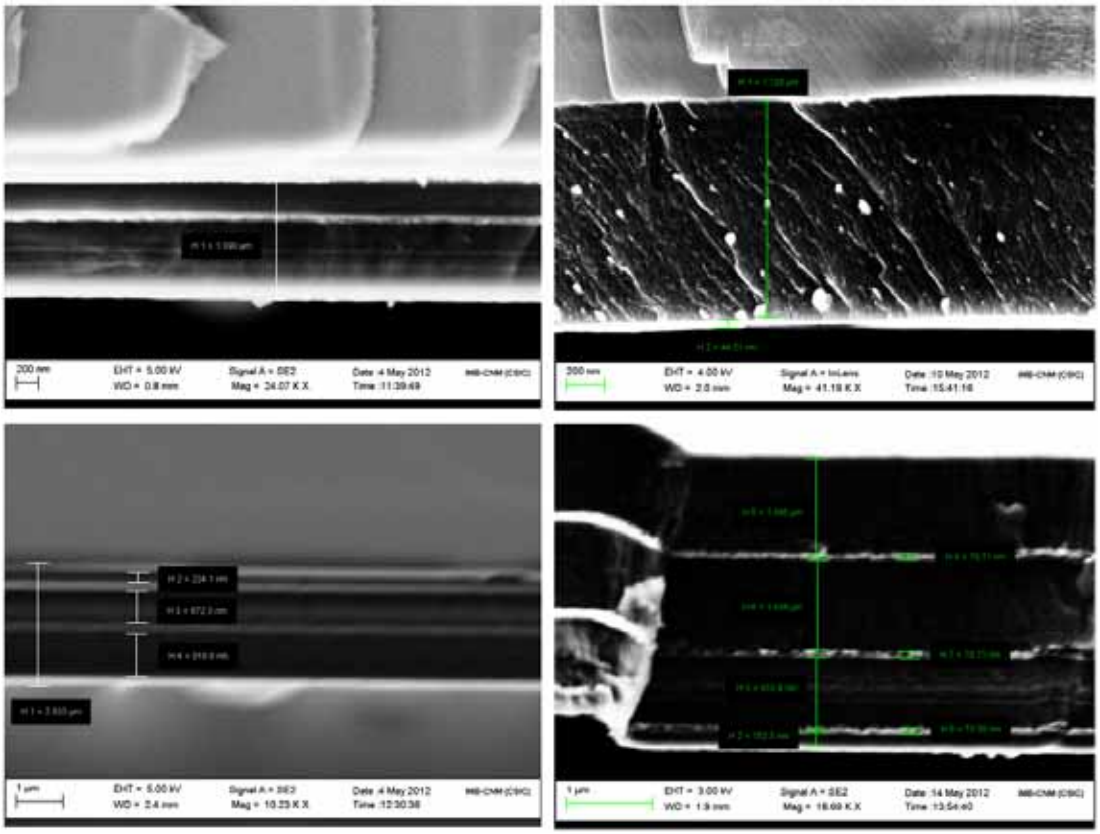

Figure A.11: SEM images of the cross section of electron-beam deposited 10B coatings on silicon substrate - SEM images of the cross sections of electron-beam deposited 10B coatings on silicon substrate where the bright bands display the Titanium coatings and the dark bands the ^{10}B layers. The ^{10}B total thicknesses are: (a) 1.090 μm of two Ti/^{10}B superimposed layers, (b) 1.138 μm (c) 2.633 μm of Ti/^{10}B layers, (d) 3.351 μm of Ti/^{10}B layers.

The purity of the deposits was checked by energy dispersive X–ray (EDX) analysis with an Auriga scanning electron microscope. Figure A.12 shows the EDX analysis done to a 1 μm thick ^{10}B layer, where data confirm the composition of the evaporated material: 85% boron and roughly 12% titanium. Besides of the elements of the deposits, a little percent of oxygen was detected as well (it is likely that this element came from the substrate and not from air absorbed in the deposit because in the latter case other elements, such as nitrogen, would have been detected as well).

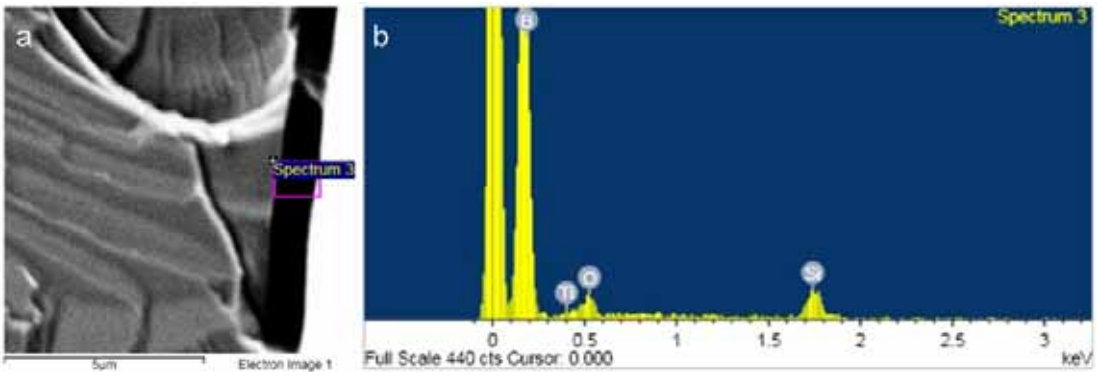

Figure A.12: EDX analysis of 1μm thick ^{10}B layer - (a) SEM image of 1 μm thick ^{10}B on silicon substrate in which the section subjected to X-ray spectroscopy is framed. (b) EDX graph with the identified elements which compose the up-side of the sample: boron, titanium, oxygen and silicon.

In order to assess the viability in the natural environment, cycles with the characteristics specified in Table A.9 were performed. After this cycle, the coatings remained well adhered.

Table A.9: Temperature cycle testing parameters

Parameters	Values
Cycle No.	10
Minimum Temperature	40°C
Maximum Temperature	100°C
Stabilization Time (T_{max})	1 min
Stabilization Time (T_{min})	3 min

Results have shown that adhesively bonding multiple layers of ^{10}B made by EBPVD onto silicon substrates and detectors, with variable thickness from 0.35 μm to 3 μm, are reliability.

A.2.2 Backfilled ^{10}B

Applying the EBPVD process over perforated structures (similar to the prototypes proposed in section 3.5), it was proved that inside of the drillings there were columnar nano and micro crystalline structures of ^{10}B. These were nucleated and agglomerated in clusters of nanoparticles, with an extremely small size [30–100] nm. Figure A.13

shows four SEM images of one of such perforated prototypes in which is evaporated 1 μm thickness of ^{10}B: on the drilling up-side (trench openings) is deposited around 1 μm thickness of ^{10}B (Fig. A.13 (b)), and inside it (trench walls) ^{10}B is got caught to the wall side (Fig. A.13 (c) and (b)). It was observed two highlight phenomenons inside the trench walls: (i) the growth inside the trench walls 'follows' the morphology that was created by the DRIE etched when the trenches were done, and (ii) the ^{10}B deposit looks to grow in columnar extension.

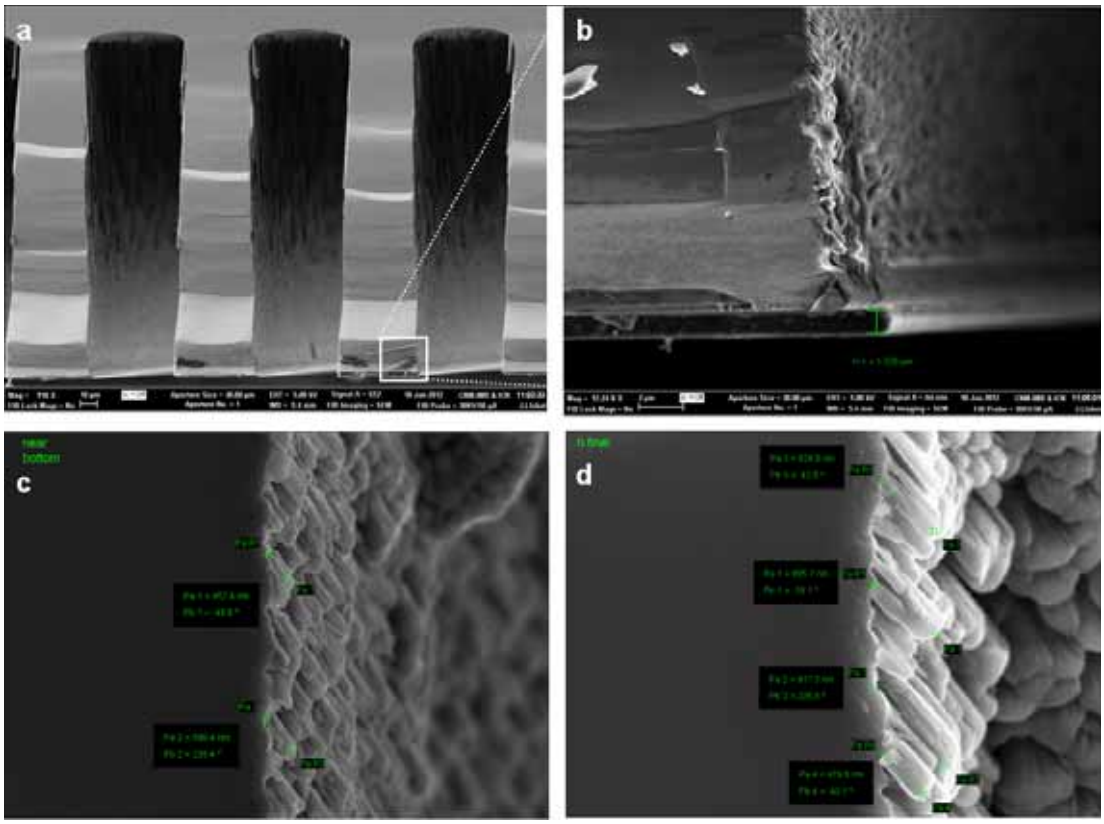

Figure A.13: Perforated prototypes backfilled with ^{10}B - SEM images of cross–sections of a perforated prototype backfilled with ^{10}B evaporated by EBPVD: (a) Cross–section of some of the perforations (trenches of 200 μm height and 50 μm width). (b) Top–side of one trench opening with 1 μm ^{10}B deposited. (c) and (d) Images near the trench bottom (around 200 μm depth) that show how the average height of the ^{10}B *columns* decreases as one moves deeper to the bottom of the trench.

Other interesting effect observed is display in Figure A.14: it shows a SEM image of the nucleation phenomenon, which presents a grainy form. Nucleation affects directly

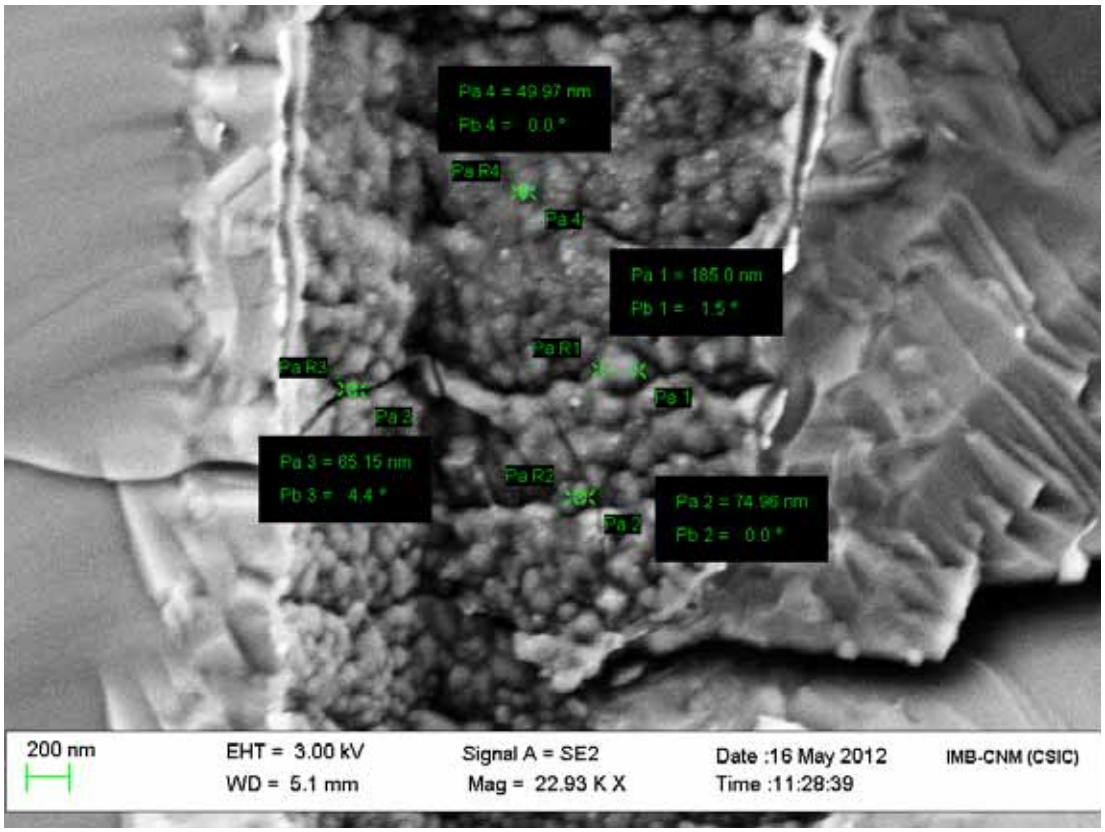

Figure A.14: ^{10}B **nanoparticles grown inside trenches** - SEM image of ^{10}B nanoparticles produced via physical vapor deposition. Spherical conglomerates of ^{10}B nano-clusters.

in the packing efficiency of the ^{10}B within the trenches. A low packing density could reduce the whole calculated neutron absorption efficiency, as is explained in Section 2.4.3.1. Therefore, it is necessary to control the size of the evaporated ^{10}B as much as possible in order to increase the packing density within the trench walls. Some observed features deserve to be commented:

- It was observed that the ^{10}B covers well the device surface, even in surface contours or patterned samples.

- The ^{10}B deposited seems to follow a crystalline type of growth, growing preferentially in the normal direction to the surface over which it condenses.

- In principle, the size of the ^{10}B deposited crystals is small, in the order of nanometers, but it is grouped into clusters of ^{10}B nanoparticles.

- If the trench aspect ratio is low, it is likely that the entrance of the trench (up-side opening) would become to be blocked when some microns of material is evaporated.

Additionally it is eye-catching the fact that those clusters of ^{10}B nanoparticles seem to have a fractal growth behaviour: first, it was observed under visual inspection (with a scanning electron microscopy) that the deposits presented self-similarity features at different scales, i.e. fractal growth behaviours [149]; secondly, the topography of the materials deposited with CVD or PVD draws self-similar features that allow to apply the description of the fractal analysis method [150]. In particular, it has been already reported that the structure of some boron crystals depends highly on the morphology of the substrate on which is deposited [151].

Figure A.15 shows one of the last depositions over one of the etched 3D structures (proposed in section 3.5) in which it was evaporated 3 μm thick of ^{10}B.

With the evaporation method we have yielded good performance to cover trench walls, however it has not been optimized yet to fill completely the trenches, and therefore is an ongoing task.

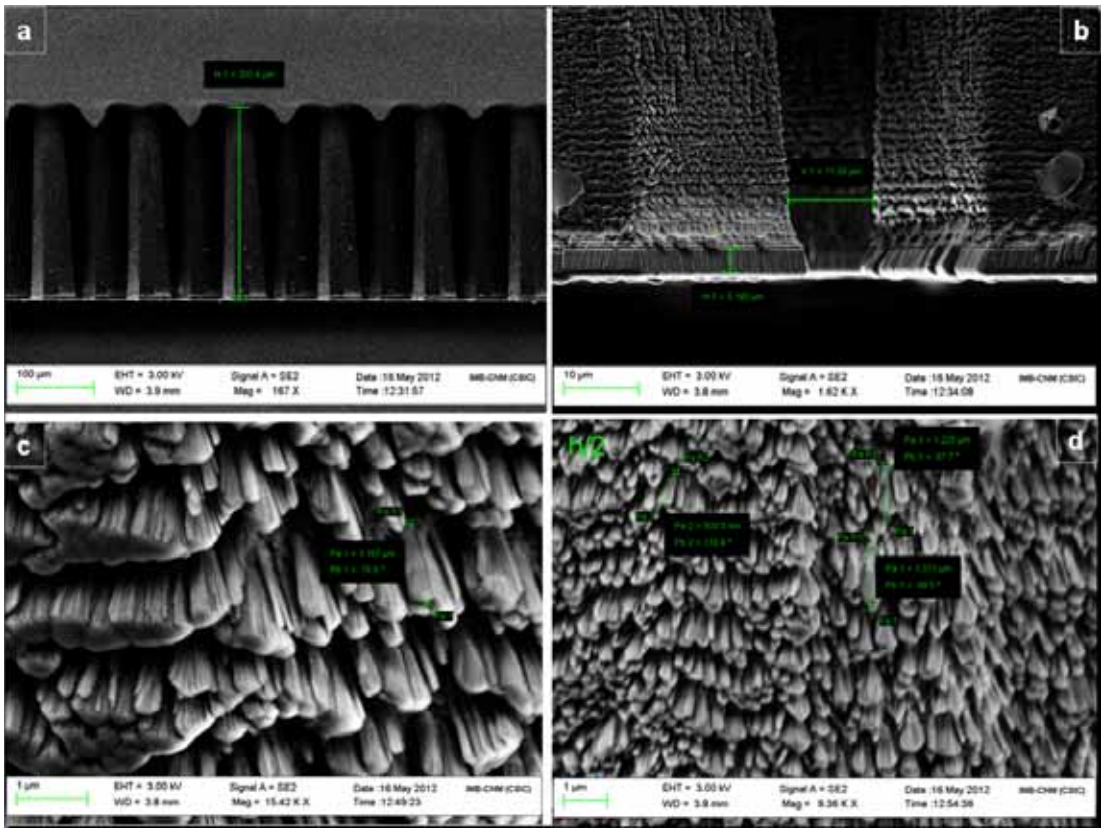

Figure A.15: Backfilled ^{10}B of 3 μm thick - (a) SEM image of a cross–section of one of the etched structures with drillings of 250 μm depth. (b) Picture where ^{10}B 3 μm thickness over the planar surface is visualized. (c) Detail of the ^{10}B deposited in the columnar walls where ^{10}B columns of average 1.23 μm height are grown up to. (d) SEM image at column half height where the average height of the ^{10}B grown columns is from 800 nm to 1.3 μm.

A.3 Boron Carbide

Boron carbide (B_4C) is a stable monocrystalline material, not hygroscopic, and the third hardest material known (with a Mohs hardness of 9.5). B_4C has high wear resistance, high Young's modulus, and high thermal and chemical stability. Table A.10 summarizes the main boron carbide physical and chemical properties.

Table A.10: B_4C Characteristics

Molecular Weight	55.3 g/mole
Density	2.52 g/cm^3
Boiling Point	3500 °C
Melting Point	2450-2763 °C
Solubility in Water	insoluble
Thermal Conductivity	30-42 W/cm/K @25°C
Thermal Expansion Coefficient	510^{-6}/°C
Young's Modulus	450-470 GPa
Specific Heat	12.5 Cal/mol/C
Thermal conductivity	17-42 W/m·K
Heat of Fusion	1350-2030 Cal/g

In this work $^{10}B_4$C enriched 99% in ^{10}B was synthesized as target for RF sputtering machine. Sputter deposition is an overlay process based on a physical vapor deposition method. The method consists in accelerating ions by an electric field towards the surface of a target (material that is going to be deposited). Then, the kinetic energy of the collided ions is transferred to the atoms of the target surface that are released and deposited on a substrate. The sputtering system is used extensively in the semiconductor industry for thin–film deposition and etching [102]. There are three types of sputtering: DC (diode), RF (radio frequency), or magnetron. In this work a built–in RF magnetron sputtering located in the Department de Física Aplicada i Óptica (Universitat de Barcelona) was used [152, 153, 154, 155].

A sputtering B_4C target enriched in ^{10}B ($> 99\%$), bonded to a Cu–plate, was made. The substrates (pieces of wafers and detectors) were cleaned in ultrasonic baths and deionized water and dried with blown N_2. Then, the detectors were mounted in a mechanical support which was fitted inside the RF sputtering machine (see Figure

A.16).

Figure A.16: RF Sputtering machine for PVD - Photographs of the RF sputtering machine used in this work. The detectors were placed within the substrate holder, which is positioned in front of the $^{10}B_4C$ target.

Prior to deposition, the whole chamber of the system has to be evacuated and the substrate degassed, which takes several hours. Later, a low argon[1] partial pressure was kept, and the substrate was heated by a quartz lamp below 300 $°C$. The chamber base pressure was below 10^{-4} Pa, the RF power was 400 W, increasing the RF power in steps of 50 W waiting 5 minutes after each step. The control over the energy of the bombardment of the argon ions is a key point because this has influence on the mechanical properties of B_4C films [155]: when the argon ion energy increases, the stress of the B_4C coating increases as well.

Several deposits were carried out in different sessions, measuring the coating with a Dektak profilometer to obtain the parameters that give the required thicknesses. All the films had excellent adhesion (as shown by peel-tests) and uniformity. Figure A.17 shows a microscope image of one of the ultra–thin 3D detectors (section 4.2) covered with 1.5 μm $^{10}B_4C$ coating, which was used for the measurements carried out detailed in section 5.3.2. Figure A.18 displays a photo of four detectors that were covered by different thicknesses: 2.2, 1.5, 1, and 0.5 μm of $^{10}B_4C$ coatings (from left to right).

[1]Argon is one of the common processing gases used in RF sputtering. In this work, this gas was mixed with N_2 (in a low percentage) in order to reduce the stress of the coating.

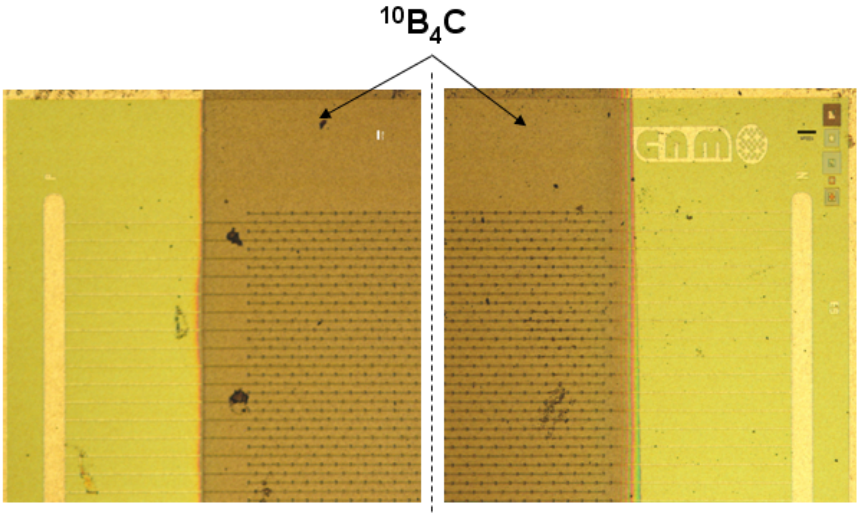

Figure A.17: Microscope photo of 1.5 μm of $^{10}B_4C$ coating over an ultra–thin 3D detector - Photos of the lateral sections of an ultra–thin 3D detector over which has been deposited 1.5 μm of $^{10}B_4C$ by RF sputtering. The boron carbide film shows a brown colour. The contact strips were protected to avoid the coating (green tone).

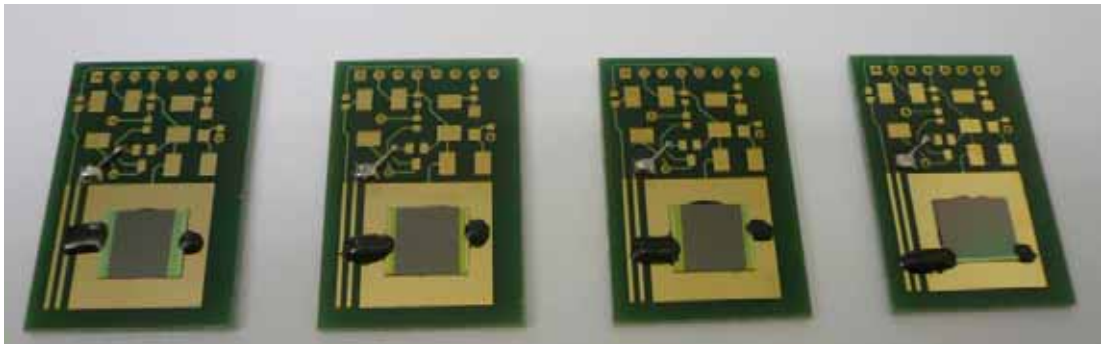

Figure A.18: $^{10}B_4C$ coatings over ultra–thin 3D detectors - From left to right: 2.2, 1.5, 1, and 0.5 μm thick of $^{10}B_4C$ coatings. The boron carbide deposited shows a grey tone, matching the active area of the detector. Lateral zones (green tone) are without coating to let free the metal contacts where the wire-bonding has to be done (protected by the black epoxy). These detectors are mounted in printed circuit boards, ready to be tested.

A. COATING METHODS OF NEUTRON CONVERTERS

These are the first process of $^{10}B_4C$ coatings of more than 1 μm thickness over silicon detectors reported so far.

Appendix B

Readout electronics

When a ionizing radiation goes through a detector, it induces a small electrical current. From the electrical point of view, such detector is a current source (with a internal resistance an capacitance) as Figure B.1.a shows. Even though there is not any ionizing particle, there is a small current which is called *leakage current*. When the detector generates a current, with its capacitance, it determines a voltage. The signal from the charged particles detected in the silicon is typically of the order of picoamperes, so it must be amplified correctly. Hence, the measured voltage is the input of the amplifier, as Figure B.1.b shows. This voltage modulates the resistance of an amplifying device, which is usually a transistor. The change in resistance modifies the current in the output circuit, giving a output voltage above the load resistor, which unfortunately has an associated noise. In the next sections are detailed how these issues were managed.

There are two modes for measuring radiation detector signals: current mode and pulse mode. In the first mode, it is measured the total current of the detector, whereas in the pulse mode is counted the individual pulses generated by the particles, giving a pulse height spectrum. In most of the radiation detectors the amplitude of the pulses is proportional to the initial charge signal. In mixed radiation fields, it is possible to select relatively counts of pulses coming from the different particles using thresholds. For instance, the events that want to be measured can have a characteristic signal amplitude that is distinguishable of other type of events, or they might be identified by their simultaneous presence in two detectors. In this work, we have applied the pulse counting mode. In order to obtain a pulse height spectrum, the electronics searches for the maximum of the signal in a pre–defined windows around the pulse, digitizing this

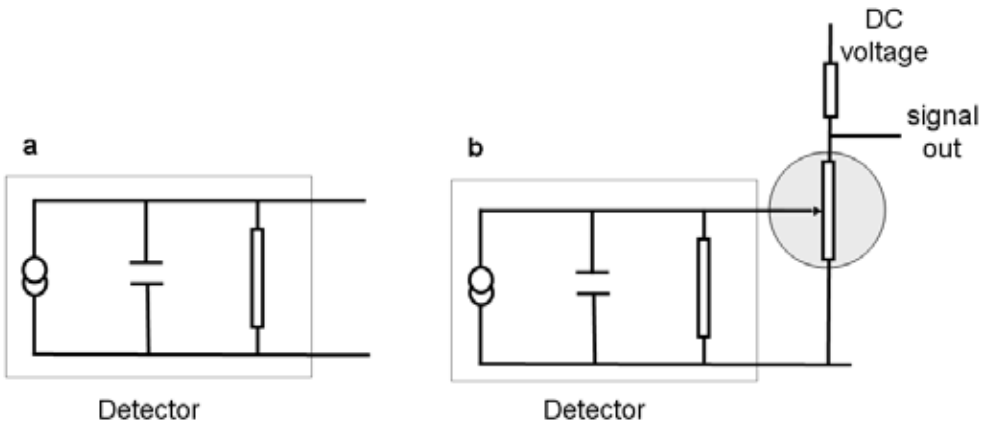

Figure B.1: Electronic circuit that represents a detector - (a) The detector behaves as a current source with an internal resistance and a capacitance. (b) The out voltage of the detector is the input voltage of the amplifier.

maximum value, and sends it to a PC. This is iteratively done for a large number of pulses, obtaining finally a histogram.

First of all, an energy threshold setting (low level discrimination (LLD) has to be fixed above the noise that is present in each measurement, in such a way that only the signals above this threshold are counted. The electronic noise has several causes: (i) pick–up noise such as ubiquitous electromagnetic radiation caused by external devices without relation with the measuring itself, noise from the digital part of the electronics and the readout computer, (ii) thermal noise of the resistors and the shot noise. To avoid the pick–up noise is usually recommended to enclose the detector in a Faraday cage (box made out of a good conductor, as aluminum). Note that power lines or signal output lines that enter within the Faraday cage can insert noise. The readout electronic systems presented in this appendix were always closed in an aluminum box that works as Faraday cage.

The main goal in the design of the electronics is optimizing the signal–to–noise (S/N) ratio. Note that the S/N ratio is rather inversely proportional to the square root of the capacitance, so this should be minimized as much as possible. Two electronic configurations were designed along this work: the first one was used in the experimental measurements presented in Chapter 5; the second configuration was developed to reduce the electronic noise by placing all its components into a single board and it will be used in the new generation of neutron sensors.

In short, the equipment needed to perform the measures carried out along this work consisted mainly of:

1. A power supply with two independent channels of ±5 V to power the electronics.
2. A HV power source to power the detector.
3. An oscilloscope to verify the signals.
4. A pulse generator to verify the proper operation of the system with a pulse test.
5. A multichannel analyzer (MCA) to obtain and analyze the spectrum of the measure.
6. A laptop to run a data acquisition program.
7. A built–in electronics which deals with the readout of the signal coming from the detector.

B.1 First Readout Electroincs

The first electronics is a simple built–in portable readout electronics that integrates the function of preamplifier, amplifier, and pulse shaping in an electronic board (10 cm length), as Figure B.2 shows.

The semiconductor detector is connected in a different board such that this allows the user to change detectors in order to test them easily. Figure B.3 shows a sketch of the main components of this system: the preamplifier converts the current signal created in the detector in a voltage pulse large enough to be treated and adapted with the minimum noise level possible. The decay time of the voltage pulse is determined by the RC constant of the integrator circuit. The pulse shaping transforms the voltage pulse in a semi-Gaussian pulse to improve the signal–to–noise ratio. The circuit that performs the basic function is composed of a high-pass filter followed by a low-pass filter. These two filters attenuate the signal at high and low frequencies where there is no useful information, improving the signal–to–noise ratio. During the process of signal adaptation and shaping, this is attenuated so it is necessary to incorporate an amplifier stage. This stage is designed so that the amplitude of the output pulse of the system is proportional to the energy deposited by the incident particles in the detector [156, 157].

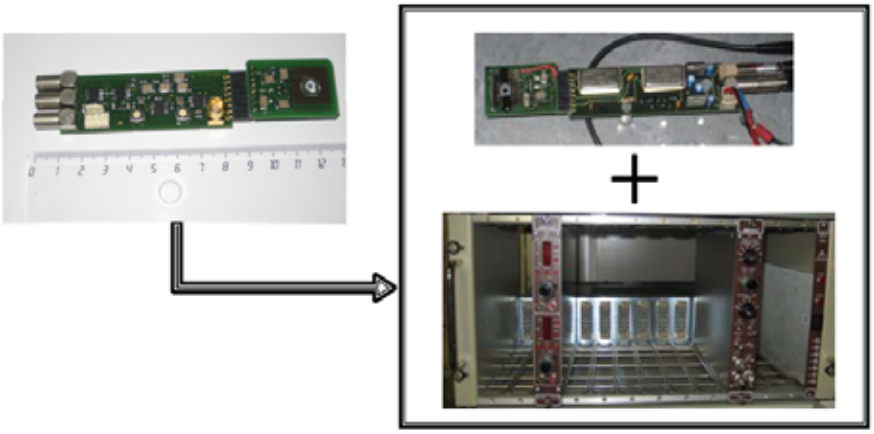

Figure B.2: Built–in portable readout electronics - The customized system (left) groups in a small board the functions of the preamplifier, amplifier, and pulse shaping, which were managed by a preamplifier board plus a NIM module (right).

It is combined with a computer–controlled multichannel pulse–height analyzer (MCA) to obtain the spectrum of the measure.

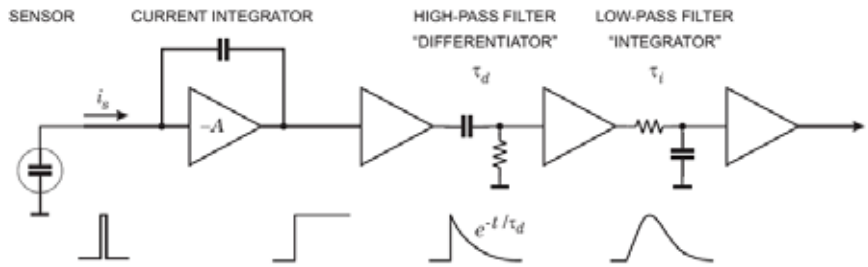

Figure B.3: Readout electronic basic sketch in a nuclear detector - From left to right: sensor, current integrator, high-pass and low-pass filters.

The three functions of preamplification, shaping, and amplification were implemented into an electronic board, working as a small and portable readout system powered by ±5 V. Fig. B.4 shows in detail the electronic diagram of the total integrated system. The semiconductor detector is mounted on a separated board in order to allow users to test different detectors with the same system. Fig. B.2, left, shows a picture of the finished electronic board with the detector board connected. The signal pulse resulting from a detected neutron by a silicon detector with a boron–based converter layer and the readout electronics shown in Fig. B.4 has an amplitude of 1.5 V/MeV,

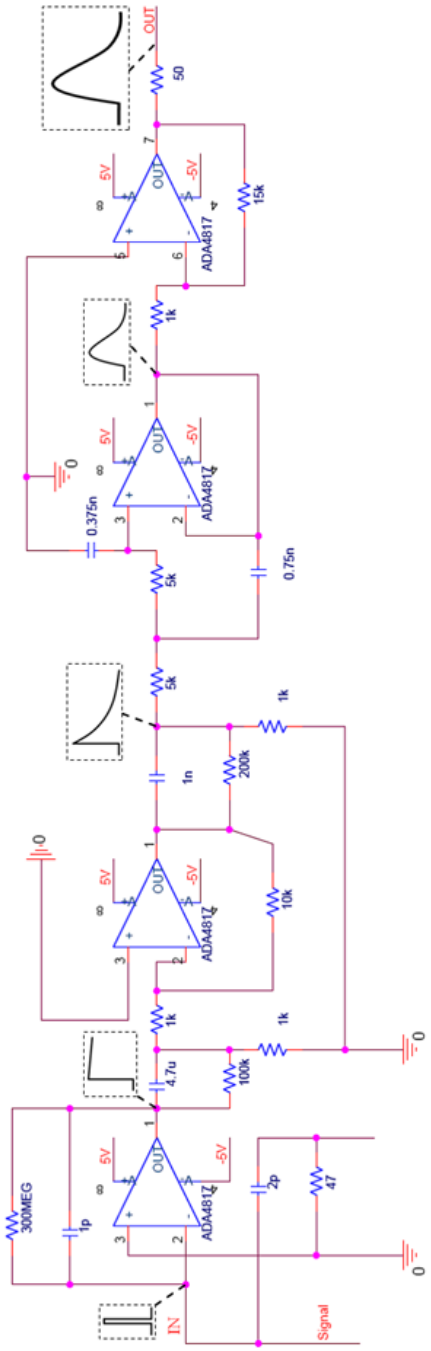

Figure B.4: Electronic diagram of the readout electronics with preamplifier, amplifier and pulse shaping.

a noise level of 60 mV (V_{pp}) and a shaping time value of 2.5 μs. It is also possible to adapt the parameters of the amplification and shaping stages in order to use the system with other types of detectors and particles, with different input signals.

B.2 New Readout Electronics

Another electronics have been assembled to allow us to use two detectors one with boron-based converter and another bare at the same time and in order to make the functions of the MCA, using a digital counter. Figure B.5 shows the bloc-diagram of the total integrated system. They are two identical circuits that consist of a preamplifier,

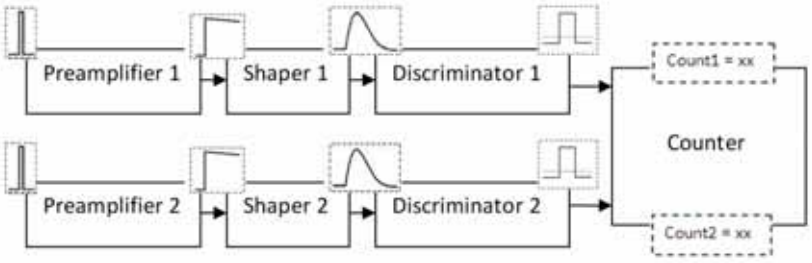

Figure B.5: Electronic diagram of the new readout electronics -

a shaper, and a discriminator, which connect a bare and an adapted detectors to the system. The discriminator gives 5 V output (power supply) when the input signal exceeds a certain threshold. This threshold is set above the noise level to avoid *false* signals. The operation of this electronics is the same than the first one above but this allows to receive two signals at the same time. Finally, the counter is a microprocessor that counts all the particles that have passed through the detector. Figure B.6 shows a picture of the new electronics specifying its components.

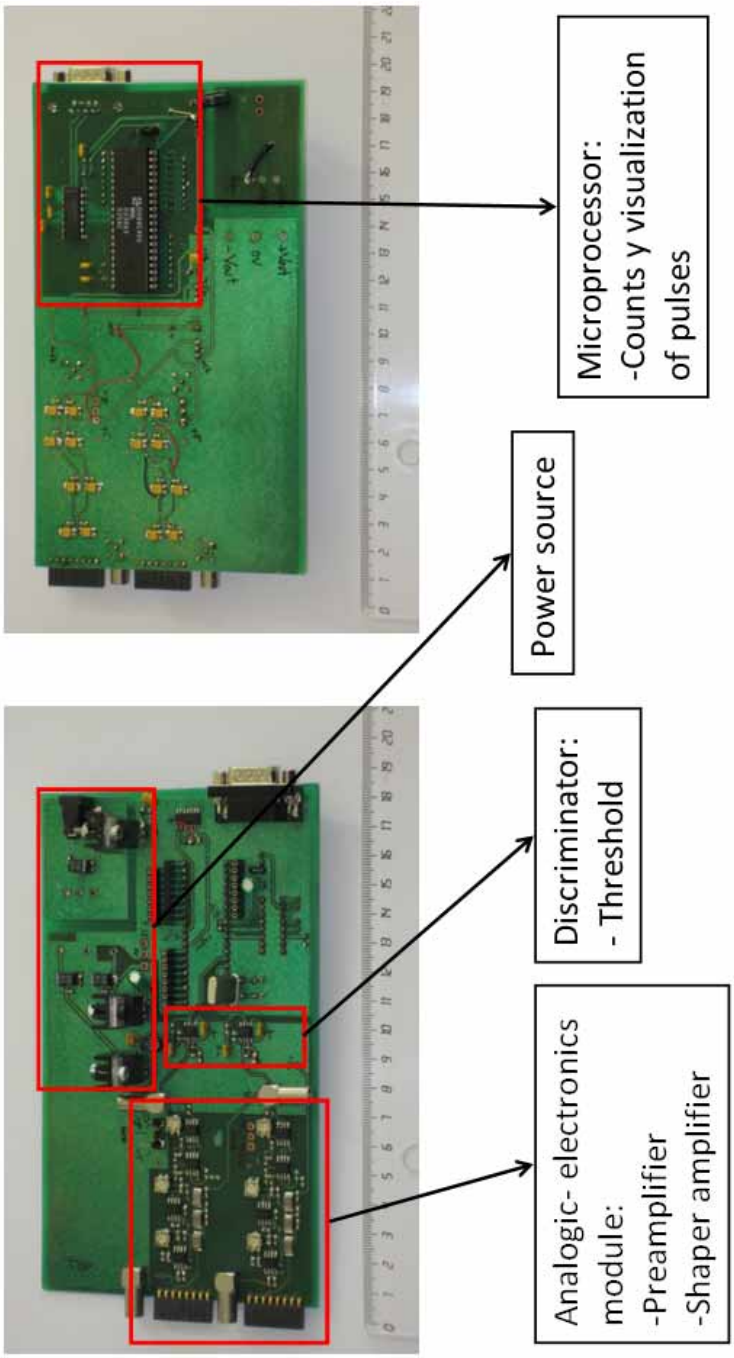

Figure B.6: Picture of the new portable readout electronics system

Appendix C

Characterization techniques

Once the fabrication process of the wafers has been completed, devices without fabrication defects must be selected. After, these detectors have to be characterized electrically. Those with the best performance are chosen to be calibrated with standard radioactive sources.

C.1 Electrical characterization

The detectors are electrically characterized in the IMB–CNM laboratories with two measurement setup: (1) a Cascade Microtech probe station with thermal chuck, two Keithley 2410 sources/meters, and a Labview program to the out readout (Figure C.1), and (2) a KarlSuss PA200 probe station connected with a HP4155 Semiconductor Parameter Analyzer. Both probe stations are closed inside a Faraday box to avoid electromagnetic interferences and light exposure.

Most of the electrical characterizations of detectors consisted on I–V and $1/C^2$–V curves. There are three main parameters to characterize a detector: leakage current, full depletion voltage, and charge collection efficiency (CCE). The first two are assessed by electrical characterization, explained as follows, and the CCE by using a radioactive source with the method explained below.

- Leakage current: when a diode is reverse biased, there is a small amount of current (nano or micro amperes) that flows through the semiconductor junction, called leakage current. This appears even in the absence of ionizing carriers, as a result of the finite conductivity of the detector. Leakage current usually fluctuates and it

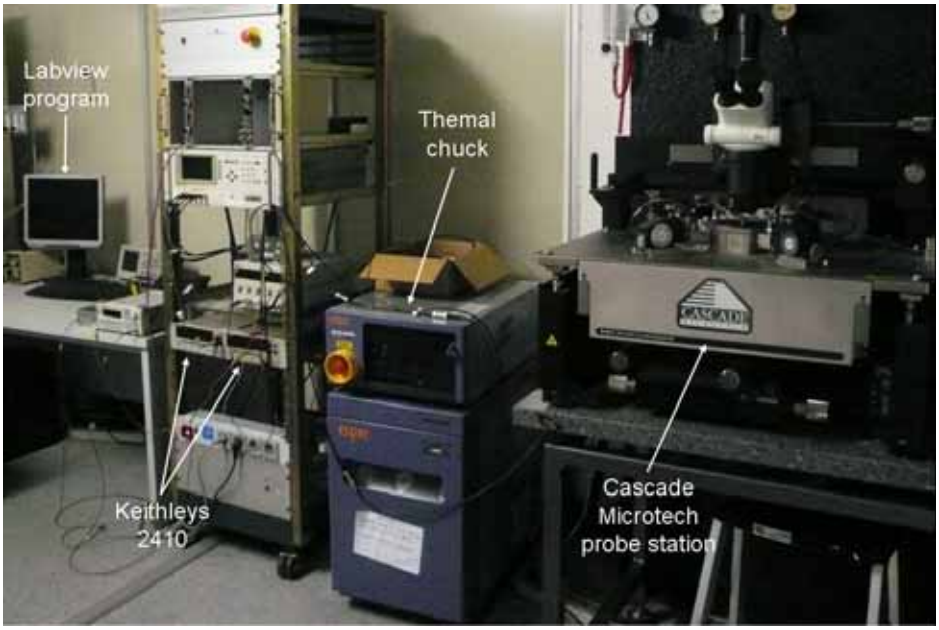

Figure C.1: Set-up used for the electrical characterization - The set-up consists of: a probe station (Cascade Microtech model), a Thermal chuck, two Keithleys 2410, and a PC with the Labview program used to save the data.

might distort the small signal current coming from a ionizing particle. Therefore this is an important shot noise component and it is essential to reduce it as much as possible. The value of the leakage current limits the smallest signal pulse that can be taken as detector output. Moreover, the origins of this leakage current are related to the bulk volume and surface of the detector:

- Bulk leakage currents increase within the volume of the detector. This is caused by two mechanisms: (i) processes of charge generation (minority carriers) on both sides of the junction and that generate a steady-state current; (ii) the thermal generation of e-h pairs within the depletion region. Both mechanisms increase with the volume of the depletion region. The second one may be reduced by cooling.
- Surface leakage currents appear at the edges of the junction since the voltage gradients that are supported in these small distances. This type of leakage current depends on several factors such as humidity, contamination, type of detector encapsulation used, etc.

- Full depleted voltage (V_{FD}): in silicon sensors, which have to be polarized in reverse to work as a radiation detector, V_{FD} is provided by the C–V curves. Figure C.2 shows an typical CV curve for a p–on–n PAD detector. As it is explained in subsection 2.4.3, it is possible to deduce the V_{FD} as the interception point between the fitted curves.

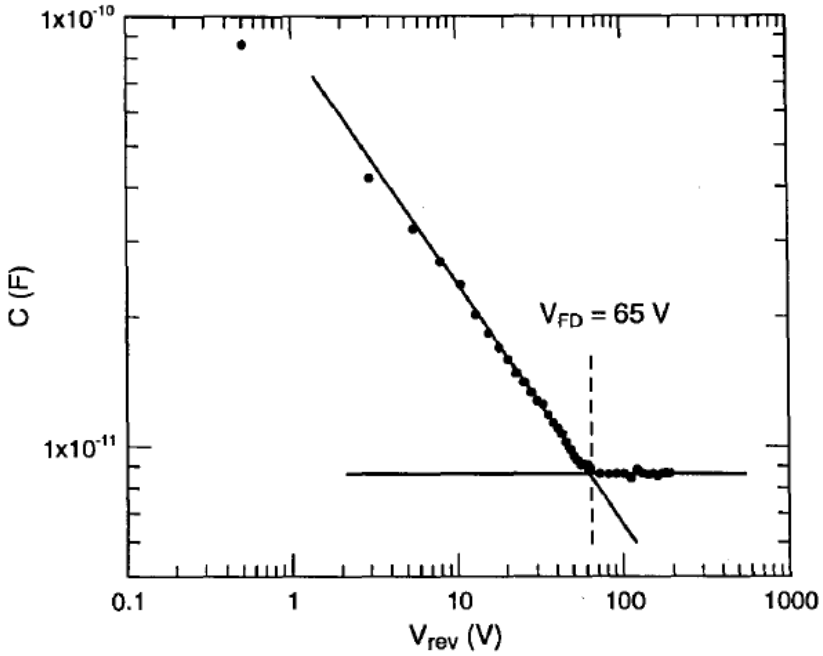

Figure C.2: Capacitance-voltage curve for p-on-n PAD detectors - Example of characteristic curve for a PAD detectors fabricated at the clean room facilities [103].

The leakage current of all the detectors on each wafer manufactured in this work has been tested with a probe station where the samples are protected of the exposition to light and electromagnetic interferences (within a Faraday shield box). The probe station is connected to Keithley voltage/current measurement instruments, which is read by a Labview program specifically coded for such purpose. In order to carried out the characterization, the voltage is swept in the detector for a wide range of bias (from forward bias to reverse bias generally at $20°C$, depending of the structure of the detector) while the current is recorded. The plotted result is the I–V characterization curve. Figure C.3 shows the common behavior of the I-V curve in a standard diode: at reverse bias, the current remains very low until the breakdown. Therefore, from these

measurements can be evaluated the leakage current directly. The I–V characterization curves are commented for each device in the Chapter 4.

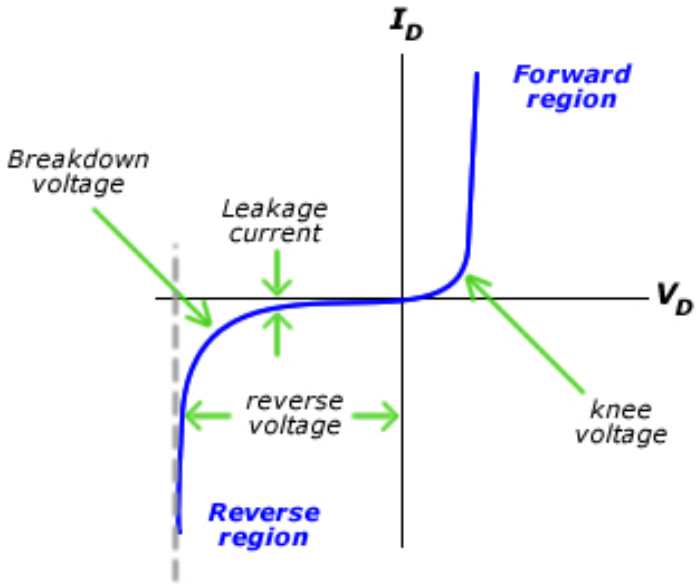

Figure C.3: I–V curve of a typical planar diode - Current versus applied voltage across a diode.

After electrical characterization, the selected detectors are mounted in printed circuit boards (explained in Appendix B.1). Then, the wire-bonded is done using an Ultrasonic Wire bonder employing a 25 μm-thick aluminum wire. The wires are covered with protective resin. Finally, the detectors are ready to be calibrated with radiation sources.

C.2 Calibration with radioactive sources

The charge collection efficiency and the calibration in energy are evaluated using an alpha source (370 Bq activity) which is formed by three isotopes, each of them with a characteristic energy: ^{239}Pu (E=5244.50 keV, τ=24110 years), ^{241}Am (E=5637.81 keV, τ=432.2 years), ^{244}Cu (E=5901.61 keV, τ=18.10 years). Figure C.4 shows the small set–up used to carry out these measurements. Figure C.5 shows one of the spectrum from the alpha calibration source obtained with one of the surface barrier detectors fabricated (section 4.1.2) without any converter layer. The readout system

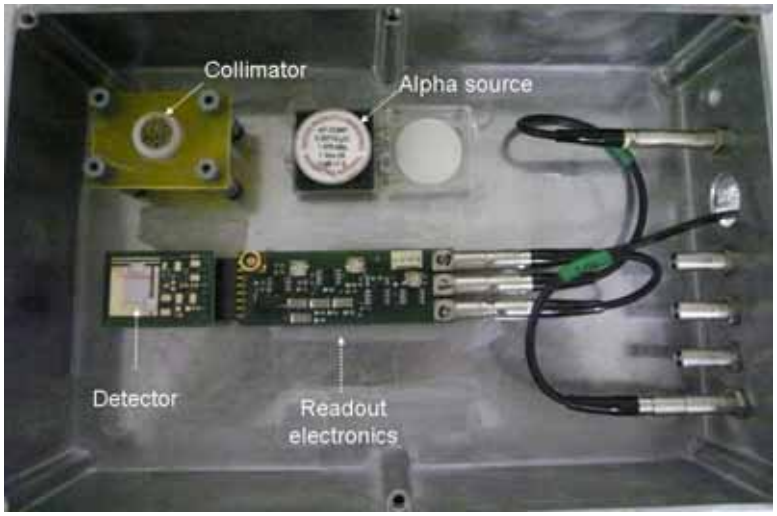

Figure C.4: Set–up of calibration - The set–up is inside an aluminum box and consists of the detector connected to its readout electronics and an alpha source that irradiates the detectors and is deposited over a handmade collimator with Cu cylinders.

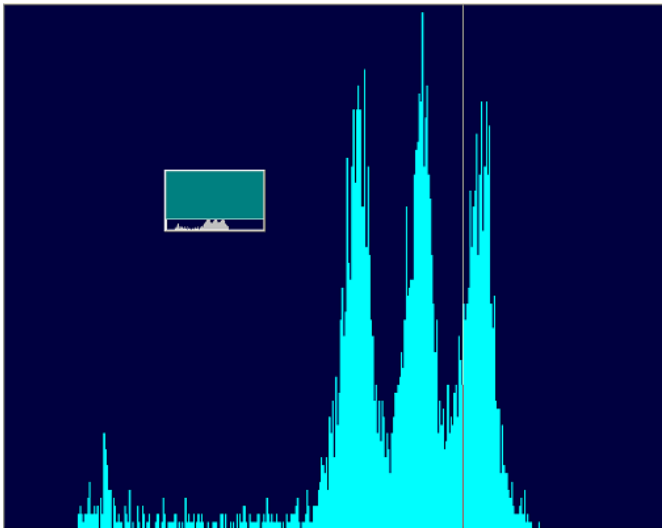

Figure C.5: Spectrum from an alpha calibration source - Spectrum for alpha particles emitted by the ^{239}Pu, ^{241}Am, ^{244}Cu isotopes, with 5244.50, 5637.81, and 5637.81 keV energies respectively.

showed in Appendix B.1 was coupled to a Maestro Multi Channel Analyzer (MCA) to obtained the spectrum of this measure.

Appendix D

Other applications

D.1 Medicine nuclear: particle therapy

The exposition to radiation produces a great diversity of biochemical effects over the tissue. The response of the cells depends on the amount of energy deposited by the incident radiation and the pattern of energy deposition distribution of the tracks. These ionization processes occur on the scale of DNA (nanometers), and therefore the biological damage might be high or even irrevocable (cell mutation, cell death, i.a.). The radiation therapy (RT) is based on that premise as basis of its performance. RT treats about 52% of cancers [158], but it may be an aggressive treatment limited near a vital organ due to the high risk side effects. New techniques of noninvasively treating have been introduced in recent years such as Intensity Modulated Radiation Therapy (IMRT) or Particle Therapy (PT), also known as hadron therapy[1], to propose other alternatives with fewer side effects. This new treatment normally uses protons and/or charged light ions as alphas and carbon nuclei at high energies [159]. Although the radiation therapy using hadrons was proposed by Robert Wilson more than a half-century ago [160], it has been slowly implemented because a PT system requires a cyclotron or a synchrotron facility to work and these are more complex and expensive than the RT accelerators [161]. Figure D.1 displays a chronological diagram of the evolution of the hadron therapy field over the last seventy years [162].

[1]Hadrontherapy is a form of radiotherapy that uses elementary particles like protons or carbon ions instead of the X-rays.

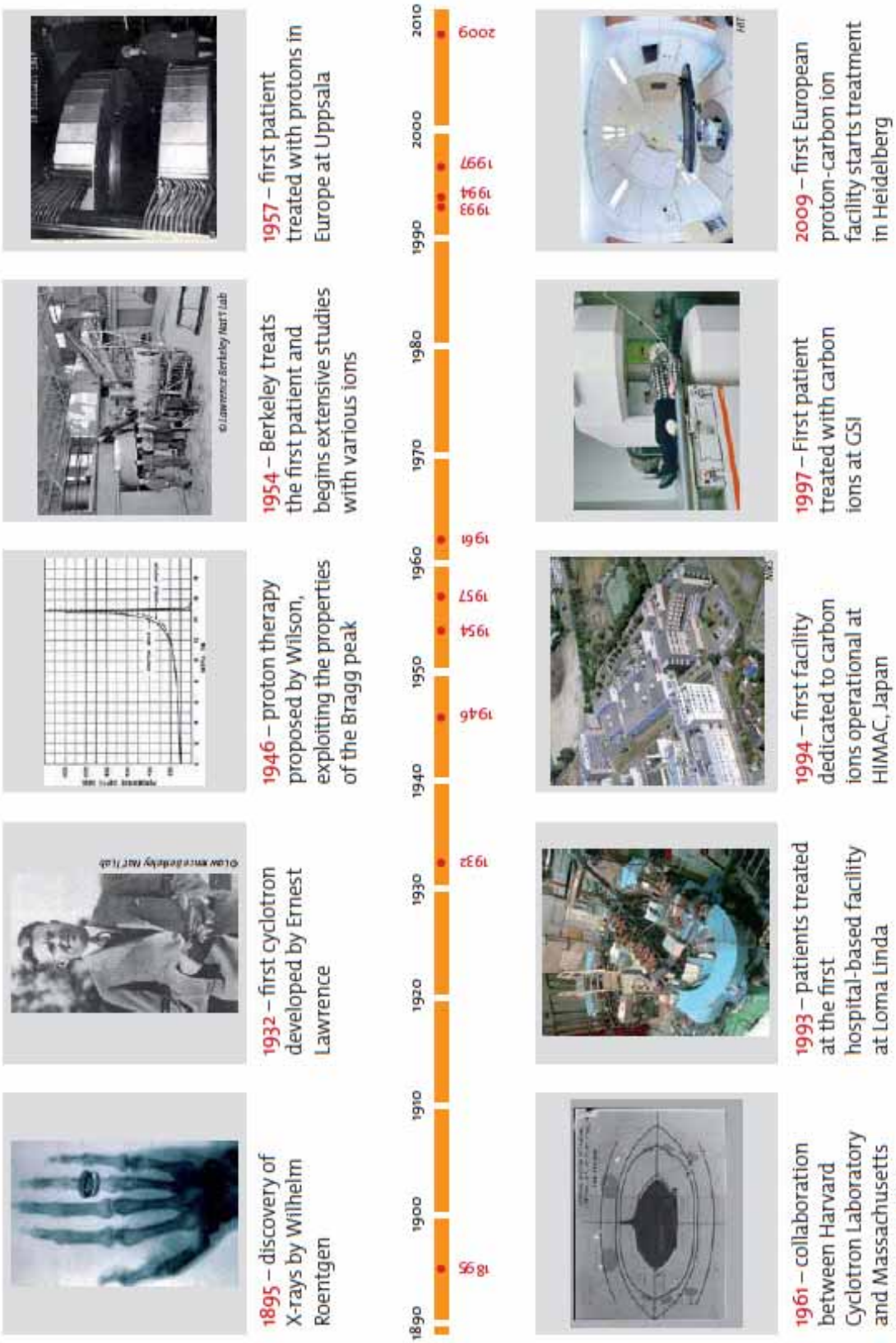

Figure D.1: Chronological diagram of the implementation of hadron therapy

In particular, using high linear energy transfer (LET)[1] particles, PT is believed to benefit the effective dose delivered because the energy can be deposited more selectively than γ–rays due to the Bragg peak[2] effect. Figure D.2 shows a graph with several Bragg curves for particles used in nuclear medicine at their energy average values used in treatment. The depth–dose curves for photons and electrons (conventional radiation beam used in radiotherapy) are different from those of proton beams: since charged particles with high energy have little scattering when go through the matter, the highest delivered dose takes place at the end of their range, before stopping (Bragg peak). Thus the main advantage of this method is that is theoretically able to kill the cancer cells while minimizing damage in normal tissue because it provides a better dose distribution [163].

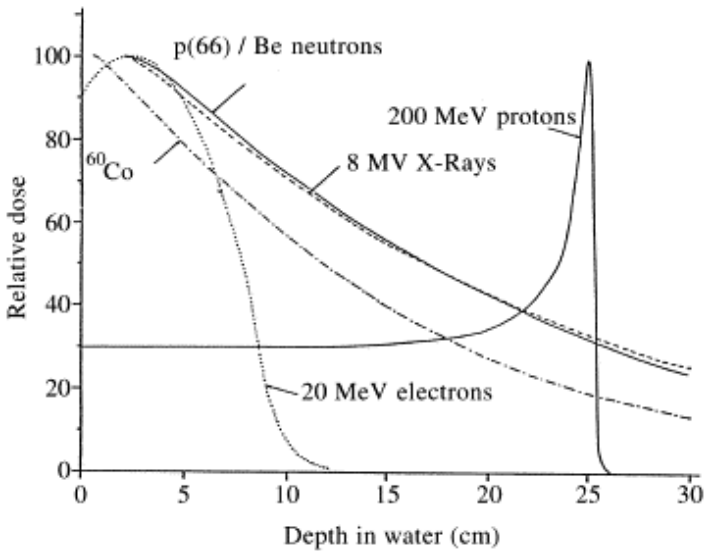

Figure D.2: Depth dose curves for photons, neutrons, and protons - Photons come from a ^{60}Co source and an 8 MeV linear accelerator, neutrons are generated by 66 MeV protons incident on a ^{9}Be target, and protons come from an accelerator. The plot shows that protons at high energy deliver the highest dose near the end of their range (Bragg peak), with a peak narrow enough to focus the released dose on a concrete volume [164].

[1]LET is a measure of the energy transferred to a material when an ionizing particle go through it. Whereas Stopping Power focuses on the energy loss of the particle ($\frac{dE}{dx}$), LET deals with the energy transferred through secondary electrons to the material surrounding its track.

[2]The Bragg peak is a pronounced peak on the Bragg curve, which plots the stopping power versus the path length of the incident particle inside the matter.

Summarizing, in particle therapy it is possible to:

- Match the Bragg peak to the cancer position very precisely using modern imaging techniques such as computed tomography and magnetic resonance scans.
- Reduce the radiation dose to nearby healthy tissue and critical organs.
- Focus the dose in clinically complex locations, for example in the brain, eye, and neck, i.a.

Despite improvements, there are not so many reports of PT efficacy, and some studies regard necessary a better understanding of the dose distributions inside patients because the nuclear non–elastic interactions might cause side effects. In the last years, new silicon devices have allowed microdosimetric measurements [165], but the diode structures ($\geq$10 μm) were developed on thicker substrates which may cause backscattering, complicating the characterization of the Relative Biological Effectiveness (RBE)[1].

However, the ultra–thin 3D detector developed in this thesis (section 4.2) can be slimmed up to a total thickness of 10 μm or 20 μm, down to the level of the average cell size[2], and thus providing a closest measurement of silicon ΔE. Therefore, the ultra-thin 3D detectors could enable direct measurements of LET at any given point within an irradiated volume. This will exploit the dependency of the response of the detectors on the LET of the radiation used [166], and could yield a three–dimensional distribution of linear energy transfer. The data obtained from the RBE characterization can then be used to benchmark treatment planning systems (TPS) as well as Monte Carlo codes. The top of the Figure D.3 shows an ultra-thin 3D silicon detector of 20 μm-thick where the support wafer has been removed with partial KOH etching which stops at the silicon oxide interface of the SOI wafer (photo of the front and back sides); in the back side is visualized the drop of around 300 μm thickness that has been removed and in the bottom a SEM image of such detectors is displayed.

[1]RBE is the ratio of biological effectiveness of an ionizing radiation relative to another provided both give the same amount of absorbed energy. It is defined as RBE=D_X/D_R, being D_X the reference absorbed dose of radiation of type 'X' and D_R the absorbed dose of the radiation of type 'R' that causes the same biological damage that the reference one.

[2]Note that the average eukaryotes cell size ranges from 10 to 100 μm

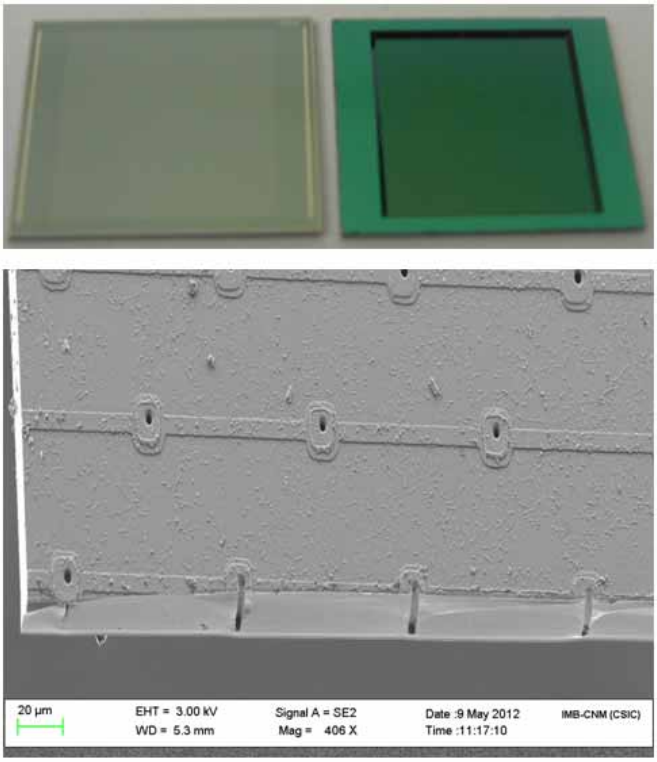

Figure D.3: Ultra-thin 3D detector slimmed

The first tests of CCE and LET measurement in a proton therapy facility are going to be carried out shortly.

D.2 Nuclear security

As said in section 1.2.2, neutron detection is necessary to intercept radiological threats. Under the support of the REWARD project (see subsection 1.3.3), and as a first proof–of–concept, the first tests are going to be carried out with the detectors developed in section 4.2, covered with ^{10}B deposited by EBPVD or by RF Sputtering (Appendix A). Since these detectors are limited in efficiency up to around 4.5%, it is planed to stack several ultra-thin 3D detectors, as Figure D.4 displays, to increase the overall neutron efficiency. Neutron detector stacking methods have been frequently proposed as a feasible alternative to increase the efficiency [167].

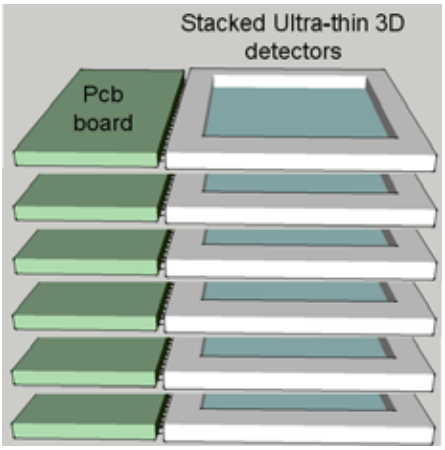

Figure D.4: Illustration of stacked ultra-thin 3D detectors - The configuration of stacking consists of several detectors lined up. In this particular case, each detector is connected with its own readout electronics, but these may be connected to each other to assess the whole efficiency.

On the other hand, the problem of the low efficiency may be overcome by etching 3D structures into the silicon bulk and filling them with the converter material, as was explained in section 2.4.3.2. A set of perforated prototypes (some of them explained in section 3.5) is being manufactured in the IMB–CNM clean room facilities.

References

[1] X George Xu, Bryan Bednarz, and Harald Paganetti. **A review of dosimetry studies on external-beam radiation treatment with respect to second cancer induction.** *Physics in medicine and biology*, **53**(13):R193–241, July 2008. 2

[2] Glenn F. Knoll. *Radiation Detection and Measurement*. 2000. 2, 16, 28, 44, 52

[3] Richard T. Kouzes, James H. Ely, Luke E. Erikson, Warnick J. Kernan, Azaree T. Lintereur, Edward R. Siciliano, Daniel L. Stephens, David C. Stromswold, Renee M. Van Ginhoven, and Mitchell L. Woodring. **Neutron detection alternatives to 3He for national security applications**. *Nuclear Instruments and Methods in Physics Research Section A: Accelerators, Spectrometers, Detectors and Associated Equipment*, **623**(3):1035–1045, November 2010. 3, 32, 37

[4] Gerhard Lutz. *Semiconductor Radiation Detectors*. 1999. 4

[5] a N Caruso. **The physics of solid-state neutron detector materials and geometries.** *Journal of physics. Condensed matter : an Institute of Physics journal*, **22**(44):443201, November 2010. 4

[6] L.D. Muminov, R.A. and Tsvang. **High-Efficiency Semiconductor Thermal-Neutron Detectors**. *Translated from Atomnaya Énergiya*, **62**(4):265–267, 1987. 5, 58

[7] A J Peurrung. **Recent developments in neutron detection**. *Nuclear Instruments and Methods in Physics Research*, **443**(September 1999):400–415, 2000. 5, 48

[8] ICRP Publication 103. **The 2007 Recommendations of the International Commision on Radiological Protection**. Technical report, International Commision on Radiological Protection (ICRP), 2007. 9

[9] ICRP (International Commision on Radiological Protection). **The 2007 Recommendations of the International Commision of Radiological Protection, ICRP Publication 103**. Technical report, 2007. 7

[10] The American Association of Physicist in Medicine (APPM). **Neutron Measurements Around High Energy X-Ray RT Machines**. Technical report, 1986. 8

[11] Maria José García Fusté. *Neutron spectrometry in complex n-gamma fields: Application to LINAC and PET facilities*. PhD thesis, 2010. 8, 167

[12] T.M. Edwards R. Barquero, R. Mendez, H.R. Vega-Carrillo, M.P. Iñiguez. **Neutron Spectra and Dosimetric features around an 18 MV Linac Accelerator**. *Health Physics*, **88**:48–59, 2005. 8

[13] S G Vaijapurkar, Kana Ram Senwar, J S Hooda, and a Parihar. **The performance evaluation of gamma- and neutron-sensitive superheated emulsion (bubble) detectors.** *Radiation protection dosimetry*, **130**(3):285–90, January 2008. 8

[14] F. Gómez, F. Sánchez-Doblado, a. Iglesias, and C. Domingo. **Active on-line detector for in-room radiotherapy neutron measurements**. *Radiation Measurements*, **45**(10):1532–1535, December 2010. 8, 11

[15] S.A. Martinez Ovalle. *Estudio Monte Carlo con MCNPX de la dosimetría de fotoneutrones producidos en aceleradores de uso clínico*. PhD thesis, Universidad de Granada, 2010. 9, 167, 168

[16] C. Domingo, M.J. García-Fusté, E. Morales, K. Amgarou, J.a. Terrón, J. Roselló, L. Brualla, L. Nuñez, R. Colmenares, F. Gómez, G.H. Hartmann, F. Sánchez-Doblado, and F. Fernández. **Neutron spectrometry and determination of neutron ambient dose equivalents in different LINAC radiotherapy rooms**. *Radiation Measurements*, **45**(10):1391–1397, December 2010. 9

[17] IAEA. **IAEA Illicit Trafficking Database (ITDB)**. 10

[18] A. Ansari. *Radiation Threats and Your Safety*. 2010. 10

[19] Davide Cester. *Innovative techniques for detection of radioactive and nuclear materials*. PhD thesis, 2011. 10

[20] F Gómez, a Iglesias, and F Sánchez Doblado. **A new active method for the measurement of slow-neutron fluence in modern radiotherapy treatment rooms.** *Physics in medicine and biology*, **55**(4):1025–39, February 2010. 11

[21] REWARD Collaboration. **REWARD (Real Time Wide Area Radiation Surveillance System)**. 12, 13

[22] J. Chadwick. **The Existence of a Neutron**. *Proceedings of the Royal Society A: Mathematical, Physical and Engineering Sciences*, **136**(830):692–708, June 1932. 16

[23] Ervin B. Podgorsak. *Radiation Physics for Medical Physicists*. Springer edition, 2005. 16, 27

[24] J.E. Turner. *Atoms, radiation and radiation protection*. 2007. 19, 50, 51

[25] Madsen V.A. Bauer, R.W., Anderson, J.D., Grimes S.M. **Application of Simple Ramsauer Model to Neutron Total Cross Sections**. *International Conference on Nuclear Data for Science and Technology*, 1997. 19

[26] ENDF. **Evaluated Nuclear Data File (ENDF)**. 20, 21, 26

[27] Barbalace J.K. **Table of Elements with Neutron Capture**. 30

[28] S. Tavernier. *Experimental Techniques in Nuclear and Particle Physics*. 2010. 33, 42

[29] J H Ely. **Boron-Lined Neutron Detector Measurements**. *Contract*, 2009. 40

[30] Rolf Arlt, Marcin Balcerzyk, Maciej Kapusta, Michael Majorov, Radoslaw Marcinkowski, Paul Schotanus, Martha Swoboda, and Dariusz Wolski. **6LiI(Eu) in Neutron and gamma-ray Spectrometry-Highly Sensitive Thermal Neutron Detector**. **52**(6):3151–3156, 2005. 42

[31] C.F.G. Delaney and E.C. Finch. *Radiation Detectors-Physical Principles and Applications*. 1992. 43

[32] H. Spieler. *Semiconductor Detector Systems*. 2005. 43

[33] Daniela Bassignana. *New technologies of silicon position-sensitive detectors for future tracker systems*. PhD thesis, 2012. 45, 115

[34] S.M. Sze. *Physics of Semiconductor Devices*. 1969. 45

[35] S.M. Sze. *Physics of Semiconductor Devices*. 1981. 46

[36] Josef Uher. *3D neutron detectors*. PhD thesis, 2007. 47, 58, 64

[37] Kevin Osberg, Nathan Schemm, Sina Balkr, Jennifer I Brand, M Susan Hallbeck, Peter A Dowben, and Michael W Hoffman. **A Handheld Neutron-Detection Sensor System Utilizing a New Class of Boron Carbide Diode**. *Sensors (Peterborough, NH)*, **6**(6):1531–1538, 2006. 47

[38] David Emin and T. L. Aselage. **A proposed boron-carbide-based solid-state neutron detector**. *Journal of Applied Physics*, **97**(1):013529, 2005. 47

[39] a D Harken and B W Robertson. **Comparative modelling of performance limits of solid-state neutron detectors based on planar B-rich capture layers**. *Journal of Physics D: Applied Physics*, **39**(23):4961–4968, December 2006. 47

[40] C. Lundstedt, a. Harken, E. Day, B.W. Robertson, and S. Adenwalla. **Modeling solid-state boron carbide low energy neutron detectors**. *Nuclear Instruments and Methods in Physics Research Section A: Accelerators, Spectrometers, Detectors and Associated Equipment*, **562**(1):380–388, June 2006. 47

[41] S. Almaviva, M. Marinelli, E. Milani, G. Prestopino, a. Tucciarone, C. Verona, G. Verona-Rinati, M. Angelone, D. Lattanzi, M. Pillon, R. M. Montereali, and M. a. Vincenti. **Thermal and fast neutron detection in chemical vapor deposition single-crystal diamond detectors**. *Journal of Applied Physics*, **103**(5):054501, 2008. 47

[42] R.V. Babcock, R.E. Davis, S.L. Ruby, K.H. Sun, and E.D Wolley. **Coated Semiconductor is tiny neutron detector**. *Nucleonics*, (19):116–122, 1959. 48

[43] C Petrillo, F Sacchetti, and N J Rhodes. **Solid state neutron detectors**. *Quantum*, **378**(96):541–551, 1996. 48

[44] Stanislav Pospisil, Carlos Granja, and Claude Leroy. **Neutrons and their Detection with Silicon Diodes**. **12**(1):12–16, 2010. 49

[45] NIST. **Physical reference data website**. 50

[46] James F. Ziegler. **Srim-2003**. *Nuclear Instruments and Methods in Physics Research Section B: Beam Interactions with Materials and Atoms*, **219-220**:1027–1036, June 2004. 52

[47] Ashish Jain, S. Anthonysamy, K. Ananthasivan, R. Ranganathan, Vinit Mittal, S.V. Narasimhan, and P.R. Vasudeva Rao. **Characterization of electrodeposited elemental boron**. *Materials Characterization*, **59**(7):890–900, July 2008. 53

[48] D S Mcgregor, M D Hammig, Y Yang, H K Gersch, and R T Klann. **Design considerations for thin film coated semiconductor thermal neutron detectors I : basics regarding alpha particle emitting neutron reactive films Li**. *Nuclear Instruments and Methods in Physics Research*, **500**:272–308, 2003. 57, 100

[49] Adam M Conway, Tzu F Wang, Nimanlendu Deo, Chin L Cheung, and Rebecca J Nikolic. **Numerical Simulations of Pillar Structured Solid State Thermal Neutron Detector : Efficiency and Gamma Discrimination**. *October*, **56**(5):2802–2807, 2009. 58, 64

[50] B Philips, F Kub, E Novikova, E Wulf, and C Fitzgerald. **Neutron detection using large area silicon detectors**. *Nuclear Instruments and Methods in Physics Research Section A: Accelerators, Spectrometers, Detectors and Associated Equipment*, **579**(1):173–176, August 2007. 58

[51] Douglas S Mcgregor, Raymond T Klann, Holly K Gersch, Elsa Ariesanti, Jeffrey D Sanders, and Brian Vanderelzen. **New Surface Morphology for Low Stress Thin-Film-Coated Thermal Neutron Detectors**. **49**(4):1999–2004, 2002. 63

[52] D.S. McGregor, W.J. McNeil, S.L. Bellinger, T.C. Unruh, and J.K. Shultis. **Microstructured semiconductor neutron detectors**. *Nuclear Instruments and Methods in Physics Research Section A: Accelerators, Spectrometers, Detectors and Associated Equipment*, **608**(1):125–131, September 2009. 63

[53] J.K. Shultis and D.S. McGregor. **Design and performance considerations for perforated semiconductor thermal-neutron detectors**. *Nuclear Instruments and Methods in Physics Research Section A: Accelerators, Spectrometers, Detectors and Associated Equipment*, **606**(3):608–636, July 2009. 63

[54] J Kenneth Shultis and Douglas S Mcgregor. **Efficiencies of Coated and Perforated Semiconductor Neutron Detectors**. *System*, **53**(3):1659–1665, 2006. 63

[55] S.L. Bellinger, R.G. Fronk, W.J. McNeil, T.J. Sobering, and D.S. McGregor. **Enhanced variant designs and characteristics of the microstructured solid-state neutron detector**. *Nuclear Instruments and Methods in Physics Research Section A: Accelerators, Spectrometers, Detectors and Associated Equipment*, **652**(1):387–391, October 2011. 63

[56] W.J. McNeil. *Perforated diode neutron sensors*. PhD thesis, 2010. 63

[57] S.L. Bellinger. *Advanced Microstructured Semiconductor Neutron Detectors: Design, Fabrication, and Performance*. PhD thesis, 2011. 63

REFERENCES

[58] R. J. Nikolic. **Roadmap for high efficiency solid-state neutron detectors**. *Proceedings of SPIE*, **6013**:601305–601305–9, 2005. 64, 197

[59] R. J. Nikolic, Q. Shao, L. F. Voss, a. M. Conway, R. Radev, T. F. Wang, M. Dar, N. Deo, C. L. Cheung, L. Fabris, C. L. Britton, and M. N. Ericson. **¡title¿Si pillar structured thermal neutron detectors: fabrication challenges and performance expectations¡/title¿**. *Nanotechnology*, **8031**:803109–803109–11, May 2011. 64

[60] Justin Clinton. *Optimization and Characterization of a Novel Self Powered Solid State Neutron Detector by*. PhD thesis, 2011. 64, 65

[61] Giulio Pellegrini. *Technology Development of 3D Detectors for High Energy Physics and Medical Imaging*. PhD thesis, 2002. 65, 128

[62] M. Pellegrini, G., Balbuena, J., Bassignana, D., Cabruja, E., Fleta, C., Guardiola, C., Lozano, M., Quirion, D., Ullán. **3D Double Sided Detector Fabrication at IMB-CNM**. *Systems Engineering Procedia*, 2012. 65, 116, 128, 175

[63] S. Metropolis, N and Ulam. **The Monte Carlo Method**. *Journal of the American Statistical Association*, **44**(247), 1949. 66

[64] Carlo Jacoboni and Paolo Lugli. *The Monte Carlo Method for Semiconductor Device Simulation*. Springer-v edition, 1989. 67

[65] M.L. Jungberg, S-E Strand, and M.A. King. *Monte Carlo in Nuclear Medicine-Applications in diagnostic imaging*. Institute edition, 1998. 67, 69

[66] H. Zaidi and G. Sgouros. *Therapeutic Applications of Monte Carlo Calculations in Nuclear Medicine*. Institute edition, 2003. 67

[67] C Guardiola, K Amgarou, F García, C Fleta, D Quirion, and M Lozano. **Geant4 and MCNPX simulations of thermal neutron detection with planar silicon detectors**. *Journal of Instrumentation*, **6**(09):T09001–T09001, September 2011. 67

[68] C Guardiola, C Fleta, K Amgarou, and M Lozano. **Monte Carlo simulations of a microstructured silicon detector with high efficiency for thermal neutrons**. *Journal of Instrumentation*, **7**(06):T06003–T06003, June 2012. 67

[69] C. Guardiola, J. Calvo, M. Lozano, C. Corral, and G. Pellegrini. **Procedimiento para el depósito de capas gruesas de boro**, 2012. 67, 116

[70] Stephen M. Seltzer. **Electron-photon Monte Carlo calculations: The ETRAN code**. *International Journal of Radiation Applications and Instrumentation. Part A. Applied Radiation and Isotopes*, **42**(10):917–941, January 1991. 71

[71] EGS Support. **EGS (Electron Gamma Shower) code**. 71

[72] FLUKA Support. **FLUKA (FLUktuierende KAskade)**. 71

[73] Sempau J. Salvat F., Fernández-Varea J., Acosta E. **PENELOPE (PENetration and Energy LOss of Positrons and Electrons) code**. Technical report. 71

[74] PHITS Support. **PHITS (Particle and Heavy Ion Transport code System)**. 71

[75] National Research Council Canada. **BEAMnrc code**. 72

[76] Ziegler J. **SRIM (Stopping and Range of Ions in Matter) code**. 72

[77] LANL collaboration. **MCNP (Monte Carlo N-Particle) code**. 72

[78] LANL collaboration. **MCNPX (Monte Carlo N-Particle eXtended) code**. 72

[79] GEANT4 Collaboration. **GEANT4 (Geometry ANd Tracking) code**. 72, 95

[80] D.B. Pelowitz. **MCNPX User's Manual Version 2.6.0**. Technical report, 2008. 72, 78

[81] MCNPX Document Page. **http://mcnpx.lanl.gov/documents.html**. 73, 149

[82] Bryan Bednarz and X George Xu. **Monte Carlo modeling of a 6 and 18 MV Varian Clinac medical accelerator for in-field and out-of-field dose calculations: development and validation.** *Physics in medicine and biology*, **54**(4):N43–57, February 2009. 74

[83] Nuclear Data Service. **Evaluated Nuclear Data Library Descriptions**. 76

[84] LANL. **Libraries for Monte Carlo Transport Codes**. 76

[85] S. Agostinelli, J. Allison, K. Amako, J. Apostolakis, H. Araujo, P. Arce, M. Asai, D. Axen, S. Banerjee, G. Barrand, F. Behner, L. Bellagamba, J. Boudreau, L. Broglia, a. Brunengo, H. Burkhardt, S. Chauvie, J. Chuma, R. Chytracek, G. Cooperman, G. Cosmo, P. Degtyarenko, a. Dell'Acqua, G. Depaola, D. Dietrich, R. Enami, a. Feliciello, C. Ferguson, H. Fesefeldt, G. Folger, F. Foppiano, a. Forti, S. Garelli, S. Giani, R. Giannitrapani, D. Gibin, J.J. Gómez Cadenas, I. González, G. Gracia Abril, G. Greeniaus, W. Greiner, V. Grichine, a. Grossheim, S. Guatelli, P. Gumplinger, R. Hamatsu, K. Hashimoto, H. Hasui, a. Heikkinen, a. Howard, V. Ivanchenko, a. Johnson, F.W. Jones, J. Kallenbach, N. Kanaya, M. Kawabata, Y. Kawabata, M. Kawaguti, S. Kelner, P. Kent, a. Kimura, T. Kodama, R. Kokoulin, M. Kossov, H. Kurashige, E. Lamanna, T. Lampén, V. Lara, V. Lefebure, F. Lei, M. Liendl, W. Lockman, F. Longo, S. Magni, M. Maire, E. Medernach, K. Minamimoto, P. Mora de Freitas, Y. Morita, K. Murakami, M. Nagamatu, R. Nartallo, P. Nieminen, T. Nishimura, K. Ohtsubo, M. Okamura, S. O'Neale, Y. Oohata, K. Paech, J. Perl, a. Pfeiffer, M.G. Pia, F. Ranjard, a. Rybin, S. Sadilov, E. Di Salvo, G. Santin, T. Sasaki, N. Savvas, Y. Sawada, S. Scherer, S. Sei, V. Sirotenko, D. Smith, N. Starkov, H. Stoecker, J. Sulkimo, M. Takahata, S. Tanaka, E. Tcherniaev, E. Safai Tehrani, M. Tropeano, P. Truscott, H. Uno,

L. Urban, P. Urban, M. Verderi, a. Walkden, W. Wander, H. Weber, J.P. Wellisch, T. Wenaus, D.C. Williams, D. Wright, T. Yamada, H. Yoshida, and D. Zschiesche. **Geant4a simulation toolkit**. *Nuclear Instruments and Methods in Physics Research Section A: Accelerators, Spectrometers, Detectors and Associated Equipment*, **506**(3):250–303, July 2003. 81

[86] J Allison, K Amako, J Apostolakis, H Araujo, P Arce Dubois, M Asai, G Barrand, R Capra, S Chauvie, R Chytracek, G A P Cirrone, G Cooperman, G Cosmo, G Cuttone, G G Daquino, M Donszelmann, M Dressel, G Folger, F Foppiano, J Generowicz, V Grichine, S Guatelli, P Gumplinger, A Heikkinen, I Hrivnacova, A Howard, S Incerti, V Ivanchenko, T Johnson, F Jones, T Koi, R Kokoulin, M Kossov, H Kurashige, V Lara, S Larsson, F Lei, O Link, F Longo, M Maire, A Mantero, B Mascialino, I Mclaren, P Mendez Lorenzo, K Minamimoto, K Murakami, P Nieminen, L Pandola, S Parlati, L Peralta, J Perl, A Pfeiffer, M G Pia, A Ribon, P Rodrigues, G Russo, S Sadilov, G Santin, T Sasaki, D Smith, N Starkov, S Tanaka, E Tcherniaev, B Tomé, A Trindade, P Truscott, L Urban, M Verderi, A Walkden, J P Wellisch, D C Williams, D Wright, and H Yoshida. **Geant4 Developments and Applications**. *Physics*, **53**(1):270–278, 2006. 81

[87] S Jan, G Santin, D Strul, S Staelens, and K Assi. **My IOPscience GATE : a simulation toolkit for PET and SPECT**. *Online*, **4543**, 2004. 82

[88] P. Arce, P. Rato, M. Canadas, and J. I. Lagares. **GAMOS: A Geant4-based easy and flexible framework for nuclear medicine applicationso**. *Nuclear Science Symposium Conference Record*, pages 3162–3168, 2008. 82

[89] Geant 4 Collaboration (CERN). **GEANT4 User's Guide for Application Developers**. Technical report. 82, 84, 87, 91, 93

[90] GATE Collaboration. **GATE: Simulations of Preclinical and Clinical Scans in Emission Tomography, Transmission Tomography and Radiation Therapy**. 82

[91] ATLAS Collaboration. **ATLAS Experiment**. 83

[92] FERMILAB collaboration SLAC, GEANT4. **CLEP- A class library for High Energy Physics**. 84

[93] W.G. Linstrom, P.J., Mallard. **NIST Chemistry WebBook**, 2005. 85

[94] Wallace E. **Constructive solid geometry**. 91

[95] G4Collaboration. **Summary of Hadronic Processes, Models and Cross Sections for Physics List QGSP_BERT**. 92

[96] Josef Uher. *3D neutron detectors*. PhD thesis, Czech Technical University, Prague, 2007. 100

[97] Shirin a. Enger, Per Munck af Rosenschold, Arash Rezaei, and Hans Lundqvist. **Monte Carlo calculations of thermal neutron capture in gadolinium: A comparison of GEANT4 and MCNP with measurements**. *Medical Physics*, **33**(2):337, 2006. 101

[98] S Ã Garny, V Mares, and W Ru. **Nuclear Instruments and Methods in Physics Research A Response functions of a Bonner sphere spectrometer calculated with GEANT4**. **604**:612–617, 2009. 101

[99] R. Lemrani, M. Robinson, V.a. Kudryavtsev, M. De Jesus, G. Gerbier, and N.J.C. Spooner. **Low-energy neutron propagation in MCNPX and GEANT4**. *Nuclear Instruments and Methods in Physics Research Section A: Accelerators, Spectrometers, Detectors and Associated Equipment*, **560**(2):454–459, May 2006. 101

[100] Sylvia Garny, Gerhard Leuthold, Vladimir Mares, Herwig G Paretzke, Werner Rühm, Monte Carlo, and A Calculation With Geant. **GEANT4 Transport Calculations for Neutrons and Photons Below 15 MeV**. *Quality*, **56**(4):2392–2396, 2009. 101

[101] Y Yeh, C Wang, H Liu, T Liu, and G Lin. **Simulating neutron propagations with FLUKA ,**. *Ieee Nuclear Science Symposium Conference Record*, pages 2016–2018, 2007. 101

[102] Hong Xiao. *Introduction to Semiconductor Manufacturing Technology*. 2001. 115, 194, 209

[103] Celeste Fleta Corral. *Tecnología de detectores de partículas de silicio resistentes a la radiación*. PhD thesis, 2006. 115, 222

[104] M.J. García, K. Amgarou, C. Domingo, and F. Fernández. **Neutron response study of two CR-39 personal dosemeters with air and Nylon converters**. *Radiation Measurements*, **40**(2-6):607–611, November 2005. 117, 145

[105] H. Xiao. *Introduction to Semiconductor Manufacturing Technology*. 2001. 119, 135, 195

[106] K. Chino. **Behavior of Al-Si Schottky-Barrier Diodes under heat-treatment**. *Solid-State Electronics*, **16**(1):119–121, 1973. 122

[107] A. Basterfield, J. Shannon JM, Gill. **Nature of barrier height variations in alloyed Al-Si schottky-barrier diodes**. *Solid-State Electronics*, **18**(3):290–291, 1975. 122

[108] M Luszik-Bhadra. **A prototype personal neutron dosemeter with one silicon diode.** *Radiation protection dosimetry*, **96**(1-3):227–9, January 2001. 125

[109] M. Sasaki, T. Nakamura, N. Tsujimura, O. Ueda, and T. Suzuki. **Development and characterization of real-time personal neutron dosemeter with two silicon detectors**. *Nuclear Instruments and Methods in Physics Research Section A: Accelerators, Spectrometers, Detectors and Associated Equipment*, **418**(2-3):465–475, December 1998. 125

[110] A Rannou. **Dosimètre individuel électronique pour les neutrons : Saphydose-n**. *Sciences-New York*, **35**(2):223–230, 2000. 125

[111] S I Parkera, C J Kenneya, and J Segalb. **3D - A proposed new architecture for solid-state radiation detectors** . *Sensors (Peterborough, NH)*, **395**:328–343, 1997. 125

REFERENCES

[112] G. Pellegrini, F. Garcia, J. Balbuena, E. Cabruja, M. Lozano, R. Orava, and M. Ullan. **Fabrication and simulation of novel ultra-thin 3D silicon detectors**. *Nuclear Instruments and Methods in Physics Research Section A: Accelerators, Spectrometers, Detectors and Associated Equipment*, **604**(1-2):115–118, June 2009. 125

[113] Francisco García, G. Pelligrini, J. Balbuena, M. Lozano, R. Orava, and M. Ullan. **A novel ultra-thin 3D detectorFor plasma diagnostics at JET and ITER tokamaks**. *Nuclear Instruments and Methods in Physics Research Section A: Accelerators, Spectrometers, Detectors and Associated Equipment*, **607**(1):57–60, August 2009. 125

[114] J.P. Balbuena Valenzuela. *Development of innovative silicon radiation detectors*. PhD thesis, 2012. 126

[115] Michael Köhler, Richard Bates, Celeste Fleta, Karl Jakobs, Manuel Lozano, Chris Parkes, Ulrich Parzefall, Giulio Pellegrini, and Jens Preiss. **Comparative measurements of highly irradiated n-in-p and p-in-n 3D silicon strip detectors**. *Nuclear Instruments and Methods in Physics Research Section A: Accelerators, Spectrometers, Detectors and Associated Equipment*, **659**(1):272–281, December 2011. 128

[116] G. Pellegrini, M. Lozano, M. Ullán, R. Bates, C. Fleta, and D. Pennicard. **First double-sided 3-D detectors fabricated at CNM-IMB**. *Nuclear Instruments and Methods in Physics Research Section A: Accelerators, Spectrometers, Detectors and Associated Equipment*, **592**(1-2):38–43, July 2008. 134

[117] C Guardiola, C Fleta, D Quirion, J Rodríguez, M Lozano, F Teixidor, C Viñas, a R Popescu, C Domingo, and K Amgarou. **First investigations of a silicon neutron detector with a carborane converter**. *Journal of Instrumentation*, **6**(11):P11001–P11001, November 2011. 144, 181

[118] C Ã Guardiola, C Fleta, M Lozano, and G Pellegrini. **Silicon planar detectors adapted to slow neutron detection**. *International Journal*, 2010. 144, 181

[119] C Guardiola, C Fleta, G Pellegrini, F García, D Quirion, J Rodríguez, and M Lozano. **Ultra-thin 3D silicon sensors for neutron detection**. *Journal of Instrumentation*, **7**(03):P03006–P03006, March 2012. 144, 181

[120] C Guardiola, J Rodríguez, C Fleta, D Quirion, and M Lozano. **Portable Silicon Neutron Detector System**. *Spectrum*, pages 1–4, 2011. 148

[121] Bhaskar Mukherjee. **Development of a simple neutron irradiation facility with variable average energy using a light water moderated 241Am/Be source**. *Health (San Francisco)*, **9002**(95):5–7, 1995. 149

[122] R. Khelifi, P. Bode, and a. Amokrane. **Flux calculation in LSNAA using an 241Am-Be source**. *Journal of Radioanalytical and Nuclear Chemistry*, **274**(3):639–642, August 2007. 149

[123] Mythili Subramanian, Bernard Phlips, Fritz Kub, and Senior Member. **Characteristics of a Silicon on Insulator Neutron Detector**. *Ieee Nuclear Science Symposium Conference Record*, pages 1306–1309, 2009. 149

[124] S Croft. **THE USE OF NEUTRON INTENSITY CALIBRATED 9 Be (a , n) SOURCES AS 4438 keV GAMMA-RAY REFERENCE STANDARDS**. *Source*, **281**:103–116, 1989. 154

[125] M. Wielunski, R. Schütz, E. Fantuzzi, a. Pagnamenta, W. Wahl, J. Palfálvi, P. Zombori, a. Andrasi, H. Stadtmann, and Ch. Schmitzer. **Study of the sensitivity of neutron sensors consisting of a converter plus Si charged-particle detector**. *Nuclear Instruments and Methods in Physics Research Section A: Accelerators, Spectrometers, Detectors and Associated Equipment*, **517**(1-3):240–253, January 2004. 154

[126] A.R. Sattler. **Ionization Produced by Energetic Silicon Atoms within a Silicon Lattice ***. **405**(1963), 1965. 154

[127] Y Hosono. **Fast neutron detector using PIN-type silicon photodiode**. *Pulse*, **9002**(95), 1995. 154

[128] V. Linhart, I. Bědajánek, P. Bém, M. Götz, M. Honusek, S. Pospísil, and E. Šimečková. **Measurements of fast-neutron-induced signals in silicon pad detectors**. *Nuclear Instruments and Methods in Physics Research Section A: Accelerators, Spectrometers, Detectors and Associated Equipment*, **563**(1):263–267, July 2006. 154

[129] Ali Asghar Mowlavi and Rahim Koohi-Fayegh. **Determination of 4.438 MeV gamma-ray to neutron emission ratio from a (241)Am-(9)Be neutron source.** *Applied radiation and isotopes : including data, instrumentation and methods for use in agriculture, industry and medicine*, **60**(6):959–62, June 2004. 154

[130] ICRU. **Stopping of Ions heavier than Helium**. Technical report, International Commision on Radiation Units and Measurements (ICRU), 2005. 156

[131] NIST. **ESTAR-Stopping-power and range tables for electrons**. 158

[132] J Pena, L Franco, F Gómez, a Iglesias, J Pardo, and M Pombar. **Monte Carlo study of Siemens PRIMUS photoneutron production.** *Physics in medicine and biology*, **50**(24):5921–33, December 2005. 167

[133] ICMAB. **Institute of Material Science of Barcelona**. 189

[134] R.N. Grimes. *Carboranes*. 1970. 189

[135] David a Morgan, Jeremy Sloan, and Malcolm L H Green. **Direct imaging of o-carborane molecules within single walled carbon nanotubes.** *Chemical communications (Cambridge, England)*, (20):2442–3, October 2002. 189

[136] Boggavarappu Kiran, Anakuthil Anoop, and Eluvathingal D Jemmis. **Control of stability through overlap matching: closo-carborynes and closo-silaborynes.** *Journal of the American Chemical Society*, **124**(16):4402–7, April 2002. 189

[137] Núñez R González-Campo, A., Boury B., Teixidor F. **Carboranyl Units Bringing Unusual Thermal and Structural Properties to Hybrid Materials Prepared by Sol-Gel Process**. *Organometallic Chemistry*, (c):4344–4353, 2006. 189

[138] Andrew G Douglass, Krzysztof Czuprynski, Michelle Mierzwa, and Piotr Kaszynski. **An assessment of carborane-containing liquid crystal for potential device application**. *Materials Research*, **8**(11):2391–2398, 1998. 189

[139] Masateru Ito, Xin Wei, Peng-lei Chen, Haruhisa Akiyama, and Mutsuyoshi Matsumoto. **A novel method for creation of free volume in a one-component self- assembled monolayer . Dramatic size effect of para-carborane {**189
. *October*, **i**:478–483, 2005.

[140] Verena M Ahrens, Sven Stadlbauer, and Annette G Beck-sickinger. **Incorporation of ortho-Carbaboranyl-N-Modified l-Lysine into NeuropeptidNeuropeptide Y Receptor Y 1 - and Y 2 -Selective Analogues**. *Journal of Medicinal Chemistry*, pages 2368–2377, 2011. 189

[141] S. Franssila. *Introduction to Microfabrication*. 2004. 191

[142] MSDSBoron. **Material Safety Data Sheet (MSDS) Boron.** 194

[143] Hoffman D.W. Thornton, John A. **Stress-related effects in thin films**. *Thin Solid Films*, **171**:5–31, 1989. 196

[144] S Labov, S Bowyer, and G Steele. **Boron and silicon: filters for the extreme ultraviolet.** *Applied optics*, **24**(4):576, February 1985. 197

[145] George E. Thomas. **New technique for producing thin boron films**. *Nuclear Instruments and Methods in Physics Research Section A: Accelerators, Spectrometers, Detectors and Associated Equipment*, **282**(1):124–127, October 1989. 197

[146] Manuela Vidal-Dasilva, Mónica Fernández-Perea, José a Méndez, José a Aznárez, and Juan I Larruquert. **Electron-beam deposited boron coatings for the extreme ultraviolet.** *Applied optics*, **47**(16):2926–30, June 2008. 197

[147] D S Mcgregor, R T Klann, H K Gersch, and Y H Yang. **Thin-film-coated bulk GaAs detectors for thermal and fast neutron measurements**. **466**:126–141, 2001. 197

[148] S L Bellinger, R G Fronk, W J Mcneil, T J Sobering, and D S Mcgregor. **Improved High Efficiency Stacked Microstructured Neutron Detectors Backfilled With Nanoparticle LiF**. *Methods*, **59**(1):167–173, 2012. 197

[149] B.B. Mandelbrot. *The fractal geometry of nature*. W.h. freem edition, 1983. 207

[150] W Kwaśny. **Predicting properties of PVD and CVD coatings based on fractal quantities describing their surface**. *Manufacturing Engineering*, **37**(2):125–192, 2009. 207

[151] H.H. Durmazuçar G. Gündüz. **Effect of fractal structure on epitaxial growth**. *Journal of Materials Science Letters*, **17**:1821–1823, 1998. 207

[152] E Martnez, A Lousa, and J U Esteve. **Micromechanical and microtribological properties of BCN thin films near the B 4 C composition deposited by r . f . magnetron sputtering**. *Diamond and Related Materials*, pages 1892–1896, 2001. 209

[153] E Pascual, E Mart, J Esteve, and A Lousa. **Boron carbide thin films deposited by tuned-substrate RF magnetron sputtering**. *Diamond and Related Materials*, **8**:402–405, 1999. 209

[154] Universitat De Barcelona. **BCN thin films near the B C composition deposited by radio frequency magnetron sputtering**. *Diamond and Related Materials*, **9**:502–505, 2000. 209

[155] A Lousa, J Esteve, E Pascual, and E Martínez. **Effect of ion bombardment on the properties of B 4 C thin films deposited by RF sputtering**. *Thin Solid Films*, **356**:210–213, 1999. 209, 210

[156] H. Spieler. *Semiconductor detector systems*. Oxford University Press, 2005. 215

[157] P. Hill, W. and Horowitz. *The art of electronics*. Cambridge University Press, 1989. 215

[158] Geoff Delaney, Susannah Jacob, Carolyn Featherstone, and Michael Barton. **The role of radiotherapy in cancer treatment: estimating optimal utilization from a review of evidence-based clinical guidelines.** *Cancer*, **104**(6):1129–37, September 2005. 226

[159] H A D Ronic, Paula L Petti, and Arlene J Lennox. **Had:ronic radiotherapy 1**. *Therapy*, pages 155–197, 1994. 226

[160] R R WILSON. **RADIOLOGICAL USE OF FAST PROTONS**. *Radiology*, **47**(5):487–491, 1946. 226

[161] Koji Noda. **REVIEW OF HADRON THERAPY ACCELERATORS WORLDWIDE AND FUTURE TRENDS**. *Proceedings of IPAC2011*, **i**:3784–3788. 226

[162] ENLIGHT Collaboration. **ENLIGHT-The European Network for LIGht ion Hadron Therapy**. 226

[163] Niels Bassler, Oliver Jäkel, Christian Skou Sø ndergaard, and Jørgen B Petersen. **Dose- and LET-painting with particle therapy.** *Acta oncologica (Stockholm, Sweden)*, **49**(7):1170–6, October 2010. 228

[164] R Orecchia, A Zurlo, A Loasses, M Krengli, G Tosi, S Zurrida, P Zucali, and U Veronesi. **Review Particle Beam Therapy (Hadrontherapy): Basis for Interest and Clinical Experience**. *Science*, **34**(4), 1998. 228

[165] P D Bradley, a B Rosenfeld, and M Zaider. **Solid state microdosimetry.** *Nuclear instruments & methods in physics research. Section B, Beam interactions with materials and atoms*, **184**(1-2):135–57, September 2001. 229

[166] T Kanai, M Sudo, N Matsufuji, and Y Futami. **Initial recombination in a parallel-plate ionization chamber exposed to heavy ions.** *Physics in medicine and biology*, **43**(12):3549–58, December 1998. 229

[167] Steven L Bellinger, Ryan G Fronk, Timothy J Sobering, and Douglas S Mcgregor. **High-efficiency microstructured semiconductor neutron detectors that are arrayed , dual-integrated , and stacked**. *Applied Radiation and Isotopes*, **70**(7):1121–1124, 2012. 230

Scientific contributions

Publications

- C. Guardiola, F. Gómez, C. Fleta, J. Rodríguez, D. Quirion, G. Pellegrini, A. Lousa, L. Martínez-de-Olcoz, M. Pombar, M. Lozano, *Neutron measurements with ultra-thin 3D silicon sensors in radiotherapy treatment rooms*, submitted to Physics in Medicine and Biology, September 2012.

- G. Pellegrini, J. Balbuena, D. Bassignana, E. Cabruja, C. Fleta, C. Guardiola, M. Lozano, D. Quirion, M. Ullán , *3D Double Sided Detector Fabrication at IMB-CNM*, Nuclear Instruments and Methods in Physics Research A, http://dx.doi.org/10.1016/j.nima.2012.05.087, May 2012.

- C. Guardiola, K. Amgarou, C. Fleta, M. Lozano, *Monte Carlo simulations of a microstructured silicon detector with high efficiency for thermal neutrons*, Journal of Instrumentation, doi:10.1088/1748-0221/7/06/T06003, June 2012.

- C. Guardiola, C. Fleta, G. Pellegrini, F. Garca, D. Quirion, J. Rodríguez, M. Lozano, *Ultra-thin 3D silicon sensors for neutron detection*, Journal of Instrumentation, doi: 10.1088/1748-0221/7/03/P03006, February 2012.

- C. Guardiola, C.Fleta, D. Quirion, J. Rodríguez, M. Lozano, F. Teixidor, C. Vias, C. Domingo, K. Amgarou, *First investigations of a silicon neutron detector with a carborane converter*, Journal of Instrumentation, doi: 10.1088/1748-0221/6/11/P11001, November 2011.

- C. Guardiola, K. Amgarou, F. García, C.Fleta, D. Quirion, M. Lozano, *Geant4 and MCNPX simulations of thermal neutron detection with planar silicon*

detectors, Journal of Instrumentation, doi: 10.1088/1748-0221/6/09/ T09001, September 2011.

- C. Guardiola, C. Fleta, M. Lozano, G. Pellegrini, *Silicon planar detectors adapted to slow neutron detection*, International Journal of Numerical Modelling: Electronic Networks, Devices and Fields, doi:10.1002/jnm.754, July 2010.

Proceedings

- F. García, G. Pellegrini, M. Lozano, J.P. Balbuena, C. Fleta, C. Guardiola, D. Quirion, *Ultra Thin 3D Silicon Detector for Plasma Diagnostics at the ITER Tokamak*, 2011 IEEE Nuclear Science Symposium and Medical Imaging Conference, pp 199-201, 2011.

- C. Guardiola, J. Rodríguez, C. Fleta, D. Quirion, M. Lozano, *Portable Silicon Neutron Detector System*, Proceeding of the 8th Spanish Conference on Electron Devices, CDE'2011, art. no. 5744236., 2011.

- C. Guardiola, M. Lozano, G. Pellegrini, *Neutron Detection with Silicon Devices*, Proceeding of the 7th Spanish Conference on Electron Devices, CDE'2009, art. no. 4800428, pp. 54-56., 2009.

Patents

- **Deposit of ^{10}B thick coatings by evaporation.**
  Inventors: C. Guardiola, J. Calvo, M. Lozano, C. Fleta, G. Pellegrini, F. García.
  Patent ref: P201231604.

- **Solid-liquid neutron detector.**
  Inventors: C. Guardiola, M. Lozano, C. Fleta, G. Pellegrini, D. Quirion.
  Patent ref: P201231769.

Participation in Projects

- **RAMPO**:Portable Multi-Radiometer.
  Granted by: Catalunya's Generalitat (VALTEC09-2-0094).
  Directed by: Manuel Lozano Fantoba (IMB-CNM).

- **NEUTOR III**: Development of a high sensitivity neutron monitor based on thin silicon diodes with neutron converter layers.
  Granted by: Spanish Ministry of Science and Innovation (CIT-300000-2009-011).
  Directed by: María Celeste Fleta Corral (IMB-CNM).

- **REWARD**: Real-time Wide-Area Radiation Surveillance System .
  Granted by: 7th Framework Programme for Research (FP7-SEC-2011-1).
  Directed by: Manuel Lozano Fantoba (IMB-CNM).

Acknowledgements